INSTALLED JET NOISE

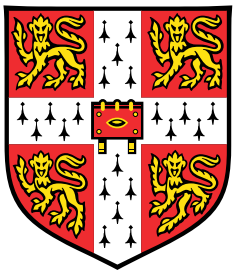

Benshuai Lyu

Department of Engineering
University of Cambridge

This thesis is submitted for the degree of
Doctor of Philosophy

Hughes Hall

February 27, 2018

..
ii

Installed jet noise

Benshuai Lyu

This thesis studies the prediction and reduction of installed jet noise, combining both analytical and experimental techniques. In the prediction part, it starts with formulating a low-order but robust isolated jet noise prediction model, based on which a remarkably fast code (with pre-informed data) is developed. A semi-empirical low-order model is then developed to predict installed jet noise. The model consists of two parts, the first of which is based on the Lighthill's acoustic analogy theory. The second part embraces Amiet's approach to model the sound due to the scattering of jet instability waves.

It is shown that the significant low-frequency noise enhancement observed in installed jet experiments is due to the scattering of near-field instability waves. The trailing edge scattering model can successfully predict noise spectra at all distinct angles. The sound due to instability wave scattering is only significant at low frequencies and it is negligible at high frequencies. The high-frequency sound alteration, however, is due to the scattering of Lighthill's quadruple sources. This quadrupole-induced sound is either efficiently shielded at 90° to the jet axis on the shielded side or enhanced by around 3 dB at 90° on the reflected side. But these effects gradually diminish as the observer angle decreases. The high-frequency spectra can be robustly predicted at large observer angles while deviation occurs at low observer angles due to jet refraction effects.

An experimental study on installed jet noise is then conducted to enhance our understanding of installed jet noise and to further validate the prediction model. It is demonstrated that increasing H (the separation distance between the jet centreline and the flat plate) causes the low-frequency enhancement to decrease exponentially but results in little change for both the shielding and reflection effects at high frequencies. Increasing L (the distance between the trailing edge of the plate and jet nozzle exit), on the other hand, produces stronger noise intensification at low frequencies and slightly more effective shielding or reflection effects at high frequencies. The installation effects are found to be less pronounced as the Mach number increases. Excellent agreement between the experimental results and model predictions is achieved at low frequencies for all plate positions and Mach numbers tested. At high frequencies, the noise spectra at 90° on the reflected side on can also be correctly predicted. At lower observer angles, deviations occur due to jet refraction effects.

In the noise reduction part, an experimental study is firstly carried out to study the effects of lobed nozzles on installed jet noise at constant flow rates. It is found that lobed nozzles do not noticeably change the installed jet noise spectra at low frequencies. However, they do result

in a slight noise reduction at high frequencies. The effects of lobed nozzles are only slightly different on the two sides of the flat plate. To understand why lobed nozzles hardly change low-frequency installed jet noise, an analytical stability analysis for lobed vortex sheets is performed. The results show that lobed jets change both the convection velocity and the temporal growth rate of instability waves. The changes become more pronounced as the number of lobes N and the penetration ratio ϵ increase. However, instability waves of different orders are affected differently by the lobe geometry. In particular, little change occurs for mode 0, while high-order jet instability waves change significantly when $N > 1$. Based on the analytical results, it is postulated that the little change of the low-frequency installed jet noise observed in the experiment could be either due to the realistic jet mean flow becoming axisymmetric too quickly, or due to the fact that the 0th-order jet instability waves are not sensitive to the lobe geometry.

A second set of experiments in the noise reduction part is carried out to explore the possibility of reducing installed jet noise by using two pylons. It is proposed that the two pylons may be able to suppress jet instability waves, and hence reduce installed jet noise, by imposing two normal-velocity-vanishing boundary conditions at different azimuthal angles. The results show that installed jet noise is reduced by around $2 \sim 3$ dB at low frequencies. At high frequencies, a noise increase is observed, which is due to a conservative constant-flow-rate comparison. It is concluded that using two pylons to reduce installed jet noise has significant practical potential.

I would like to dedicate this thesis to my beloved parents.

Declaration

I hereby declare that

- this dissertation is the results of my own work and includes nothing which is the outcome of work done in collaboration except as declared in the Preface and specified in the text;
- this dissertation is not substantially the same as any that I have submitted, or, is being concurrently submitted for a degree or diploma or other qualification at the University of Cambridge or any other University or similar institution except as declared in the Preface and specified in the text. I further state that no substantial part of my dissertation has already been submitted, or, is being concurrently submitted for any such degree, diploma or other qualification at the University of Cambridge or any other University or similar institution except as declared in the Preface and specified in the text;
- this dissertation contains fewer than 65,000 words including appendices, bibliography, footnotes, tables and equations and has fewer than 150 figures, and therefore, it does not exceed the prescribed word limit.

Benshaui Lyu
February 27, 2018

Acknowledgement

First, I am deeply indebted to my supervisor, Prof Dame Ann Dowling, who has always been able to provide instrumental suggestions. This thesis would not have been possible without her tremendous support, considerable encouragement and effective supervision. Prof Dowling is patient, kind, knowledgeable and a world-renowned expert in the field of aeroacoustics. Her vast knowledge in acoustical physics has helped me tremendously over the past three years. I especially thank her for consistently maintaining regular meetings with me, no matter how busy she is. Those regular meetings have been crucial in my study.

Second, I would like to gratefully thank my advisor, Dr Anurag Agarwal, for his invaluable advice on both my study and my life. In particular, I thank him for his valuable suggestions during our preliminary meeting and his generous help in finding relevant literature. I also thank Dr Karthik Depuru-Mohan for his kind help in answering my questions about Fluent software. I express my sincere gratitude to Ms Robena French for her wonderful coordination in arranging those regular meetings with Prof Dowling and her incredible kindness in helping me sorting out many paper forms.

Special thanks go to the technician of the Acoustics Laboratory, Mr John Hazlewood, especially for his help in setting up the experimental rig and in his ingenious way of sorting out electrical cables. I specially thank the technician of the Aerodynamics Laboratory, Mr Sam Flint, for his enthusiastic help on Solidworks. I am very grateful for having the wonderful colleagues working together in the Acoustics Laboratory and miss terribly the tea and cake sessions that we use to have together. I also wish to thank all the other wonderful people that I have been working with throughout the years.

Last, but in no way the least, my deepest thanks go to my loving parents, who have been constantly supporting me to pursue my dream for more than 20 years, without which every exciting moment in my life would not have been possible. I am extremely lucky to have Benzhen, Lianlian and Shujie in my life. Their constant care, love and especially understanding during my pursing the Doctor degree are the best gifts I have ever received.

Contents

List of Figures

List of Tables

Nomenclature

Acronyms

BEM	Boundary Element Method
CABARET	Compact Accurately Boundary-Adjusting high-REsolution Technique
CFD	Computational Fluid Dynamics
CONJURE	Calculating Observer-dependent Noise of Jets Utilizing RANS's Efficiency
DNS	Direct Numerical Simulation
FSS	Fine-Scale Spectrum
FW-H	Ffowcs Williams-Hawkings
JSI	Jet Surface Interaction
JSR	Jet Surface Reflection
LEE	Linearized Euler Equation
LES	Large Eddy Simulation
LSS	Large-Scale Spectrum
LST	Linear Stability Theory
NPR	Nozzle Pressure Ratio
ODE	Ordinary Differential Equation
PIV	Particle Image Velocimetry
POD	Proper Orthogonal Decomposition

PSD	Power Spectral Density
PSE	Parabolized Stability Equation
RANS	Reynolds Average Navier-Stokes simulation
SPL	Sound Pressure Level
WKB	Wentzel-Kramers-Brillouin

Greek Symbols

α	Streamwise wavenumber of instability waves
α_d	Flap deflection angle
β	Doppler factor $\sqrt{1-M_a^2}$
δ	Conventional generalized δ function
δ_{ij}	Kronecker delta
ϵ	Penetration ratio
ϵ_m	Defined to be 1 for $m = 0$ and 2 otherwise
ϵ_s	Jet spreading rate
η	Spectral correlation coefficient
η'	Small perturbation of the vortex-sheet radius
η_i'	Fluctuation sources defined as $-\rho v_i'' h_0'' - q_i' + \sigma_{ij} v_j''$
$\tilde{\eta}_i$	Fluctuation sources defined as $\tilde{H}_i - \tilde{T}_{ij}\tilde{v}_j$
ε	Turbulence dissipation rate
Γ	Function defined in Chapter 5
γ	Gas specific ratio
γ_0	Radial decay rate
γ_c	Convective radial decay rate

G^a	Adjoint Green's function
k_0	Acoustic wavenumber ω/c_0
λ	Eigenvalue of matrix $\boldsymbol{A}$
λ_n	Eigenvalues
μ	Scattering-related wavenumber
μ_A	Scattering-related wavenumber
μ_i	Characteristic wavenumber $\sqrt{\alpha^2 - \Omega^2/\bar{c}^2}$ inside the vortex sheet
μ_o	Characteristic wavenumber $\sqrt{\alpha^2 - \Omega^2/\bar{c}^2}$ outside the vortex sheet
ν	Dynamic viscosity
Ω	$\omega - \alpha U$
ω	Angular frequency
Ω_0	A domain in the ambient region
$\bar{\Pi}$	Reduced spectrum
$\bar{\varphi}$	Stretched azimuthal angle for the observer in the spherical coordinate system
$\bar{\varphi}_0$	Stretched azimuthal angle for the source in the spherical coordinate system
Φ	Acoustic PSD
ϕ	Azimuthal coordinate in the cylindrical coordinate system
Φ_N	Acoustic PSD due to near-field scattering
ϕ_n	Eigenfunctions
Φ_Q	Acoustic PSD due to quadrupole sources
Π	Correlation-defined spectrum
π	Coupled fluctuation quantity $\rho h'' + \rho' \tilde{h}$
Π_0	Single-sided modal PSD measured at $\sigma = \sigma_0$

Π_s	Single-sided modal PSD
Ψ	Entropy and viscous sources of Lilley's equation
ψ	Potential for perturbation velocity
ψ^+	Velocity potential outside the vortex sheet
Ψ_n^+	Separated-form potentials outside the vortex sheet
ψ^-	Velocity potential inside the vortex sheet
Ψ_n^-	Separated-form potentials inside the vortex sheet
φ	Azimuthal angle in the spherical coordinate system
ζ	Independent pressure variable of Lilley's equation
$\bar{\rho}$	Base flow density
$\bar{\rho}_i$	Base flow density inside the vortex sheet
$\bar{\rho}_o$	Base flow density outside the vortex sheet
ρ	Fluid density
ρ'	Fluctuation density
ρ_0	Ambient fluid density
$\bar{\sigma}$	Stretched radial coordinate for the observer in the cylindrical coordinate system
$\bar{\sigma}_0$	Stretched radial coordinate for the source in the cylindrical coordinate system
σ	Radial coordinate in the cylindrical coordinate system
σ_0	Radius of jet plume
σ_1	A fixed radial coordinate
σ_2	A fixed radial coordinate
σ_{ij}	Viscous stress
$\bar{\theta}$	Stretched polar angle for the observer in the spherical coordinate system

$\bar{\theta}_0$ Stretched polar angle for the source in the spherical coordinate system

τ_s Eddy life time

θ Polar angle (e.g. observer angle) in the spherical coordinate system

$\tilde{\tau}_{ij}$ Base flow tensor components defined as $\delta_{ij}\bar{p} - \tilde{T}_{ij} - \bar{\sigma}_{ij}$

Roman Symbols

$\boldsymbol{A}$ Eigen matrix

A Amplitude of the derivatives of the Green's function

a Mean radius of the vortex sheet

a_ϵ Mean radius of the lobed nozzle in the experiment

a_i Complex numbers of small moduli

A_m Expansion coefficients in front of $E_n^{\pm}$

A_{ijkl} Amplitudes of R_{ijkl}

$\boldsymbol{B}$ General matrix

$\boldsymbol{B}_2$ General matrix

B_m Expansion coefficients in front of Hankel functions

$\bar{c}$ Local speed of sound for base flow

$\bar{C}^+$ Non-normalized expansion coefficients outside the vortex sheet

$\bar{C}^-$ Non-normalized expansion coefficients inside the vortex sheet

$\bar{\boldsymbol{C}}^+$ Vector form of $\bar{C}_n^+$

$\bar{\boldsymbol{C}}^-$ Vector form of $\bar{C}_n^-$

$\boldsymbol{C}$ General vector

$\boldsymbol{C}^+$ Vector form of C_n^+

$\boldsymbol{C}^-$ Vector form of C_n^-

c	Chord length, Chapter 5
c	Local speed of sound $\gamma p/\rho$
c_0	Ambient speed of sound
c_τ	Proportionality constant for τ_s
c_i	Proportionality constant for l_i
c_k	Expanding coefficients, Chapter 3
C_m^n	Binomial coefficient
C_n^+	Expansion coefficients outside the vortex sheet
C_n^-	Expansion coefficients inside the vortex sheet
c_p	Specific heat at constant pressure
c_v	Specific heat at constant volume
C_{1n}	Arbitrary constant
C_{2n}	Arbitrary constant
C_{ijkl}	Amplitude constants for A_{ijkl}
$\boldsymbol{D}_i$	Column vectors of matrix $\boldsymbol{B}$ $(i = \cdots -2, 1, 2 \ldots)$
D	Conventional material derivative operator
D_0	Conservative-form differential operator
$\overline{\mathrm{D}}$	Base-flow defined material derivative operator
D	Jet diameter
d	Span
D_n	Functions defining the dispersion relationship
D_{ij}^k	Directivity terms
$\boldsymbol{e}_\phi$	Unit vector in the azimuthal direction

$\boldsymbol{e}_\sigma$	Unit vector in the radial direction
$\hat{E}'_i$	Fourier transform of E'_i
$\tilde{e}_{ij}$	Fluctuation sources defined as $\tilde{T}_{ij} - \delta_{ij}(\gamma - 1)\tilde{H}_0$
E	An error function
E_0	An error function
E'_i	Zero-mean total enthalpy flux fluctuations
E^+_m	Eigenfunctions outside the vortex sheet
E^-_m	Eigenfunctions inside the vortex sheet
e_{ij}	Defined as $-(\rho v''_i v''_j + \tilde{T}_{ij} - \sigma'_{ij})$
e'_{ij}	Fluctuation sources defined as $-\rho v''_i v''_j + \sigma'_{ij} + \delta_{ij}\frac{\gamma-1}{2}\rho v''^2$
$\bar{f}_m$	Transformed f_m
$\hat{f}$	Fourier Transform of function f
$\mathcal{F}$	Function defining the vortex sheet profile
$\mathcal{F}_p$	Function defining the perturbed vortex sheet profile
f	General mathematical function
f_m	Separated functions of radius σ
$\boldsymbol{G}$	Gauge vector
$\hat{G}^a$	Fourier Transform of Green's function G^a
g	General mathematical function
G^s	Green's function for the causal adjoint problem
g_n	Components of Gauge vector $\boldsymbol{G}$
g_{ij}	Propagation tensor components
$\tilde{h}$	Base flow enthalpy (e.g. Favre average)

$\tilde{h}_0$	Defined as $\tilde{h} + \frac{1}{2}\tilde{v}^2$
$\tilde{H}_0$	Non-linear term in the base flow energy equations
$\tilde{H}_j$	Non-linear terms in the base flow energy equations
H	Separation distance between the jet centreline and the wing or flat plate
h	Fluid enthalpy
h''	Fluctuation enthalpy (e.g. Favre average)
h_0	Total enthalpy
h_0''	Defined as $h'' + v''^2/2$
$H_n^{(1)}$	Hankel functions of the first kind
$H_n^{(2)}$	Hankel functions of the second kind
$\boldsymbol{I}$	Diagonal matrix
$\boldsymbol{I}_c$	First-order coupling matrix
$\boldsymbol{I}_d$	Fully coupled matrix
$\boldsymbol{I}_i$	Column vectors of the identity matrix ($i = \cdots -2, 1, 2 \ldots$)
$\boldsymbol{I}_k$	Fully coupled matrix
$\boldsymbol{I}_s$	First-order coupling matrix
$\tilde{\boldsymbol{I}}_d$	Normalized fully coupled matrix
$\tilde{\boldsymbol{I}}_k$	Normalized fully coupled matrix
I_n	Modified Bessel functions of the first kind
I_{ijkl}	Sound propagation tensor components
J_n	Bessel functions of the first kind
$\bar{k}_z$	Mean streamwise wavenumber
$\boldsymbol{K}$	Diagonal matrix

$\boldsymbol{K}_c$	First-order coupling matrix
$\boldsymbol{K}_s$	First-order coupling matrix
$\tilde{\boldsymbol{K}}_d$	Normalized fully coupled matrix
$\tilde{\boldsymbol{K}}_k$	Normalized fully coupled matrix
k	Turbulence intensity
k_1	ω/U_c
k_2	Spanwise wavenumber
K_n	Modified Bessel functions of the second kind
k_z	Wavenumber in the z direction
k_z'	Wavenumber in the z direction
$\boldsymbol{K}_d$	Fully coupled matrix
$\hat{\mathcal{L}}^a$	Linear adjoint operator in the frequency domain
$\mathcal{L}$	Linear differential operator
$\mathcal{L}^a$	Adjoint operator of $\mathcal{L}$
L	Distance between jet exit and the wing's or the plate's trailing edge
l_i	Eddy correlation lengths
$\bar{M}$	Local base flow Mach number U/c_0
$\boldsymbol{m}$	Vector form of m_j
M	Largest mode number included
m	Azimuthal mode number
M_0	Jet Mach number
M_a	Ambient Mach number
m_j	Momentum fluctuation $\rho v_j''$

$\boldsymbol{n}$	Unit vector perpendicular to the lobed profile
N	Number of lobes
n	Azimuthal mode number
N_0	Small integer
$\bar{p}$	Base flow pressure
$\hat{p}$	Separated-form fluctuation pressure
$\hat{p}'$	Fourier Transformation of p'
$\hat{p}_i$	Separated-form fluctuation pressure inside the vortex sheet
$\hat{p}_o$	Separated-form fluctuation pressure outside the vortex sheet
P	Near-filed pressure spectrum
p	Pressure
p'	Fluctuation pressure
p_∞	Ambient pressure
p'_e	New independent fluctuation variable
p_f	Far-field sound pressure due to instability wave scattering
p_{ij}	Total stress tensor components in the fluid
$\bar{q}_j$	Base flow heat flux per unit volume
q_j	Heat flux per unit volume
q'_j	Fluctuation heat flux per unit volume
$\bar{R}$	Stretched distance
$\bar{r}$	Stretched radial coordinate for the observer in the spherical frame
$\bar{R}'$	Stretched distance
$\bar{r}_0$	Stretched radial coordinate for the source in the spherical frame

$\mathcal{R}$	Vortex sheet profile
Re	Reynolds number
R	Cross correlation
R	Gas constant, Chapter 3
r	Radial coordinate in the spherical coordinate system
R_{ijkl}	Space-time correlation tensor components
$\bar{S}$	Stretched distance
$\hat{S}'$	Fourier transform of S'
σ'_{ij}	Fluctuation viscous stress components
$\tilde{\sigma}_{ij}$	Base flow viscous stress components
S	Entropy
S'	Full source term
S_0	Stretched distance
St	Strouhal number
$\hat{T}_{ij}$	Fourier Transform of Lighthill stress tensor components
$\hat{T}'_{ij}$	Fourier transform of T'_{ij}
τ	Time
$\tilde{T}_{ij}$	Non-linear tensor components in the base flow momentum equations
T	Fluid temperature
T	Time interval for Fourier Transforms, Chapter 4 and 5
t	Time
T_∞	Ambient temperature
T_j	Jet temperature

T_{ij}	Lighthill stress tensor components
T'_{ij}	Zero-mean momentum fluctuation stress components
$\bar{U}_c$	Averaged convection velocity
$\boldsymbol{U}$	Steady base flow velocity
U	Parallel flow streamwise velocity
u	Statistical quantity
u^*	Wall friction velocity
U_a	Ambient flow velocity
U_c	Convection velocity of instability waves
u'_i	New independent fluctuation variables $m_i/\bar{\rho}$
U_j	Jet exit velocity
U_z	Defined to be U inside but 0 outside of the vortex sheet
$\bar{v}_i$	Base flow velocity in the i direction
$\boldsymbol{v}$	Fluid velocity
$\boldsymbol{v}'$	Perturbation velocity
$\boldsymbol{v}'^+$	Perturbation velocity outside the vortex sheet
$\boldsymbol{v}'^-$	Perturbation velocity inside the vortex sheet
$\hat{v}_i$	Separated-form fluctuation velocity in the i (i can be σ, ϕ or z) direction
$\tilde{\boldsymbol{v}}$	Vector form of $\tilde{v}_j$
$\tilde{v}$	Defined as $\sqrt{\tilde{v}_i \tilde{v}_i}$
$\tilde{v}_i$	Base flow velocity in the i direction (e.g. Favre average)
V	Integration volume
v''	Defined as $\sqrt{v''_i v''_i}$

v_i	Velocity in the i direction
v_i''	Fluctuation velocity in the i direction (e.g. Favre average)
v_i'	Fluctuation velocity in the i (i can be 1, 2, 3, σ, ϕ or z) direction
v_i^a	Fluctuation velocity in the i direction relative to the ambient flow
V_y	Integration volume
$V_{\Delta y}$	Integration volume
W	Width of the flap cut-out
$\bar{x}_i$	Stretched Cartesian coordinates
x_i	Cartesian coordinates ($i = 1, 2, 3$)
$\bar{y}_i$	Stretched Cartesian coordinates
$\boldsymbol{\Delta y}$	Vector form of Δy_i
$\boldsymbol{x}$	Position vector
$\boldsymbol{y}$	Position vector
Δy_i	Separation distance in the i direction
y^+	Dimensionless wall distance
$\bar{z}$	Stretched streamwise coordinate for the observer in the cylindrical coordinate system
$\bar{z}_0$	Stretched streamwise coordinate for the source in the cylindrical coordinate system
z	Streamwise coordinate in the cylindrical coordinate system

Part I

INTRODUCTION

Chapter 1

Introduction

Aircraft noise is believed to be one of the most commonly reported residential disturbances (Pepper et al., 2003). Air traffic is, however, continuously increasing and expected to double by 2031 (Federal Aviation Administration, 2011). Governments in many countries have therefore enacted legislative control, and aircraft manufacturers are now exposed to more and more stringent noise regulations (Casalino et al., 2008).

The noise for a modern commercial aircraft comprises different components, for example airframe noise, fan noise, jet noise etc. Among the different noise sources, jet noise is believed to be the dominant component. Since the debut of high-bypass-ratio turbofan engines, aircraft noise has been reduced by more than 20 EPNdB, due in large part to the reduction of jet noise (Casalino et al., 2008). However, in modern high-bypass-ratio turbofan engines, the jet still contributes to more than half of the acoustic energy during take-off (Casalino et al., 2008). Further research on jet noise mitigation is still in urgent demand.

Jet noise is generated by the high speed turbulent jet flow exiting through the engine exhaust. The unsteady pressure fluctuations within the turbulent jet are able to radiate sound to the far-field. This can be better understood by simplifying the turbulent flow to an eddy agglomerate, as shown in figure 1.1. The eddies, represented by the spirals in figure 1.1, refer to the coherent swirling structures appearing in the turbulent flow. The eddies are convected by the jet mean

Figure 1.1: Turbulent jet flow exiting through an engine exhaust.

flow. They are inherently unsteady and can be regarded as sound sources. The far-field sound is thus comprised of the contributions from different eddies. As can be seen from figure 1.1, the sizes of the eddies vary, with small ones close to the exhaust radiating high frequency sound and large ones further downstream contributing to sound in the low-frequency regime.

The eddy agglomerate is, however, only a qualitative explanation. A quantitative and also more rigorous theory is the well-known acoustic analogy of Lighthill (1952). The analogy equation is obtained by rearranging the Navier-Stokes equation, and is therefore exact. It showed that the noise due to turbulent jets is equivalent to that produced by a distribution of quadrupole sources. The strength of these quadrupoles can be expressed as the Lighthill stress tensor, $T_{ij} = \rho v_i v_j + p_{ij} - (\rho - \rho_0)c_0^2\delta_{ij}$, where ρ is the fluid density, ρ_0 ambient fluid density, v_i and v_j the Cartesian velocity components in the i and j direction respectively $(i, j = 1, 2, 3)$, p_{ij} the stress tensor, c_0 the speed of sound and δ_{ij} Kronecker delta. One of the most important early discoveries from the Lighthill theory was that the far-field sound intensity produced by a subsonic jet is proportional to the eighth power of the jet Mach number. Since then, this important discovery has led to a significant reduction of jet noise by increasing the bypass-ratio of jet engines.

Based on the Lighthill's acoustic analogy theory, a large amount of research has been conducted. Theoretical works include improved acoustic analogy theories by taking into account the effects of source convection, mean flow refraction etc (Williams, 1963; Lilley, 1974; Dowling et al., 1978; Goldstein, 2003). Extensive experimental study was also carried out, confirming the excellent validity of the eighth-power law and providing a comprehensive jet noise database. Analysing the experimental data also enabled various generalizations of the jet noise spectra and accordingly suggestions of the sound source mechanisms. It is worth noting that the vast majority of research work during this time is for an isolated nozzle and jet. But the realistic configuration of a modern aircraft often involves the jet engines installed below the aircraft wings, as shown in figure 1.2. The effects of wings and other high-lift devices on the

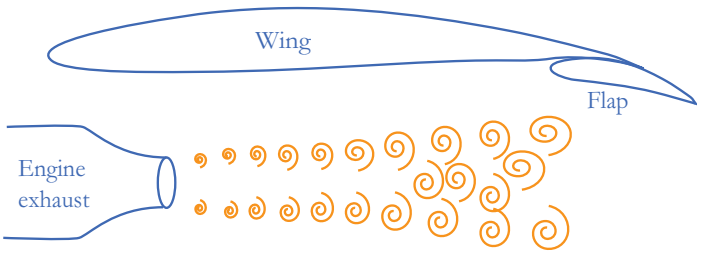

Figure 1.2: The schematic illustration of an installed engine.

jet noise is often referred to as the jet installation effects and the resulting jet is commonly

called an installed jet and compared to the isolated jet. Research has shown that the presence of solid boundaries can greatly affect acoustic source behaviours (Curle, 1955; Williams and Hall, 1970). Consequently, the close presence of aircraft wings can significantly alter jet noise heard in the far-field (Bushell, 1975; Fisher et al., 1977; Way and Turner, 1980; Shearin, 1983). The investigation into installed jet noise has been, however, rather limited. Particularly, there is a general lack of reliable prediction models and also of the understanding of the noise alteration mechanism. This thesis aims to bridge the gap, i.e. to develop a reliable model that can predict installed jet noise robustly, to advance the understanding of the noise alteration mechanism, and ultimately, to aid the development of innovative noise reduction techniques.

The rest of this thesis is structured as follows. Chapter 2 presents a literature review on isolated and installed jet noise, with the primary focus on installed jet noise. As will become clear in the rest of this thesis, jet instability waves play an important role in the context of installed jet noise. Therefore, Chapter 3 is devoted to a review on the stability theories of jets. In Chapter 4, a low-order prediction model for isolated jet noise is developed and the results are compared with experiments. Chapter 5 develops a hybrid prediction model for installed jet noise. The results are also validated against experimental data. In the following chapter, an experimental study on installed jet noise is carried out, where both the effects of plate positions and Mach numbers are examined. Chapter 7 firstly presents a set of experimental results on the noise from lobed jets. To understand the results, an analytical stability analysis for lobed jets is performed. Chapter 8 explores the possibility of reducing installed jet noise by using two pylons, while Chapter 9 concludes this thesis and outlines future work.

Chapter 2

Jet Noise Review

In this chapter, a brief review of the existing literature on jet noise is presented. Before presenting the research work on installed jet noise, the literature on the prediction models for isolated jet noise is briefly reviewed. In the following review of installed jet noise, both experiments and prediction models are presented in a detailed chronological order.

2.1 Isolated jet noise

Due to the inherent difficulties of identifying the sound sources in a turbulent jet, acoustic analogy theories have long been the standard approach to predict jet noise. Critical investigation started in 1952, when Sir James Lighthill published the first part of his well-known paper "On sound generated aerodynamically" (Lighthill, 1952), marking also the birth of "aeroacoustics" (Tam, 1998). By rearranging Navier-Stokes equations, Lighthill showed that

$$\left(\frac{\partial^2}{\partial t^2} - c_0^2 \frac{\partial^2}{\partial x_i \partial x_i}\right)(\rho - \rho_0) = \frac{\partial^2 \left(\rho v_i v_j + p_{ij} - c_0^2(\rho - \rho_0)\delta_{ij}\right)}{\partial x_i \partial x_j}, \tag{2.1}$$

where t denotes time and x_i $(i = 1, 2, 3)$ denotes the Cartesian coordinate in the i direction. The solution of $\rho - \rho_0$ can be obtained by making use of the well-known free-space Green's function provided the right hand side of equation 2.1 is known. At high Reynolds number, viscous forces are negligible compared with inertial forces. And if the mean flow is further assumed to be isothermal such that pressure fluctuation is exactly cancelled by $c_0^2(\rho - \rho_0)$, the source term on the right hand side of equation 2.1 can be approximated by $\rho v_i v_j$. By further assuming the turbulence eddies are acoustically compact, the far-field sound intensity is shown to vary with the eighth power of the jet velocity. The famous eighth-power law has been shown in very good agreement with experimental results for jets up to a Mach number of

0.9 (Viswanathan, 2009; Karabasov, 2010; Williams, 1963).

The eddies considered in Lighthill's paper are, however, stationary. In a real jet, the eddies are in fact convecting with the mean flow. A well-established effect of the source motion is the Doppler effect, which was correctly captured by Williams (1963). It was shown that the sound intensity is altered by a factor of $(1 - M_0 \cos\theta)^{-5}$, where M_0 is the Mach number of the jet and θ is the observer angle to the direction of eddy convection. Thus, at high supersonic speed, the sound intensity varies with the third power of the jet velocity for $\theta \neq \pi/2$.

In addition to convecting the eddies, the mean flow has yet another effect on the sound emitted from the quadrupole sources: it refracts the sound. This was noted by Mani (1976) and Lilley's model took this refraction effect into consideration (Lilley, 1974). It is worth noting that Lilley's model considered a mean flow profile that only depends on radius, and that has been pointed out to be inaccurate (Colonius et al., 1997; Tam and Auriault, 1998). A more general acoustic analogy theory was proposed by Goldstein (2003), in which a spreading mean flow was considered. The theory decomposes the total flow field into a base and a fluctuation part, and the mean-flow refraction effects are accounted for by the linear operator on the left hand side of the resulting equation, with all the non-linear terms appearing on the right hand side as sources. As pointed out by Samanta et al. (2006), all the acoustic analogy theories can predict the far-field sound correctly provided that the source terms are sufficiently accurate. But considering the mean-flow effects on noise propagation explicitly results in more accurate and robust predictions.

The acoustic analogy theories regard different non-linear terms as equivalent sound sources. These quantities can be calculated using unsteady Navier-Stokes simulations such as Large Eddy Simulations (LES), but this is computationally expensive. However, many practical problems in industry, in particular those at early design stages, require a prediction approach with fast turn-around cycles for potential optimizations. To meet this demand, an approach relying solely on Reynolds Average Navier-Stokes (RANS) simulations (for example using $k - \varepsilon$ model for turbulence) was proposed to predict jet noise, see Khavaran et al. (1994), Bailly et al. (1994) and Bailly et al. (1996) for example. In 1999, Tam and Auriault (1999) further explored this idea and used the information supplied by the $k - \varepsilon$ turbulence model to predict the jet mixing noise from fine-scale turbulence by drawing an analogy between the fine-scale turbulence with the gas kinetic theory. Their model was relatively new as it was not based on the prevailing acoustic analogy theories. Three additional empirical constants describing the space-time correlation function were needed, and they were obtained by fitting the model to experimental data. Despite of the introduced empiricism, the far-field sound predicted this way was found

in excellent agreement with experiment measurements for different jet operating conditions at large observer angles ($120° < \theta < 60°$).

Three year later, Morris and Farassat (2002) compared the model proposed by Tam and Auriault (1999) and the model based on Lighthill's acoustic analogy, both of which used the RANS-calculated flow data. They found that for the same source information obtained from RANS (using $k - \varepsilon$ turbulence model) calculations, the former model yields better agreement with experiments. But they showed that the poorer agreement of Lighthill's acoustic analogy is not due to the inherent flaw of the theory, but due to the inconsistent models for the fourth-order space-time correlation functions used in the two approaches. And they also showed that if consistent models for sources are used, the two seemingly different approaches are equivalent with each other. The work of coupling acoustic analogy theories with RANS calculations was also undertaken by Self (2004). They argued that the poor agreement achieved using Lighthill's acoustic analogy by Morris and Farassat (2002) is due to the independence of the turbulence time scale on frequency. They proposed that the time scale also varies with frequency, and the resulted far-field spectrum at 90° can better agree with experiment results if this frequency-dependence is considered. It is worth noting that the proportionality constants used in these models were all obtained by best fitting the far-field sound, which seems to be rather empirical.

In 2010, the work by Karabasov et al. (2010) addressed the empirical issue. They found by analysing LES data that the fourth-order space-time correlation function at different locations throughout the jet can be well approximated by making use of the length and time scales obtained from RANS calculations, together with appropriate proportionality constants. The set of proportionality constants were obtained by comparing with the LES study, rather than fitting far-field sound. In addition, they found that the turbulent sound sources are not isotropic and only a few components of the fourth-order source correlation tensor are significant. They reported that the new model informed by LES yielded accurate predictions in the far-field for both large and small observer angles ($30° < \theta < 45°$). This approach was further explored to predict the jet noise for chevron nozzles by Mohan et al. (2015) and produced excellent agreement with experimental data at both large and small observer angles.

The approach for jet noise prediction based on acoustic analogy theories represents a mathematically rigorous way of solving the turbulent jet noise puzzle. The other way, which is more empirical, is exemplified by fitting experiment data. In 1996, Tam et al. (1996) analysed a large amount of experimental data, and proposed two sound similarity spectra for high-speed jets which gave the best fit to all the noise data that were available to them at that time. The first similarity spectrum is for the sound at large observer angles to the jet, and is flatter than the

other one for small observer angles. The spectrum for large observer angles to the jet is interpreted to be due to the fine-scale turbulence in the jet mixing layer and thus referred to as fine-scale spectrum (FSS). On the other hand, the sound spectrum at small observer angles is explained to be due to large coherent structures in the jet and thus called large-scale spectrum (LSS).

Despite the empiricism introduced by fitting experimental data, the FSS and LSS models seem to work surprisingly well for many jet noise experiments. The two similarity spectra seem to suggest the presence of two different sound source mechanisms. As mentioned above, Morris and Farassat (2002) showed that FSS model is equivalent to Lighthill's acoustic analogy if consistent models for the fourth-order space-time correlation functions are used. The large coherent structures as mentioned in the LSS model is suggested to be induced by the Kelvin-Helmholtz instability waves that originate from the jet mixing layer and then convectively grow and decay downstream. Extensive investigations into the instability waves of a round jet have been carried out. We do not aim to include a review on this at this stage, but postpone it to the next chapter.

Even though the distinction between the sound spectra at large and small observer angles is evident, the role played by the instability waves on jet noise is still not universally agreed. As mentioned above, it was shown by Karabasov et al. (2010) that the turbulence sources are not as isotropic as assumed by Lighthill (1952), and the far-field sound at small observer angles can be well predicted using equivalent quadrupole theories if source non-isotropy is taken into account. This indicates that the apparent difference between the two spectra might be purely due to the combination of Doppler amplification and the inhomogeneous directivity of quadrupole sources. Despite the continuing debate on the importance of the linear instability waves for isolated jet noise, we will find in subsequent chapters that their role for installed jet noise is indispensable. Having given a very brief overview of isolated jet noise, in the following section we will present a more detailed review on installed jet noise, which is the main topic of this thesis.

2.2 Installed jet noise

The existing research work is divided into three groups in chronological order and their corresponding research themes are discussed. Before presenting the literature, various geometrical parameters are defined, as shown in figure 2.1. The observer point A, normally underneath an aircraft on the ground, is in the far-field of the jet at a distance r from the jet nozzle. The polar angle θ and azimuthal angle φ defined in figure 2.1, together with the radius r, form a spherical

coordinate system with the zenith located downstream on the jet exhaust centre line. The plane $\varphi = 0$ is commonly referred to as the fly-over plane. Such a configuration has two important

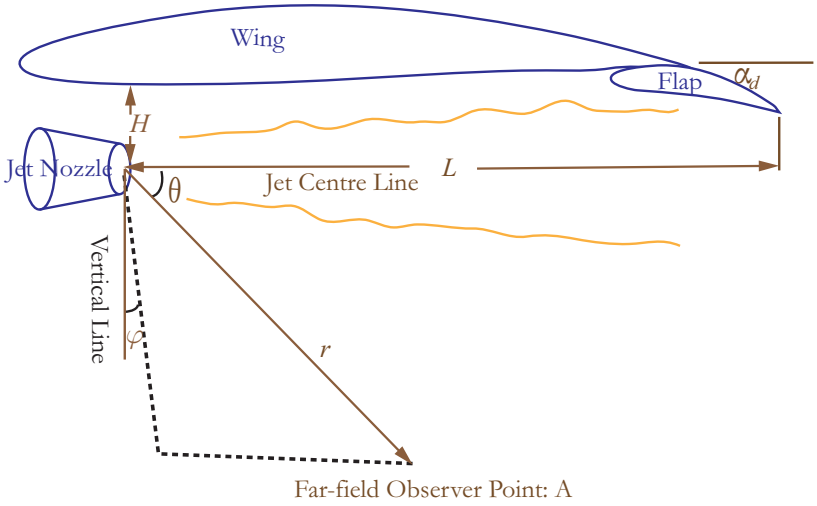

Figure 2.1: The schematic of a typical jet-wing-flap system.

geometric parameters defining the position of the engine relative to the wing: the distance H between the jet centre line and the wing surface and the distance L between jet nozzle and the trailing edge of the flap. As far as the installed jet noise is concerned, one expects the jet operating condition to have an important impact on the sound radiated to the far-field, as described by the jet nozzle diameter D, the jet exit velocity U_j, the jet spread rate ϵ_s etc. The impact of varying H and L on the far-field noise will be referred to as *the engine position effect*, while that of varying D, U_j, ϵ_s will be called *the jet condition effect* in this thesis. When the flap is deployed, both the deflected angle α_d and the width W of flap cut-out in a real flight vehicle have influences on the installed jet noise, and this is similarly given the name *the flap position effect*.

As early as the 1970s, it was known experimentally that a jet engine mounted under a wing produces larger noise than an isolated one, especially at low frequencies (Bushell, 1975; Head and Fisher, 1976; Szewczyk, 1979; Bryce, 1979). The excess noise is commonly referred to as jet installation noise. Extensive research has been conducted to investigate the acoustic properties of installed jet noise since then. Generally, the investigations fall roughly into three categories:

- Identifying installed noise sources by studying the acoustic characteristics of installed jet noise, the engine position effect, jet condition effect and flap position effect;
- Developing installed jet noise prediction models;
- Investigating noise reduction techniques.

2.2.1 Installed jet noise before 1980

The investigations on jet installation noise in the 1970s mainly focused on the first category, normally by examining experimental test data at either model or practical scales.

The extra noise produced by an installed engine was noticed by Bushell (1975) in the early 1970s when he compared the in-flight installed jet noise with the static isolated jet noise for a full-scale aircraft. Later in 1976, in order to study the acoustic characteristics of low frequency enhancement of the installed jet noise and to identify the corresponding noise sources, Head and Fisher (1976) presented a series of experimental results on the low frequency augmentation of jet noise with the close presence of a solid shield. The experiment was carried out with a cold, subsonic, round jet and a similar rectangular jet, both of which produced results similar in all respects. Engine position effect and the jet condition effect of varying the mean jet velocity were investigated: it was found that increasing H results in less noise at low frequencies and decreasing L follows the same trend and shifts the peak frequency to higher frequencies and that the velocity dependence of the peak of the low frequency augmentation is to the sixth power. It was then concluded that the additional low frequency noise measured in the far-field of a jet operating in close proximity to a solid shield was generated by a dipole source near the shield trailing edge. In 1979, Szewczyk (1979) compared the installed jet noise in flight for a full-scale coaxial jet with the noise data from static model tests. They confirmed that the differences between them were caused by several mechanisms, with the aircraft installation effect being an important factor.

By the end of the 1970s, it was known that there are at least two different noise generation mechanisms for installed jets. The first is jet-surface-reflection (JSR), dominating the installed noise at high frequencies; and the other is jet-surface-interaction (JSI), dominating installed noise at low frequencies. It was observed that the low frequency enhancement has a dipole-like directivity. Both the engine position and jet condition were found to have considerable influence on installed jet noise.

2.2.2 Jet installation effects in the 1980s

Extensive research covering all the three categories mentioned above were carried out during the 1980s. The work in the first category comprises that of Way and Turner (1980) and that of Shearin (1983).

In 1980, Way and Turner (1980) presented a number of model tests demonstrating under-wing installation effects on engine exhaust noise. The tests used a model-scale wing of the Tristar aircraft and a coaxial jet with the primary one heated to simulate a real jet condition.

Then the model wing was repositioned relative to the jet exhaust to encompass the configuration of the MacDonnell Douglas DC-10 aircraft. By positioning the engine further downstream and closer to the wing under-surface, a test aiming to simulate a smaller two-engined aircraft powered by turbo-fan engines under the wings was also carried out. The far-field noise was measured in the fly-over plane at angles from 45 to 150 degrees to the engine intake axis. Tests were conducted for both take-off and approach conditions.

For the Tristar configuration without deployed flap, the noise increase was found over the entire frequency range for both take-off and approach conditions, with the forward-arc more pronounced. The high frequency augmentation is about 2 dB in the forward arc, and the low frequency enhancement is up to 10 dB at the peak frequency. The deployed flap has little effect on high frequency noise while around a 2 dB increase was observed in the low frequency range. For the DC-10 configuration, it was found that shortening the cut-out width W has strong effect on low frequency noise amplification. For the third configuration called the *project model*, the high frequency noise spectrum is similar to that of the Tristar, and it was believed that the jet-wing interaction was weaker. Shortening the width of cutout W had the same effect as for the DC-10. It was argued that the jet-wing reflection directivity is strongly affected by the mean flow of the jet, for example, at a relative low frequency the noise increase is only noticed in the forward arc, which can be explained by the large noise refraction and attenuation by the jet at the rear arc. A linear empirical model was provided to describe this directivity at high frequencies. A jet-wing interaction model was also extended to the coaxial jet case using the method given by Head and Fisher (1976) but gave poor results. Then a jet-flap correlation model was also developed, giving encouraging agreement with the experimental data. The flight effect was only briefly discussed, and it was noted that it tended to decrease the augmentation due to all different mechanisms.

Three years later, aiming at identifying the jet installation noise sources, Shearin (1983) conducted a number of model-scale jet-wing-flap interaction tests at NASA Langley Research Centre. The experiments assumed a static ambient air flow. The jet and wing-flap models were chosen to represent the typical geometrical characteristics of a wide-body midrange transport aeroplane. A 6 cm exit-diameter nozzle was operated without a forward flight stream. The engine position parameters H and L, and the flap position parameters α_d and W were varied systematically.

Three frequency ranges involving different noise generation mechanisms were identified. The large amplification of noise from that of the free jet observed in the low frequency regime was attributed to the interaction of the jet and wing undersurface. The major noise source at

middle frequencies was believed to be due to the interaction between the jet and the side edges of the flap cutout, with an additional noise from the flap trailing edge source (Howe, 1978; Amiet, 1976b, 1978). For the high frequency regime, the noise increase was primarily due to the jet noise reflecting off the surface of the wing and flap. It was also suggested that the jet impinging on the flap cutout contributes to the noise in the high frequency regime when the local jet diameter is larger than the cutout size.

In conjunction with the above experimental studies, several attempts to develop prediction models for installed jet noise have also been made. These include the works by Stevens et al. (1983) and Sengupta (1983), which fall into the second category mentioned above.

In 1983, Stevens *et al.* published a work on predicting the jet noise in flight by summing up the installed jet noise and installed core noise measured for a model-scale aircraft. The jet noise in flight was obtained from a comprehensive noise test programme conducted jointly by Rolls-Royce and the Lockheed-California Company in 1979. Only the noise data for the clean-configured aircraft (with flaps and gear retracted) was selected. The noise had been corrected for atmospheric absorption, airframe background noise and the one-engine operating condition. The model-scale installed jet noise data was obtained by conducting a model-scale test with a coaxial jet and a free-stream simulating the flight condition. The isolated core noise levels were obtained from tests using engines of appropriate type mounted on static test stands. The installation effects for the core noise was evaluated by measuring a white-noise response with no jet flow. Then the installation effects for the core noise was combined with the core noise to formulate the installed core noise. By combining the installed jet noise and installed core noise, they found that the summed exhaust noise agrees well with the flight test data at low frequencies. But at high frequencies, the noise predicted from ground-test data deviates strongly from the full-scale fight test, especially in the forward arc.

In the same year as Stevens *et al.* published their work, Sengupta proposed a numerically fitted model based on the scale model testes carried out on a Boeing-757 configuration (Sengupta, 1983). The tests were conducted at a static condition. A 1/13-scale model of the wing-flap and engine system of the Boeing-757 was tested in an anechoic chamber with far-field noise signals picked up at angles ranging from 50 to 120 degrees in the fly-over plane. The near-field signal was also sensed at angles from 30 to 150 degrees. The same scale model was also tested in a 9-ft by 9-ft wind tunnel to investigate the flight effects, the details of which can be found in Miller's paper (Miller, 1983). The jet-wing interaction and jet-flap interaction noise were obtained by an energy subtraction (subtraction of the mean squared sound pressures), i.e. the jet-wing interaction noise was obtained by subtracting the isolated jet noise from the overall

noise measured with only the jet and wing and the jet-flap noise was obtained by subtracting both the isolated jet noise and jet-wing interaction noise from the overall noise measured with the jet, wing and deflected flap. The resulting spectrum and directivity patterns were approximated using polynomials obtained by fitting the experimental data. The prediction model was modified by adding Sound Pressure Levels (SPLs) based on equations empirically derived from the experimental data to account for each of the parametric variations of L, H and W. Then the combined effects of varying L, H and W were taken into account in a purely heuristic manner (a linear superimposition was not adopted as it gives a significant over-prediction).

Using this numerically inferred model, they noticed that the peak frequency of jet-wing interaction noise is inversely proportional to the transit time of the eddies travelling from the nozzle exit to the wing trailing edge. They also found that the predicted directivity pattern is consistent with previous theoretical predictions and the levels predicted in this way are consistent with the subsequent 747-JT9D and 707-CFM56 flight tests data. But varying L, H and W yields large discrepancies between the model and experimental results.

Attempts trying to reduce the installation effects of jet noise, as characterised by the third category, were first made by Wang (1980). In his paper (Wang, 1980) (and a subsequent journal paper (Wang, 1981)), Wang reported an experimental test on jet noise performed on a model-scale jet-wing system. The wing models were made of materials having different acoustic surface properties, including plywood covered with aluminium sheet, fibreglass blanket covered by wire mesh and composite honeycomb structure sandwiched by an aluminium sheet backplate and a 60-cgs-rayl DynaRohr surface. The test was conducted in an anechoic chamber with special ventilation systems. In the experiment, the engine position parameters H and L were varied. Tests of different jet velocities were also carried out. The far-field sound was measured in the normal reference plane (fly-over plane) and oblique planes ($\varphi = \varphi_0$) at different angles.

The experimental results showed that the wing models with specially treated surfaces can substantially reduce the noise enhancement at high frequencies. The installation noise also tends to drop when either the axial distance L decreases or the vertical distance H increases. Increasing the jet velocity shifts the peak of low frequency enhancement to higher frequency region. An interesting observation is the larger high frequency noise enhancement at oblique planes than that in the normal reference plane. This was explained to be due to the jet refraction and reflection effect on high frequency noise propagation. The weaker noise amplification at low frequency at lower angles (closer to the jet centre line) observed in the tests also suggests the presence of a dipole source.

By the end of 1980s, it had been noticed that the JSR noise is systematically lower than

3 dB that predicted by well-known theories. This was found to be due to the refraction and attenuation effect of the jet itself. It had also been further confirmed that the JSI noise has a dipole-like directivity pattern. And it was suggested that three noise generation mechanisms are present in the observed installed jet noise: high frequency surface reflection, middle frequency edge diffraction (including trailing-edge noise and noise due to side edges of the cut-out) and low frequency jet-surface interaction noise. The prediction models proposed at this time were generally quite empirical and heuristic, e.g. by fitting experimental data and superimposing parametric changes heuristically. Thus, these models were inherently unable to capture everything correctly, and in some cases, those deviations were too large to give anything useful. Regarding the noise reduction technique, it had been found that changing the acoustic surface properties of the wing can lead to a pronounced noise reduction especially at high frequencies. But the effects of these special wing surface treatments on the aerodynamic performance, and thus the practical usefulness of those techniques, were still yet to be discovered.

2.2.3 Investigations since 1990s

Since 1990s, with the rapid development and growing popularity of Computational Fluid Dynamics, studies on jet installation effects have evolved to incorporate numerical analysis. Experimental work was still quite active, while attempts to develop a prediction model gained more and more attention.

The research work focusing on the first category includes that of Mead and Strange (1998), Pastouchenko and Tam (2007), Bondarenko et al. (2012), Brown (2013) and Semiletov et al. (2016).

In 1998, aiming at investigating the jet noise at the sidelines, where it is generally more difficult to meet legislative regulation, a number of tests were carried out to investigate the under-wing installation effects on sideline jet noise (Mead and Strange, 1998). The tests covered three different wing models: a simple rectangular flat plate, a flat plate cut to the planform of the wing, and a detailed three-dimensional model of the wing. The far-field noise signal was picked up at azimuthal angles ranging from 5 to 65 degrees, each of which contained data at rear arc (60 degrees), middle arc (90 degrees) and forward arc (120 degrees) positions. The jet conditions varied from bypass-only (only the bypass flow), low power to high power coaxial jet flow.

For the rectangular flat plate under high power coaxial jet flow, at the rear arc position, the low frequency augmentation exhibits a dipole-like directivity pattern, while the high frequency enhancement shows a non-uniform directivity pattern in the azimuthal plane, which has been

attributed to jet refraction and reflection. At the middle arc position, high frequency directivity is not pronounced, while in the forward arc both the high and low frequency installation noise presents directional non-uniformity. At a low power jet flow condition, the low frequency augmentation increases greatly due to the different order of dependence of jet noise and jet-interaction noise on the characteristic flow velocity. At a bypass-only flow condition, the only difference from that under high power coaxial jet flow is that the directivity at high frequency becomes less evident, which was explained as the absence of primary-secondary interaction noise which is generated near the wing trailing edge at the high-power condition. When flight effects are incorporated, the low frequency enhancement reduces and its peak frequency shifts to higher frequencies.

When the planform flat plate was used, both low and high frequency amplification is reduced. The peak frequency of low frequency augmentation shifts towards higher frequencies. The pylon's presence gives little difference. The real wing model tests with bypass-only flow showed little difference from planform flat plate tests, the only difference being that the curvature of trailing edge alters the directivity of jet-wing interaction noise. There is also little difference under high-power jet flow conditions which was explained by the primary-secondary interaction sources being located downstream of the wing trailing edge. As expected, low-power tests give higher installation noise. When flight conditions are included, the jet-wing interaction noise shows a greater reduction while the reflection effects are largely unaffected except for some small changes in azimuthal directivity.

More, recently, instead of doing experimental tests, the effects of the wing-and-flap system on jet noise radiation were investigated numerically by Pastouchenko and Tam (2007). The numerical computations were performed in three steps: computing the downwash from the wing flap by solving Euler equations, solving the distorted jet flow via a parabolized RANS $k-\varepsilon$ turbulence model and evaluating the far-field noise using the extended Tam and Auriault fine-scale turbulence noise theory. It was argued that the principal mechanism of the excess noise radiation is the impact of the downwash of the wing flap on the jet flow, causing the jet to deflect downward and to distort laterally which brings about an increase of the turbulence in the jet. The computed result only agrees with experimental observations at high frequencies, indicating that this argument might be in error.

Bondarenko et al. (2012) also presented a numerical study of the jet-wing interaction using an in-house high-order finite difference LES code. Five configurations were calculated: jet alone, clean wing, jet with clean wing, flap-deployed wing and jet with flap-deployed wing. Near-field pressure, velocity field and turbulent statistics were analysed. The far-field sound

was obtained by performing a Ffowcs Williams-Hawkings (FW-H) integral.

It was found that the jet-wing interaction causes the aerodynamic lift coefficient on the wing surface to drop from 0.21 to 0.13, which was attributed to the effects of the jet on the flow recirculation zone. The jet centre line velocity experiences a sudden increase after leaving the nozzle, which was explained to be due to the divergent nozzle used. The computed results showed that the jet does not impinge on the wing until near the wing trailing edge. When the deflected flap was considered, it was shown that the vortical flow interacts significantly with the wing flap. The jet flow bends towards the wing by a very small angle then bends away from the wing because the presence of the flap. The presence of the flap also compensates the drop of aerodynamic pressure coefficients on the wing surface. The far-field noise was evaluated by FW-H integrals over three different surfaces. The integral over the rigid surface gives a dipole-like directivity pattern while larger surface integral gives much higher noise level and almost uniform directivity pattern. The latter result seemed to be somewhat unexpected as even isolated jet noise has a strong directivity.

Another very recent numerical study was performed by Semiletov et al. (2016). The flow was modelled using the Compact Accurately Boundary-Adjusting high-REsolution Technique (CABARET) and the acoustic results were obtained using the FW-H method. The results were then compared with a similar experiment. It was found that the numerical results could capture the same relative trends of the spectra behaviour as observed in the experiment, especially that installed jet noise is most pronounced at 90° but negligible at 30° to the jet axis.

In contrast to performing a numerical study, another recent study by Brown featured a large number of experimental tests aiming at investigating the jet-surface interaction noise (Brown, 2013). The surface length varied from 2 to 20 jet diameters while the distance from the jet centre line to the surface was changed from 1 to 16 jet diameters. Jets were operated at different jet exit conditions including subsonic cold, subsonic hot, under-expanded, ideally expanded and over-expanded supersonic jet.

The experimental results showed that, for cold subsonic jets, the presence of a rigid surface enhances the noise radiation at low frequencies in a dipole-like manner which was attributed to the jet-surface interaction. The author claimed that both jet-surface scrubbing noise and the trailing edge noise were involved. The results also confirmed a decrease of jet-surface interaction noise when the distance H increases. In addition, the study showed that the jet-surface interaction noise scales between U_j^5 and U_j^6. For a hot jet, an interesting fact was that the isolated hot jet tends to radiate less noise at all frequencies, and the shielding effects of the surface at high frequencies are more pronounced. In addition, heating the jet reduces both the

peak frequency and the amplitude of the jet-surface interaction noise.

Very recently, an experimental investigation of the acoustic scattering due to a flat plate in the vicinity of a turbulent subsonic round jet was carried out by Cavalieri et al. (2014). A flat plate of $9D \times 15D$ was placed nearby a round jet at $L = 5.5D$ with varying H. An aerodynamic measurement was performed first for turbulent jets at Mach numbers between 0.4 and 0.6. The results showed that when the flat plate is not very close to the jet, for example, when $H > 1.25D$, little change to the jet mean flow and turbulent statistics along the centrelines occurs. The following acoustic study showed that the far-field sound is enhanced significantly at low frequencies and there is a significant correlation between the sound at 90° to the jet on the reflected and shielded sides. Besides, there is a 180° phase difference between the two acoustic signals that are symmetric across the flat plate. The enhanced sound exhibits an exponential dependence on the radial separation distance H between the flat plate and the jet centreline.

Regarding the studies in the second category, both Bhat and Blackner (1998) and Moore (2004) have developed their prediction models. While Bhat and Blackner chose to analyse their experimental data measured at the Boeing Company and develop their prediction method empirically, Moore's prediction method was based on a 3D ray-theory. The model made use of the jet blockage profiles for core and bypass mean flows developed by Moore and Mead (2003) to account for the refraction and attenuation effects of the jet on the reflected sound. As the moving wing and flap system has an impact on the emission time of the image sources, a method of tracing the emission time of direct sources was adopted.

Five cases were tested. It was found that the jet-flap reflection has a large impact on the noise field shape, altering the polar peak position from that of isolated sources and creating a new peak directly under the engine. A small deflected flap angle is favourable as the strong directivity peaks of the image sources are then out of the reception range. Rolling the aircraft creates an asymmetrical field shape. As the blockage range is large for the bypass sources, the resulting field shape has a wider distribution along the lateral direction. Increasing the altitude also results in the same tendency.

Recently, some scattering-based models were proposed, including those by Cavalieri et al. (2014), Vera et al. (2015) and Piantanida et al. (2016). In Vera's work, for an assumed plane-wave-like incident field the scattered pressure on the surface of a semi-infinite flat plate was obtained by making use of Wiener-Hopf method and the far-field sound was obtained using Amiet's approach. However, the proposed form of the statistical spectrum of "the incident field required to calculate the far-field sound is hard to obtain in experimental measurements". In addition, the ambient flow (non-trivial in a real flight certification process) was neglected in

their modelling. Cavalieri et al. (2014) and Piantanida et al. (2016) adopted another approach in their work, where an inferred near-field pressure source of the wave-packet form was used. The far-field sound was calculated numerically using two approaches: a tailored Green's function for a semi-infinite flat plate and a Boundary Element Method (BEM) for flat plates of finite dimensions. Cavalieri et al. (2014) showed that both the model captured the noise enhancement at $St = 0.2$ within an error of around 2 dB. It was explained that the larger error obtained at higher frequencies, for example at $St = 0.4$, was due to the dominance of the acoustic field nearby the edge. While the Green's function approach ignored the side edges of the plate plate, the BEM approach yielded a multi-lobed directivity due to the scattering of side edges. In the work of Piantanida et al. (2016), using the same two approaches, it was showed that "a good overall agreement with the experiments in terms of the dependence of the radiated levels and directivity on the radial jet-plate separation and sweep angle" was achieved. Since the sound source was assumed to be of a wave-packet form, it remained to be shown to what extent the acoustic scattering of small-scale turbulence contributed to the far-field noise. In particular, it was unclear whether the under-prediction of the models at $St = 0.2$ was mainly caused by ignoring wave packets of high-order azimuthal modes or by the scattering of small-scale turbulence. The wave-packet approach was used earlier by Papamoschou (2010) to predict the jet noise shielding effects with an inferred wave packet and a monopole as sources. Reasonable results were obtained with limitations at high frequencies caused by the deterministic characteristics of the sound sources.

Attempts to try to reduce the installation effects of jet noise, as characterised by the third category, were also made in the work of Piantanida et al. (2016). They reported that if the wing was swept, the installed jet noise could be reduced effectively, and the larger the swept angle was, the more effective the sound reduction was. This proposition was later further explored by Nogueira et al. (2017). As another attempt, Bastos et al. (2017) carried out an experimental study to examine the effects of chevron nozzles on installed jet noise. The results were compared with the installed spectra for a round nozzle. It was found that when the plate was placed sufficiently far away from the jet, the chevron nozzle could reduce installed jet noise at all frequencies, similar to that for a round nozzle. However, when the plate was closely integrated with the jet, the low-frequency reduction provided by chevron nozzles became negligible.

So far, there has been little doubt about the jet installation effects at high frequencies: the noise is generated by the fine eddies and reflected off the wing and flap surface; the reflected noise is refracted and attenuated by the presence of the turbulent jet plume which results in a noise increase systematically less than 3 dB and creates a non-uniform directivity in both

the fly-over and azimuthal plane. On the other hand, the noise mechanism at low frequencies has not been accepted unanimously. One effect that has been confirmed, however is that the low frequency installed noise has a dipole-like directivity pattern in the far-field. There is also disagreement about whether trailing-edge noise is a significant component. In addition to the trailing-edge noise, Shearin (1983) suggested a jet-surface interaction noise was the dominant cause of the noise increase at the lowest end of the frequency range, while Brown (2013) argued that jet-scrubbing noise only made a minor contribution. Pastouchenko and Tam (2007) even argued it was the downwash effect of the wing flap causing more turbulence in the jet that was the principal mechanism. However, examination of the acoustic properties of the low frequency installed noise and its dependence on the engine position, jet condition and flap position leads one to believe that the dominant effect is the trailing-edge noise. This is because: a). The dipole characteristics are in agreement with the directivity pattern of trailing-edge noise at low frequencies (Head and Fisher, 1976; Wang, 1980; Mead and Strange, 1998; Bondarenko et al., 2012; Brown, 2013; Amiet, 1976b; Roger and Moreau, 2005; Cavalieri et al., 2014); b). decreasing L results in a reduced noise and a frequency shift toward high frequencies (Head and Fisher, 1976; Way and Turner, 1980; Stevens et al., 1983; Wang, 1980, 1981; Shearin, 1983); c). there exists a high correlation between the pressure field near the trailing-edge and the far-field sound (Head and Fisher, 1976); d). the dependence of sound intensity on the characteristic jet velocity is to the 5 to 6 power (Head and Fisher, 1976; Brown, 2013).

While models for installed jet noise (such as the 3D ray theory by Moore and Mead (2003)) have given encouraging results at high frequencies, models for installed jet noise at low frequencies are either quite empirical based or relying significantly on numerical computations. Having recognised that trailing-edge noise probably contributes most to the overall noise enhancement at low frequencies, a feasible way of developing a fast and accurate model for the low-frequency regime is to make use of approaches for trailing-edge noise such as Amiet's model (Amiet, 1976b; Roger and Moreau, 2005) to relate the far-field sound to near-field pressure fluctuations. We will discuss this approach further in the following chapters.

Chapter 3

Jet Instability Waves Review

Jet instability waves were identified a long time ago. An early reported observation was in the nineteenth century, when Leconte noticed the response of coal-gas jets to music (Leconte, 1858). The phenomenon that jets can respond to sound was subsequently confirmed by further experiments (Tyndall, 1867). One area where jet instability was extensively studied subsequently was in laminar-turbulent transition (Michalke, 1984), where it plays an important role. However, jet instability analysis was also found to be able to explain the large coherent flow structures observed in turbulent jets (Crow and Champagne, 1971).

These coherence structures, or instability waves, are not only interesting in the study of turbulence, but are also relevant to the sound generation in turbulent jets. The details on the connection between the coherent structures and the far-field sound is given in a recent review by Jordan and Colonius (2013). The importance of instability waves on sound generation is unanimously accepted for supersonic jets (Tam, 1995). Although there is a continuing debate on its role in jet noise for subsonic jets, one of the important mechanisms of installed jet noise, as can be seen in the following chapters, is due to the scattering of jet instability waves. To properly model this mechanism, a good understanding of jet instabilities is essential. This chapter thus introduces this subject. However, in light of the enormous amount of literature on this topic, this review cannot be exhaustive. The first section of this chapter reviews some of the important studies on the experimentally discovered large coherent flow structures. The second section provides an overview of the development of jet instability theories while the following section discusses how linear stability theories were used to explain large coherent structures. The essential equations of stability analysis are presented in the last section.

3.1 Large coherent flow structures

It may seem surprising to many outsiders that turbulence is still an open question of modern physics. Despite centuries of relentless studies by many of the greatest minds in human history, not much is known on turbulence. This is mainly due to two particular difficulties. The first, from the mathematical perspective, is the non-linearity of the Navier-Stokes Equations. Mathematics to date is still not able to tackle the problems of general non-linear partial differential equations, such as the Navier-Stokes equations. The existence and uniqueness of the solutions to the Navier-Stokes equations are still unknown, let alone how the solutions, if they exist, can be calculated. One of the problems with the non-linear Navier-Stokes equations is that, in some parameter regimes, the flows demonstrate extreme sensitivity to initial or inlet flow conditions leading to chaotic flows. The second difficulty, from the physical perspective, arises from the extremely wide range of time and length scales observed in turbulence. These not only prevent conventional spectral analysis, but also pose a great difficulty for today's Direct Numerical Simulations (DNS) which resolve all scales. For example, by the time of writing this thesis (2017), the maximum Reynolds number Re (based on the characteristic flow width and velocity) that a DNS using massive parallel computing facilities is capable of reaching is around the order of 10^4, still two to three orders of magnitude lower than most industrial applications. Moreover, the number of floating-point operations grows roughly as Re^3 (Orszag, 1970). Hence DNS studies for nearly all industrial flows are not yet possible.

3.1.1 Discovery of large coherent structures

Prior to the 1970s, the prevailing view was that turbulence in free shear flows such as jets was an agglomeration of incoherent small-scale fluctuations. However, this view was changed soon after the seminal experiment carried out by Crow and Champagne (1971), where large coherent structures were both qualitatively and quantitatively observed. Given the important status of this experimental work, and the fact that much of subsequent theoretical works on jet instabilities were based on it, some of its major findings are summarized as follows.

Qualitative study of these structures was carried out first using flow visualization techniques. A water jet exiting from a 2.5-inch pipe of 9 inches long was used to study the near-field instability waves, giving a Reynolds number (based on the jet diameter D) from order 10^2 to 10^3. Flow visualization showed that the instability is sinuous at the lowest Reynolds number 10^2 and gradually becomes helical as the Reynolds number rises. As the Reynolds number increases further the instability waves tighten and form "bulbous lobes", and finally break into a train of axisymmetric puffs. For Reynolds numbers in the range of 10^4 to 10^5, an air jet (seeded

with CO_2) was used. At such high Reynolds numbers, the initial shear layers of the jet are thin and it was found that two different axisymmetric structures are distinguishable: these were instability waves on the surface of jet column within the first 2 or 3 diameters and large-scale puffs formed periodically at around 4 diameters downstream the nozzle exit. As the Reynolds number increases the inlet shear layer becomes increasingly thin and the surface waves become increasingly shorter. The large-scale structures, on the other hand, remain roughly the same and the average Strouhal number (based on the frequency of puff appearance and the jet diameter D) is roughly a constant around 0.3.

Quantitative study was difficult due to the random background turbulence. To overcome this difficulty, the jet was forced upstream the nozzle to provide a reference signal and the boundary layer within the nozzle was tripped to destroy the surface ripples. The velocity fluctuation response was measured downstream by hot-wire anemometry and schlieren photography. At a Strouhal number of 0.3, the measured fluctuation amplitude 4 diameters downstream the jet exit increases linearly with forcing amplitude and then saturates to a rough constant as the forcing amplitude increases still further. Forcing at this preferred frequency enhances mixing between the jet and the ambient fluid and causes the mean-flow profile to decay more quickly. At lower frequencies, the response remains linear until a higher forcing amplitude, while at higher frequencies it tends to saturate at a small forcing amplitude. When the forcing is very weak the response appears to be linear and the growth rate increases with frequency, which is in accord with linear instability theories (Batchelor and Gill, 1962). Therefore, linear stability theories do not predict the dominant preference of the Strouhal number 0.3 observed in the experiment and it was suggested that it is due to non-linear effects.

The hot-wire was then moved to other axial stations in order to study the axial profile of the velocity fluctuation intensity. The profile was found to be a combination of the unforced turbulence intensity profile and the growth-saturation-decay profile associated with the forcing upstream of the nozzle exit. At constant forcing amplitude, as the Strouhal number increases the saturation location moves upstream with the maximum saturation amplitude obtained at Strouhal number 0.3. The profiles for different forcing amplitudes were also studied at the same forcing Strouhal number. When the forcing amplitude is low, the forced response profiles within the first 6 diameters downstream of the nozzle exit increase linearly as the forcing amplitude increases. Although the response amplitude still saturates at a certain axial location, it is due to the spreading of the flow rather than the non-linearity due to large wave amplitudes. Further increasing the forcing amplitude inevitably introduces non-linear saturation, leading to a shift of the peak-intensity location towards upstream.

The experiment of Crow and Champagne (1971) clearly showed the existence of orderly structures in circular turbulent jets. These results were later extended to planar mixing layers of different densities and velocities (Brown and Roshko, 1974; Winant and Browand, 1974). The planar mixing layers were found to be dominated by large structures. These large structures convect at virtually constant speed, and they are not very sensitive to the density differences across the mixing layers. Further evidence of the existence of the large coherent structures in turbulent jets was found in subsequent works such as that of Dimotakis and Brown (1976), among many others. The review by Jordan and Colonius (2013) contains a much more detailed discussion on the signatures of these large coherent structures.

In the work of Crow and Champagne (1971), the observed the surface ripples and large puffs were interpreted as the orderly structures. Quantitative analysis was performed in a statistical manner, therefore unable to show the fluctuations' spatial correlation. This was later examined by Fuchs (1972). A high degree of correlation was found for the pressure fluctuations in planes normal to the jet centreline. The correlation scale obtained was much longer than that in the fine-scales associated with turbulence. This provided yet another piece of evidence on the existence of not only large, but also coherent structures. By 1980s, it had been widely accepted that both large coherent structures and small-scale incoherent turbulent fluctuations appear in transitional and turbulent flows.

3.1.2 Extracting coherent structures

Although in the early 1970s it was accepted that large coherent structures exist in turbulent jets, it was not known what these structures looked like and how they could be extracted experimentally. This question had not been fully answered in the work of Crow and Champagne (1971), because the measured axial profiles of the fluctuation intensity contained no phase information. One approach to extracting this spatial information is through phase averaging. This would require a reference signal, in other words, the jet would have to be forced at an upstream location. The measured fluctuation signals at different axial stations are then compared with this reference signal to calculate the phase delay between them. These obtained phase delays are then averaged in the ensemble space to calculate the averaged phase delays. Such a method has been used to distil the amplitude and phase information of these large structures in various works such as those by Hussain (1986) and Hussain and Zaman (1981).

However, concerns had been raised as to how a forced jet resembles a natural jet. New analysis tools are needed to extract the spatial details of the large structures without using forcing. This has been made possible with the Proper Orthogonal Decomposition (POD)

method (Berkooz et al., 1993). The POD has several other names in other disciplines, such as Karhunen-Loeve decomposition or principal component analysis, and it appears to have been discovered independently by a few different authors, such as Kosambi (1943), Loeve (1945) and Karhuen (1946), to name a few (see Sirovich (1987) or Berkooz et al. (1993) for a review). The POD method was first used to analyse turbulent flows by Lumley (1967). The essential idea of POD is to find an optimal set of basis functions to expand a statistical function based on its ensemble properties, and the procedure can be summarized as follows.

Let $u(x)$ denote a statistical function of x. In order to find an optimal set of functions to expand $u(x)$, first let $R(x, x')$ denote the cross correlation function (second-order moment), $\langle u(x)u^*(x')\rangle$, where $\langle\rangle$ denotes an ensemble average and $*$ denotes complex conjugate. Then the basis functions $\phi_n(x)$ can be found by solving

$$\int_V R(x, x')\phi_n(x')\mathrm{d}\, x' = \lambda_n\phi_n(x), \tag{3.1}$$

where V denotes the interval over which $u(x)$ is defined. Using the fact that $R(x, x') = R^*(x', x)$, one can show that the basis functions are mutually orthogonal. Assuming that this basis set is also complete, it can be readily shown from equation 3.1 that

$$R(x, x') = \sum_n \lambda_n\phi_n(x)\phi_n(x'), \tag{3.2}$$

where we have assumed that $\phi_n(x)$ form a normalized orthogonal basis. If we use the same basis to expand $u(x)$ we have

$$u(x) = \sum_k c_k\phi_k(x), \tag{3.3}$$

where c_k denote the expansion coefficients. From equation 3.2, it can be readily shown that

$$\langle c_k c_l^*\rangle = \lambda_k\delta_{kl}, \tag{3.4}$$

where δ_{kl} denotes the usual Kronecker delta. Equation 3.4 effectively shows that different modes are statistically uncorrelated. In other words, the function $u(x)$ is decomposed into different modes, each of which are mutually uncorrelated. The disparity between the values of λ_n shows how coherent the statistical quantity u is with respect to x. When the $u(x)$ is statistically homogeneous, the POD expansion degrades to Fourier expansion.

The POD method has been adopted to study the large coherent structures in turbulent flow in numerous studies (Arndt et al., 1997; Sukuzi and Colonius, 2006; Tinney et al., 2008a; Tinney and Jordan, 2008; Gudmundsson and Colonius, 2011). Arndt et al. (1997) were among the first to use the POD method to decompose the near-field pressure fluctuations measured

around a turbulent jet. In their work, the near-field pressure fluctuations were measured at the outer edge of a jet mixing layer. The cross correlation of the pressure was then calculated. Because of stationarity, the correlation was expand using Fourier Series for time and the azimuthal angle coordinate. The POD decomposition was carried out for the streamwise coordinate x to calculate the eigenvalue λ_n for each eigen mode n. It was found that λ_n decays very rapidly as n increases. The massive magnitude difference implies that the pressure is predominantly coherent. It was also found that the axisymmetric mode is the dominant mode whose spectrum is larger than the spectra of other azimuthal modes. For each azimuthal mode, it was found that the eigenvectors exhibit an amplification-saturation-decay profile and that the convection velocity appears to be the same for all the frequencies of interest (around 0.58 of the jet exit velocity for Strouhal numbers in the range of 0.2 and 2, for example). High-frequency eigenvectors were found to saturate nearer the nozzle, i.e. for smaller x, while low-frequency components saturate further downstream.

Equipped with the POD method, it has been shown that linear stability theories can be used to explain the observed large coherent structures in natural turbulent jets, as reviewed in later sections.

3.2 Jet instability theories

Jet instability theories considers linearized perturbations of flow quantities on a steady base flow, for example the jet mean (time) flow. Figure 3.1 shows a schematic of the time-averaged flow field of a turbulent jet. Due to the entrainment of the ambient air, the jet spreads gradually

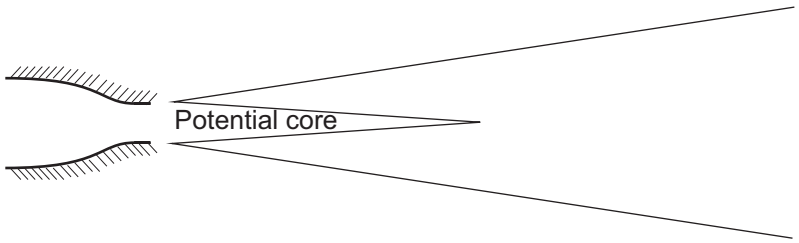

Figure 3.1: The schematic of the time-averaged jet flow field of a turbulent jet.

downstream the nozzle exit, which can be seen from figure 3.1. This spreading results in different mean velocity profiles at different axial locations. However, the streamwise mean velocity within the first few jet diameters downstream the jet nozzle exit remains constant inside a conic region, which is widely referred to as the potential core of the jet mean flow. Downstream the potential core, the velocity profile becomes flatter and smoother.

This realistic jet mean flow complicates an analytical study of its stability characteristics. Therefore, different approximations were adopted in the early-days jet instability models. These models evolved as more and more realistic base flows were used, and they appear to have gone through three distinct stages of development. In the first stage, a strictly parallel flow was assumed and various cross-section velocity profiles were considered. For example, it could be a vortex sheet or a fully developed jet mean flow profile. In the second stage, a locally-parallel assumption was used. It is referred to as the "locally-parallel analysis", because the local time mean velocity profile at each axial station was used and treated as if they were parallel in the subsequent stability analysis. This partly captures the effects of divergence of realistic jet flows. The last approach exploits the powerful technique of the Wentzel-Kramers-Brillouin (WKB) method, and the analysis is more theoretically satisfactory than the locally-parallel analysis. A detailed review of these approaches is given in the following sections.

3.2.1 Parallel flow analysis

Although jet instability was observed in the early nineteenth century, an analytical study of this phenomenon was not performed until 1879 by Rayleigh (1879). To simplify the problem, the flow was assumed to be both inviscid and incompressible. In his subsequent work, the Rayleigh's Inflexion Point Criterion was proposed. This was further extended by Batchelor and Gill (1962), when they revisited the problem of the stability characteristics of an incompressible jet. The incompressible Navier-Stokes and continuity equations were linearized around a base flow, and four coupled differential equations were obtained. Once the viscous term had been neglected for a high Reynolds number flow, these four equations were reduced to one single equation for the radial velocity fluctuation after using the method of separation of variables. The analytical dispersion relationship was obtained for the cylindrical vortex sheet flow and an extended flow instability criterion was obtained for more realistic jet mean flow profiles. However, it should be noted that even though the velocity profile was more realistic, the base flow used for the stability analysis was still a strictly parallel flow. The approach of using a local velocity profile as if it were strictly uniform and parallel in the axial direction is now referred to as *local stability analysis* (Ho and Huerre, 1984), as opposed to the *global stability analysis*, where the overall realistic flow is used throughout the stability analysis. Another concept that is worth clarifying is the difference between the *temporal stability analysis* and the *spatial stability analysis*. The temporal stability analysis studies the real and imaginary part of the angular frequency ω as a function of the wavenumber α which is assumed to the real. The spatial stability analysis examines the complex number(s) α while ω is taken to be real.

In the analytical works of Rayleigh (1879) and Batchelor and Gill (1962), the effects of compressibility and viscosity were ignored. Lessen et al. (1965) investigated how compressibility effects change the stability characteristics of jets. The viscous effects were not included in their work. Note that a cylindrical vortex sheet model was used to simplify the problem. A more realistic mean flow profile was later studied by Michalke (1971). In his work, a local stability analysis was performed using the velocity profile measured at two diameters downstream the jet nozzle in the experiment of Crow and Champagne (1971). The predicted phase speed and amplification rate agreed well with the experiments.

Viscous effects were later examined by Lessen and Singh (1973) and Morris (1976). The compressibility effects were not taken into account. In Lessen's work, the fully-developed jet profile was used while Morris (1976) conducted a stability analysis for three different jet mean velocity profiles, representing various development stages of a jet. The four linearized equations developed by Batchelor and Gill (1962) for viscous flows were used. It was shown that the critical Reynolds number increases as the velocity profile varies from a top-hat to a fully developed form.

3.2.2 Locally-parallel flow analysis

The local stability analysis discussed above assumed a strictly parallel flow as a model for the realistic jet. The cross-section velocity profile was chosen to best represent the entire diverging flow field using various velocity profiles, as shown by Morris (1976). However, as pointed out by Mattingly and Chang (1974), this approach was not applicable to the realistic jet, since the jet profiles at different axial locations are different and this changes the stability characteristics. Instead, they proposed an approach, which is nowadays commonly referred to as *locally-parallel analysis*. This implies that a local stability analysis is performed at each axial location. The velocity profile for each local stability analysis is the cross-section velocity profile of a realistic jet at the corresponding axial location. This appears to have explained the failure of achieving agreement between the experimental results and the spatial stability analysis performed in the work of Crow and Champagne (1971). Subsequent works took both the viscous and compressibility effects into account, such as that of Morris (1983).

3.2.3 Multi-scale WKB analysis

The locally-parallel analysis gave better agreement with experimental results. However, this was still not equivalent to a global analysis. Because, for example, the jet-spreading effects were only partially considered. While the locally-parallel assumption yielded a good agreement with

experiments for local parameters, the local phase speed for example, quantities which depend on cumulative effects, such as the amplitude gain over an axial distance, have not been verified. In order to study this, the slowly-diverging mean flow effects were examined by Crighton and Gaster (1976) using a multi-scale method. This fully exploited the fact that the jet is spreading slowly compared to the short scale determined by the frequency and phase speed of the instability waves. This work was an extension of earlier works on multi-scale analysis of other types of shear flows. It was shown that the approximation based on a slow axial change of the mean flow leads at worst to general trends in agreement with those found in several independent sets of measurements, and at best to excellent numerical agreement for the wavelength, phase speed and gain in pressure perturbation amplitude.

Using the multi-scale method, Crighton and Gaster (1976) obtained the $O(1)$ solution for the fluctuation stream function by considering the existence criterion of an appropriate $O(\epsilon_s)$ solution. The small jet spreading rate ϵ_s is used to quantify the slowness of jet diverging. Compared with the locally-parallel analysis, the obtained $O(1)$ solution more properly accounts for the effects of jet spreading. This is because the $O(1)$ solution contains an extra amplitude modulation, in addition to the changes of eigenfunction and eigenvalues captured by the locally-parallel analysis. Though Crighton and Gaster's study was deemed to be more theoretically satisfactory, it had its own limitations. The most important one is that only the axisymmetric disturbance can be analysed, since there it uses the fluctuation stream function, which does not exist for more general three-dimensional disturbances.

This limitation can be overcome by numerically solving the *Parabolized Stability Equation* (PSE), the results of which agree better with experimental results compared to other Linear Stability Theories (LST) (Bertolotti and Herbert, 1991; Herbert, 1997). The PSE method requires more computational resources than LST, but this is still much cheaper than a Large Eddy Simulation. This is because an explicit form of solution is assumed to account for part of the jet spreading effects. However, this also restricts the analysis to be only valid for slowly-spreading jets and the frequency cannot be too low. In addtion to enabling the study of non-axisymmetric modes, another advantage of using PSE is that it can also account for viscous effects. Much recent work on jet instabilities is based on the PSE method (Sukuzi and Colonius, 2006; Arndt et al., 1997; Gudmundsson and Colonius, 2011). These works will be reviewed in the following section.

3.3 Are large coherent flow structures instability waves?

Crow and Champagne (1971) made an early attempt to explain the large coherent structures

observed in forced jets using linear stability theories. In their work, they used the simplified parallel-flow theory of Batchelor and Gill (1962), and assumed a vortex-sheet-like incompressible base flow. Crow and Champagne (1971) performed both temporal and spatial stability analysis, and they found that the predicted wavelength and convection velocity from temporal theory agree well with experimental results. The spatial theory, on the other hand, yielded quite different results. In the same year, Michalke (1971) carried out a local stability analysis using the jet mean flow profile at 2 jet diameters downstream the nozzle exit. Compared to the vortex-sheet profile used by Crow and Champagne (1971), the new velocity profile represented a more realistic jet. The results showed that both the phase speed and the amplification rate agree well with experimental results. Three years later, using the locally-parallel analysis, Mattingly and Chang (1974) further confirmed the failure of the spatial stability analysis used by Crow and Champagne (1971) was due to the inappropriate use of a top-hat velocity profile. The agreement between theories and experiments became increasingly better. As one can expect, the results based on the more advanced WKB analysis showed excellent agreement with experimental results (Crighton and Gaster, 1976).

The aforementioned works showed that instability waves can successfully explain the large coherent structures observed in forced jets. However, it remained unclear whether this is also true for natural jets. Thanks to the advent of POD method, it has now been shown that linear stability theories can also successfully explain the large coherent structures in natural jets. In particular, theoretical predictions agree well with experimental observations in terms of the near-field pressure fluctuations, see Sukuzi and Colonius (2006), Tinney and Jordan (2008) and Gudmundsson and Colonius (2011) for example. The advantage of comparing the pressure fluctuations is that they can be measured at appropriate locations in the flow such that they do not suffer from the significant contamination of turbulence that the velocity perturbations do.

Following the earlier work of Arndt et al. (1997), which showed qualitatively agreement between the POD eigenfunction of the near-field pressure fluctuations and that predicted using linear theories, quantitative comparison was made by Sukuzi and Colonius (2006). The results showed that the POD modes of the near-field pressure fluctuations agree well with the instability waves predicted from linear stability theories. The agreement is good from the nozzle exit to the end of the potential core and is particularly good for the most unstable frequencies. Five years later, this work was further extended by Gudmundsson and Colonius (2011). They extended the work of Sukuzi and Colonius (2006) in two ways: the first was that the eigenfunction of the instability waves were calculated using Linear Parabolized Equations (PSE), which more properly accounted for the diverging effects of the jet mean flow; the second was that the

velocity fluctuations were also studied using the POD method and compared with the pressure fluctuations. The results showed that the instability waves calculated from PSE agree well with the experimental measurements at nearly all resolved frequencies and azimuthal numbers. The amplitudes of the POD modes inferred from the velocity decomposition are also consistent with those from pressure decomposition.

The POD method was also used to extract the large coherent structures from velocity field by Tinney et al. (2008a). In his work, the instantaneous flow velocities of a cold Mach 0.85 jet on the normal-to-axial planes at different axial positions were measured. The Particle Image Velocimetry (PIV) system was targeted at planes at discrete streamwise locations between 3 and 8 jet diameters in 0.25 diameter increments. Fourier series was used in the azimuthal direction while the POD was used in the streamwise direction. In agreement with previous findings, the first POD mode was found to contain the largest energy for each azimuthal mode. The main finding, which also agrees with previous investigations, was that at upstream axial locations the eigenvalues peaks at azimuthal mode 5 but further downstream the peaks gradually shift to mode 2 at the end of potential core. This indicated that higher-order structures dominate near the nozzle and lower-order structures prevail further downstream. Though the results were not compared with linear stability theories, the extracted velocity structures did qualitatively resemble instability waves. The POD decomposition of velocity fluctuations was also performed in the work of Gudmundsson and Colonius (2011) and then compared with theoretical predictions. The POD eigen modes were found to be similar to the theoretical ones, though the agreement was generally less good than that for the pressure fluctuations. This was somewhat expected since the velocity fluctuations were contaminated by small-scale turbulence.

In summary, the large coherent structures in forced turbulent jets can be successfully explained using linear stability theories. This also appears to be the case for natural jets. Therefore, it is now generally accepted that the large coherent structures observed in turbulent jets are the results of instability waves.

3.4 Linear stability analysis of jets

In this section, we start from the fundamental equations and derive the important linearized equations governing small-amplitude disturbances. To demonstrate the procedure of a typical stability analysis, the linearized equations are solved for an axisymmetric base flow of vortex sheet type. When Reynolds number is high, we expect the dynamics of small-amplitude disturbances to be virtually independent of viscous effects. Therefore, we start our derivation from the inviscid continuity, momentum and energy equations in the Cartesian coordinate system,

aiming to include the effects of compressibility. Let the operator $\mathrm{D}/\mathrm{D}t$ denote the material derivative (in the following equations, Einstein summation rule is implied)

$$\frac{\mathrm{D}}{\mathrm{D}t} = \frac{\partial}{\partial t} + v_j \frac{\partial}{\partial x_j}, \tag{3.5}$$

then these equations can be written as

$$\frac{\mathrm{D}\rho}{\mathrm{D}t} + \rho \frac{\partial v_j}{\partial x_j} = 0, \tag{3.6a}$$

$$\rho \frac{\mathrm{D}v_i}{\mathrm{D}t} + \frac{\partial p}{\partial x_i} = 0, \tag{3.6b}$$

$$\rho \frac{\mathrm{D}(h + v_j v_j/2)}{\mathrm{D}t} - \frac{\partial p}{\partial t} = 0, \tag{3.6c}$$

where h is the enthalpy of the fluid and p is the pressure. Combining the continuity and momentum equations with the equation of state for a perfect gas $p = \rho RT$, where R is the gas constant and T is the fluid temperature, the temperature in the energy equation can be eliminated and the energy equation becomes

$$\frac{\mathrm{D}p}{\mathrm{D}t} + \gamma p \frac{\partial v_j}{\partial x_j} = 0, \tag{3.7}$$

where γ is the gas specific ratio.

As a routine procedure, the total flow quantities such as p, ρ and v_i are decomposed into a base and a fluctuation part, i.e.

$$p = \bar{p} + p', \tag{3.8a}$$

$$\rho = \bar{\rho} + \rho', \tag{3.8b}$$

$$v_i = \bar{v}_i + v_i', \tag{3.8c}$$

where the base flow is denoted by an overbar and the fluctuation flow is denoted by a prime. Note that we have not yet restricted the base flow field in any way, therefore the overbar quantities can be chosen arbitrarily. Here we choose them such that they satisfy the inviscid continuity, momentum and energy equations, as shown in equation 3.6. Substituting equation 3.8 into equation 3.6, then subtracting the base flow equations and ignoring second-order small quantities, one can show that the fluctuation flow quantities are governed by the following equations:

$$\frac{\overline{\mathrm{D}}\rho'}{\overline{\mathrm{D}}t} + v_j' \frac{\partial \bar{\rho}}{\partial x_j} + \rho' \frac{\partial \bar{v}_j}{\partial x_j} + \bar{\rho} \frac{\partial v_j'}{\partial x_j} = 0, \tag{3.9a}$$

$$\bar{\rho} \left(\frac{\overline{\mathrm{D}}v_i'}{\overline{\mathrm{D}}t} + v_j' \frac{\partial \bar{v}_i}{\partial x_j} \right) + \rho' \frac{\overline{\mathrm{D}}\bar{v}_i}{\overline{\mathrm{D}}t} + \frac{\partial p'}{\partial x_i} = 0, \tag{3.9b}$$

$$\frac{\overline{\mathrm{D}}p'}{\overline{\mathrm{D}}t} + v_j' \frac{\partial \bar{p}}{\partial x_j} + \gamma \bar{p} \frac{\partial v_j'}{\partial x_j} + \gamma p' \frac{\partial \bar{v}_j}{\partial x_j} = 0, \tag{3.9c}$$

where the linear derivative operator $\overline{\mathrm{D}}/\overline{\mathrm{D}}t$ is defined to be

$$\frac{\overline{\mathrm{D}}}{\overline{\mathrm{D}}t} = \frac{\partial}{\partial t} + \bar{v}_j \frac{\partial}{\partial x_j}. \tag{3.10}$$

3.4.1 Parallel base flows

As mentioned in Section 3.2, these equations can be greatly simplified by assuming the flow to be parallel. Despite of the fact that parallel flow is an over-simplification, the parallel flow stability theory does form the basis of modern theories. More importantly, the physical insights that one can gain from some of the analytical solutions often make this simple theory more valuable. Therefore, in the following derivations, we restrict our base flow to be strictly parallel and only vary in the cross-stream direction. The base flow thus satisfies

$$\bar{v}_i = U(x_2, x_3)\delta_{i3}. \tag{3.11}$$

This immediately implies that $\overline{\mathrm{D}}/\overline{\mathrm{D}}t = \frac{\partial}{\partial t} + U\frac{\partial}{\partial x_1}$. One can easily verify that equation 3.9 reduces to

$$\frac{\overline{\mathrm{D}}\rho'}{\overline{\mathrm{D}}t} + v'_j \frac{\partial \bar{\rho}}{\partial x_j} + \bar{\rho}\frac{\partial v'_j}{\partial x_j} = 0, \tag{3.12a}$$

$$\bar{\rho}\left(\frac{\overline{\mathrm{D}}v'_i}{\overline{\mathrm{D}}t} + v'_j \frac{\partial \bar{v}_i}{\partial x_j}\right) + \frac{\partial p'}{\partial x_i} = 0, \tag{3.12b}$$

$$\frac{\overline{\mathrm{D}}p'}{\overline{\mathrm{D}}t} + \gamma\bar{p}\frac{\partial v'_j}{\partial x_j} = 0. \tag{3.12c}$$

It is useful to note that the continuity equation essentially decouples from the momentum and energy equations. Therefore, it suffices to consider only the three momentum and one energy equations. In a cylindrical coordinate system (z, σ, ϕ) whose origin coincides with the Cartesian coordinate system, if we further restrict the base flow only vary with σ, then the governing equations change to

$$\bar{\rho}\left(\frac{\partial v'_z}{\partial t} + U(\sigma)\frac{\partial v'_z}{\partial z} + v'_\sigma \frac{\mathrm{d}U(\sigma)}{\mathrm{d}\sigma}\right) + \frac{\partial p'}{\partial z} = 0, \tag{3.13a}$$

$$\bar{\rho}\left(\frac{\partial v'_\sigma}{\partial t} + U(\sigma)\frac{\partial v'_\sigma}{\partial z}\right) + \frac{\partial p'}{\partial \sigma} = 0, \tag{3.13b}$$

$$\bar{\rho}\left(\frac{\partial v'_\phi}{\partial t} + U(\sigma)\frac{\partial v'_\phi}{\partial z}\right) + \frac{1}{\sigma}\frac{\partial p'}{\partial \phi} = 0, \tag{3.13c}$$

$$\frac{\partial p'}{\partial t} + U(\sigma)\frac{\partial p'}{\partial z} + \gamma\bar{p}\left(\frac{1}{\sigma}\frac{\partial v'_\sigma \sigma}{\partial \sigma} + \frac{\partial v'_z}{\partial z} + \frac{1}{\sigma}\frac{\partial v'_\phi}{\partial \phi}\right) = 0, \tag{3.13d}$$

where v'_z, v'_σ and v'_ϕ denote the fluctuation velocity in the streamwise, radial and azimuthal directions, respectively.

For each of the fluctuation quantity, such as the pressure p', try a separable solution of the form

$$p'(z,\sigma,\phi,t) = \hat{p}(\sigma)\mathrm{e}^{\mathrm{i}(\alpha z + n\phi - \omega t)}, \tag{3.14}$$

where n is an integer representing the azimuthal mode number. Upon defining $\Omega = \omega - \alpha U(\sigma)$, with the above equation, equation 3.13 becomes (Morris, 2010)

$$\mathrm{i}\bar{\rho}\Omega\hat{v}_z - \rho\hat{v}_\sigma\frac{\mathrm{d}U}{\mathrm{d}\sigma} - \mathrm{i}\alpha\hat{p} = 0, \tag{3.15a}$$

$$\mathrm{i}\bar{\rho}\Omega\hat{v}_\sigma - \frac{\mathrm{d}\hat{p}}{\mathrm{d}\sigma} = 0, \tag{3.15b}$$

$$\bar{\rho}\Omega\hat{v}_\phi - \frac{n}{\sigma}\hat{p} = 0, \tag{3.15c}$$

$$\mathrm{i}\Omega\hat{p} - \gamma\bar{p}\left(\frac{1}{\sigma}\frac{\mathrm{d}\hat{v}_\sigma\sigma}{\mathrm{d}\sigma} + \mathrm{i}\alpha\hat{v}_z + \mathrm{i}\frac{n}{\sigma}\hat{v}_\phi\right) = 0, \tag{3.15d}$$

where the hat quantities are defined similarly as $\hat{p}$ shown in equation 3.14. The four equations can be easily combined to have a single second-order ordinary differential equation for the pressure $\hat{p}$, i.e.

$$\frac{\mathrm{d}^2\hat{p}}{\mathrm{d}\sigma^2} + \left(\frac{1}{\sigma} + \frac{2\alpha}{\Omega}\frac{\mathrm{d}U}{\mathrm{d}\sigma} - \frac{1}{\bar{\rho}}\frac{\mathrm{d}\bar{\rho}}{\mathrm{d}\sigma}\right)\frac{\mathrm{d}\hat{p}}{\mathrm{d}\sigma} + \left(\frac{\Omega^2}{\bar{c}^2} - \alpha^2 - \frac{n^2}{\sigma^2}\right)\hat{p} = 0, \tag{3.16}$$

where we have defined the base flow local speed of sound $\bar{c} \equiv \sqrt{\gamma\bar{p}/\bar{\rho}}$. Equation 3.16 describes the small fluctuation pressure on a base shear flow. Since sound is also a small-amplitude pressure fluctuation, one can expect this same equation governs the sound propagation through a parallel axisymmetric shear flows, as shown by Lilley (1974). This same equation was also derived by Pridmore-Brown (1958) when he studied the sound propagation through a duct flow. We will come across this equation in subsequent chapters when we develop jet noise models.

The vortex sheet solution

When a general shear flow profile $U(\sigma)$ is given, equation 3.16 often has no solutions of simple analytical form and has to be be solved numerically. An analytical solution can be, however obtained, if the flow has a "top-hat" profile, i.e. the problem reduces to a compressible stability analysis of a simple vortex sheet. We re-derive such a result in this chapter as it provides useful insights into the stability characteristics of more realistic jets. Inside the vortex sheet, we have

a uniform velocity U, and equation 3.16 reduces to the nth Bessel function

$$\sigma^2 \frac{\mathrm{d}^2\hat{p}}{\mathrm{d}\sigma^2} + \sigma \frac{\mathrm{d}\hat{p}}{\mathrm{d}\sigma} + \left(\mu_i^2\sigma^2 - n^2\right)\hat{p} = 0, \tag{3.17}$$

where $\mu_i = \sqrt{\alpha^2 - \Omega^2/\bar{c}^2}$. Here, the branch cut is chosen such that $0 \leq \arg\mu_i < \pi$. Combine with the boundary condition that the solution at $\sigma = 0$ should be finite, one can show that solution to equation 3.17 is given by

$$\hat{p}_i = C_{1n} J_n(\mu_i \sigma), \tag{3.18}$$

where $\hat{p}_i$ denotes the fluctuation pressure inside the vortex sheet, C_{1n} is an arbitrary constant and $J_n(z)$ is the nth Bessel function of the first kind. Since n is a positive integer, $J_n(z)$ is an entire function of z with finite value at $z = 0$. Choosing the principal value such that $0 \leq \arg\mu_i < \pi$ does not loss generality, since we know that $J_n(-z) = (-1)^n J_n(z)$. Similarly, the equation outside the vortex sheet also takes the form of the nth Bessel equation, i.e.

$$\sigma^2 \frac{\mathrm{d}^2\hat{p}}{\mathrm{d}\sigma^2} + \sigma \frac{\mathrm{d}\hat{p}}{\mathrm{d}\sigma} + \left(\mu_o^2\sigma^2 - n^2\right)\hat{p} = 0, \tag{3.19}$$

where $\mu_o = \sqrt{\alpha^2 - \Omega^2/\bar{c}^2}$. The branch cut is chosen such that $0 \leq \arg\mu_o < \pi/2$ to satisfy the boundary condition at $\sigma \to \infty$. The solution corresponding to an outgoing wave can be found to be

$$\hat{p}_o = C_{2n} H_n^{(1)}(\mu_o \sigma), \tag{3.20}$$

where $\hat{p}_o$ denotes the fluctuation pressure outside the vortex sheet, C_{2n} is an arbitrary constant and $H_n^{(1)}(z)$ is the Hankel function of the first kind. Note that if we choose the branch cut such that $\pi \leq \arg\mu_o < 3\pi/2$, the proper solution would be $C_{2n} H_n^{(2)}(\mu_o\sigma)$, where $H_n^{(2)}(z)$ is the Hankel function of the second kind. Since $H_n^{(2)}(-z) = (-1)^{n+1} H_n^{(1)}(z)$, here we can use the Hankel function of the first kind without losing generality.

On the surface of the vortex sheet, two conditions have to be met: the kinematic and the dynamic boundary conditions. The dynamic boundary condition is simple, i.e. $\hat{p}_i = \hat{p}_o$ on the cylindrical surface $\sigma = a$, where a is the radius of the vortex sheet. Assume that the perturbed interface is given by $\sigma = a + \eta'(x, \theta, t)$, then the kinematic boundary condition states that the free surface satisfies

$$\frac{\mathrm{D}(\sigma - a - \eta')}{\mathrm{D}t} = 0. \tag{3.21}$$

Substituting the flow quantities on both sides of the vortex sheet into equation 3.21 and eliminating the variable η', we obtain the kinematic boundary condition at $\sigma = a$,

$$\bar{\rho}_o \omega^2 \frac{\mathrm{d}\hat{p}_i}{\mathrm{d}\sigma} = \bar{\rho}_i (\omega - \alpha U)^2 \frac{\mathrm{d}\hat{p}_o}{\mathrm{d}\sigma}, \tag{3.22}$$

where $\bar{\rho}_o$ and $\bar{\rho}_i$ are the base flow densities outside and inside the vortex sheet, respectively. Combining the dynamic and kinematic boundary conditions, one can show that in order to have a pair of non-trivial solutions,

$$D_n(\omega,\alpha) = \bar{\rho}_i(\omega-\alpha U)^2 J_n(\mu_i a)\mu_o H_n^{(1)\prime}(\mu_o a) - \bar{\rho}_o\omega^2\mu_i J_n'(\mu_i a)H_n^{(1)}(\mu_o a) = 0 \quad (3.23)$$

has to hold. This is the dispersion relation, from which we can find the eigenvalues. For spatial stability analysis, we assume a real number α and find the complex ω such that $D_n(\omega,\alpha)=0$. For temporal stability analysis, we designate a real value to the angular frequency ω and calculate the complex number α to let $D_n(\omega,\alpha)$ vanish. More generally, both α and ω can be treated as complex numbers, and such an analysis is referred to as the *spatial-temporal stability analysis*.

Realistic shear flow solutions

As demonstrated in the vortex sheet case, equation 3.16 needs to be solved to obtain the eigenvalues which determine the stability characteristics of a parallel jet. The dispersion relation in this simple case is in an analytical form. Although it is not of an algebraic form, one can still solve this equation readily using numerical methods. For a more general flow with the velocity profile $U(\sigma)$ varying with radius σ, it is unlikely to be possible to obtain an analytical solution to equation 3.16. A numerical scheme is required to solve for the eigenvalues. There are various methods to perform such an analysis, such as the shooting method and the full-discretization method, which are reviewed in detail by Morris (2010).

3.4.2 Flow diverging and other effects

When the base flow is not parallel, equation 3.9 cannot be further simplified. However, by assuming a slowly diverging and incompressible flow, a multi-scale analysis can be performed. Detailed derivations are not repeated here and the interested reader can refer to Crighton and Gaster (1976), Tam and Morris (1980) and Saric and Nayfeh (1975).

At high Reynolds number, it is expected that instability waves can be well modelled by inviscid theories. A large portion of literature therefore ignores the viscous effects. However, it is useful to know how viscous effects would change the characteristics of instability waves. Some authors have carried out studies on this. However, these effects, together with the effects of Mach number (compressibility), jet total temperature ratio and jet shear layer thickness, are not reviewed in this chapter, and the details can be found in the recent review by Morris (2010).

Part II

PREDICTION

Chapter 4

Isolated Jet Noise Prediction

Modern theoretical approaches to jet noise research date back to 1952, when Lighthill published his acoustic analogy theories. Ever since, isolated jet noise has been heavily studied. Due to the lack of the understanding of turbulence, acoustic analogy theories have been the dominant methods. Lighthill's theory shows that the far-field noise produced by an isolated jet at static ambient condition is equivalent to that by a distribution of external stress in the form of quadrupole sources in an unbounded and static flow field. This implies that both the generation and the propagation effects of sound inside the mean shear jet flow can be accounted for by the equivalent sources. Although this is mathematically rigorous, one can expect that this approach is not in accord with the actual physics and therefore is likely to be error-prone. Many attempts to improve Lighthill's analogy have emerged thereafter (Lighthill, 1952; Williams, 1963; Lilley, 1974; Goldstein, 2003) to account for the propagation effects explicitly. Among them the generalized acoustic analogy approach proposed by Goldstein (2003) provides a general rational basis for these theories and proves to be more robust in the accurate prediction of isolated jet noise.

Therefore, in this chapter, we combine this theory with the techniques of adjoint Green's functions and the assumption of a locally-parallel jet mean flow, then proceed to develop a low order efficient jet noise prediction model that compares very well with experimental results. The model is implemented by the author in a highly efficient numerical code, CONJURE, capable of predicting far-field noise spectra at various observer angles within seconds. This is a substantial improvement to most existing codes, which typically take hours or even days. This improvement results from a convenient form of Runge-Kutta equations, an innovative way of solving the involved boundary-value equations and also a maximized analyticity of the final equations. Though the formulation is not totally new, for example, some of results obtained

in this chapter are partly similar to some previous work (Afsar, 2009; Karabasov et al., 2010; Mohan et al., 2015), such a highly efficient implementation in numerical codes is new and exceedingly useful.

4.1 The analogy equations

Due to the complicated algebra and the large number of introduced symbols, the essential beginning part of the Goldstein analogy theory on which we base our model is re-derived in this section, while the full analogy theory is reproduced in Appendix B.

Under the Cartesian coordinate system defined in Chapter 2, the Navier Stokes equation reads

$$\frac{\partial \rho}{\partial t} + \frac{\partial}{\partial x_j}\rho v_j = 0, \tag{4.1a}$$

$$\frac{\partial \rho v_i}{\partial t} + \frac{\partial}{\partial x_j}\rho v_i v_j + \frac{\partial p}{\partial x_i} = \frac{\partial \sigma_{ij}}{\partial x_j}, \tag{4.1b}$$

$$\frac{\partial (\rho h_0 - p)}{\partial t} + \frac{\partial}{\partial x_j}\rho h_0 v_j = -\frac{\partial q_j}{\partial x_j} + \frac{\partial v_i \sigma_{ij}}{\partial x_j}, \tag{4.1c}$$

where h_0 denotes the total enthalpy, q_j heat flux per unit volume (in the j direction) and σ_{ij} the viscous stress. Other quantities have been defined in both Chapter 1 and 2. In order to close the above equations, we need the state equations of the perfect gas, i.e.

$$p = \rho R T, \tag{4.2a}$$

$$h = c_p T, \tag{4.2b}$$

where c_p represents the specific heat at constant pressure and h the enthalpy of the fluid.

As a routine procedure, we decompose the basic flow variables into a base part and a fluctuation part. This is similar to the instability analysis described in Chapter 3. The difference is that, however, we allow h and v_i to be decomposed somewhat differently from ρ and p. To show this difference, we use $\tilde{}$ and $''$ to denote the base and fluctuation parts of h and v_i, respectively. The other decomposition, on the other hand, is given in Chapter 3. The main flow quantities can therefore be written as

$$\rho = \bar{\rho} + \rho',\ p = \bar{p} + p',\ \sigma_{ij} = \bar{\sigma}_{ij} + \sigma'_{ij},\ h = \tilde{h} + h'',\ v_i = \tilde{v}_i + v''_i. \tag{4.3}$$

As shown above, the base flow quantities are given by $\bar{\rho}$, $\bar{p}$, $\bar{\sigma}_{ij}$, $\tilde{h}$, $\tilde{v}_i$ etc. We choose them in a

way that the following base-flow equations hold:

$$\frac{\partial \bar{\rho}}{\partial t} + \frac{\partial}{\partial x_j}\bar{\rho}\tilde{v}_j = 0, \tag{4.4a}$$

$$\frac{\partial \bar{\rho}\tilde{v}_i}{\partial t} + \frac{\partial}{\partial x_j}\bar{\rho}\tilde{v}_i\tilde{v}_j + \frac{\partial \bar{p}}{\partial x_i} = \frac{\partial}{\partial x_j}(\tilde{T}_{ij} + \bar{\sigma}_{ij}), \tag{4.4b}$$

$$\frac{\partial(\bar{\rho}\tilde{h}_0 - \bar{p})}{\partial t} + \frac{\partial}{\partial x_j}\bar{\rho}\tilde{h}_0\tilde{v}_j = \frac{\partial \tilde{H}_0}{\partial t} + \frac{\partial}{\partial x_j}\tilde{H}_0\tilde{v}_j + \frac{\partial}{\partial x_j}\tilde{H}_j - \frac{\partial \bar{q}_j}{\partial x_j} + \frac{\partial \tilde{v}_i\bar{\sigma}_{ij}}{\partial x_j}. \tag{4.4c}$$

In the above equations, $\tilde{T}_{ij}$, $\tilde{H}_0$ and $\tilde{H}_j$ are to be determined a later stage, and $\tilde{h}_0$ is defined as

$$\tilde{h}_0 \equiv \tilde{h} + \frac{1}{2}\tilde{v}^2,$$

where $\tilde{v}^2 \equiv \tilde{v}_i\tilde{v}_i$. Note here $\tilde{v}$ is not defined according to the base flow decomposition, it is only used to substitute $\tilde{v}_i\tilde{v}_i$. By defining the non-linear differential operator

$$\mathrm{D}_0 f = \frac{\partial f}{\partial t} + \frac{\partial}{\partial x_j}\tilde{v}_j f,$$

equation 4.4 can be written in a more compact form as

$$\mathrm{D}_0\bar{\rho} = 0, \tag{4.5a}$$

$$\mathrm{D}_0\bar{\rho}\tilde{v}_i + \frac{\partial \bar{p}}{\partial x_i} = \frac{\partial}{\partial x_j}(\tilde{T}_{ij} + \bar{\sigma}_{ij}), \tag{4.5b}$$

$$\mathrm{D}_0\bar{\rho}\tilde{h}_0 - \frac{\partial \bar{p}}{\partial t} = \mathrm{D}_0\tilde{H}_0 + \frac{\partial}{\partial x_j}(\tilde{H}_j - \bar{q}_j + \tilde{v}_i\bar{\sigma}_{ij}). \tag{4.5c}$$

Substituting equation 4.3 into equation 4.1a then subtracting equation 4.4a, one has

$$\frac{\partial}{\partial t}\rho' + \frac{\partial}{\partial x_j}\left(\rho v_j'' + \tilde{v}_j\rho'\right) = 0.$$

Upon defining a new fluctuation variable $m_j = \rho v_j''$ one can write the above equation into

$$\mathrm{D}_0\rho' + \frac{\partial}{\partial x_j}m_j = 0. \tag{4.6}$$

It should be noted that for fluctuation flow quantities D_0 is a linear operator. Similarly, the momentum equation simplifies to

$$\mathrm{D}_0(m_i + \rho'\tilde{v}_i) + \frac{\partial}{\partial x_j}m_j\tilde{v}_i + \frac{\partial p'}{\partial x_i} = \frac{\partial}{\partial x_j}(\sigma_{ij}' - \rho v_i''v_j'' - \tilde{T}_{ij}). \tag{4.7}$$

The algebra involved in the energy equation is more complex, but it can be shown that after substituting equation 4.3 into equation 4.1c and subtracting the base flow equation from it, one

attains

$$\frac{\partial}{\partial t}\left(\left[\rho h'' + \rho'\tilde{h}\right] + \frac{1}{2}\left[\rho(2\tilde{v}_i v_i'' + v_i'' v_i'') + \rho'\tilde{v}_i\tilde{v}_i\right]\right) +$$
$$\frac{\partial}{\partial x_j}\left(\left[\rho(h''\tilde{v}_j + \tilde{h}v_j'' + h''v_j'') + \rho'\tilde{h}\tilde{v}_j\right] + \left[\frac{1}{2}\rho v_j(2\tilde{v}_i v_i'' + v_i'' v_i'') + \frac{1}{2}(\rho v_j'' + \rho'\tilde{v}_j)\tilde{v}_i\tilde{v}_i\right]\right) -$$
$$\frac{\partial}{\partial t}p' = -\frac{\partial}{\partial x_j}q_j' + \frac{\partial}{\partial x_j}(\sigma_{ij}v_i'' + \sigma_{ij}'\tilde{v}_i) - \mathrm{D}_0\tilde{H}_0 - \frac{\partial}{\partial x_j}\tilde{H}_j.$$

We try to write the above equation in a more compact form by using the operator D_0, i.e.

$$\begin{aligned}
&\mathrm{D}_0\left(\left[\rho h'' + \rho'\tilde{h}\right] + \frac{1}{2}\left[\rho(2\tilde{v}_i v_i'' + v_i'' v_i'') + \rho'\tilde{v}_i\tilde{v}_i\right]\right) + \\
&\frac{\partial}{\partial x_j}\left(\left[\rho(\tilde{h}v_j'' + h''v_j'')\right] + \left[\frac{1}{2}\rho v_j''(2\tilde{v}_i v_i'' + v_i'' v_i'') + \frac{1}{2}\rho v_j''\tilde{v}_i\tilde{v}_i\right]\right) - \frac{\partial}{\partial t}p' \qquad (4.8)\\
&= -\mathrm{D}_0\tilde{H}_0 - \frac{\partial}{\partial x_j}\left(\tilde{H}_j + q_j' - \sigma_{ij}v_i'' - \sigma_{ij}'\tilde{v}_i\right).
\end{aligned}$$

Making use of the definition of m_j yields

$$\begin{aligned}
&\mathrm{D}_0\left(\left[\rho h'' + \rho'\tilde{h}\right] + \frac{1}{2}\left[\rho(2\tilde{v}_i v_i'' + v_i'' v_i'') + \rho'\tilde{v}_i\tilde{v}_i\right]\right) + \\
&\frac{\partial}{\partial x_j}\left(m_j\tilde{h}_0 + \left[\rho v_j''(h'' + \tilde{v}_i v_i'' + \frac{1}{2}v_i'' v_i'')\right]\right) - \frac{\partial}{\partial t}p' \qquad (4.9)\\
&= -\mathrm{D}_0\tilde{H}_0 - \frac{\partial}{\partial x_j}\left(\tilde{H}_j + q_j' - \sigma_{ij}v_i'' - \sigma_{ij}'\tilde{v}_i\right).
\end{aligned}$$

If we define a coupled fluctuation quantity (of zero time mean) $\pi \equiv \rho h'' + \rho'\tilde{h}$, then we can show that the energy equation reduces to

$$\begin{aligned}
&\mathrm{D}_0\left(\pi + \boldsymbol{m}\cdot\tilde{\boldsymbol{v}} + \frac{1}{2}\rho'\tilde{v}_i\tilde{v}_i\right) + \mathrm{D}_0\frac{1}{2}\rho v''^2 + \frac{\partial}{\partial x_j}m_j\tilde{h}_0 - \frac{\partial}{\partial t}p' \\
&= -\mathrm{D}_0\tilde{H}_0 - \frac{\partial}{\partial x_j}\left(\rho v_j''(h'' + \tilde{v}_i v_i'' + \frac{1}{2}v_i'' v_i'') + \tilde{H}_j + q_j' - \sigma_{ij}v_i'' - \sigma_{ij}'\tilde{v}_i\right), \qquad (4.10)
\end{aligned}$$

where for the sake of brevity we have defined $v''^2 = v_i'' v_i''$.

The momentum equation can be simplified by differentiating the quadratic terms on the left-hand sides by parts and using the continuity equation. Before proceeding, it useful to note the general property of the operator D_0, i.e.

$$\begin{aligned}
\mathrm{D}_0(fg) &= \frac{\partial fg}{\partial t} + \frac{\partial fg\tilde{v}_j}{\partial x_j} \\
&= \frac{\partial f}{\partial t}g + f\frac{\partial g}{\partial t} + \frac{\partial f\tilde{v}_j}{\partial x_j}g + f\tilde{v}_j\frac{\partial g}{\partial x_j} \\
&= (\mathrm{D}_0 f)g + f(\mathrm{D}_0 g) - fg\frac{\partial\tilde{v}_j}{\partial x_j}, \qquad (4.11)
\end{aligned}$$

where f and g are general functions of t and x_j. Therefore, with the definition of $e_{ij} \equiv -(\rho v_i'' v_j'' + \tilde{T}_{ij} - \sigma_{ij}')$, the momentum equation can now be written as

$$\mathrm{D}_0 m_i + \frac{\partial p'}{\partial x_i} + m_j \frac{\partial \tilde{v}_i}{\partial x_j} + \tilde{v}_i \frac{\partial m_j}{\partial x_j} + \tilde{v}_i \mathrm{D}_0 \rho' + \rho' \mathrm{D}_0 \tilde{v}_i - \rho' \tilde{v}_i \frac{\partial \tilde{v}_j}{\partial x_j} = \frac{\partial e_{ij}}{\partial x_j}. \tag{4.12}$$

Use the continuity equation to cancel out the two terms in the middle of the left hand side of the above equation and use the base-flow momentum equation to rewrite the resulting equation as

$$\mathrm{D}_0 m_i + \frac{\partial p'}{\partial x_i} + m_j \frac{\partial \tilde{v}_i}{\partial x_j} + \rho' (-\frac{1}{\bar{\rho}} \frac{\partial \tilde{\tau}_{ij}}{\partial x_j} + \tilde{v}_i \frac{\partial \tilde{v}_j}{\partial x_j}) - \rho' \tilde{v}_i \frac{\partial \tilde{v}_j}{\partial x_j} = \frac{\partial e_{ij}}{\partial x_j}, \tag{4.13}$$

where $\tilde{\tau}_{ij} = \delta_{ij}\bar{p} - \tilde{T}_{ij} - \bar{\sigma}_{ij}$. This equation equals to

$$\mathrm{D}_0 m_i + \frac{\partial p'}{\partial x_i} + m_j \frac{\partial \tilde{v}_i}{\partial x_j} - \frac{\rho'}{\bar{\rho}} \frac{\partial \tilde{\tau}_{ij}}{\partial x_j} = \frac{\partial e_{ij}}{\partial x_j}. \tag{4.14}$$

The simplification of the energy equation is more complicated than that of the momentum equation, but the essential steps remain the same: we make use of the base flow continuity equation, the aforementioned operator property and the momentum equation (before differentiating by parts). From the full and base flow gas state equation (the base flow is also chosen to satisfy the state equation), one can show that

$$\pi = \frac{c_p}{R} p'.$$

Therefore, the energy equation (equation 4.10) can be expanded to be

$$\begin{aligned} &\frac{c_v}{R}\mathrm{D}_0 p' + \frac{\partial m_j \tilde{h}}{\partial x_j} + \frac{\partial p' \tilde{v}_j}{\partial x_j} - \frac{m_i}{\bar{\rho}} \frac{\partial \tilde{\tau}_{ij}}{\partial x_j} - \rho' \tilde{v}^2 \frac{\partial \tilde{v}_j}{\partial x_j} + (m_j \tilde{v}_i) \frac{\partial \tilde{v}_i}{\partial x_j} + \rho' \tilde{v}_j \mathrm{D}_0 \tilde{v}_j + \tilde{v}_j \mathrm{D}_0 m_j \\ &= -\mathrm{D}_0 (\frac{1}{2}\rho v''^2 + \tilde{H}_0) - \frac{\partial}{\partial x_j}(\rho v_j'' h_0'' + \tilde{H}_j + q_j' - v_i'' \sigma_{ij}) - \frac{\partial}{\partial x_j}(\rho v_j'' v_i'' \tilde{v}_i - \tilde{v}_i \sigma_{ij}'), \end{aligned}$$

where c_v is the specific heat at constant volume and h_0'' is defined as $h'' + v''^2/2$. For an ideal gas, one can show $c_v = c_p - R$. The above equation can be shown to be equivalent to

$$\begin{aligned} &\frac{c_v}{R}\mathrm{D}_0 p' + \frac{\partial m_j \tilde{h}}{\partial x_j} + \frac{\partial p' \tilde{v}_j}{\partial x_j} - \frac{m_i}{\bar{\rho}} \frac{\partial \tilde{\tau}_{ij}}{\partial x_j} \\ &= -\mathrm{D}_0 (\frac{1}{2}\rho v''^2 + \tilde{H}_0) - \frac{\partial}{\partial x_j}(\rho v_j'' h_0'' + \tilde{H}_j - \tilde{T}_{ij}\tilde{v}_i + q_j' - v_i'' \sigma_{ij}) \\ &\quad + e_{ij} \frac{\partial \tilde{v}_i}{\partial x_j} + \left\{ \frac{\partial e_{ij}}{\partial x_j} \tilde{v}_i + \rho' \tilde{v}^2 \frac{\partial \tilde{v}_j}{\partial x_j} - (m_j \tilde{v}_i) \frac{\partial \tilde{v}_i}{\partial x_j} - \rho' \tilde{v}_j \mathrm{D}_0 \tilde{v}_j - \tilde{v}_j \mathrm{D}_0 m_j \right\}. \end{aligned} \tag{4.15}$$

Through use of the momentum equation (equation 4.7), the expression in the curly braces can be found to be

$$\tilde{v}_i(\tilde{v}_i \mathrm{D}_0\rho' + \tilde{v}_i\frac{\partial m_j}{\partial x_j} - \rho'\tilde{v}_i\frac{\partial \tilde{v}_j}{\partial x_j} + \frac{\partial p'}{\partial x_i}) + \rho'\tilde{v}^2\frac{\partial \tilde{v}_j}{\partial x_j}. \tag{4.16}$$

After making use of the continuity equation, one obtains the simplified energy equation

$$\begin{aligned}&\frac{c_v}{R}\mathrm{D}_0 p' + \frac{\partial m_j\tilde{h}}{\partial x_j} + p'\frac{\partial \tilde{v}_j}{\partial x_j} - \frac{m_i}{\bar{\rho}}\frac{\partial \tilde{\tau}_{ij}}{\partial x_j}\\ &= -\mathrm{D}_0(\frac{1}{2}\rho v''^2 + \tilde{H}_0) - \frac{\partial}{\partial x_j}(\rho v_j'' h_0'' + \tilde{H}_j - \tilde{T}_{ij}\tilde{v}_i + q_j' - v_i''\sigma_{ij}) + e_{ij}\frac{\partial \tilde{v}_i}{\partial x_j}.\end{aligned} \tag{4.17}$$

4.2 Isolated jet noise formulation

We have reproduced Goldstein's acoustic analogy in the preceding section and Appendix B. Based on those results, this section starts to formulate a convenient form for isolated jet noise prediction. It is worth noting that equations B.11a, B.11b and B.11c (in Appendix B) are the exact consequences of rearranging the Navier-Stokes equations. Therefore, they are exact and are applicable for any type of flow. However, for noise prediction of an isolated jet (a cold and round jet for example), additional assumptions can be made and these equations are not necessarily of the most convenient form. Thus, in this section, instead of using equation B.11, we start from the Linearized Euler Equations (LEEs) and aim to develop a low-order efficient model for isolated jet noise prediction.

4.2.1 The analogy equations for isolated jet noise

As mentioned above, to formulate a suitable form for jet noise prediction, we start from the inhomogeneous LEEs (equations 4.6, 4.14 and 4.17) obtained as above, i.e.

$$\mathrm{D}_0\rho' + \frac{\partial}{\partial x_j}m_j = 0, \tag{4.18a}$$

$$\mathrm{D}_0 m_i + \frac{\partial p'}{\partial x_i} + m_j\frac{\partial \tilde{v}_i}{\partial x_j} - \frac{\rho'}{\bar{\rho}}\frac{\partial \tilde{\tau}_{ij}}{\partial x_j} = \frac{\partial e_{ij}}{\partial x_j}, \tag{4.18b}$$

$$\begin{aligned}\frac{c_v}{R}\mathrm{D}_0 p' + \frac{\partial m_j\tilde{h}}{\partial x_j} + p'\frac{\partial \tilde{v}_j}{\partial x_j} - \frac{m_i}{\bar{\rho}}\frac{\partial \tilde{\tau}_{ij}}{\partial x_j} &= -\mathrm{D}_0(\frac{1}{2}\rho v''^2 + \tilde{H}_0) + e_{ij}\frac{\partial \tilde{v}_i}{\partial x_j}\\ &\quad - \frac{\partial}{\partial x_j}(\rho v_j'' h_0'' + \tilde{H}_j - \tilde{T}_{ij}\tilde{v}_i + q_j' - v_i''\sigma_{ij}),\end{aligned} \tag{4.18c}$$

where

$$
\begin{aligned}
m_j &= \rho v_j'', \\
e_{ij} &= -(\rho v_i'' v_j'' + \tilde{T}_{ij} - \sigma_{ij}'), \\
\tilde{\tau}_{ij} &= \delta_{ij}\bar{p} - \tilde{T}_{ij} - \bar{\sigma}_{ij}.
\end{aligned}
$$

Before proceeding to simplify these equations, it is necessary to define the two types of decompositions mentioned in the preceding section. Here we choose the "bar" type flow quantities to be the time averages of the total flow quantities, and the "tilde" quantities to be the Favre averages defined as

$$\tilde{v}_i = \frac{\overline{\rho v_i}}{\bar{\rho}}. \tag{4.19}$$

It is useful to notice a few properties of the Favre average. Similar to the time average, for any two functions of time f and g, the Favre average can be shown to satisfy

$$
\begin{aligned}
\widetilde{fg} - \tilde{f}\tilde{g} &= \widetilde{f''g''}, \\
\widetilde{f''} &= 0.
\end{aligned}
$$

Because $\tilde{h}_0$ is not defined as the Favre average of h, but as $\tilde{h} + \frac{1}{2}\tilde{v}^2$, one can show

$$\overline{\rho h_0} = \bar{\rho}\tilde{h} + \bar{\rho}\frac{1}{2}\widetilde{v^2} = \bar{\rho}\tilde{h} + \frac{1}{2}\bar{\rho}\widetilde{v^2} + \frac{1}{2}\bar{\rho}\widetilde{v''^2} = \bar{\rho}\tilde{h}_0 + \frac{1}{2}\bar{\rho}\widetilde{v''^2}. \tag{4.20}$$

Using this equation, we can verify

$$-\bar{\rho}(\widetilde{h_0 v_j} - \tilde{h}_0\tilde{v}_j) - \frac{1}{2}\tilde{T}_{ii}\tilde{v}_j = -\bar{\rho}\widetilde{h_0''v_j''} + \tilde{v}_i\tilde{T}_{ij}.$$

This identity will be used to obtained the expression for $\tilde{H}_j$ in the following derivations.

Now we are in a position to derive the equations that the base flow satisfies. We do so by taking the time average of the Navier Stoke equations. Upon making use of the Favre averaged quantities, we obtain the base flow equations

$$\frac{\partial\bar{\rho}}{\partial t} + \frac{\partial}{\partial x_j}\bar{\rho}\tilde{v}_j = 0, \tag{4.21a}$$

$$\frac{\partial\bar{\rho}\tilde{v}_i}{\partial t} + \frac{\partial}{\partial x_j}\bar{\rho}\tilde{v}_i\tilde{v}_j + \frac{\partial\bar{p}}{\partial x_i} = \frac{\partial}{\partial x_j}(\tilde{T}_{ij} + \bar{\sigma}_{ij}), \tag{4.21b}$$

$$\frac{\partial(\bar{\rho}\tilde{h}_0 - \bar{p})}{\partial t} + \frac{\partial}{\partial x_j}\bar{\rho}\tilde{h}_0\tilde{v}_j = \frac{\partial\tilde{H}_0}{\partial t} + \frac{\partial}{\partial x_j}\tilde{H}_0\tilde{v}_j + \frac{\partial}{\partial x_j}\tilde{H}_j - \frac{\partial\bar{q}_j}{\partial x_j} + \frac{\partial\tilde{v}_i\bar{\sigma}_{ij}}{\partial x_j}, \tag{4.21c}$$

where the source terms are given by

$$\begin{aligned}\tilde{T}_{ij} &= -\bar{\rho}\widetilde{v_i'' v_j''},\\ \tilde{H}_j &= -\bar{\rho}\widetilde{v_j'' h_0''} + \tilde{T}_{ij}\tilde{v}_i + \overline{v_i''\sigma_{ij}},\\ \tilde{H}_0 &= \frac{1}{2}\tilde{T}_{ii}.\end{aligned}$$

The term in red is an extra term compared to the expression given in Goldstein's discussion (Goldstein, 2003). Now we can express the term $\tilde{\tau}_{ij}$ in terms of mean velocity (note in the rest of this chapter, we still refer to Favre-averaged velocity as the mean flow velocity). Using the mean-flow momentum equation one can verify

$$\frac{\partial \tilde{\tau}_{ij}}{\partial x_j} = \frac{\partial}{\partial x_j}(\delta_{ij}\bar{p} - \tilde{T}_{ij} - \bar{\sigma}_{ij}) = -\mathrm{D}_0\bar{\rho}\tilde{v}_i = -\frac{\partial}{\partial x_j}\bar{\rho}\tilde{v}_i\tilde{v}_j. \tag{4.22}$$

This means that under the choice of the aforementioned base flow, we can write the LEE equations as

$$\mathrm{D}_0\rho' + \frac{\partial}{\partial x_j}m_j = 0, \tag{4.23a}$$

$$\mathrm{D}_0 m_i + \frac{\partial p'}{\partial x_i} + m_j\frac{\partial \tilde{v}_i}{\partial x_j} + \frac{\rho'}{\bar{\rho}}\frac{\partial}{\partial x_j}\bar{\rho}\tilde{v}_i\tilde{v}_j = \frac{\partial e_{ij}}{\partial x_j}, \tag{4.23b}$$

$$\begin{aligned}\frac{c_v}{R}\mathrm{D}_0 p' + \frac{\partial m_j\tilde{h}}{\partial x_j} + p'\frac{\partial \tilde{v}_j}{\partial x_j} + \frac{m_i}{\bar{\rho}}\frac{\partial}{\partial x_j}\bar{\rho}\tilde{v}_i\tilde{v}_j &= -\mathrm{D}_0(\frac{1}{2}\rho v''^2 + \tilde{H}_0)\\ &\quad - \frac{\partial}{\partial x_j}(\rho v_j'' h_0'' + \tilde{H}_j - \tilde{T}_{ij}\tilde{v}_i + q_j' - v_i''\sigma_{ij}) + e_{ij}\frac{\partial \tilde{v}_i}{\partial x_j}.\end{aligned} \tag{4.23c}$$

where

$$\begin{aligned}e_{ij} &= -(\rho v_i'' v_j'' + \tilde{T}_{ij} - \sigma_{ij}'),\\ \tilde{T}_{ij} &= -\bar{\rho}\widetilde{v_i'' v_j''},\\ \tilde{H}_j &= -\bar{\rho}\widetilde{v_j'' h_0''} + \tilde{T}_{ij}\tilde{v}_i + \overline{v_i''\sigma_{ij}},\\ \tilde{H}_0 &= \frac{1}{2}\tilde{T}_{ii}.\end{aligned}$$

Let us invoke the no-viscous-effects and no-heat-source assumptions. This would imply that both σ_{ij} and q_i vanish. Therefore, we are left with

$$\mathrm{D}_0\rho' + \frac{\partial}{\partial x_j}m_j = 0, \tag{4.24a}$$

$$\mathrm{D}_0 m_i + \frac{\partial p'}{\partial x_i} + m_j\frac{\partial \tilde{v}_i}{\partial x_j} + \frac{\rho'}{\bar{\rho}}\frac{\partial}{\partial x_j}\bar{\rho}\tilde{v}_i\tilde{v}_j = \frac{\partial T_{ij}'}{\partial x_j}, \tag{4.24b}$$

$$\frac{c_v}{R}\mathrm{D}_0 p' + \frac{\partial m_j\tilde{h}}{\partial x_j} + p'\frac{\partial \tilde{v}_j}{\partial x_j} + \frac{m_i}{\bar{\rho}}\frac{\partial}{\partial x_j}\bar{\rho}\tilde{v}_i\tilde{v}_j = \frac{1}{2}\mathrm{D}_0 T_{ii}' - \frac{\partial E_j'}{\partial x_j} + T_{ij}'\frac{\partial \tilde{v}_i}{\partial x_j}, \tag{4.24c}$$

where

$$T'_{ij} = e_{ij} = -(\rho v''_i v''_j + \tilde{T}_{ij}),$$
$$E'_j = (\rho v''_j h''_0 - \bar{\rho}\widetilde{v''_j h''_0}).$$

The above equations govern the inviscid perturbations over a mean flow and are obtained from equation 4.18. On the other hand, much of the derivation shown by Goldstein is based on equation B.11 and therefore is different from that shown in equation 4.24. However, the base flow equations, obtained in this section, are the defined in the same manner as those in Goldstein's paper. One can verify that these base flow equations are the equivalent to those discussed by Goldstein (2003) except the extra term $\overline{v''_i \sigma_{ij}}$ obtained in this section. We believe this extra term is somehow missed out in Goldstein's paper. In practical cases, however, this term turns out to be small and should not alter the final results considerably.

Parallel flow assumption

As demonstrated in Chapter 3, assuming the mean flow to be parallel would imply a significant simplification to equation 4.24. Previous studies have shown that for jet noise prediction, the parallel-flow assumption serves as a good approximation for medium to high frequencies (Tam and Auriault, 1998; Karabasov et al., 2010) (the implementation is locally parallel to be more precise, see more discussion in the following sections). The significant simplification to the problem therefore makes this approximation worthwhile.

However, before we invoke this assumption, it is worth noting that this would imply the exclusion of the instability waves in the Green's function to be calculated at at later stage (Dowling et al., 1978; Agarwal et al., 2004; Karabasov et al., 2010). The role of linear instability waves in sound generation in subsonic jets is still open to some debate, although it is widely accepted that they are important noise sources in supersonic jets due to the so-called Mach-wave mechanism. On the other hand, the existence of large coherent structures in turbulent jet flows, which is believed to be closely related to the linear instability waves at the early stage of an evolving jet, is widely accepted, thanks to the extensive previous work (Crow and Champagne, 1971; Brown and Roshko, 1974; Winant and Browand, 1974; Dimotakis and Brown, 1976; Fuchs, 1972; Crighton and Gaster, 1976; Sukuzi and Colonius, 2006; Tinney and Jordan, 2008; Gudmundsson and Colonius, 2011). A recent review of Jordan and Colonius (2013) provides a detailed exposition of the signature of these coherent structures, and it shows that, up to the potential core, these structures can be satisfactorily predicted using linear stability models. However, there is not yet agreement about the mechanisms through which large coherent

structures contribute to the far-field sound in subsonic jets. A possible scenario, for example, is that these instability waves provide an early mechanism of evolving disturbances and lead to a non-linear transition to turbulence further downstream, which may dominate the sound generation. The success of some recent prediction models using acoustic analogy theories for a wide range of observer angles appears to support such a scenario (Karabasov et al., 2010; Mohan et al., 2015). The local-parallel flow assumption employed here will therefore be based on these works.

Some recent work (Lesshafft et al., 2010; Schmidt et al., 2017; Jeun et al., 2016; Semeraro et al., 2016; Tissot et al., 2016; Towne et al., 2017) on global analysis and resolvent analysis (or input-output analysis) investigated the global instability modes and the optimal forcing modes (based on energy gains) of the turbulent mean flow, respectively. Some of the results (see, for example, Schmidt et al. (2017) and Semeraro et al. (2016)) were compared with the extracted coherent structures from either LES or experimental databases and generally good agreement was achieved. These results however cannot conclusively prove that it is these coherent modes that dominate the far-field sound. More specifically, the global analysis ignores the so-called non-linear forcing and investigates the eigenvalues and eigenvectors of the resulting linear operator. It shows that these eigenvectors are the intrinsic disturbance modes that the turbulent jet mean flow supports under a linearized approximation. Because of this, the physical sound sources in a turbulent jets, which may well be related to non-linearity, are still not established. On the other hand, the resolvent analysis keeps the non-linear forcing terms and therefore renders the equations to be exact. In this sense, the resolvent framework is equivalent to the acoustic analogy theories. Unlike the global analysis, the resolvent analysis characterizes the dynamics of the system based on the energy gains. In other words, it identifies the most effective disturbance modes that would maximize the output physical quantity of interest. However, the characteristics of the forcing are independent to the dynamics of the system. Hence, the flow structures or events that are responsible for the dominant sound generation are still yet to be known. The acoustic analogy approach attempts to quantify the sources through the more localized spatial-temporal cross correlation functions while the resolvent framework analyses the projection of the sources to the resolvent modes. In any case, the two approaches are not mutually exclusive and we adopt the acoustic analogy approach in this study with the locally-parallel flow assumption.

To invoke the parallel-flow assumption, let

$$\bar{p} = p_\infty,\ \bar{\rho} = \bar{\rho}(x_2,\ x_3),\ \tilde{v}_1 = U(x_2, x_3),\ \tilde{v}_2 = \tilde{v}_3 = 0,$$

then the LEE equations reduce to

$$\frac{\overline{\mathrm{D}}}{\overline{\mathrm{D}}t}\rho' + \frac{\partial}{\partial x_j}m_j = 0, \tag{4.25a}$$

$$\frac{\overline{\mathrm{D}}}{\overline{\mathrm{D}}t}m_i + \frac{\partial p'}{\partial x_i} + m_j\frac{\partial \tilde{v}_i}{\partial x_j} = \frac{\partial T'_{ij}}{\partial x_j}, \tag{4.25b}$$

$$\frac{1}{\gamma-1}\frac{\overline{\mathrm{D}}}{\overline{\mathrm{D}}t}p' + \frac{\partial m_j\tilde{h}}{\partial x_j} = \frac{1}{2}\mathrm{D}_0 T'_{ii} - \frac{\partial}{\partial x_j}E'_j + T'_{ij}\frac{\partial \tilde{v}_i}{\partial x_j}. \tag{4.25c}$$

Clearly the continuity equation is decoupled now because there is no term involving ρ' appearing in the momentum and energy equations (if we treat all the terms on the right hand side of the two equations as already known).

We are now in a position to combine the momentum and energy equations into one single equation for p'. We do so because we are more interested in the pressure fluctuation p', which is interpreted as sound in the far-field. If we let $u'_i = m_i/\bar{\rho}$, the two equations become

$$\bar{\rho}\frac{\overline{\mathrm{D}}}{\overline{\mathrm{D}}t}u'_i + \frac{\partial p'}{\partial x_i} + \bar{\rho}u'_j\frac{\partial \tilde{v}_i}{\partial x_j} = \frac{\partial T'_{ij}}{\partial x_j}, \tag{4.26a}$$

$$\frac{1}{\gamma-1}\frac{\overline{\mathrm{D}}}{\overline{\mathrm{D}}t}p' + \frac{\gamma p_\infty}{\gamma-1}\frac{\partial u'_j}{\partial x_j} = \frac{1}{2}\mathrm{D}_0 T'_{ii} - \frac{\partial}{\partial x_j}E'_j + T'_{ij}\frac{\partial \tilde{v}_i}{\partial x_j}. \tag{4.26b}$$

Further simplifying the above equations yields

$$\frac{\overline{\mathrm{D}}}{\overline{\mathrm{D}}t}u'_i + \frac{1}{\bar{\rho}}\frac{\partial p'}{\partial x_i} + u'_j\frac{\partial \tilde{v}_i}{\partial x_j} = \frac{1}{\bar{\rho}}\frac{\partial T'_{ij}}{\partial x_j}, \tag{4.27a}$$

$$\frac{1}{\gamma p_\infty}\frac{\overline{\mathrm{D}}}{\overline{\mathrm{D}}t}p' + \frac{\partial u'_j}{\partial x_j} = \frac{\gamma-1}{\gamma p_\infty}\left(\frac{1}{2}\mathrm{D}_0 T'_{ii} - \frac{\partial}{\partial x_j}E'_j + T'_{ij}\frac{\partial \tilde{v}_i}{\partial x_j}\right). \tag{4.27b}$$

Taking the divergence of the first equation and the convective differentiation of the second equation, one can show

$$\frac{\overline{\mathrm{D}}}{\overline{\mathrm{D}}t}\frac{\partial u'_i}{\partial x_i} + \frac{\partial u'_i}{\partial x_1}\frac{\partial U}{\partial x_i} + \frac{\partial}{\partial x_i}\left(\frac{1}{\bar{\rho}}\frac{\partial p'}{\partial x_i} + u'_j\frac{\partial \tilde{v}_i}{\partial x_j}\right) = \frac{\partial}{\partial x_i}\frac{1}{\bar{\rho}}\frac{\partial T'_{ij}}{\partial x_j}, \tag{4.28a}$$

$$\frac{1}{\gamma p_\infty}\frac{\overline{\mathrm{D}}^2}{\overline{\mathrm{D}}t^2}p' + \frac{\overline{\mathrm{D}}}{\overline{\mathrm{D}}t}\frac{\partial u'_j}{\partial x_j} = \frac{\gamma-1}{\gamma p_\infty}\frac{\overline{\mathrm{D}}}{\overline{\mathrm{D}}t}\left(\frac{1}{2}\mathrm{D}_0 T'_{ii} - \frac{\partial}{\partial x_j}E'_j + T'_{ij}\frac{\partial \tilde{v}_i}{\partial x_j}\right). \tag{4.28b}$$

Subtracting equation 4.28b from equation 4.28a, one obtains

$$\begin{aligned} 2\frac{\partial u'_i}{\partial x_1}\frac{\partial U}{\partial x_i} + \frac{\partial}{\partial x_i}\frac{1}{\bar{\rho}}\frac{\partial p'}{\partial x_i} - \frac{1}{\gamma p_\infty}\frac{\overline{\mathrm{D}}^2}{\overline{\mathrm{D}}t^2}p' \\ = \frac{\partial}{\partial x_i}\frac{1}{\bar{\rho}}\frac{\partial T'_{ij}}{\partial x_j} - \frac{\gamma-1}{\gamma p_\infty}\frac{\overline{\mathrm{D}}}{\overline{\mathrm{D}}t}\left(\frac{1}{2}\mathrm{D}_0 T'_{ii} - \frac{\partial}{\partial x_j}E'_j + T'_{ij}\frac{\partial \tilde{v}_i}{\partial x_j}\right). \end{aligned} \tag{4.29}$$

To cancel the remaining term involving u_i', we multiply the momentum equation by $\partial U/\partial x_i$ to obtain

$$\frac{\overline{\mathrm{D}}u_i'}{\overline{\mathrm{D}}t}\frac{\partial U}{\partial x_i}+\frac{1}{\bar{\rho}}\frac{\partial p'}{\partial x_i}\frac{\partial U}{\partial x_i}=\frac{1}{\bar{\rho}}\frac{\partial T_{ij}'}{\partial x_j}\frac{\partial U}{\partial x_i}. \tag{4.30}$$

Taking the convective differentiation of equation 4.29 yields

$$\begin{aligned}2\frac{\partial U}{\partial x_i}\frac{\overline{\mathrm{D}}}{\overline{\mathrm{D}}t}\frac{\partial u_i'}{\partial x_1}+\frac{\overline{\mathrm{D}}}{\overline{\mathrm{D}}t}\left(\frac{\partial}{\partial x_i}\frac{1}{\bar{\rho}}\frac{\partial p'}{\partial x_i}\right)-\frac{1}{\gamma p_\infty}\frac{\overline{\mathrm{D}}^3}{\overline{\mathrm{D}}t^3}p'\\ =\frac{\overline{\mathrm{D}}}{\overline{\mathrm{D}}t}\left(\frac{\partial}{\partial x_i}\frac{1}{\bar{\rho}}\frac{\partial T_{ij}'}{\partial x_j}\right)-\frac{\gamma-1}{\gamma p_\infty}\frac{\overline{\mathrm{D}}^2}{\overline{\mathrm{D}}t^2}\left(\frac{1}{2}\mathrm{D}_0T_{ii}'-\frac{\partial}{\partial x_j}E_j'+T_{ij}'\frac{\partial\tilde{v}_i}{\partial x_j}\right).\end{aligned} \tag{4.31}$$

Equation 4.30 can now be used to eliminate the u_i' term in equation 4.31 to yield

$$\begin{aligned}-2\frac{1}{\bar{\rho}}\frac{\partial^2 p'}{\partial x_i\partial x_1}\frac{\partial U}{\partial x_i}+\frac{\overline{\mathrm{D}}}{\overline{\mathrm{D}}t}\left(\frac{\partial}{\partial x_i}\frac{1}{\bar{\rho}}\frac{\partial p'}{\partial x_i}\right)-\frac{1}{\gamma p_\infty}\frac{\overline{\mathrm{D}}^3}{\overline{\mathrm{D}}t^3}p'\\ =\frac{\overline{\mathrm{D}}}{\overline{\mathrm{D}}t}\left(\frac{\partial}{\partial x_i}\frac{1}{\bar{\rho}}\frac{\partial T_{ij}'}{\partial x_j}\right)-\frac{\gamma-1}{\gamma p_\infty}\frac{\overline{\mathrm{D}}^2}{\overline{\mathrm{D}}t^2}\left(\frac{1}{2}\mathrm{D}_0T_{ii}'-\frac{\partial}{\partial x_j}E_j'+T_{ij}'\frac{\partial\tilde{v}_i}{\partial x_j}\right)-2\frac{1}{\bar{\rho}}\frac{\partial^2 T_{ij}'}{\partial x_j\partial x_1}\frac{\partial U}{\partial x_i}.\end{aligned} \tag{4.32}$$

If one multiplies the above equation by $\bar{\rho}$ and defines the base flow local speed of sound as $\bar{c}\equiv\sqrt{\gamma p_\infty/\bar{\rho}}$ (as shown in Chapter 3), one can show

$$\begin{aligned}\frac{\overline{\mathrm{D}}^3}{\overline{\mathrm{D}}t^3}p'-\frac{\overline{\mathrm{D}}}{\overline{\mathrm{D}}t}\left(\frac{\partial}{\partial x_i}\bar{c}^2\frac{\partial p'}{\partial x_i}\right)+2\bar{c}^2\frac{\partial^2 p'}{\partial x_i\partial x_1}\frac{\partial U}{\partial x_i}=\\ -\frac{\overline{\mathrm{D}}}{\overline{\mathrm{D}}t}\left(\frac{\partial}{\partial x_i}\bar{c}^2\frac{\partial T_{ij}'}{\partial x_j}\right)+(\gamma-1)\frac{\overline{\mathrm{D}}^2}{\overline{\mathrm{D}}t^2}\left(\frac{1}{2}\mathrm{D}_0T_{ii}'-\frac{\partial}{\partial x_j}E_j'+T_{ij}'\frac{\partial\tilde{v}_i}{\partial x_j}\right)+2\bar{c}^2\frac{\partial^2 T_{ij}'}{\partial x_j\partial x_1}\frac{\partial U}{\partial x_i}.\end{aligned} \tag{4.33}$$

The linear operator on the left hand side of equation 4.33 is known as the Pridmore-Brown operator, which was obtained when sound propagation through the shear flow in a duct was examined (Pridmore-Brown, 1958). As we mentioned in Chapter 3, it governs the propagation of small pressure fluctuations in shear flows.

Equation 4.33 is closely related to Lilley's equation (Lilley, 1974), i.e.

$$\frac{\mathrm{D}^3}{\mathrm{D}t^3}\zeta-\frac{\mathrm{D}}{\mathrm{D}t}\left(\frac{\partial}{\partial x_i}c^2\frac{\partial\zeta}{\partial x_i}\right)+2\frac{\partial v_j}{\partial x_i}\frac{\partial}{\partial x_j}c^2\frac{\partial\zeta}{\partial x_i}=-2\frac{\partial v_j}{\partial x_i}\frac{\partial v_k}{\partial x_j}\frac{\partial v_i}{\partial x_k}+\Psi, \tag{4.34}$$

where the new variable ζ is defined as $(1/\gamma)\ln(p/p_\infty)$, c denotes the local speed of sound $\gamma p/\rho$ and the small term Ψ due to entropy (denoted by S) fluctuation and viscosity is given by

$$2\frac{\partial v_j}{\partial x_i}\frac{\partial}{\partial x_j}\frac{1}{\rho}\frac{\partial\sigma_{ik}}{\partial x_k}-\frac{\mathrm{D}}{\mathrm{D}t}\frac{\partial}{\partial x_i}\frac{1}{\rho}\frac{\partial\sigma_{ij}}{\partial x_j}+\frac{1}{c_p}\frac{\mathrm{D}^3S}{\mathrm{D}t^3}. \tag{4.35}$$

As noted by Goldstein (1976), the above equation can also be recovered by taking the material directive of the both sides of Phillip's equation. Like the analogy equation obtained by Lighthill,

Lilley's equation is also exact. However, it must be emphasized that Lilley's equation is for the total flow field variables, whereas equation 4.33 is for small perturbations over a steady base flow. But it can be shown that when Lilley's equation is linearized around a strictly parallel mean flow, the Pridmore-Brown operator in equation 4.33 results (Goldstein, 1976). The source terms, however, are very complicated (Colonius et al., 1997; Goldstein, 2001).

As noted, the left hand side of Equation 4.33 governs how sound propagates through a parallel shear flow. The shear flow profile does not have to be axisymmetric. However, when axisymmetry is imposed, the left hand side of equation 4.33 reduces to that of equation 3.16 shown in Chapter 3 after the method of separation of variable is used. Compared with equation 3.16, equation 4.33 contains inhomogeneous source terms, which have been neglected in equation 3.16 as high-order (hence smaller) terms. In contrast, equation 4.33 keeps these non-linear terms, and interprets them as the sound sources of a turbulent flow. Provided these sources can be obtained, or properly modelled, the sound pressure can be determined by solving this equation. However, it is interesting to note that when the base flow approaches to zero, i.e. when $U \to 0$, the above equation reduces to

$$\frac{\partial^3}{\partial t^3}p' - \frac{\partial}{\partial t}\left(\bar{c}^2\frac{\partial^2 p'}{\partial x_j \partial x_j}\right) = \frac{\gamma-1}{2}\frac{\partial^3}{\partial t^3}T'_{ii} - \frac{\partial}{\partial t}\frac{\partial T'_{ij}}{\partial x_i \partial x_j}. \tag{4.36}$$

Therefore, the above equation does not reduce to Lighthill's acoustic analogy. The extra terms come from the $\delta_{ij}(p' - c_0^2\rho')$ as mentioned by Lilley and Goldstein (Lilley, 1974; Goldstein, 2003) (it is only equal to 0 for the first-order approximation, the extra term accounts for high-order fluctuations).

4.2.2 The direct and adjoint Green's functions

Equation 4.33 is a third-order inhomogeneous linear differential equation (assuming the right hand side is known). To write it in a more compact form, let $\mathcal{L}$ denote the operator on the left hand side, i.e.

$$\mathcal{L} = \frac{\overline{\mathrm{D}}^3}{\overline{\mathrm{D}}t^3} - \frac{\overline{\mathrm{D}}}{\overline{\mathrm{D}}t}\left(\frac{\partial}{\partial x_i}\bar{c}^2\frac{\partial}{\partial x_i}\right) + 2\bar{c}^2\frac{\partial U}{\partial x_i}\frac{\partial^2}{\partial x_i \partial x_1}, \tag{4.37}$$

and $S'(\boldsymbol{x}, t)$ denote the sources terms appearing on the right hand, i.e.

$$-\frac{\overline{\mathrm{D}}}{\overline{\mathrm{D}}t}\left(\frac{\partial}{\partial x_i}\bar{c}^2\frac{\partial T'_{ij}}{\partial x_j}\right) + (\gamma-1)\frac{\overline{\mathrm{D}}^2}{\overline{\mathrm{D}}t^2}\left(\frac{1}{2}\mathrm{D}_0 T'_{ii} - \frac{\partial}{\partial x_j}E'_j + T'_{ij}\frac{\partial \tilde{v}_i}{\partial x_j}\right) + 2\bar{c}^2\frac{\partial^2 T'_{ij}}{\partial x_j \partial x_1}\frac{\partial U}{\partial x_i}. \tag{4.38}$$

Equation 4.33 then becomes

$$\mathcal{L}p'(\boldsymbol{x}, t) = S'(\boldsymbol{x}, t). \tag{4.39}$$

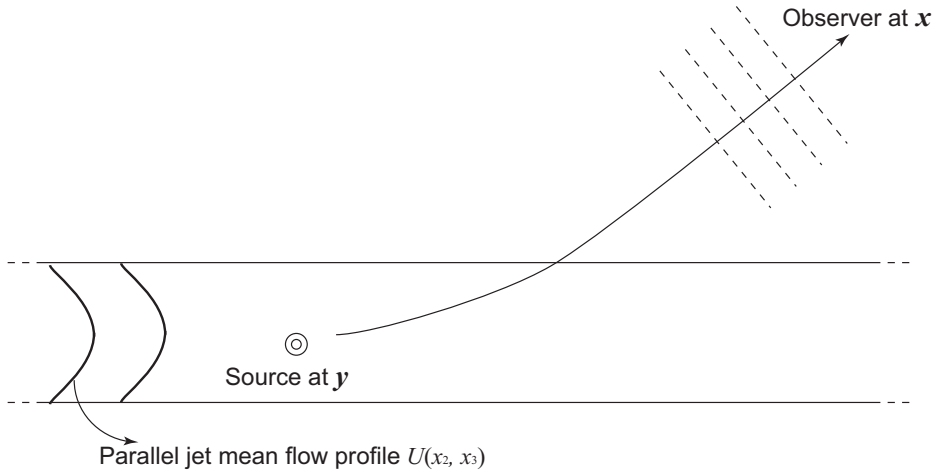

Figure 4.1: The sound emitted by the source at $\boldsymbol{y}$ propagates through a parallel jet mean flow reaching the observer located at $\boldsymbol{x}$ in the far field.

This equation can be solved using a Green's function. The Green's function is defined as the solution to the equation

$$\mathcal{L}G(\boldsymbol{x}, t; \boldsymbol{y}, \tau) = \delta(\boldsymbol{x} - \boldsymbol{y})\delta(t - \tau), \tag{4.40}$$

where $\delta(\boldsymbol{x})$ is the conventional generalized δ function, $\boldsymbol{y}$ the source position and τ the time when the source emits sound. Physically, $G(\boldsymbol{x}, t; \boldsymbol{y}, \tau)$ describes the sound pressure field at the observer point $\boldsymbol{x}$ at time t emitted by a source located at $\boldsymbol{y}$ at time τ. This can be shown clearly by figure 4.1. The radially non-uniform jet mean flow causes sound to bend away from the jet axis. This refraction effect is accounted for by the operator $\mathcal{L}$, and therefore by the Green's function $G(\boldsymbol{x}, t; \boldsymbol{y}, \tau)$. Due to the linearity of equation 4.39, it can be readily shown that

$$p'(\boldsymbol{x}, t) = \int_{-\infty}^{\infty} \int_{V_y} G(\boldsymbol{x}, t; \boldsymbol{y}, \tau) S'(\boldsymbol{y}, \tau) \mathrm{d}\, y^3 \mathrm{d}\, \tau, \tag{4.41}$$

where V_y is the volume that the source $S'(\boldsymbol{y}, \tau)$ occupies. However, for a general jet mean flow profile $U(x_2, x_3)$, it is unlikely to be possible to find an analytical solution for $G(\boldsymbol{x}, t; \boldsymbol{y}, \tau)$. A numerical calculation is therefore necessary. The solution obtained these way is a function of $\boldsymbol{x}$ and t while $\boldsymbol{y}$ and τ are fixed arguments. But equation 4.41 shows that integrals over $\boldsymbol{y}$ and τ are needed. This would imply that the numerical calculation of $G(\boldsymbol{x}, t; \boldsymbol{y}, \tau)$ would have to be performed multiple times. This is not only expensive but also not necessary. A well-known approach to avoid this problem is to use the adjoint Green's function.

Time-dependent adjoint Green's function

To show how equation 4.39 can be solved using the adjoint Green's function, the Cartesian coordinates $\boldsymbol{x}$ and time t are firstly replaced with $\boldsymbol{y}$ and τ, respectively. Equation 4.39 becomes

$$\mathcal{L}p'(\boldsymbol{y},\tau) = S'(\boldsymbol{y},\tau). \tag{4.42}$$

We multiply both side of this equation by a function $G^a(\boldsymbol{y},\tau;\boldsymbol{x},t)$ (to be specified at a later

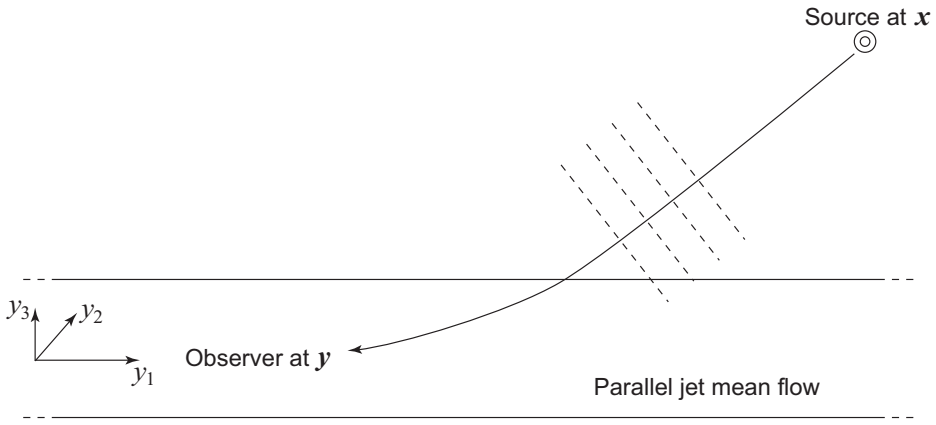

Figure 4.2: The sound emitted by the source at $\boldsymbol{x}$ is scattered by a parallel jet mean flow and the observer is located at $\boldsymbol{y}$.

stage) and integrate over the volume V_y and the entire time interval, then we have

$$\int_{-\infty}^{\infty}\int_{V_y} \mathcal{L}p'(\boldsymbol{y},\tau)G^a(\boldsymbol{y},\tau;\boldsymbol{x},t)\mathrm{d}\,y^3\mathrm{d}\,\tau = \int_{-\infty}^{\infty}\int_{V_y} G^a(\boldsymbol{y},\tau;\boldsymbol{x},t)S'(\boldsymbol{y},\tau)\mathrm{d}\,y^3\mathrm{d}\,\tau. \tag{4.43}$$

Upon integrating by parts (boundary terms vanish if G^a satisfies an appropriate adjoint causality condition), we have

$$\int_{-\infty}^{\infty}\int_{V_y} p'(\boldsymbol{y},\tau)\mathcal{L}^aG^a(\boldsymbol{y},\tau;\boldsymbol{x},t)\mathrm{d}\,y^3\mathrm{d}\,\tau = \int_{-\infty}^{\infty}\int_{V_y} G^a(\boldsymbol{y},\tau;\boldsymbol{x},t)S'(\boldsymbol{y},\tau)\mathrm{d}\,y^3\mathrm{d}\,\tau, \tag{4.44}$$

where $\mathcal{L}^a$ denotes the adjoint linear operator of $\mathcal{L}$. Note that the integral is with respect to $\boldsymbol{y}$ and τ, therefore $\mathcal{L}^a$ is an operator having effects on $\boldsymbol{y}$ and τ. If we choose $G^a(\boldsymbol{y},\tau;\boldsymbol{x},t)$ such that

$$\mathcal{L}^aG^a(\boldsymbol{y},\tau;\boldsymbol{x},t) = \delta(\boldsymbol{y}-\boldsymbol{x})\delta(\tau-t), \tag{4.45}$$

then we would obtain

$$p'(\boldsymbol{x},t) = \int_{-\infty}^{\infty}\int_{V_y} G^a(\boldsymbol{y},\tau;\boldsymbol{x},t)S'(\boldsymbol{y},\tau)\mathrm{d}\,y^3\mathrm{d}\,\tau. \tag{4.46}$$

The function $G^a(\boldsymbol{y},\tau;\boldsymbol{x},t)$ is referred to as the adjoint Green's function. It describes the adjoint field at $\boldsymbol{y}$ due to a far-field point source at $\boldsymbol{x}$, as shown in figure 4.2. This problem is commonly referred to the adjoint problem, as opposed to the direct problem. If this adjoint Green's function can be found, then equation 4.46 shows that equation 4.33 can be readily solved using $G^a(\boldsymbol{y},\tau;\boldsymbol{x},t)$. However, from equation 4.46, we see immediately that the Green's function $G^a(\boldsymbol{y},\tau;\boldsymbol{x},t)$ must satisfy the causal condition for the direct problem, not for the adjoint problem (in particular G^a must vanish when $t<\tau$).

Frequency-dependent adjoint Green's function

The adjoint Green's function considered so far is in the time domain. For convenience of computation it is often desired to obtain the Green's function in the frequency domain. We choose the time variation factor $e^{-\mathrm{i}\omega\tau}$ and then define the Fourier transformation of function $f(\tau)$ as

$$\hat{f}(\omega) = \frac{1}{2\pi}\int_{-\infty}^{\infty} f(\tau)e^{\mathrm{i}\omega\tau}\mathrm{d}\,\tau. \tag{4.47}$$

Taking the Fourier transformation of equation 4.45, one can show

$$\hat{\mathcal{L}}^a\tilde{G}^a(\boldsymbol{y},\omega;\boldsymbol{x},t) = \frac{1}{2\pi}\delta(\boldsymbol{y}-\boldsymbol{x})\mathrm{e}^{\mathrm{i}\omega t}, \tag{4.48}$$

where $\hat{\mathcal{L}}^a$ is the linear operator in the frequency domain (with $\partial/\partial\tau$ replaced by $-\mathrm{i}\omega$). Due to linearity of this equation, we expect $\tilde{G}^a$ to have a factor of $\mathrm{e}^{\mathrm{i}\omega t}$. Therefore, we can cancel this term and obtain

$$\hat{\mathcal{L}}^a\hat{G}^a(\boldsymbol{y};\boldsymbol{x},\omega) = \frac{1}{2\pi}\delta(\boldsymbol{y}-\boldsymbol{x}), \tag{4.49}$$

where

$$\frac{1}{2\pi}\int_{-\infty}^{\infty} G^a(\boldsymbol{y},\tau;\boldsymbol{x},t)\mathrm{e}^{\mathrm{i}\omega(\tau-t)}\mathrm{d}\,\tau = \hat{G}^a(\boldsymbol{y};\boldsymbol{x},\omega). \tag{4.50}$$

Now let us take the Fourier transform of equation 4.46 to obtain

$$\begin{aligned}\hat{p}'(\boldsymbol{x},\omega) &= \frac{1}{2\pi}\int_{V_y}\int_{-\infty}^{\infty} S'(\boldsymbol{y},\tau)\mathrm{e}^{\mathrm{i}\omega\tau}\mathrm{d}\,\tau\int_{-\infty}^{\infty} G^a(\boldsymbol{y},\tau;\boldsymbol{x},t)\mathrm{e}^{-\mathrm{i}\omega(\tau-t)}\mathrm{d}\,y^3\mathrm{d}\,t\\ &= 2\pi\int_{V_y}\hat{G}^a(\boldsymbol{y};\boldsymbol{x},-\omega)\hat{S}'(\boldsymbol{y},\omega)\mathrm{d}\,y^3.\end{aligned} \tag{4.51}$$

If the adjoint Green's function $\hat{G}^a(\boldsymbol{y};\boldsymbol{x},\omega)$ can be found in the frequency domain, equation 4.51 shows that $\hat{p}'(\boldsymbol{x},\omega)$ can be readily calculated by performing a volume integration, provided the source term $\hat{S}'(\boldsymbol{y},\omega)$ is known. We must emphasize again that $\hat{G}^a$ must satisfy the casual condition of the direction problem, not the adjoint problem. This implies that the wavefronts of sound are travelling from the observer at $\boldsymbol{y}$ to the source at $\boldsymbol{x}$ as if time were reversed (for the adjoint problem). This is not physically intuitive. However, this problem can be easily remedied by defining

$$\hat{G}^s(\boldsymbol{y};\boldsymbol{x},\omega) \equiv \hat{G}^a(\boldsymbol{y};\boldsymbol{x},-\omega), \tag{4.52}$$

where $\hat{G}^s$ denotes the Green's function for the causal adjoint problem, i.e. the adjoint problem is now transformed into a normal scattering problem. Equation 4.51 can now be written as

$$\hat{p}'(\boldsymbol{x},\omega) = 2\pi \int_{V_y} \hat{G}^s(\boldsymbol{y};\boldsymbol{x},\omega)\hat{S}'(\boldsymbol{y},\omega)\mathrm{d}\, y^3. \tag{4.53}$$

4.2.3 Calculation of the frequency-dependent adjoint Green's function

Since $\hat{G}^s(\boldsymbol{y};\boldsymbol{x},\omega)$ is defined as $\hat{G}^a(\boldsymbol{y};\boldsymbol{x},-\omega)$, it can be shown from equation 4.49 that the governing equation for $\hat{G}^s$ is

$$\begin{aligned} -(\mathrm{i}\omega + U\frac{\partial}{\partial y_1})^3\hat{G}^s + \frac{\partial}{\partial y_i}\left(\bar{c}^2\frac{\partial}{\partial y_i}(\mathrm{i}\omega + U\frac{\partial \hat{G}^s}{\partial y_1})\right) \\ + 2\frac{\partial^2}{\partial y_i \partial y_1}\left(\bar{c}^2\hat{G}^s\frac{\partial U}{\partial y_i}\right) = \frac{1}{2\pi}\delta(\boldsymbol{y}-\boldsymbol{x}). \end{aligned} \tag{4.54}$$

The Cartesian coordinates y_1, y_2 and y_3 are shown in figure 4.2. Three cylindrical coordinates (z,σ,ϕ) for the observer's position $\boldsymbol{y}$ can be defined such that $z = y_1$, $\sigma = \sqrt{y_2^2 + y_3^2}$ and the source $\boldsymbol{x}$ is in the plane of $\phi = 0$ (azimuthal angle). For the source's position $\boldsymbol{x}$ we again define r to be the radial distance and θ the polar angle (the angle between the source's radial direction and the downstream of the jet centreline) between the source and the Cartesian origin. From figure 4.2, one can see that the parallel base flow is only nonzero for a bounded radial region. In addition, the base flow of an isolated round jet is axisymmetric. Hence, in the following analysis, we restrict our attention to an axisymmetric base flow. One can use $\sigma < \sigma_0$, where σ_0 denotes the radius of the parallel jet plume, to denote the region inside the base flow, where $U = U(\sigma)$ and $\bar{\rho} = \bar{\rho}(\sigma)$. Outside this region, $U = 0$ and $c = c_0$, hence equation 4.54 reduces to

$$(\nabla^2 + k_0^2)\hat{G}^s = \frac{-\mathrm{i}}{2\pi\omega c_0^2}\delta(\boldsymbol{y}-\boldsymbol{x}), \tag{4.55}$$

where $k_0 = \omega/c_0$.

The solution to the above equation using the method of separation of variables is well-known (for example see Tam and Auriault (1998)). Upon invoking the far-field approximation and expanding the incident sound wave, the pressure field outside the jet can be written as

$$\hat{G}^s(\boldsymbol{y};\boldsymbol{x},\omega)|_{\sigma>\sigma_0} = \frac{\exp(-\mathrm{i}k_0(z\cos\theta - r))}{8\pi^2\omega c_0^2 r} \sum_{m=0}^{\infty} \left[(-\mathrm{i})^m \epsilon_m J_m(k_0\sigma\sin\theta) + B_m H_m^{(1)}(k_0\sigma\sin\theta)\right]\cos m\phi, \tag{4.56}$$

where B_m are expansion coefficients to be determined by matching solutions and ϵ_m is defined to be 1 for $m = 0$ and 2 otherwise. Then the pressure field inside the jet plume can be written as

$$\hat{G}^s(\boldsymbol{y};\boldsymbol{x},\omega)|_{\sigma<\sigma_0} = \frac{\exp(-\mathrm{i}k_0(z\cos\theta - r))}{8\pi^2\omega c_0^2 r} \sum_{m=0}^{\infty} f_m(\sigma)\cos m\phi. \tag{4.57}$$

Substituting equation 4.57, one can show that the function f_m satisfies (Tam and Auriault, 1998)

$$\begin{aligned}\frac{\mathrm{d}^2 f_m}{\mathrm{d}\sigma^2} + \left[\frac{-4\cos\theta}{(1-\bar{M}\cos\theta)}\frac{\mathrm{d}\bar{M}}{\mathrm{d}\sigma} - \frac{1}{\bar{\rho}}\frac{\mathrm{d}\bar{\rho}}{\mathrm{d}\sigma} + \frac{1}{\sigma}\right]\frac{\mathrm{d}f_m}{\mathrm{d}\sigma} \\ + \left[\frac{\omega^2(1-\bar{M}\cos\theta)^2}{\bar{c}^2} + \frac{3\cos\theta}{1-\bar{M}\cos\theta}\left(\frac{1}{\bar{\rho}}\frac{\mathrm{d}\bar{\rho}}{\mathrm{d}\sigma}\frac{\mathrm{d}\bar{M}}{\mathrm{d}\sigma} - \frac{1}{\sigma}\frac{\mathrm{d}\bar{M}}{\mathrm{d}\sigma} - \frac{\mathrm{d}^2\bar{M}}{\mathrm{d}\sigma^2}\right)\right. \\ \left. - \frac{m^2}{\sigma^2} - k_0^2\cos^2\theta\right] f_m = 0,\end{aligned} \tag{4.58}$$

where the local base flow Mach number is defined as $\bar{M}(\sigma) = U(\sigma)/c_0$. For a general base flow velocity profile $U(\sigma)$, equation 4.58 needs to be calculated numerically.

4.2.4 Jet noise formulation using the adjoint Green's function

Based on the solution from the preceding sections, one can proceed to derive the equations for calculating the isolate jet noise in the far-field. Using the frequency-dependent adjoint Green's function $\hat{G}^s(\boldsymbol{y};\boldsymbol{x},\omega)$, equation 4.53 shows that

$$\begin{aligned}\hat{p}'(\boldsymbol{x},\omega) = 2\pi\int_{V_y}\hat{G}^s\left\{-(-\mathrm{i}\omega + U\frac{\partial}{\partial y_1})\frac{\partial}{\partial y_i}(\bar{c}^2\frac{\partial\hat{T}'_{ij}}{\partial y_j})\right. \\ + (\gamma-1)(-\mathrm{i}\omega + U\frac{\partial}{\partial y_1})^2\left(\frac{1}{2}\mathrm{D}_0\hat{T}'_{ii} - \frac{\partial}{\partial y_j}\hat{E}'_j + \hat{T}'_{ij}\frac{\partial\tilde{v}_i}{\partial y_j}\right) \\ \left. + 2\bar{c}^2\frac{\partial^2\hat{T}'_{ij}}{\partial y_j\partial y_1}\frac{\partial U}{\partial y_i}\right\}\mathrm{d}\,y^3\mathrm{d}\,\tau,\end{aligned} \tag{4.59}$$

where $\hat{G}^s, \hat{T}'_{ij}$ and $\hat{E}'_i$ represent function $\hat{G}^s(\boldsymbol{y};\boldsymbol{x},\omega), \hat{T}'_{ij}(\boldsymbol{y},\omega)$ and $\hat{E}'_i(\boldsymbol{y},\omega)$, respectively, and $\hat{T}'_{ij}(\boldsymbol{y},\omega)$ and $\hat{E}'_i(\boldsymbol{y},\omega)$ denote the Fourier transforms of $T'_{ij}(\boldsymbol{y},\tau)$ and $E'_i(\boldsymbol{y},\tau)$ respectively. It may be a good approximation by assuming that the speed of sound does not vary significantly within the flow and is close to the value of the ambient speed of sound (for cold jets), i.e. $\bar{c}^2 = c_0^2$. This is a particularly good approximation when the jet (cold jet) exit Mach number is not very high. Therefore $\bar{c}$ in equation 4.59 can be replaced with c_0 and taken out of the differentiation operators. Upon subsequently integrating by parts, one can obtain

$$\begin{aligned}\hat{p'}(\boldsymbol{x},\omega) = 2\pi \int_{V_y} \hat{T}'_{ij} \Bigg\{ & 2c_0^2 \left(\frac{\partial^2 U}{\partial y_i \partial y_j} \frac{\partial \hat{G}^s}{\partial y_1} + \frac{\partial U}{\partial y_i} \frac{\partial^2 \hat{G}^s}{\partial y_j \partial y_1} \right) - \frac{\gamma-1}{2} \delta_{ij} (U \frac{\partial}{\partial y_1} + \mathrm{i}\omega)^3 \hat{G}^s \\ & + (\gamma-1) \frac{\partial U}{\partial y_j} (U \frac{\partial}{\partial y_1} + \mathrm{i}\omega)^2 \hat{G}^s \delta_{1j} \\ & + c_0^2 \left(\mathrm{i}\omega \frac{\partial^2 \hat{G}^s}{\partial y_i \partial y_j} + \frac{\partial}{\partial y_i \partial y_j} U \frac{\partial \hat{G}^s}{\partial y_1} \right) \Bigg\} \\ & + \hat{E}'_j (\gamma-1) \frac{\partial}{\partial y_j} (U \frac{\partial}{\partial y_1} + \mathrm{i}\omega)^2 \hat{G}^s \, \mathrm{d}\, y^3. \end{aligned} \tag{4.60}$$

We have mentioned that for isolated round jets the mean flow is axisymmetric. Besides, equation 4.58 is obtained under the assumption of this axisymmetry. Therefore, it is necessary to rewrite the above equation in the cylindrical coordinate, after which the form of $\hat{G}^s$ shown in equation 4.57 can be used. One can then show that equation 4.60 changes to

$$\begin{aligned}\hat{p'}(\boldsymbol{x},\omega) = 2\pi \int_{V_y} & -3\mathrm{i}k_z c_0^2 \left[\hat{T}'_{\sigma\sigma} \frac{\mathrm{d}^2 U}{\mathrm{d}\sigma^2} + \hat{T}'_{\phi\phi} \frac{1}{\sigma} \frac{\mathrm{d}U}{\mathrm{d}\sigma} \right] \hat{G}^s \\ & - 4\mathrm{i}k_z c_0^2 \left[\hat{T}'_{\sigma\sigma} \frac{\mathrm{d}U}{\mathrm{d}\sigma} \frac{\partial \hat{G}^s}{\partial \sigma} + \hat{T}'_{\sigma\phi} \frac{\mathrm{d}U}{\mathrm{d}\sigma} \frac{1}{\sigma} \frac{\partial \hat{G}^s}{\partial \phi} + \hat{T}'_{\sigma z} \frac{\mathrm{d}U}{\mathrm{d}\sigma} \frac{\partial \hat{G}^s}{\partial z} \right] \\ & + (-\mathrm{i}k_z U + \mathrm{i}\omega) c_0^2 \left[\hat{T}'_{\sigma\sigma} \frac{\partial^2 \hat{G}^s}{\partial \sigma^2} + 2\hat{T}'_{\sigma\phi} \frac{\partial}{\partial \sigma} \frac{1}{\sigma} \frac{\partial \hat{G}^s}{\partial \phi} + \hat{T}'_{\phi\phi} \left(\frac{1}{\sigma} \frac{\partial \hat{G}^s}{\partial \sigma} + \frac{1}{\sigma^2} \frac{\partial^2 \hat{G}^s}{\partial \phi^2} \right) \right. \\ & \qquad \left. + 2\hat{T}'_{\phi z} \frac{1}{\sigma} \frac{\partial^2 \hat{G}^s}{\partial \phi \partial z} + 2\hat{T}'_{\sigma z} \frac{\partial^2 \hat{G}^s}{\partial z \partial \sigma} + \hat{T}'_{zz} \frac{\partial^2 \hat{G}^s}{\partial z^2} \right] \\ & - \frac{\gamma-1}{2} \delta_{ij} (-\mathrm{i}k_z U + \mathrm{i}\omega)^3 \hat{G}^s \left(\hat{T}'_{\sigma\sigma} + \hat{T}'_{\phi\phi} + \hat{T}'_{zz} \right) + (\gamma-1)(-\mathrm{i}k_z U + \mathrm{i}\omega)^2 \hat{G}^s \hat{T}'_{z\sigma} \frac{\mathrm{d}U}{\mathrm{d}\sigma} \\ & + (\gamma-1)(-\mathrm{i}k_z U + \mathrm{i}\omega)^2 \left(\frac{\partial \hat{G}^s}{\partial \sigma} \hat{E}'_\sigma + \frac{1}{\sigma} \frac{\partial \hat{G}^s}{\partial \phi} \hat{E}'_\phi + \frac{\partial \hat{G}^s}{\partial z} \hat{E}'_z \right) \\ & + 2(\gamma-1) k_z \omega \hat{G}^s \hat{E}'_\sigma \frac{\mathrm{d}U}{\mathrm{d}\sigma} - k_z^2 (\gamma-1) \hat{G}^s \hat{E}'_\sigma \frac{\mathrm{d}U^2}{\mathrm{d}\sigma} \mathrm{d}\, y^3, \end{aligned} \tag{4.61}$$

where we have let k_z to denote the acoustic wavenumber in the z direction, i.e. $k_z = k_0 \cos\theta$. Rewrite the integrand in the above equation to yield

$$\begin{aligned}
\hat{p}'(\boldsymbol{x},\omega) = 2\pi \int_{V_y} \mathrm{d}\, y^3\, \hat{T}'_{\sigma\sigma} \Bigg\{ & -3\mathrm{i}k_z c_0^2 \frac{\mathrm{d}^2 U}{\mathrm{d}\sigma^2}\hat{G}^s - 4\mathrm{i}k_z c_0^2 \frac{\mathrm{d}U}{\mathrm{d}\sigma}\frac{\partial \hat{G}^s}{\partial \sigma} \\
& + \mathrm{i}\Omega c_0^2 \frac{\partial^2 \hat{G}^s}{\partial \sigma^2} - \frac{\gamma-1}{2}(\mathrm{i}\Omega)^3 \hat{G}^s \Bigg\} \\
& + \hat{T}'_{\sigma\phi} \left\{ -4\mathrm{i}k_z c_0^2 \frac{\mathrm{d}U}{\mathrm{d}\sigma}\frac{1}{\sigma}\frac{\partial \hat{G}^s}{\partial \phi} + 2\mathrm{i}\Omega c_0^2 \frac{\partial}{\partial \sigma}\frac{1}{\sigma}\frac{\partial \hat{G}^s}{\partial \phi} \right\} \\
& + \hat{T}'_{\sigma z} \left\{ -4k_z^2 c_0^2 \frac{\mathrm{d}U}{\mathrm{d}\sigma}\hat{G}^s + 2\Omega k_z c_0^2 \frac{\partial \hat{G}^s}{\partial \sigma} + (\gamma-1)\Omega^2 \frac{\mathrm{d}U}{\mathrm{d}\sigma}\hat{G}^s \right\} \\
& + \hat{T}'_{\phi\phi} \left\{ -3\mathrm{i}k_z c_0^2 \frac{1}{\sigma}\frac{\mathrm{d}U}{\mathrm{d}\sigma}\hat{G}^s + \mathrm{i}\Omega c_0^2 \left(\frac{1}{\sigma}\frac{\partial \hat{G}^s}{\partial \sigma} + \frac{1}{\sigma^2}\frac{\partial^2 \hat{G}^s}{\partial \phi^2} \right) - \frac{\gamma-1}{2}(\mathrm{i}\Omega)^3 \hat{G}^s \right\} \\
& + \hat{T}'_{\phi z} \left\{ 2\Omega k_z c_0^2 \frac{1}{\sigma}\frac{\partial \hat{G}^s}{\partial \phi} \right\} \\
& + \hat{T}'_{zz} \left\{ -\mathrm{i}\Omega k_z^2 c_0^2 \hat{G}^s - \frac{\gamma-1}{2}(\mathrm{i}\Omega)^3 \hat{G}^s \right\} \\
& + \hat{E}'_{\sigma} \left\{ -(\gamma-1)\Omega^2 \frac{\partial \hat{G}^s}{\partial \sigma} + 2(\gamma-1)k_z \omega \frac{\mathrm{d}U}{\mathrm{d}\sigma}\hat{G}^s - k_z^2(\gamma-1)\frac{\mathrm{d}U^2}{\mathrm{d}\sigma}\hat{G}^s \right\} \\
& + \hat{E}'_{\phi} \left\{ -(\gamma-1)\Omega^2 \frac{1}{\sigma}\frac{\partial \hat{G}^s}{\partial \phi} \right\} \\
& + \hat{E}'_{z} \left\{ \mathrm{i}(\gamma-1)\Omega^2 k_z \hat{G}^s \right\},
\end{aligned} \tag{4.62}$$

where, as shown in Chapter 3, $\Omega = \omega - k_z U$. For cold jets, it is often allowable to ignore the total entropy fluctuations, i.e. all the $\hat{E}'_i$ terms vanish. When the propagation tensor elements inside the curly braces associated with $\hat{T}'_{ij}(\boldsymbol{y},\omega)$ are denoted by $g_{ij}(\boldsymbol{y};\boldsymbol{x},\omega)$, where i and j can be σ, ϕ or z, equation 4.62, after dropping the $\hat{E}'_i$ terms, can be written in a more compact form, i.e.

$$\hat{p}'(\boldsymbol{x},\omega) = 2\pi \int_{V_y} \hat{T}'_{ij}(\boldsymbol{y},\omega) g_{ij}(\boldsymbol{y};\boldsymbol{x},\omega) \mathrm{d}\, y^3. \tag{4.63}$$

The Power Spectral Density (PSD) the of far-field sound, $\Phi(\boldsymbol{x},\omega)$, can be obtained as

$$\Phi(\boldsymbol{x},\omega) = \lim_{T\to\infty} \frac{\pi}{T} \langle \hat{p}'(\boldsymbol{x},\omega)\hat{p}'^{*}(\boldsymbol{x},\omega) \rangle, \tag{4.64}$$

where $2T$ is the time interval used to perform the Fourier transformation to obtain $\hat{p}'(\boldsymbol{x},\omega)$ from $p'(\boldsymbol{x},t)$ (a finite interval is used because jet noise is a statistical signal). From equation 4.63,

one can show

$$\Phi(\boldsymbol{x},\omega) = 4\pi^2 \int_{V_y}\int_{V_{\Delta y}} R_{ijkl}(\boldsymbol{y},\boldsymbol{\Delta y},\omega) I_{ijkl}(\boldsymbol{y},\boldsymbol{\Delta y};\boldsymbol{x},\omega)\mathrm{d}\,\Delta y^3 \mathrm{d}\,y^3, \tag{4.65}$$

where

$$R_{ijkl}(\boldsymbol{y},\boldsymbol{\Delta y},\omega) = \lim_{T\to\infty}\frac{\pi}{T}\langle \hat{T}'_{ij}(\boldsymbol{y},\omega)\hat{T}'^{*}_{kl}(\boldsymbol{y}+\boldsymbol{\Delta y},\omega)\rangle, \tag{4.66}$$

$$I_{ijkl}(\boldsymbol{y},\boldsymbol{\Delta y};\boldsymbol{x},\omega) = g_{ij}(\boldsymbol{y};\boldsymbol{x},\omega) g^{*}_{kl}(\boldsymbol{y}+\boldsymbol{\Delta y};\boldsymbol{x},\omega). \tag{4.67}$$

It can be readily shown that $R_{ijkl}(\boldsymbol{y},\boldsymbol{\Delta y},\omega)$ is the Fourier Transform of the fourth-order space-time correlation function

$$R_{ijkl}(\boldsymbol{y},\boldsymbol{\Delta y},\tau) = \langle T'_{ij}(\boldsymbol{y},t) T'_{kl}(\boldsymbol{y}+\boldsymbol{\Delta y},t+\tau)\rangle. \tag{4.68}$$

It has been known that the space-time correlation function $R_{ijkl}(\boldsymbol{y},\Delta\boldsymbol{y},\tau)$ can be well represented by a Gaussian function as (Karabasov et al., 2010)

$$R_{ijkl}(\boldsymbol{y},\Delta\boldsymbol{y},\tau) = A_{ijkl}(\boldsymbol{y})\exp\left[-\frac{|\Delta y_1|}{\bar{v}_1(\boldsymbol{y})\tau_s(\boldsymbol{y})} - \ln 2\left(\left(\frac{\Delta y_1 - \bar{v}_1(\boldsymbol{y})\tau}{l_1(\boldsymbol{y})}\right)^2 + \left(\frac{\Delta y_2}{l_2(\boldsymbol{y})}\right)^2 + \left(\frac{\Delta y_3}{l_3(\boldsymbol{y})}\right)^2\right)\right], \tag{4.69}$$

where $A_{ijkl}(\boldsymbol{y}) = C_{ijkl}(2\bar{\rho}k)^2$, $l_i = c_i k^{3/2}/\varepsilon$ and $\tau_s = c_\tau k/\varepsilon$. Here $\bar{v}_1(\boldsymbol{y})$ denotes the time average of the streamwise jet velocity at the position $\boldsymbol{y}$, k turbulence intensity and ε turbulence dissipation rate. The constants C_{ijkl}, c_i and c_τ can be obtained by best fitting equation 4.69 to the space-time correlation data obtained from LES simulations. The cross-spectra is thus obtained by performing the standard Fourier transformation, which yields

$$R_{ijkl}(\boldsymbol{y},\Delta\boldsymbol{y},\omega) = \frac{l_1(\boldsymbol{y})}{2\bar{v}_1(\boldsymbol{y})\sqrt{\pi\ln 2}} A_{ijkl}(\boldsymbol{y})\exp\left[-\frac{l_1(\boldsymbol{y})^2\omega^2}{4\bar{v}_1^2\ln 2}\right] \exp\left[-\frac{|\Delta y_1|}{\bar{v}_1(\boldsymbol{y})\tau_s(\boldsymbol{y})} - \mathrm{i}\frac{\omega}{\bar{v}_1}\Delta y_1 - \ln 2\left(\left(\frac{\Delta y_2}{l_2(\boldsymbol{y})}\right)^2 + \left(\frac{\Delta y_3}{l_3(\boldsymbol{y})}\right)^2\right)\right]. \tag{4.70}$$

The tensor $I_{ijkl}(\boldsymbol{y},\Delta\boldsymbol{y};\boldsymbol{x},\omega)$ in equation 5.14 depends solely on the Green's function (and the jet mean flow). Previous studies (Karabasov et al., 2010; Mohan et al., 2015) show that the tensor R_{ijkl} only has a few non-negligible elements such as R_{zzzz}, $R_{\phi\phi\phi\phi}$, $R_{\sigma\sigma\sigma\sigma}$, $R_{z\sigma z\sigma}$, $R_{z\phi z\phi}$ etc. Therefore, one is only interested in the I_{ijkl} elements corresponding to these non-negligible sources. It has been shown that the turbulence length scales, l_i, are generally very small and $I_{ijkl}(\boldsymbol{y},\boldsymbol{\Delta y};\boldsymbol{x},\omega)$ do not vary significantly over these small scales. Therefore, it is

often satisfactory to assume $I_{ijkl}(\boldsymbol{y}, \boldsymbol{\Delta y}; \boldsymbol{x}, \omega) \approx I_{ijkl}(\boldsymbol{y}, \boldsymbol{0}; \boldsymbol{x}, \omega)$ and I_{ijkl} can thus be taken out of the inner volume integral. Under this compact source approximation, it can be shown that

$$I_{\sigma\sigma\sigma\sigma} = \left| -3k_z c_0^2 \frac{\mathrm{d}^2 U}{\mathrm{d}\sigma^2} \hat{G}^s - 4k_z c_0^2 \frac{\mathrm{d}U}{\mathrm{d}\sigma} \frac{\partial \hat{G}^s}{\partial \sigma} + \Omega c_0^2 \frac{\partial^2 \hat{G}^s}{\partial \sigma^2} + \frac{\gamma - 1}{2} \Omega^3 \hat{G}^s \right|^2, \tag{4.71a}$$

$$I_{\sigma\phi\sigma\phi} = \left| -4k_z c_0^2 \frac{\mathrm{d}U}{\mathrm{d}\sigma} \frac{1}{\sigma} \frac{\partial \hat{G}^s}{\partial \phi} + 2\Omega c_0^2 \frac{\partial}{\partial \sigma} \frac{1}{\sigma} \frac{\partial \hat{G}^s}{\partial \phi} \right|^2, \tag{4.71b}$$

$$I_{\sigma z\sigma z} = \left| -4k_z^2 c_0^2 \frac{\mathrm{d}U}{\mathrm{d}\sigma} \hat{G}^s + 2\Omega k_z c_0^2 \frac{\partial \hat{G}^s}{\partial \sigma} + (\gamma - 1)\Omega^2 \frac{\mathrm{d}U}{\mathrm{d}\sigma} \hat{G}^s \right|^2, \tag{4.71c}$$

$$I_{\phi\phi\phi\phi} = \left| -3k_z c_0^2 \frac{1}{\sigma} \frac{\mathrm{d}U}{\mathrm{d}\sigma} \hat{G}^s + \Omega c_0^2 \left(\frac{1}{\sigma} \frac{\partial \hat{G}^s}{\partial \sigma} + \frac{1}{\sigma^2} \frac{\partial^2 \hat{G}^s}{\partial \phi^2} \right) + \frac{\gamma - 1}{2} \Omega^3 \hat{G}^s \right|^2, \tag{4.71d}$$

$$I_{\phi z\phi z} = \left| 2\Omega k_z c_0^2 \frac{1}{\sigma} \frac{\partial \hat{G}^s}{\partial \phi} \right|^2, \tag{4.71e}$$

$$I_{zzzz} = \left| -\Omega k_z^2 c_0^2 \hat{G}^s + \frac{\gamma - 1}{2} \Omega^3 \hat{G}^s \right|^2. \tag{4.71f}$$

With both $R_{ijkl}(\boldsymbol{y}, \boldsymbol{\Delta y}, \omega)$ and $I_{ijkl}(\boldsymbol{y}, \boldsymbol{\Delta y}; \boldsymbol{x}, \omega)$ known, equation 4.65 can be evaluated numerically to yield the far-field PSDs. The numerical implementation can be highly efficient and robust, as will be shown in the following section.

4.2.5 CONJURE - A numerical implementation using Fortran

Based on the results derived in the preceding section, a numerical code is developed to calculate the far-field isolated jet noise. The numerical code, CONJURE - Calculating Observer-dependent Noise of Jets Utilizing RANS's Efficiency, is implemented in the Fortran programming language. The numerical code is very fast, capable of calculating the far-field sound PSDs at various observer angles of interest within seconds (with available RANS data). This section briefly introduces this code as follows.

Firstly, the code attempts to solve the causal adjoint Green's function $\hat{G}^s$ from equation 4.58, which depends on the jet base flow. Consequently, before proceeding we need to determine the velocity profile $U(\sigma)$. To have the best results without resorting to the WKB method, we use the locally-parallel flow assumption described in Chapter 3. That is to say, for each streamwise station z, we use the local mean flow profile $U(\sigma)$ at that station and then solve equation 4.58 as if the flow were strictly parallel throughout the entire region with a uniform profile of $U(\sigma)$. This locally-parallel flow has been shown to be a good approximation (Tam

and Auriault, 1998; Karabasov et al., 2010) for jet noise prediction in most cases of interest. To obtain $\hat{G}^s$ subsequently, equation 4.58 needs be solved robustly. However, equation 4.58 involves the second-order derivatives of the mean flow velocity profile. The mean flow is normally calculated using RANS simulations and therefore is only known on discrete mesh points. Moreover, near the nozzle lip the mean velocity changes abruptly, therefore the derivatives of the mean flow obtain large values and should be at best avoided for the sake of robust numerical computations.

This can be achieved by a change of variables before using Runge-Kutta methods. Firstly, we let

$$\bar{f}_m(\sigma) = \Omega^3 f_m(\sigma), \tag{4.72}$$

then Runge-Kutta method can be used to solve the equation for $\bar{f}_m$, i.e.

$$\frac{\mathrm{d}}{\mathrm{d}\sigma}\left(\frac{c_0^2}{\Omega^2}\frac{\mathrm{d}\bar{f}_m}{\mathrm{d}\sigma}\right) = \left[\frac{\omega^2\cos^2\theta}{\Omega^2} + \frac{m^2}{\sigma^2}\frac{c_0^2}{\Omega^2} - 1\right]\bar{f}_m - \frac{c_0^2}{\Omega^2}\frac{1}{\sigma}\frac{\mathrm{d}\bar{f}_m}{\mathrm{d}\sigma}. \tag{4.73}$$

As the first step of solving any second-order Ordinary Differential Equation (ODE), one needs to rewrite the ODE into a set of first-order ODEs. There can be infinitely possible ways to do so. However, some methods are more convenient than others, because the resulting low-order equation pair does not involve high-order derivatives of the mean flow. One of such equation pair is

$$\frac{\mathrm{d}\bar{f}_m}{\mathrm{d}\sigma} = k_0^2\left(1 - \bar{M}\cos\theta\right)^2\bar{g}_m, \tag{4.74a}$$

$$\frac{\mathrm{d}\bar{g}_m}{\mathrm{d}\sigma} = \left[\frac{\cos^2\theta}{(1-\bar{M}\cos\theta)^2} + \frac{m^2}{\sigma^2}\frac{1}{k_0^2(1-\bar{M}\cos\theta)^2} - 1\right]\bar{f}_m - \frac{\bar{g}_m}{\sigma}. \tag{4.74b}$$

A similar pair of equation has been obtained in the work of Afsar (2009), by considering multiple adjoint equations. These two ODEs are particularly suitable for numerically calculating the adjoint Green's function, since they do not explicitly involve derivatives of the mean flow. In this thesis, equation 4.74 is solved numerically using the 4th-order Runge-Kutta method to obtain the adjoint Green's function $\hat{G}^s$ by substiting $\bar{f}_m$ into equation 4.72 and then equation 4.57.

Secondly, the code attempts to evaluate the integral shown in equation 4.65. Under the compact source assumption mentioned in the preceding section, we have shown

$$\Phi(\boldsymbol{x},\omega) \approx 4\pi^2\int_{V_y} I_{ijkl}(\boldsymbol{y},\boldsymbol{0};\boldsymbol{x},\omega)\int_{V_{\Delta y}} R_{ijkl}(\boldsymbol{y},\boldsymbol{\Delta y},\omega)\mathrm{d}\,\Delta y^3\mathrm{d}\,y^3. \tag{4.75}$$

Equation 4.70 provides an explicit formula for $R_{ijkl}(\boldsymbol{y},\boldsymbol{\Delta y},\omega)$, therefore the inner integral over $V_{\Delta y}$ can be evaluated analytically. In addition, equation 4.71 shows a direct way of calculating $I_{ijkl}(\boldsymbol{y},\boldsymbol{0};\boldsymbol{x},\omega)$ from the adjoint Green's function $\hat{G}^s$. Notice that $\hat{G}^s$ is of the form

shown in equation 4.57, therefore we can make use of the orthogonality of the function set $\{\cos m\phi\}$ to carry out the integration over ϕ analytically for the outer volume integral. Equation 4.65 then simplifies to a two-dimensional integral, which can be efficiently calculated using numerical integration algorithms.

4.3 Validation against experiments

Numerical results from CONJURE can now be compared with experimental results. We choose the experiments carried out by Head and Fisher (1976) because there were also experimental data on installed jet noise to be used at a later stage. Since the source term $R_{ijkl}(\boldsymbol{y}, \boldsymbol{\Delta y}, \omega)$ is a model depending on the turbulent statistics, a CFD flow field calculation is firstly performed.

4.3.1 CFD flow field calculation

Turbulence is an inherently unsteady phenomenon, therefore unsteady numerical simulations such as LES are well suited for obtaining its statistics. However, to perform an LES study is computationally expensive. The usual time required even on a massively parallel computer can vary from a few days to many weeks depending on practical needs. To avoid this difficulty attempts to use time-averaged flow calculations to predict isolated jet noise have been made by many authors. For example both Khavaran et al. (1994) and Bailly et al. (1994, 1996) used time-averaged calculations with turbulence statistics obtained from $k-\varepsilon$ turbulence model for predicting supersonic jet noise. In the work of Bechara et al. (1995) a RANS calculation incorporating $k-\varepsilon$ model for turbulence to characterise the sound sources was used to predict the noise of both simple and coaxial jets. Later Tam and Auriault (1999) further explored this approach and successfully predicted jet noise at 90° to the jet by proposing an empirical sound source model analogous to gas kinetic theory. However, the three empirical constants in Tam's work were obtained by fitting to the far-field noise. On the contrary, the work by Karabasov et al. (2010) is based on Goldstein's acoustic analogy theory (Goldstein, 2003) and the proportionality constants used in its source model are obtained from analysing LES data, which therefore contains little empiricism apart from that of the $k-\varepsilon$ model for turbulence. The predicted noise at various observer angles to the jet are found to agree well with experiments. In this thesis we adopt the same approach in order to yield fast predictions. Having validated the approach in one case through comparison with the source statistics from an LES, in this section we perform a RANS study with the standard $k-\varepsilon$ turbulence model, and the source terms are subsequently modelled by making use of the time-averaged flow variables from the

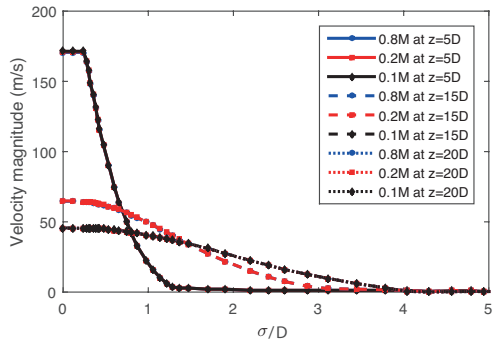

Figure 4.3: Velocity distributions in the radial direction using different meshes consisting of 0.8 million, 0.2 million and 0.1 million cells respectively.

RANS.

Computational domain

The commercial software ANSYS Fluent 16.0 is used to perform a RANS calculation of an isolated round jet with the same temperature as the ambient air. The computational domain is $30D$ and $5D$ in the streamwise and radial directions respectively. Calculations using much larger computational domains have shown little difference from those using the domain described above. The current domain size is therefore used to yield both a fast convergence and sufficiently accurate results.

Mesh

The mesh used in the calculation is generated using ANSYS Meshing 16.0. A structured quadrilateral mesh is used for the entire domain, and the mesh is much denser near the mixing layer and close to the jet. Near the mixing layer, the grid size is around $0.025D$ in the axial direction and $0.02D$ in the radial direction. The grid size inside the nozzle ($\sigma < 0.5D$) in the radial direction is nearly uniformly $0.025D$. Near the downstream boundary the grid size is around $0.2D$. The mesh consists of around 0.1 million cells. To check the mesh independence, the calculations using meshes consisting of 0.2 million and 0.8 million cells were carried out and the results yielded little difference, as shown in figure 4.3. It is shown that this number of cells (0.1 million) is sufficient to generate rapidly converging and sufficiently accurate results. A wall-function approach is used to resolve the boundary layer inside the nozzle. The chosen "standard wall function" in ANSYS Fluent is based on the work of Launder and Spalding (ANSYS, 2015; Launder and Spalding, 1974). The boundary layer mesh starts at around $y^+ = 50$,

where y^+ is the dimensionless distance of the first mesh layer to the wall based on the wall friction velocity (White, 2005). The wall friction velocity u^* is estimated using the log-law of the boundary layer (White, 2005). The boundary layer is resolved by around 15 layers, which should be sufficient according to the Fluent Theory Guide (ANSYS, 2015). Calculations using more layers show little difference for either the mean or turbulent flow quantities.

Boundary conditions

The boundary conditions for boundaries both upstream and downstream are "pressure outlets" provided in ANSYS Fluent (ANSYS, 2015). At the nozzle inlet boundary "pressure inlet" is used (ANSYS, 2015), which specifies both the stagnation pressure and the stagnation temperature. The stagnation pressure and stagnation temperature are given on the inlet boundary such that a Mach number $M_0 = 0.5$ jet is obtained, where $M_0 = U_j/c_0$. The static temperature at the inlet boundary is the same as that of the ambient air, which is set to be 300 K. The turbulence intensity at the "pressure inlet" is set to be 5%, and studies using other values have shown little change to the calculated flow field, especially after the potential core.

Turbulence models

The standard $k - \varepsilon$ model for the turbulence is used, as it gives a more realistic core length (see figure 4.4 for example) compared to other turbulent models such as realizable $k - \varepsilon$ model provided in ANSYS Fluent (ANSYS, 2015). In fact although the potential core length varies, the difference that changing turbulent models causes on the turbulent flow quantities is not significant, especially for the locations ($z > 4D$) where the sound generation is most efficient. Moreover, since the far-field sound depends on an integration over the whole turbulent flow field, little difference can be expected. As shown by Mohan et al. (2015), the use of many different turbulent models, such as $k - \varepsilon$, $k - \omega$ etc, makes little difference to the far-field sound spectrum over the entire frequency range. Therefore, we think that the use of $k - \varepsilon$ model is sufficient for the current purpose. The compressible Reynolds-Averaged Navier-Stokes equations are solved, and the ideal-gas law for air is adopted while the ambient pressure is set to be 1 atm.

RANS validations

To validate the RANS simulation, the streamwise components of the mean and fluctuation velocities (root-mean-square value), both along the lip line and centre line of jet, are compared with the experimental data published by Bridges (Bridges and Wernet, 2010), as shown in fig-

ure 4.4. From figure 4.4(a), it can be seen that the mean velocity profiles, in particular that on

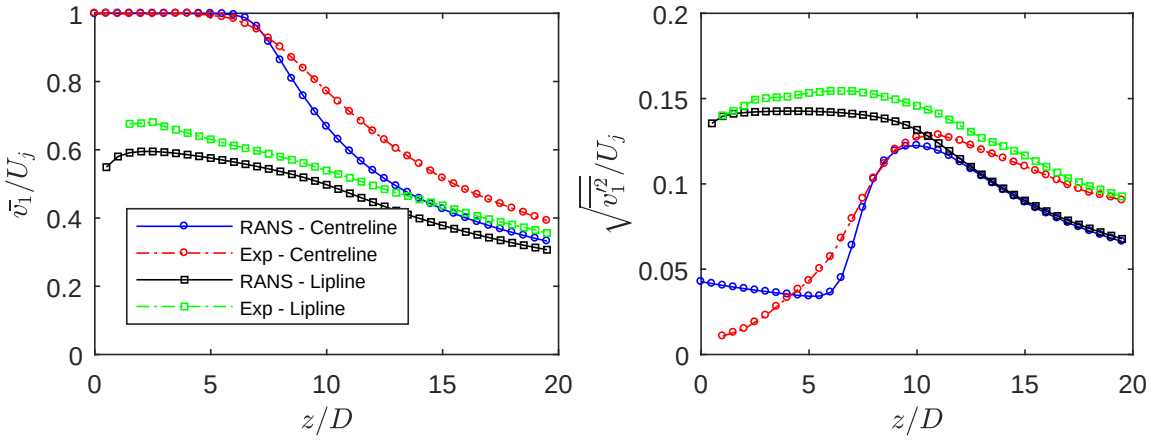

(a) Jet mean axial velocity

(b) Root-mean-square axial fluctuation velocity

Figure 4.4: Comparison of the jet mean and root-mean-square axial fluctuation velocities along the centre and lip lines between the RANS and experimental data. Isotropic turbulence is assumed for the RANS to obtain the root-mean-square axial fluctuation velocity from turbulence intensity k.

the lip line, agree well with experiment. On the centre line, the core length matches well with experimental data thought it appears that the velocity is slightly under predicted further downstream. Given that the Reynolds number for Bridge's experiment is twice that for the RANS simulation (as D are 1 inch and 2 inches for the RANS and Bridge's experiment, respectively) and the temperature ratio in the experiment is slightly different from that in the simulation, such agreement is good and the effect of any difference on the sound propagation can be expected to be negligible. Figure 4.4(b) shows the turbulent fluctuation velocity profiles on the jet lip line and centre lines. The root-mean-square value of v_1', where v_1' is the axial fluctuation velocity, is available in the experiment, but not from the RANS simulation. To facilitate comparison, we estimate this value from the turbulence intensity k by assuming that the turbulence is isotropic. This assumption however is known to be not correct (Karabasov et al., 2010; Mohan et al., 2015), therefore we expect a slight under-prediction of the axial turbulent fluctuation velocities, which can be seen from figure 4.4(b). Apart from these uncertainties, it can be seen that an overall good agreement is achieved for data on the lip line. The results on the centre line also agrees well after about $z/D = 6$. The over-prediction in the first few diameters is expected. This is because the inlet turbulence intensity is given a high-than-normal value of 5% so that the centre-line turbulence profiles near the downstream edge of the potential core can better agree with the experiment. However, as mentioned earlier, changing the inlet turbulence

intensity has no effect on the flow field after the potential core.

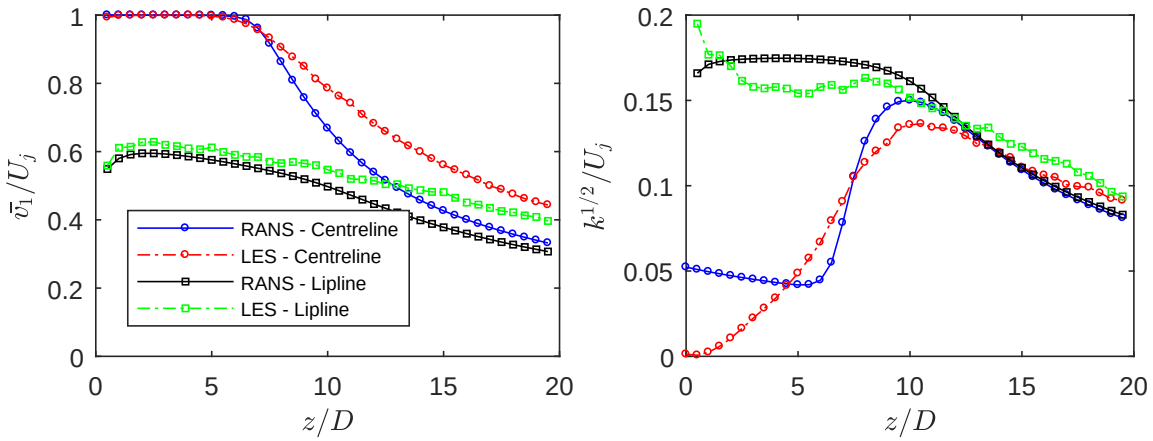

(a) Jet mean axial velocity

(b) Turbulence intensity

Figure 4.5: Comparison of the jet mean and turbulence intensity along the centre and lip lines between the RANS and LES results.

As will be mentioned in the rest of this thesis, an LES study is also performed with the same operating conditions as those in Bridges' experiment. It is therefore useful to compare the results of our RANS simulation to those obtained in the LES. Because we are now able to calculate the turbulence intensity directly from LES, we do not need to compare the root-mean-square of the axial fluctuation velocity by assuming isotropic turbulence for the RANS results. The results are shown in figure 4.5. It can be seen that a similar good agreement to that shown in figure 4.4(a) for the mean axial velocities is achieved. However, comparing figure 4.5(b) to figure 4.4(b), one sees a much better agreement for the turbulence intensity distribution, especially for the axial positions after the potential core. This shows that the cause for the under-prediction shown in figure 4.4(b) is indeed due to the assumption of isotropic turbulence (Karabasov et al., 2010; Mohan et al., 2015) and the RANS simulation is capable of predicting the jet flow accurately.

4.3.2 Far-field sound validation

With the turbulence statistics and mean flow data obtained from the RANS calculation, the sound source terms $R_{ijkl}(\boldsymbol{y}, \boldsymbol{\Delta y}, \omega)$ can be easily calculated. The proportionality constants used in approximating $R_{ijkl}(\boldsymbol{y}, \boldsymbol{\Delta}, \omega)$ are given in table 4.1 and compared with others' results. In this study, both c_i and c_τ are obtained by best fitting the correlation functions against those obtained from an LES database. The principle amplitude ($\sqrt{C_{1111}}$) uses the same value as

	M_0	$\sqrt{C_{1111}}$	c_1	c_2	c_3	c_τ
Models informed by LES:						
This study	0.5	0.25	0.4	0.23	0.23	0.3
Mohan et al. (2015)	0.9	0.25	0.26	0.08	0.08	0.14
Karabasov et al. (2010)	0.75	0.25	0.37	c_1	c_1	0.36
Models fitted from far-field sound:						
Morris and Farassat (2002)	0.91	0.26	0.78	c_1	c_1	1
Tam and Auriault (1999)	0.9	0.257	0.13	c_1	c_1	0.308

Table 4.1: The proportionality constants used in this and other studies.

those obtained in previous work, which can be seen to be nearly identical in different studies. It is worth noting that both Karabasov et al. (2010) and Mohan et al. (2015) obtained their proportionality constants by validating against an LES database (hence they contain less empiricism), while others obtained theirs by best fitting far-field sound. However, Karabasov et al. (2010) (and Morris and Farassat (2002) and Tam and Auriault (1999)) assumed that the length scales c_2 and c_3 were both equal to c_1. This isotropic assumption has been known to be incorrect (Mohan et al., 2015). Instead, they should also be informed by the LES database, which was demonstrated by Mohan et al. (2015) and this study. From table 4.1, it can be observed that the jet exit Mach numbers examined are different in the three studies informed by LES databases, which might be the reason why there is a strong variation for both c_i and c_τ.

Using equation 4.75, the far-field sound PSDs can now be readily evaluated. We are finally in a position to compare the predicted results from CONJURE with experimental measurements. Results are shown for three different observer positions, i.e. θ takes the values of 90, 45 and 30 degrees, respectively. The comparisons are shown in figures 4.6 to 4.8. As mentioned, the code is very fast. For example, for each observer angle, with the same frequency resolution shown in figures 4.6 to 4.8, it takes about 10 seconds to obtain the PSD on a normal PC. This is remarkably efficient compare to some existing codes, which can take up to hours or even days to perform the same task.

Figure 4.6 shows the comparison of far-field sound power spectra when the observer angle θ is 90 degrees. It can be seen that a very good agreement is achieved across the entire frequency range as shown. Not only the absolute magnitudes, but also the overall shapes of the noise spectra agree with each other very well. It has been known that jet noise is very sensitive to the flow conditions at the nozzle exit such as the turbulence intensity and the momentum thickness of the boundary layer near the inlet. Therefore, it is very challenging to reproduce the

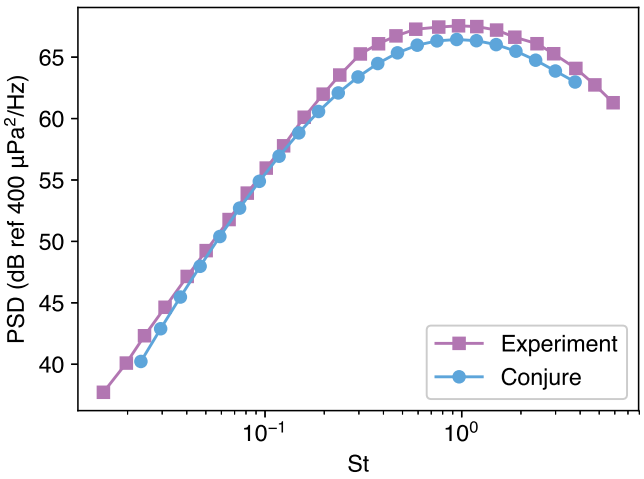

Figure 4.6: Comparison of noise spectra in 1/3 octaves between the predictions from CONJURE and experimental results for an observer at $\theta = 90°$.

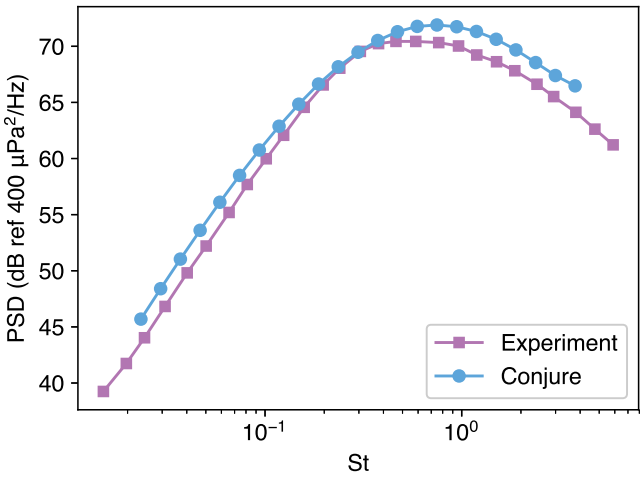

Figure 4.7: Comparison of noise spectra in 1/3 octaves between the predictions from CONJURE and experimental results for an observer at $\theta = 45°$.

exact configurations of the experiment to be used in CFD calculations. Yet the model yields a nearly perfect agreement with experiment at 90 degrees. In this sense, the code CONJURE performs remarkably well, in particular, if one considers its super efficiency. The results for an observer at 45 degrees are shown in figure 4.7. The agreement is very similar to that shown in figure 4.6. Although there are slight deviations both in the low and the high frequency regimes, the differences are nearly uniformly less than 2 dB. It is interesting to note that this less good agreement comparing to the results at 90° is somehow expected. This is because sound generated by quadrupole sources inside the shear flow has to propagate through the shear layer by a longer axial distance in order to reach the far-field observer at lower observer angles. This would inevitably cause problems for the locally-parallel flow assumption. Moreover, the smaller the observer angle is, the more pronounced this deviation would be. However, one can see from figure 4.8 that, even at 30 degrees, the maximum over-prediction at the highest frequency is still less than around 3dB. This shows that the locally-parallel flow assumption serves as a reasonably good approximation for the sake of jet noise prediction at all observer angles of interest. The significant simplification of the propagation effects, however, clearly outweighs the slight compromises of prediction accuracy.

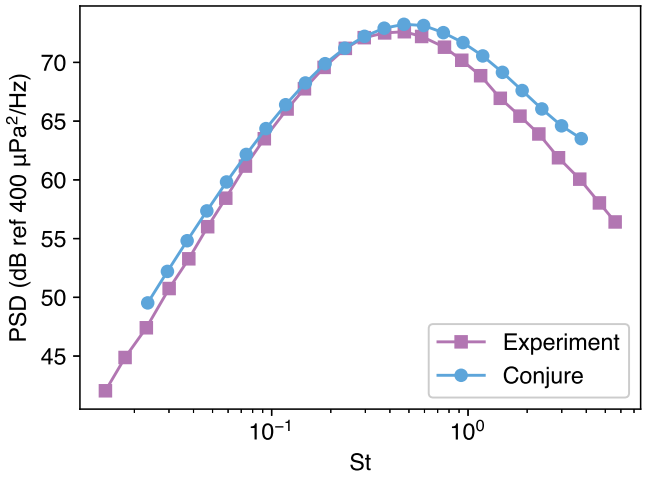

Figure 4.8: Comparison of noise spectra in 1/3 octaves between the predictions from CONJURE and experimental results for an observer at $\theta = 30°$.

4.3.3 Discussion

Section 4.3.2 shows that the model predictions agree very well with the experimental data. However, one should note that the acoustic prediction depends on the proportionality con-

stants informed by the LES. One may therefore wonder how these constants depend on the jet Mach number and nozzle geometry. This is important, because it determines whether these constants can still used in other cases where an LES database is not readily available.

As mentioned in the preceding section, table 4.1 contains the proportionality constants informed by the LES database and fitted from the far-field sound. The former approach is more appropriate and contains much less empiricism. We therefore focus on discussing the constants obtained in this manner. From table 4.1, we see that these constants are quiet different between Mach numbers 0.9 (Mohan et al., 2015) and 0.5 (this study). However, it can also be seen that c_1, c_τ and $\sqrt{C_{1111}}$ (including other $\sqrt{C_{ijkl}}$ components) remain roughly constant for Mach numbers lower than 0.75. We have mentioned that the values of c_2 and c_3 in the work of Karabasov et al. (2010) were assumed to be the same as c_1, which is now known to be inappropriate. Instead, they should also be informed by the LES database to account for the anisotropy of turbulence. It is expected that the values of c_2 and c_3 would be similar to those obtained in this study if the correct length scales had been used. It is shown by Karabasov et al. (2010) that a 10% variation of these constants leads to a sound variation within $0.2 - 0.7$ dB. Therefore, it is possible that these constants would still be valid for moderately compressible flows ($M_0 < 0.75$ for example) while a different set of constants is needed for highly compressible jets (such as $M_0 = 0.9$ shown in table 4.1). Of course, to support this argument more studies would be needed in the future. However, the moderate-compressibility argument seems quite promising and we have at least confirmed its validity at $M_0 = 0.5$ and $M_0 = 0.75$. In view of this, the prediction model in this chapter is low-order and fast and would not rely on the LES database within the range of valid proportionality constants.

This lower-order acoustic analogy approach can be readily extended to other nozzle geometries. For example, the recent work of Mohan et al. (2015) shows that, using a developed source anisotropy model, the same approach can successfully predict the noise reduction at low frequencies (and increase at high frequencies) due to the use of chevron nozzles for a wide range of observer angles. The model only needs one LES database for a particular type of chevron nozzle for validation. After validation, the model can be used, without resorting to the LES, to predict the acoustic field produced by chevron nozzles characterized by different design parameters, such as the number of serrations and the penetration ratio (Mohan et al., 2015).

More importantly, the prediction framework would work for many other modifications to the experimental rig, provided the turbulent statistics is not significantly changed, such as adding a flat plate nearby the jet. This is the essential idea underpinning the modelling strategy

of installed jet noise, as will be shown in detail in Chapter 5. In any case, provided the proportionality constants are still valid, the prediction framework described in this chapter would not need an LES database and the lower-order model would be useful in many practical applications.

4.4 Summary

This chapter develops a lower-order RANS-based isolated jet noise prediction model. It starts with a re-derivation of the analogy equations obtained by Goldstein (Goldstein, 2003). Following Lilley's approach (Lilley, 1974), we combine the analogy equations to obtain a single equation in terms of the fluctuation pressure under the locally-parallel flow assumption. The analogy equation is then solved in the frequency domain by using an adjoint Green's function, which can be calculated numerically in a very efficient manner. The space-time correlations of the equivalent sound sources are approximated using a well-validated fourth-order space-time correlation model characterized by a RANS calculation and a set of proportionality constants informed by an LES database. The far-field sound PSD can be efficiently computed using this correlation model together with the adjoint Green's function obtained numerically. The model is then implemented by the author in a highly-efficient numerical code, CONJURE.

It is shown that the low-order RANS-based jet noise prediction method presented in this chapter, and the CONJURE code implemented accordingly, perform exceedingly well in robustly calculating the far-field noise power spectral densities. Good agreement between the model-predicted and the experimentally-measured spectra is achieved for a wide range of observer angles. One of the biggest of advantages of the numerical code developed in this chapter is that it is substantially faster than most existing codes. As mentioned, the entire prediction process only takes seconds to complete with the available RANS results and proportionality constants. This is a significant improvement and this improvement results from a convenient form of Runge-Kutta equations, an innovative way of solving the involved boundary-value equations and also a maximized analyticity of the final equations. It is to be believed that the code can be very usefully in many applications where a fast prediction cycle is desired, and perhaps finds itself used in brand new areas where earlier applications are not possible due to efficiency reasons. In addition, as will be shown in Chapter 5, the isolated jet noise model implemented in this chapter provides an effective and important way to evaluate the refraction effects of the jet mean flow. This will be very useful when we compare the model results with experiments in Chapter 5.

Chapter 5

Installed Jet Noise Prediction

Acoustic analogy theories have long been the standard approaches to predict jet noise and they have proved to be sufficient in predicting isolated jet noise (Lighthill, 1952; Williams, 1963; Lilley, 1974; Goldstein, 2003), as is also described in Chapter 4. In this chapter, we attempt to adopt the same approaches to the modelling of installed jet noise. However, as we will see in subsequent sections, conventional acoustic analogy theories fail to capture an additional but important noise generation mechanism. Consequently, in this chapter we use the acoustic analogy theory in conjunction with an additional near-field scattering theory to predict the far-field sound, which results in a hybrid semi-empirical noise prediction model. The semi-empiricism results from the fact that the near-field scattering model takes an input from either an LES database or an experiment (or possibly an empirical model) on an isolated jet.

Unlike Chapter 4, where Goldstein's acoustic analogy is used to account for the refraction effects of the jet mean flow on sound prorogation explicitly, in this chapter, we use Lighthill's acoustic analogy. The reason is that we attempt to find an analytical Green's function which satisfies appropriate boundary conditions when a solid boundary is placed near the jet. We wish to do so such that the physics can be better understood. However, such a task is unlikely to be possible if we aim to include the refraction effects of the jet mean flow. Chapter 4 shows that even without the presence of solid boundaries, the resulting analogy equation is too complicated for obtaining a uniformly valid Green's function. Fortunately, ignoring refraction effects is not a serious restriction in the context of installed jet noise. As will be shown in Chapter 6, jet installation effects are more pronounced at low Mach numbers and less important at high Mach numbers. For this reason, in this chapter, we focus on a cold jet of Mach number 0.5. At this relatively low Mach number, it can be expected that refraction effects are only pronounced at low observer angles. Using Lighthill's acoustic analogy should suffice at large observer angles

(see the discussion on this in Section 5.2). Besides, the installation effects are most notable at low frequencies, and the propagation of low-frequency sound is less sensitive to the shear of a jet mean flow. Consequently, in this chapter, we choose to start from the Lighthill's analogy equation.

5.1 The hybrid model

5.1.1 Lighthill's acoustic analogy

In Lighthill's original work (Lighthill, 1952, 1954), turbulence-generated noise was studied in the absence of any solid boundaries. The effect of boundaries on sound generation aerodynamically was investigated by Curle (1955). Curle's theory states that the effect of a solid boundary is equivalent to a distribution of dipole sources (unsteady force source) in addition to the Lighthill's quadrupole sources. The dipole strength is equal to the surface pressure. Therefore, in order to use Curle's approach to calculate far-field sound, the pressure on the solid boundaries has to be known beforehand. The pressure on the surface of the plate depends on the quadrupole sources and is difficult to obtain when the surface is non-compact, where there may be significant phase cancellation of the sound from the dipole sources. An alternative approach, which is much more advantageous, is that one can use the Green's function that satisfies the boundary condition on the solid surfaces. Then, the far-field sound, including both the incident field due to the quadrupole sources and the scattered field due to solid boundaries, can be readily obtained by performing a volume integration of the product of the Green's function and the quadrupole sources. This is the approach that we use in this chapter.

To use the latter approach, the Green's function satisfying the rigid-wall boundary conditions at the upper and lower surfaces of the aircraft wing and flap needs to be obtained. While this could be done numerically by, for example, boundary element method, we seek an analytical solution so that the physics of the jet-wing interaction can be understood. Therefore, we simplify the geometry by replacing the wing-flap system with a semi-infinite flat plate, as shown in figure 5.1. This is believed to be valid especially when the acoustic wavelength is shorter than the wing size (Amiet, 1976b; Roger and Moreau, 2005). Then we start with the equation obtained by Lighthill (Lighthill, 1952), i.e.

$$\left(\frac{\partial^2}{\partial t^2} - c_0^2\nabla^2\right)(\rho - \rho_0) = \frac{\partial^2 T_{ij}}{\partial x_i \partial x_j}, \tag{5.1}$$

where $x_i\,(i = 1, 2, 3)$ denote the Cartesian coordinates shown in figure 5.1. It should be emphasized that this Cartesian frame has its origin at the middle of the plate's trailing edge,

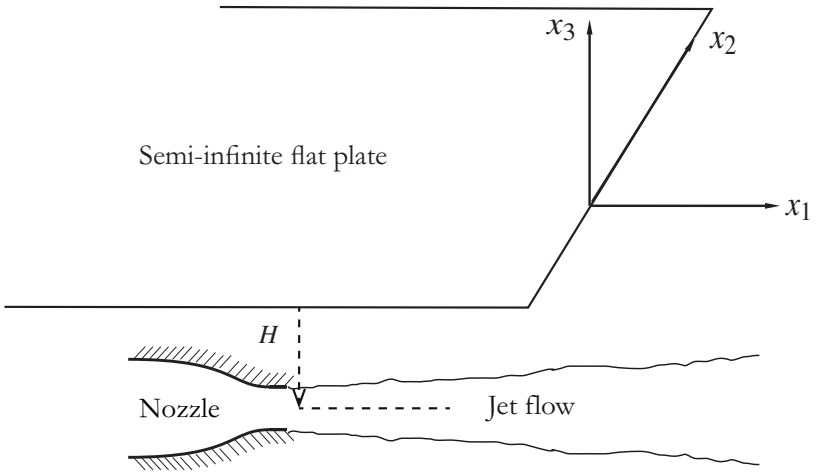

Figure 5.1: Schematic of the simplified model with a semi-infinite flat plate.

and is therefore different from that used for the isolated jet noise prediction. As we already mentioned in preceding chapters, the Lighthill's stress tensor has the form of

$$T_{ij} = \rho v_i v_j + p_{ij} - (\rho - \rho_0) c_0^2 \delta_{ij}, \tag{5.2}$$

where v_i and v_j still denote the velocity components in the i and j direction respectively and p_{ij} the stress tensor. Other flow quantities are defined in preceding chapters. When Reynolds number is high, which is so for most industrially relevant jet flows (and for many laboratory jets), the viscous terms in T_{ij} can be ignored (Lighthill, 1952; Goldstein, 2003; Karabasov et al., 2010). Also when the mean temperature of the jet is same as that of the ambient fluid, which is a good approximation for cold jets at low Mach numbers, the assumption that fluctuations in pressure is balanced out by the product of the density fluctuations and c_0^2 can be made (Lighthill, 1952). T_{ij} can thus be approximated by

$$T_{ij} \approx \rho v_i v_j.$$

In realistic full-scale tests, there exists a uniform ambient flow U_a in x_1 direction due to the forward flight of the aircraft. We aim to include this ambient mean flow effect in our model, and to do that it is convenient to express the fluid velocity in terms of the fluctuation velocity (relative to the ambient background flow) v_i^a, i.e. $v_i = v_i^a + U_a \delta_{i1}$. Substituting this definition into equation 5.1 and making use of the mass conservation equation, equation 5.1 can be formulated as

$$\left(\frac{\partial}{\partial t} + U_a \frac{\partial}{\partial x_1} \right)^2 \rho' - c_0^2 \nabla^2 \rho' = \frac{\partial^2 \rho v_i^a v_j^a}{\partial x_i \partial x_j}, \tag{5.3}$$

where we define the density fluctuation $\rho' \equiv \rho - \rho_0$. Note that this definition of ρ' is not identical to and should not be confused with that defined in Chapter 3 across the flow field. However, they become identical in the far-field where the mean density $\bar{\rho}$ is the ambient density ρ_0. By assuming a $e^{i\omega t}$ time dependence, equation 5.3 can be written as

$$\left(i\omega + U_a \frac{\partial}{\partial x_1}\right)^2 \rho'(\boldsymbol{x}, \omega) - c_0^2 \nabla^2 \rho'(\boldsymbol{x}, \omega) = \frac{\partial^2 \hat{T}_{ij}(\boldsymbol{x}, \omega)}{\partial x_i \partial x_j}. \tag{5.4}$$

where $\rho'(\boldsymbol{x}, \omega)$ and $\hat{T}_{ij}(\boldsymbol{x}, \omega)$ are the Fourier transformations of $\rho'(\boldsymbol{x}, t)$ and $\rho v_i^a v_j^a$ respectively (note because we assume an $e^{i\omega}$ time dependence, the Fourier transformation is the complex conjugate of the one defined in Chapter 3).

Note that although we subtract the ambient uniform flow U_a from v_i, the source term on the right hand side of equation 5.4 still comprises of both linear and non-linear fluctuation terms. This source term is the direct results of Lighthill's acoustic analogy (with the ambient mean flow). The linear terms are known to account for the jet mean flow refraction effects and, therefore, should be most appropriately treated as propagation effects rather than sources (Lighthill, 1952; Lilley, 1974; Goldstein, 2003). If we do so, Lilley's or Goldstein's acoustic analogy theory is recovered. Therefore, the non-linear sources terms left are the same as the equivalent sources resulting from Lilley's or Goldstein's acoustic analogy theory.

As mentioned earlier in this Chapter, we do not use the Goldstein's acoustic analogy equation in order to obtain an analytical Green's function in the next section. However, we also do not want to treat the linear part of the source terms as sound sources, because they in fact characterize the propagation effects. Besides, the more appropriate non-linear source terms have been studied extensively and have been shown to be well described by a simple source model. Hence, when modelling the sources on the right hand side of equation 5.4, we drop the linear terms (hence the mean-flow refraction effects), and only the non-linear fluctuation terms (the Favre average is used for velocities, see Goldstein (2003) for example) are used. However, one can expect this to be acceptable both at low frequencies and for an observer at 90° to the jet centreline, where the refraction effects are negligible. Now provided the source terms are known, equation 5.4 can be solved by using the Green's function satisfying appropriate boundary conditions. In the following sections, the Green's function is formulated first and the source term is obtained by performing CFD calculations.

The acoustic Green's function

From equation 5.4, the Green's function satisfies the convective wave equation

$$\left(\mathrm{i}\omega + U_a\frac{\partial}{\partial x_1}\right)^2 G(\boldsymbol{x};\,\boldsymbol{y}) - c_0^2\nabla^2 G(\boldsymbol{x};\,\boldsymbol{y}) = \delta(\boldsymbol{x}-\boldsymbol{y}). \tag{5.5}$$

This equation, together the rigid-wall boundary conditions at the upper and lower surfaces of the flat plate, needs to be solved to obtain the Green's function.

Letting $k_0 = \omega/c_0$, $M_a = U_a/c_0$, and $\beta^2 = 1 - M_a^2$, and then making the coordinate transformation, $x_1 = \bar{x}_1$, $x_2 = \bar{x}_2/\beta$, $x_3 = \bar{x}_3/\beta$, $y_1 = \bar{y}_1$, $y_2 = \bar{y}_2/\beta$ and $y_3 = \bar{y}_3/\beta$, it is shown that the solution to equation 5.5 (satisfying the rigid-wall boundary conditions on the upper and lower surfaces of the semi-infinite plate) can be found (Macdonald, 1915; Jones, 1972; Roger et al., 2016; Lyu and Dowling, 2016) as

$$G = \frac{\beta^2 \mathrm{e}^{-\mathrm{i}\frac{k_0 M_a}{\beta^2}\bar{y}_1}}{4\pi c_0^2}\left(\frac{\mathrm{e}^{-\mathrm{i}\frac{k_0}{\beta^2}\bar{R}}}{\bar{R}}E(u_{\bar{R}}) + \frac{\mathrm{e}^{-\mathrm{i}\frac{k_0}{\beta^2}\bar{R}'}}{\bar{R}'}E(u_{\bar{R}'})\right), \tag{5.6}$$

where $E(x)$ is an error function defined by

$$E(x) = \frac{\mathrm{e}^{\mathrm{i}\pi/4}}{\sqrt{\pi}}\int_{-\infty}^{x}\mathrm{e}^{-\mathrm{i}u^2}\,\mathrm{d}\,u,$$

and $\bar{R}$ and $\bar{R}'$ are given by

$$\begin{aligned}\bar{R} &= \sqrt{(x_1-y_1)^2 + \beta^2(x_2-y_2)^2 + \beta^2(x_3-y_3)^2},\\ \bar{R}' &= \sqrt{(x_1-y_1)^2 + \beta^2(x_2-y_2)^2 + \beta^2(x_3+y_3)^2}.\end{aligned} \tag{5.7}$$

Here

$$\begin{aligned}u_{\bar{R}} &= 2\sqrt{\frac{k_0\bar{\sigma}\bar{\sigma}_0}{\beta^2(\bar{S}+\bar{R})}}\cos\left(\frac{\bar{\varphi}-\bar{\varphi}_0}{2}\right),\\ u_{\bar{R}'} &= 2\sqrt{\frac{k_0\bar{\sigma}\bar{\sigma}_0}{\beta^2(\bar{S}+\bar{R}')}}\cos\left(\frac{\bar{\varphi}+\bar{\varphi}_0}{2}\right),\end{aligned} \tag{5.8}$$

where $\bar{S} = \sqrt{(\bar{\sigma}+\bar{\sigma}_0)^2 + (\bar{z}-\bar{z}_0)^2}$ and $(\bar{\sigma},\,\bar{\varphi},\,\bar{z})$ and $(\bar{\sigma}_0,\,\bar{\varphi}_0,\,\bar{z}_0)$ denote the corresponding cylindrical coordinates of the observer location and sound source location in the stretched Cartesian coordinate system $(\bar{x}_1,\,\bar{x}_2,\,\bar{x}_3)$ respectively, as shown in figure 5.2. It is straightforward to show that

$$\begin{aligned}\bar{\sigma} = \sqrt{x_1^2+\beta^2x_3^2}, \quad \bar{\sigma}_0 = \sqrt{y_1^2+\beta^2y_3^2},\\ \cos(\bar{\varphi}) = \frac{-x_1}{\bar{\sigma}}, \quad \cos(\bar{\varphi}_0) = \frac{-y_1}{\bar{\sigma}_0},\\ \bar{z} = \beta x_2, \quad \bar{z}_0 = \beta y_2.\end{aligned} \tag{5.9}$$

Similarly, the corresponding spherical coordinates of the observer and source positions in the stretched coordinate system are represented by $(\bar{r},\ \bar{\theta},\ \bar{\varphi})$ and $(\bar{r}_0,\ \bar{\theta}_0,\ \bar{\varphi}_0)$, respectively.

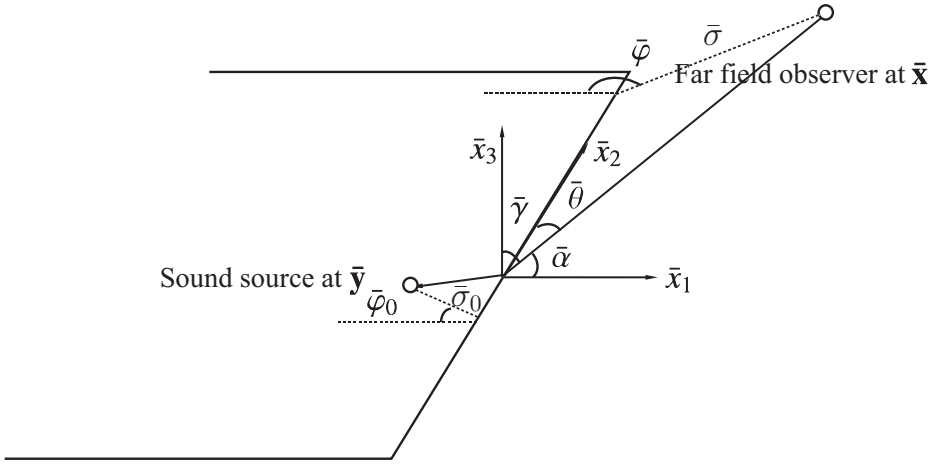

Figure 5.2: The schematic illustration of the stretched coordinates.

The above Green's function without mean flow effects has been used by Williams and Hall (1970) to investigate the scattering of quadrupole sources in the vicinity of the trailing edge of a half plane. It was also used in some of recent studies on installed jet noise (Cavalieri et al., 2014; Piantanida et al., 2016; Nogueira et al., 2017; Huber et al., 2017), as described in Chapter 2. However, it is worth mentioning that this Green's function does not include a full Kutta condition, in the sense that the potential flow at the edge has an infinite velocity. The half-plane scattering Green's function including a full Kutta condition was investigated by Jones (1972). The Green's function developed by Jones was further extended by Rienstra (1981) and used by a number of authors in studying the trailing-edge noise in aeroacoustics (see for example Roger et al. (2016)). In Jones' work , it was concluded that, when there is a convecting mean flow, the Mach number of which can be used to quantify the scale of the sound source fixed at a position close the edge, including Kutta condition has negligible effects on the far-field sound for observers not near the "wake" (the half-plane $x_3 = 0$ and $x_1 > 0$). Therefore, in this study it should suffice to use the Green's function shown above.

When the far-field observer assumption is invoked, the second derivatives of the Green's

function can be obtained as

$$\frac{\partial^2 G(\boldsymbol{x};\,\boldsymbol{y})}{\partial y_2^2} = A(\boldsymbol{x}, y_1, y_2) k_0^2 D_{22}^0(y_1, y_3), \tag{5.10a}$$

$$\frac{\partial^2 G(\boldsymbol{x};\,\boldsymbol{y})}{\partial y_1 \partial y_2} = A(\boldsymbol{x}, y_1, y_2) k_0^2 \left(D_{12}^0(y_1, y_3) + \sqrt{\frac{1}{k_0 \bar{\sigma}_0}} D_{12}^1(y_1, y_3) \right), \tag{5.10b}$$

$$\frac{\partial^2 G(\boldsymbol{x};\,\boldsymbol{y})}{\partial y_2 \partial y_3} = A(\boldsymbol{x}, y_1, y_2) k_0^2 \left(D_{23}^0(y_1, y_3) + \sqrt{\frac{1}{k_0 \bar{\sigma}_0}} D_{23}^1(y_1, y_3) \right), \tag{5.10c}$$

$$\frac{\partial^2 G(\boldsymbol{x};\,\boldsymbol{y})}{\partial y_1^2} = A(\boldsymbol{x}, y_1, y_2) k_0^2 \left(D_{11}^0(y_1, y_3) + \sqrt{\frac{1}{k_0 \bar{\sigma}_0}} D_{11}^1(y_1, y_3) + \left(\sqrt{\frac{1}{k_0 \bar{\sigma}_0}} \right)^3 D_{11}^2(y_1, y_3) \right), \tag{5.10d}$$

$$\frac{\partial^2 G(\boldsymbol{x};\,\boldsymbol{y})}{\partial y_3^2} = A(\boldsymbol{x}, y_1, y_2) k_0^2 \left(D_{33}^0(y_1, y_3) + \sqrt{\frac{1}{k_0 \bar{\sigma}_0}} D_{33}^1(y_1, y_3) + \left(\sqrt{\frac{1}{k_0 \bar{\sigma}_0}} \right)^3 D_{33}^2(y_1, y_3) \right), \tag{5.10e}$$

$$\frac{\partial^2 G(\boldsymbol{x};\,\boldsymbol{y})}{\partial y_1 \partial y_3} = A(\boldsymbol{x}, y_1, y_2) k_0^2 \left(D_{13}^0(y_1, y_3) + \sqrt{\frac{1}{k_0 \bar{\sigma}_0}} D_{13}^1(y_1, y_3) + \left(\sqrt{\frac{1}{k_0 \bar{\sigma}_0}} \right)^3 D_{13}^2(y_1, y_3) \right), \tag{5.10f}$$

where

$$A(\boldsymbol{x}, y_1, y_2) = \frac{\beta^2 \mathrm{e}^{-\mathrm{i}\frac{k_0}{\beta^2}\bar{r}} \mathrm{e}^{\mathrm{i}\frac{k_0 M_a}{\beta^2} x_1}}{4\pi c_0^2 \bar{r}} \mathrm{e}^{\mathrm{i}\frac{k_0}{\beta^2}(-M_a + \cos\bar{\alpha}) y_1} \mathrm{e}^{\mathrm{i}\frac{k_0}{\beta}\cos\bar{\theta} y_2}, \tag{5.11}$$

and the detailed expressions for D_{ij}^k are shown in the appendix. The terms D_{ij}^k are properly bounded functions and determine the directivity patterns of the radiation from the corresponding quadrupoles. Therefore, the noise enhancement arises from the terms $\sqrt{1/(k_0\bar{\sigma}_0)}$ and $\sqrt{1/(k_0\bar{\sigma}_0)^3}$ appearing in front of D_{ij}^1 and D_{ij}^2, respectively. When the frequency is sufficiently low, or the quadrupole source is sufficiently close to the edge of the flat plate, the far-field sound is dominated by the term involving $\sqrt{1/(k_0\bar{\sigma}_0)}$ in the derivatives normal to the 2-axis, and is much larger than that when the plate is absent. The derivatives with one y_2 derivative have leading terms involving $\sqrt{1/(k_0\bar{\sigma}_0)}$, and therefore are not as efficient as those derivatives involving $\sqrt{1/(k_0\bar{\sigma}_0)^3}$ at low frequencies. Equation 5.10a, however, does not involve enhanced terms, hence quadrupoles aligned with the 2-axis (corresponding to $\partial^2 G(\boldsymbol{x};\,\boldsymbol{y})/\partial y_2^2$) are the least efficient sound sources when close to the edge.

CFD flow calculation

We have obtained the Green's function for the scattering problem in the preceding section. In order to solve equation 5.4 to determine the sound from the Lighthill quadrupoles, we need to obtain the source terms shown on the right hand side of equation 5.4. To obtain a low-order model with a fast prediction cycle, we again use the time-averaged RANS flow data to model these sound sources. The RANS simulation for a cold round jet of Mach number 0.5 is virtually identical to that described in Chapter 4 and the previous results are used in this chapter for the purpose of installed jet noise prediction.

Far-field sound due to Lighthill's quadrupoles

Combining the acoustic Green's function, the model of the fourth-order space-time correlation function shown in Chapter 4 and the mean flow data from the RANS simulation, we are now in a position to formulate the far-field sound power spectra. It is well established that the far-field sound perturbation can be written as

$$\rho'(\boldsymbol{x},\omega) = \int_V \hat{T}_{ij}(\boldsymbol{y},\omega)\frac{\partial^2 G(\boldsymbol{x};\,\boldsymbol{y},\omega)}{\partial y_i \partial y_j}\mathrm{d}^{\,3}y. \tag{5.12}$$

The integral in equation 5.12 is over the entire volume where $\hat{T}_{ij}(\boldsymbol{y},\omega)$ is not second-order small. By making use of the linearized relationship $p'(\boldsymbol{x},\omega) = c_0^2\rho'(\boldsymbol{x},\omega)$, one can show that

$$\Phi_Q(\boldsymbol{x},\omega) = c_0^4 \int_{V_y}\int_{V_{\Delta y}} R_{ijkl}(\boldsymbol{y},\Delta\boldsymbol{y},\omega) I_{ijkl}(\boldsymbol{x},\boldsymbol{y},\Delta\boldsymbol{y},\omega)\mathrm{d}^{\,3}\Delta y \mathrm{d}^{\,3}y, \tag{5.13}$$

where $\Phi_Q(\boldsymbol{x},\omega)$ represents the power spectral density of far-field sound, and

$$\begin{aligned} R_{ijkl}(\boldsymbol{y},\Delta\boldsymbol{y},\omega) &= \frac{1}{2\pi}\int_{-\infty}^{\infty} \overline{T_{ij}(\boldsymbol{y},t)T_{kl}(\boldsymbol{y}+\Delta\boldsymbol{y},t+\tau)}\mathrm{e}^{-\mathrm{i}\omega\tau}\mathrm{d}\,\tau, \\ I_{ijkl}(\boldsymbol{x},\boldsymbol{y},\Delta\boldsymbol{y},\omega) &= \frac{\partial^2 G(\boldsymbol{x};\,\boldsymbol{y},\omega)}{\partial y_i \partial y_j}\frac{\partial^2 G^*(\boldsymbol{x};\,\boldsymbol{y}+\Delta\boldsymbol{y},\omega)}{\partial y_k \partial y_l}, \end{aligned} \tag{5.14}$$

where $*$ denotes complex conjugate.

Similar to those mentioned in Chapter 4, the fourth-order space-time correlation function $R_{ijkl}(\boldsymbol{y},\Delta\boldsymbol{y},\tau)$ is modelled using a Gaussian function as (Karabasov et al., 2010)

$$\begin{aligned} R_{ijkl}(\boldsymbol{y},\Delta\boldsymbol{y},\tau) = A_{ijkl}(\boldsymbol{y})\exp\Bigg[&-\frac{|\Delta y_1|}{\bar{v}_1(\boldsymbol{y})\tau_s(\boldsymbol{y})} \\ &-\ln 2\left(\left(\frac{\Delta y_1 - \bar{v}_1(\boldsymbol{y})\tau}{l_1(\boldsymbol{y})}\right)^2 + \left(\frac{\Delta y_2}{l_2(\boldsymbol{y})}\right)^2 + \left(\frac{\Delta y_3}{l_3(\boldsymbol{y})}\right)^2\right)\Bigg], \end{aligned} \tag{5.15}$$

where $A_{ijkl}(\boldsymbol{y}) = C_{ijkl}(2\bar{\rho}k)^2$, $l_i = c_i k^{3/2}/\varepsilon$ and $\tau_s = c_\tau k/\varepsilon$. The proportionality constants used in this chapter is the same as those in Chapter 4. The tensor $I_{ijkl}(\boldsymbol{x}, \boldsymbol{y}, \Delta\boldsymbol{y}, \omega)$ in equation 5.14 depends solely on the Green's function. Consequently, substituting the free-space Green's function or the one developed in the first part of this section into equation 5.13 yields results for an isolated jet or installed jet respectively.

5.1.2 Near-field scattering

Outside the jet mixing layer, there is a region of near-field pressure fluctuations, which is primarily induced by hydrodynamic instability waves and decays exponentially in the radial direction (Jordan and Colonius, 2013). In the frequency regime $St > 0.1$ the waves convect at a virtually constant speed $U_c \approx 0.6 \sim 0.8U_j$ where St is the Strouhal number based on the jet diameter (Arndt et al., 1997; Tinney and Jordan, 2008; Gudmundsson and Colonius, 2011; Jordan and Colonius, 2013). Since the convection velocity is lower than the speed of sound, the pressure due to the field of a hydrodynamic wave decays exponentially in the radial direction (see the details in the following section) and therefore only contributes weakly to the far-field of an isolated jet. However, when a surface with sharp edges is present in the near-field of the jet, the previously non-radiating pressure field can be efficiently scattered into sound by the edge. Had we used the exact equivalent source terms resulting from the Lighthill acoustic analogy, this scattering contribution would have been accounted for automatically. However, as mentioned in the preceding section, in order to use the proper non-linear fluctuation sources, we drop the linear terms in the exact sources (or from another perspective, we drop the mean-flow-refraction part of the linear operator in Goldstein's acoustic analogy). This excludes the refraction effects of the mean shear flow, hence also the instability waves which should be part of the Green's function. Consequently, this suggests that the Lighthill's quadrupole sources used in this chapter are not sufficient to correctly predict the far-field of the installed jet, and the sound due to the scattering of near-field pressure originating from instability waves by the sharp edges of the aerofoil must be accounted for. In this section, the far-field sound due to the interaction between the near-field evanescent waves and the plate edge is modelled using Amiet's approach.

It is worth noting that the trailing-edge scattering mechanism of the hydrodynamic field has been suggested in several earlier works, for example those of Lawrence et al. (2011) and Bychkov and Faranosov (2014). However, the term of hydrodynamic field is not always same as the evanescent wave mentioned here, for both non-linear and linear regions of hydrodynamic field exist. The evanescent wave mentioned here accounts for only the exponentially-decaying

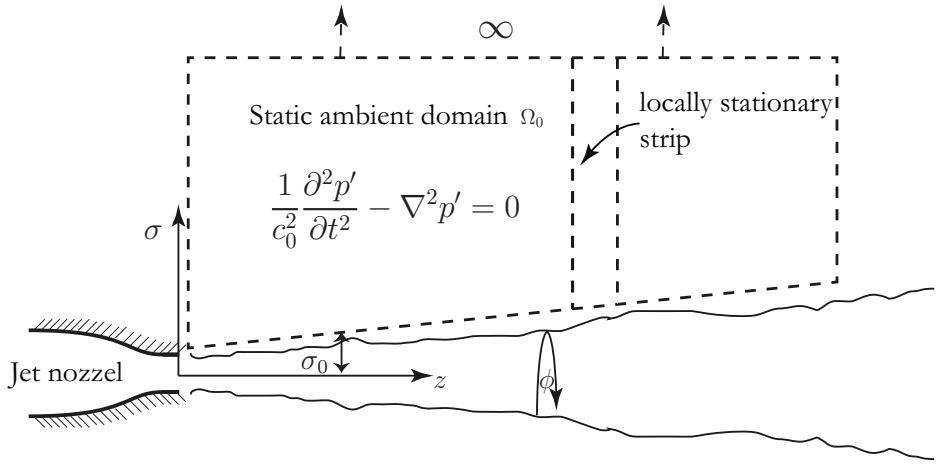

Figure 5.3: Schematic of the jet with a static ambient flow. σ, ϕ and z denote the radial, azimuthal and streamwise coordinates respectively. Immediately outside the jet plume where the flow velocity virtually vanishes, the linearized Navier-Stokes equation reduces to the classical wave equation. Due to the spreading of the jet flow, only the pressure fluctuation in the narrow strip might be regarded as a stationary function of z.

linear part (excluding both the non-linear and linear acoustic parts), the mechanisms of which cannot be captured by Lighthill's acoustic analogy. It should also be noted that the most heavily researched and cited convection velocity, which is around $0.6 \sim 0.8U_j$, is primarily for the instability waves at frequencies around $St = 0.3$. But whether this convection speed is still constant at very low frequencies is not yet known. In fact, the constant-convection-velocity assumption has been called into question by several authors (see Kerhervé et al. (2006) and Jaunet et al. (2017) for example). By analysing LES data (see the rest of this section for details) we confirmed the frequency-dependence of the convection velocity and found that this convection velocity U_c is significantly lower than $0.6U_j$ at low frequencies, e.g. for $St < 0.1$. This frequency dependence is included in our model.

The near-field evanescent waves

As the near-field evanescent waves are scattered into sound nearby the trailing edge, it is useful to investigate its properties before we move on to model the scattering mechanism, in particular its spatial correlation. To illustrate the idea, we consider here an isolated jet with static ambient flow, as shown in figure 5.3. Note that we work with an isolated jet in this section, thus it is sensible to temporarily switch to a cylindrical coordinate system with its origin located at the centre of the nozzle exit, as shown in figure 5.3. The axial and radial coordinates are, as

usual, denoted by z and σ respectively. At any axial position z, the mean jet velocity decays quickly (outside the potential core) as σ increases. Therefore, the velocity effectively vanishes when the radial distance from the jet centre line is larger than a value σ_0. Due to the spreading effect of the jet and the self-similarity exhibited by the velocity distribution along the radial lines, σ_0 would increase as z increases. Consequently, the pressure fluctuation when $\sigma > \sigma_0$, as shown by the domain Ω_0 in figure 5.3, is governed by the classical wave equation resulting from the linearization of the perturbed inviscid Navier-Stokes equations, which is standard and not repeated here.

The solution of the reduced wave equation for frequency ω in Ω_0 is also standard. If we are only interested the radially-decaying components (excluding the oscillating acoustic components), the solution must be of the form

$$p'(\omega, \boldsymbol{x}) = \sum_{m=-\infty}^{\infty} \int_{-\infty}^{\infty} \hat{p}(\omega, m, k_z) K_m(\sqrt{k_z^2 - k_0^2}\sigma) \mathrm{e}^{\mathrm{i}m\phi} \mathrm{e}^{-\mathrm{i}k_z z} \mathrm{d}\, k_z, \tag{5.16}$$

where ϕ is the azimuthal angle, $K_m(\sigma)$ is the mth modified Bessel function of the second kind and we have made use of the fact that the exponentially growing solution $I_m(\sigma)$ tending to infinity as $\sigma \to \infty$ must be excluded. As we have excluded the solutions corresponding to acoustic fluctuations, the integral interval of k_z should strictly be from $-\infty$ to $-k_0$ and from k_0 to ∞. However, since this does not affect our following derivation, we will use the interval from $-\infty$ to ∞ for simplicity.

Since the flow field is turbulent in time t, $\hat{p}(\omega, m, k_z)$ would be a statistical quantity with respect to ω. In addition, since the turbulence flow also results in the randomness of the boundary condition of the domain Ω_0, it can be expected that $\hat{p}(\omega, m, k_z)$ would be a statistical quantity with respect to m and k_z as well. Therefore, the cross-power spectral density of pressure fluctuations at two points located at the same z and ϕ but at σ_1 and σ_2 respectively would be

$$\begin{aligned} R(\omega; \sigma_1, \sigma_2) &\equiv \lim_{T\to\infty} \frac{\pi}{T} \overline{\hat{p}(\omega, \sigma_1)\hat{p}^*(\omega, \sigma_2)} \\ &= \lim_{T\to\infty} \frac{\pi}{T} \sum_{m=-\infty}^{\infty} \sum_{n=-\infty}^{\infty} \int_{-\infty}^{\infty} \int_{-\infty}^{\infty} \overline{\hat{p}(\omega, m, k_z)\hat{p}^*(\omega, n, k_z')} \\ &\quad \times K_m(\sqrt{k_z^2 - k_0^2}\sigma_1) K_n(\sqrt{k_z'^2 - k_0^2}\sigma_2) \mathrm{e}^{\mathrm{i}(m-n)\phi} \mathrm{e}^{-\mathrm{i}(k_z - k_z')z} \mathrm{d}\, k_z \mathrm{d}\, k_z' \end{aligned} \tag{5.17}$$

where $R(\omega; \sigma_1, \sigma_2)$ denotes the cross-power spectral density of the pressure at the aforementioned two points, and $2T$ is the time interval for performing temporal Fourier transforms. The overbar and star denote ensemble average and complex conjugate respectively.

Let us assume that $p'(\omega, \boldsymbol{x})$ is a statistically-stationary function of z and ϕ (Tinney and Jordan, 2008), which implies

$$\lim_{T\to\infty} \frac{\pi}{T}\overline{\hat{p}(\omega, m, k_z)\hat{p}^*(\omega, n, k_z')} = P(\omega, m, k_z)\delta(k_z - k_z')\delta_{nm}, \tag{5.18}$$

where $\delta(x)$ and δ_{mn} are the conventional generalized δ function and Kronecker delta respectively. Substituting equation 5.18 into equation 5.17 yields

$$R(\omega; \sigma_1, \sigma_2) = \sum_{m=-\infty}^{\infty} \int_{-\infty}^{\infty} P(\omega, m, k_z) K_m(\sqrt{k_z^2 - k_0^2}\sigma_1) K_m(\sqrt{k_z^2 - k_0^2}\sigma_2) \mathrm{d}\, k_z. \tag{5.19}$$

If we define the spectral correlation coefficient as

$$\eta(\omega; \sigma_1, \sigma_2) \equiv \frac{\left|\overline{\hat{p}(\omega, \sigma_1)\hat{p}^*(\omega, \sigma_2)}\right|}{\sqrt{\overline{|\hat{p}(\omega, \sigma_1)|^2}\,\overline{|\hat{p}(\omega, \sigma_2)|^2}}}, \tag{5.20}$$

it follows from equation 5.17 and equation 5.19 that

$$\eta(\omega; \sigma_1, \sigma_2) = \frac{|R(\omega; \sigma_1, \sigma_2)|}{\sqrt{R(\omega; \sigma_1, \sigma_1)R(\omega; \sigma_2, \sigma_2)}} = \frac{\left|\sum_{m=-\infty}^{\infty} \int_{-\infty}^{\infty} P(\omega, m, k_z) K_m(\gamma_0\sigma_1) K_m(\gamma_0\sigma_2) \mathrm{d}\, k_z\right|}{\sqrt{\sum_{m=-\infty}^{\infty} \int_{-\infty}^{\infty} P(\omega, m, k_z)[K_m(\gamma_0\sigma_1)]^2 \mathrm{d}\, k_z \sum_{m=-\infty}^{\infty} \int_{-\infty}^{\infty} P(\omega, m, k_z)[K_m(\gamma_0\sigma_2)]^2 \mathrm{d}\, k_z}}, \tag{5.21}$$

where $\gamma_0 \equiv \sqrt{k_z^2 - k_0^2}$ denotes the radial decay of the evanescent waves. Although using Cauchy-Schwartz inequality equation it can be readily shown that $\eta(\omega, \sigma_1, \sigma_2) \leq 1$, it is obvious that the summation over circumferential mode m makes it hard to reach any useful conclusion about how much correlation there exists between the two points. Therefore, we try to remove the summation through a modal decomposition in the ϕ direction of the near-field pressure on two co-axial circles at the same z.

The mathematical derivation is similar, except that we write

$$p'(\omega, m, r, x) = \int_{-\infty}^{\infty} \hat{p}(\omega, m, k_z) K_m(\sqrt{k_z^2 - k_0^2} r) \mathrm{e}^{-\mathrm{i}k_z x} \mathrm{d}\, k_z. \tag{5.22}$$

Repeating the above steps yields

$$R(\omega, m; \sigma_1, \sigma_2) = \int_{-\infty}^{\infty} P(\omega, m, k_z) K_m(\sqrt{k_z^2 - k_0^2}\sigma_1) K_m(\sqrt{k_z^2 - k_0^2}\sigma_2) \mathrm{d}\, k_z. \tag{5.23}$$

If we define the modal spectral correlation coefficient as

$$\eta(\omega, m; \sigma_1, \sigma_2) \equiv \frac{\left|\overline{\hat{p}(\omega, m, \sigma_1)\hat{p}^*(\omega, m, \sigma_2)}\right|}{\sqrt{\overline{|\hat{p}(\omega, m, \sigma_1)|^2}\,\overline{|\hat{p}(\omega, m, \sigma_2)|^2}}}, \tag{5.24}$$

it follows that

$$\eta(\omega, m; \sigma_1, \sigma_2) = \frac{|R(\omega, m; \sigma_1, \sigma_2)|}{\sqrt{R(\omega, m; \sigma_1, \sigma_1)R(\omega, m; \sigma_2, \sigma_2)}} = \frac{\left|\int_{-\infty}^{\infty} P(\omega, m, k_z) K_m(\sqrt{k_z^2 - k_0^2}\sigma_1) K_m(\sqrt{k_z^2 - k_0^2}\sigma_2) \mathrm{d}\, k_z\right|}{\sqrt{\int_{-\infty}^{\infty} P(\omega, m, k_z)[K_m(\sqrt{k_z^2 - k_0^2}\sigma_1)]^2 \mathrm{d}\, k_z \int_{-\infty}^{\infty} P(\omega, m, k_z)[K_m(\sqrt{k_z^2 - k_0^2}\sigma_2)]^2 \mathrm{d}\, k_z}}. \tag{5.25}$$

It is clear that for a fixed frequency ω and circumferential mode number m the coefficient would depend on the specific form of function $P(\omega, m, k_z)$. If for example, the local convective speed of the evanescent wave is a roughly-constant value, $U_c(\omega, m)$, which would mean $P(\omega, m, k_z)$ obtains a large value around $\bar{k}_z = \omega/U_c$ (note $\bar{k}_z$ is a function of both ω and m), then it follows that the approximation

$$P(\omega, m, k_z) = P(\omega, m)\delta(k_z - \bar{k}_z) \tag{5.26}$$

holds. Equation 5.25 can thus simplify to

$$\eta(\omega, m; \sigma_1, \sigma_2) = \frac{\left|P(\omega, m) K_m(\sqrt{\bar{k}_z^2 - k_0^2}\sigma_1) K_m(\sqrt{\bar{k}_z^2 - k_0^2}\sigma_2)\right|}{\sqrt{P(\omega, m)[K_m(\sqrt{\bar{k}_z^2 - k_0^2}\sigma_1)]^2 P(\omega, m)[K_m(\sqrt{\bar{k}_z^2 - k_0^2}\sigma_2)]^2}} = 1. \tag{5.27}$$

In other words, if the convective velocity of the evanescent waves were indeed dominated by a fixed value for each m and ω, then we would obtain a perfect correlation between the modal spectra of the pressure on two co-axial circles at the same z. Therefore the value of $\eta(\omega, m; \sigma_1, \sigma_2)$ can be used to determine whether there exists such a dominant convection velocity for each mode number m and frequency ω.

However, it should be noted that in order to reach this conclusion, we made use of the assumption that $p'(\omega, \boldsymbol{x})$ is a statistically-stationary function of z. However, we know that the near-field instability waves also grow and decay slowly. To avoid this difficulty we only need to consider the pressure inside a sufficiently narrow strip shown in figure 5.3. As the growth and decay occur slowly, we expect the locally stationary assumption to be a good approximation within this strip. All the preceding derivation and conclusion remain unchanged, except quantities are interpreted in a local sense and will depend on z. For example $\bar{k}_z$ is now also a function of z, which implies that the convection velocity can also vary as z changes.

To examine to what extent the dominant-convection-velocity assumption serves as a good approximation, we (note the LES simulation was carried out in collaboration with Dr Iffi Naqavi but not the subsequent analysis) carried out a hybrid RANS-implicit LES study for an isolated single stream jet from the Bridges' experimental data (set point 3) (Bridges and

Wernet, 2010). The jet diameter $D = 5.08$cm, jet Mach number $M_0 = 0.5$, jet temperature ratio $T_j/T_\infty = 0.95$ and the Nozzle Pressure Ratio (ratio of plenum pressure to atmospheric pressure) NPR $= 1.197$. The jet Reynolds number is 5.8×10^5. The LES solver discretized Favre-averaged compressible Navier-Stokes equations with an unstructured non-orthogonal, second-order finite volume scheme. The fluxes are approximated with the Roe method, where the central part is given by a kinetic energy preserving scheme (Jameson, 2008) with a fourth-order dissipative term. In the active LES flow region of interest the dissipation is kept to a minimum value, which gives stable solution. Outside the LES region dissipation is increased for the sponge region to suppress the reflecting waves from the boundaries. Implicit LES relies on this numerical dissipation to remove sub-grid scales without any sub-grid model. A dual-time step method is used to advance the solution implicitly in time. The turbulent flow is developed in a pipe of length $4D$ before exiting the nozzle. A RANS layer, with Spalart-Allmaras turbulence model, is applied in the near wall region of the pipe, which helped to reduce the grid resolution requirements. The computational domain is stretched in the streamwise ($-20D \sim 100D$) and radial ($60D$) directions, with, as mentioned above, sponge zones at the boundaries. A structured axisymmetric mesh of 24 million cells is used. The mesh being used can yield a satisfactory frequency resolution up to $St = 2$. The details of numerical methodology and grid independent studies have been discussed for various single stream jets by Naqavi et al. (2016) and the current grid distribution is the same as the validation case. To validate the LES simulation, we compared the calculated solution with Bridges experimental data (Bridges and Wernet, 2010). Both the mean flow and the turbulent fluctuation velocity profiles along the jet center line and lip line are compared. The results are shown in figures 5.4(a) to 5.4(b). It can be seen that excellent agreement between the experimental and LES data is achieved for $z/D > 2$. The disagreement for $z/D < 2$ is expected because the flow velocity is very sensitive to the inlet boundary conditions and the inlet boundary conditions in experiments are very difficult to replicate.

Figure 5.5 shows the modal spectral correlation coefficient between pressure fluctuations on a pair of coaxial circles at different radial positions using the LES data. The axial position is $z/D = 6$ and the correlation coefficient is defined between the circle at $\sigma = 1.8D$ and other circles at $\sigma = 1.9D, 2.0D, 2.1D, 2.5D, 3.0D$ respectively. Only modes $m = 0$ and $m = \pm 1$ are shown as the energy contained in mode m reduces quickly as m increases. This has been observed in several experimental studies, for example the experimental work of Tinney et al. (2008a) and Tinney and Jordan (2008). From figure 5.5 it appears that the coefficient is close to 1 at low frequencies for either mode 0 or ($\pm$)1. This implies that the assumption of a dominant

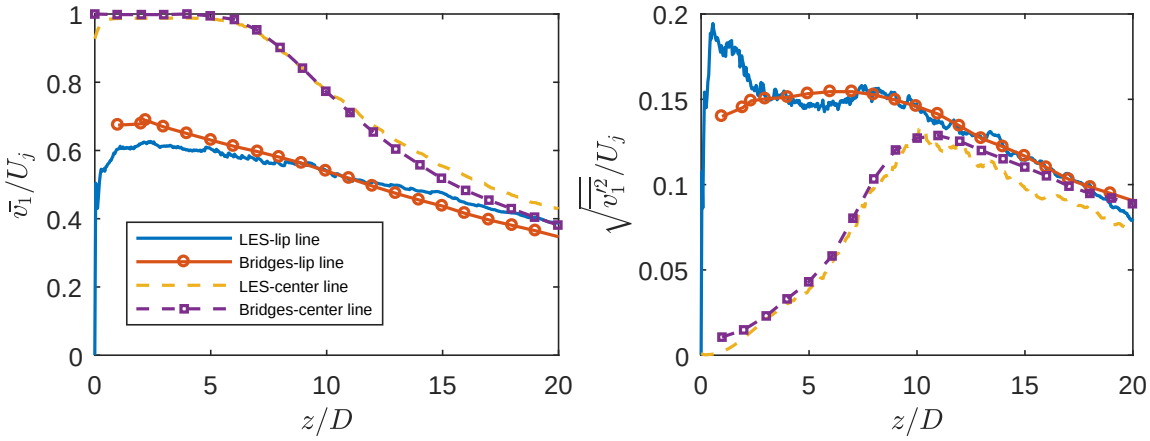

(a) Jet mean axial velocity (b) Root-mean-square axial fluctuation velocity

Figure 5.4: Comparison of the jet mean and turbulent fluctuation velocities along centre line and lip line between the LES and experimental data.

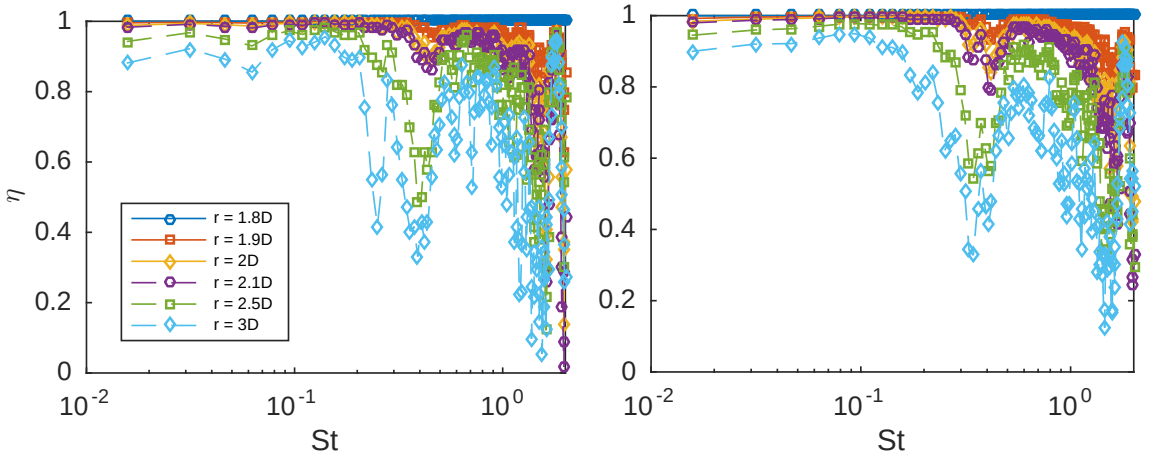

(a) Mode 0 (b) Mode ± 1

Figure 5.5: The modal spectral correlation coefficient η between the point at $\sigma = 1.8D$ and other points at different radial positions, all the points are at $z = 6D$.

convection velocity is valid. The strong oscillation at high frequencies $St > 0.2$ might well be due to acoustic contamination, particularly at large radial positions. However, as can be seen in the rest of this chapter, the near-field pressure is only significant for frequencies satisfying $St < 0.2$. Therefore, it is reasonable to assign a fixed U_c for each m and ω for the near-field evanescent waves in the scattering model to be developed in the next subsection.

To determine these convection velocities, we consider the modal PSD of the near-field pressure fluctuation along the circle located at the axial position z and radial position σ. Letting the correlation-defined spectrum

$$\Pi(\omega, m; \sigma) = \lim_{T\to\infty} \frac{\pi}{T} \left| \frac{\overline{\hat{p}(\omega, m, \sigma_{ref})\hat{p}^*(\omega, m, \sigma)}}{\sqrt{\overline{|\hat{p}(\omega, m, \sigma_{ref})|^2}}} \right|^2, \tag{5.28}$$

where σ_{ref} denotes the σ at a fixed reference point, then using equation 5.26, we have

$$\Pi(\omega, m; \sigma) = P(\omega, m) K_m^2(\sqrt{\bar{k}_z^2 - k_0^2}\sigma). \tag{5.29}$$

Hence the reduced power spectrum

$$\overline{\Pi}(\omega, m; \sigma) = \frac{\Pi(\omega, m; \sigma)}{K_m^2(\sqrt{\bar{k}_z^2 - k_0^2}\sigma)} = P(\omega, m) \tag{5.30}$$

would be independent of σ and the reduced power spectra for any σ should collapse. U_c can be evaluated from the collapsed radial decay rate γ_0.

Figure 5.6 shows the reduced power spectra for different σ. An excellent data collapse is achieved for both mode 0 and mode $(\pm)1$. This is another strong piece of evidence that there does indeed exist a dominant local convection velocity for the near-field evanescent waves for each m and ω. The convection velocities for mode 0, $(\pm)1$ and $(\pm)2$ obtained in this way are shown in figure 5.7. As shown in figures 5.5 and 5.6, both the high spatial correlation and successful collapse of the reduced spectra are only valid for frequencies $St < 0.2$. Therefore, the convection velocities are only shown in this low-frequency regime. It can be seen that the convection velocity is much lower than $0.6U_j$, which is heavily studied for instability waves at around $St = 0.3$. It is interesting to note that the frequency-dependent convection velocity curve obtained here is consistent with the finding of Kerhervé et al. (2006) by measuring the fluctuation velocity field. However, it should be noted that figure 5.7 shows the convection velocities for different azimuthal modes while the convection velocity shown by Kerhervé et al. (2006) was obtained from two-point measurements. The recent work of Jaunet et al. (2016, 2017) examined the coherence length scales and convection velocities of individual azimuthal

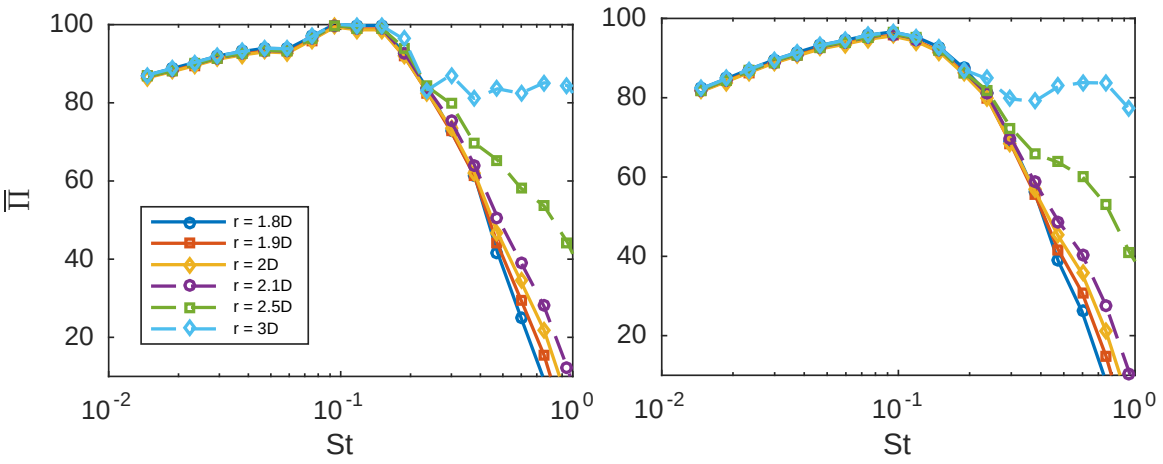

(a) Mode 0 (b) Mode ± 1

Figure 5.6: The reduced power spectra of the near-field pressure fluctuation for points at $z = 6D$ and different radial positions.

modes (mainly mode zero) for the fluctuation velocity field. It was found that they exhibited different behaviours from those from two-point measurements. In particular, the convection velocities of the 0th mode were higher than those from the two-point measurement at low frequencies (e.g. $St < 0.2$). However, the differences between them diminished at further downstream axial locations. At the axial location $z = 6.5D$ for example, the difference was virtually negligible. The trend shown in the work of Jaunet et al. (2017) is in accord with figure 5.7. From figure 5.7 we can find that the convection velocities for different azimuthal modes m do not differ significantly from each other, especially for modes 0, $(\pm)1$ and $(\pm)2$. This is consistent to the findings of Tinney et al. (2008b) obtained using the POD technique by analysing the pressure-velocity coupling. This fact is used in the following sections to simplify the scattering model.

The reason of losing the spatial correlation for the near-field pressure, and hence the failure of collapsing modal PSD, for $St > 0.2$, is mostly due to the fact that the acoustic fluctuation is dominant in this frequency regime. To show this, we take the temporal and spatial Fourier transformations of the pressure along the straight line $\sigma = 3D$, $\phi = 0$ and show the results in figure 5.8. From figure 5.8(a) it can be clearly seen that the wavenumber spectrum of the near-field pressure at high frequencies falls entirely inside the acoustic cone. This means that the pressure is effectively acoustic fluctuations rather than due to evanescent waves. Note that from figure 5.8(a) we have further confirmed that the convection velocity is a frequency dependent quantity rather than a fixed constant between $0.6U_j$ and $0.8U_j$. To better demonstrate this the

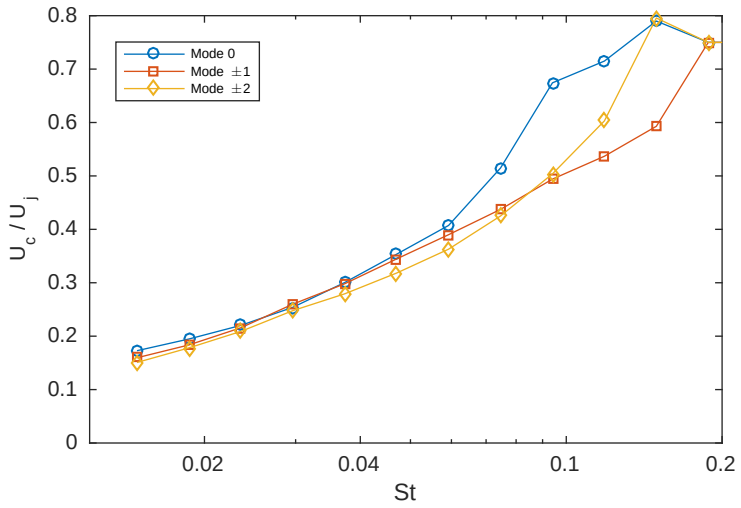

Figure 5.7: The convection velocities at different frequencies for different mode m obtained by collapsing spectra at different radial positions but at the same $z/D = 6$. Due to the dominant presence of acoustic waves at high frequencies, only low-frequency regime is shown.

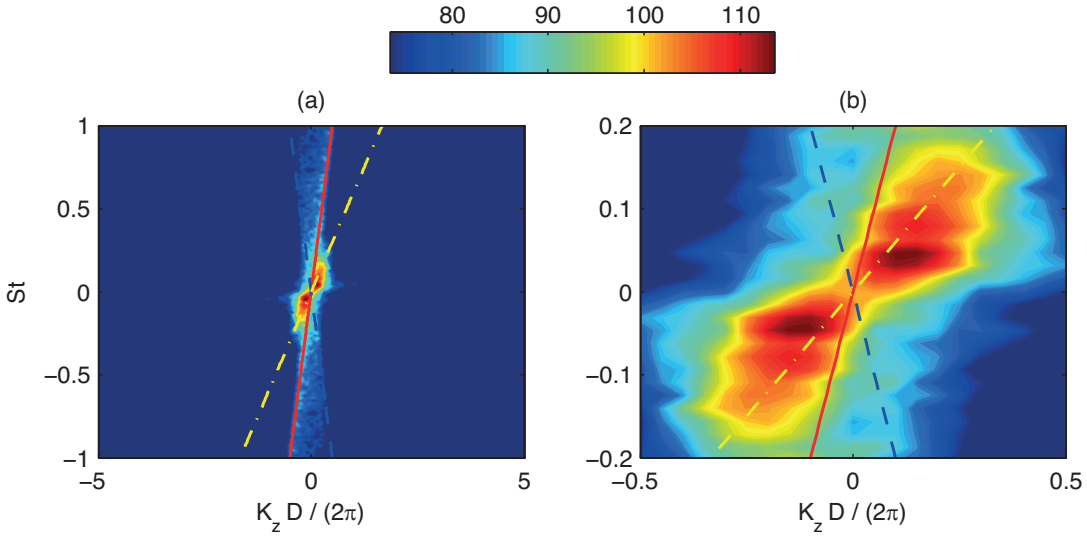

Figure 5.8: The wavenumber spectrum of the near-field pressure along the line $\sigma = 3D$, $\phi = 0$: (a) full range; (b) zoomed-in central region. The red solid and blue dashed lines correspond the convection velocities $U_c = c_0$ and $U_c = -c_0$ respectively; the dash-dotted yellow line corresponds to the convection velocity $U_c = 0.6U_j$.

central region of figure 5.8(a) is expanded in figure 5.8(b). It is clear that at low frequencies the convection velocity is significantly less than $0.6U_j$ (the convection peaks on the right hand side are below the line of $U_c = 0.6U_j$). It is worth noting that due to the size limitation of the computational domain, the highest spatial resolution we achieved is $k_z D/(2\pi) \approx 0.07$. Therefore, at very low frequencies, e.g. $St < 0.03$, the convective peaks cannot be resolved. Also worth noting is that the convection peaks we show in this figure corresponds to an overall convection velocity for the axial range $z = 0$ to $14D$, therefore it is somewhat different from the local convection velocities obtained in figure 5.7.

Near-field pressure scattering

Using the conclusions we made about the near-field pressure in the preceding section, we develop a closed-form scattering model in this section. For a realistic wing-flap system, both the trailing edge and side edges of the wing and flap are present. We again adopt the same simplification used in developing the acoustic Green's function: the wing and flap system are assumed to a semi-infinite flat plate with only a trailing edge. Due to the presence of the flat plate, we switch back to the Cartesian coordinates defined in figure 5.1 again. When the flat plate is sufficiently far away from the jet axis, for example the perpendicular distance between the plate and the jet axis is greater than $2D$, little change of the flow occurs due to the presence of the plate, and therefore the near-field evanescent waves, originating from hydrodynamic instability waves, can be found to be virtually same as that for an isolated jet (Bychkov and Faranosov, 2014). We can thus use the evanescent wave field for an isolated jet as the incident evanescent field for an installed jet. Assume the near-field pressure fluctuation is dominated by the evanescent wave of the first few modes, i.e. the pressure field can be written as

$$p'(\omega, \boldsymbol{x}) = \sum_{m=-N_0}^{N_0} \hat{p}(\omega, m) K_m(\gamma_0 \sigma) \mathrm{e}^{-\mathrm{i}k_1 x_1} \mathrm{e}^{\mathrm{i}m\phi} \tag{5.31}$$

where $\hat{p}(\omega, m)$ denotes the magnitude of the pressure fluctuations of mode m and frequency ω, K_m the mth-order modified Bessel function of the second kind and the radius σ here is now defined as $\sqrt{x_2^2 + (x_3 + H)^2}$, where H is the distance between the jet centre line to the flat plate. γ_0, as defined earlier, denotes the decay rate $\sqrt{k_1^2 - k_0^2}$ where $k_1 = \omega/U_c$. The convection velocity U_c (hence k_1) is a function of ω and m. ϕ is the azimuthal angle and N_0 is a small integer, for example according to the LES data, we find $N_0 = 1$ is sufficient.

However, equation 5.31 is the solution of the reduced wave equation with a static ambient flow. In the presence of a uniform ambient flow of speed U_a in the x_1 direction, (5.31) changes

to

$$p'(\omega,\boldsymbol{x}) = \sum_{m=-N_0}^{N_0} \hat{p}(\omega,m) K_m(\gamma_c\sigma)\mathrm{e}^{-\mathrm{i}k_1x_1}\mathrm{e}^{\mathrm{i}m\phi}, \tag{5.32}$$

where the convective radial decay rate

$$\gamma_c = \frac{\sqrt{(k_1\beta^2 + k_0M_a)^2 - k_0^2}}{\beta}.$$

When the flat plate is directly above the jet, the hypothetical incident pressure that would exist on the lower surface of the plate if the plate were *absent* is

$$p_h(\omega,x_1,x_2) = \sum_{m=-N_0}^{N_0} \hat{p}(\omega,m) K_m(\gamma_c\sqrt{x_2^2+H^2})\mathrm{e}^{-\mathrm{i}k_1x_1}$$
$$\left(\sum_{k=0}^{[\frac{|m|}{2}]} C_{|m|}^{2k}(-1)^k \frac{H^{|m|-2k}x_2^{2k}}{\sqrt{x_2^2+H^2}^{|m|}} + \mathrm{i}\,\mathrm{sgn}(m)\sum_{k=0}^{[\frac{|m|-1}{2}]} C_{|m|}^{2k+1}(-1)^k \frac{H^{|m|-2k-1}x_2^{2k+1}}{\sqrt{x_2^2+H^2}^{|m|}}\right), \tag{5.33}$$

where $[x]$ means taking the nearest integer that is not larger than x, and C_m^n is the binomial coefficient, which results from the use of de Moivre's theorem. By making use of Fourier transformation, the hypothetical incident pressure can be expressed as a superposition of a series of plane waves, namely

$$p_h(\omega,x_1,x_2) = \sum_{m=-N_0}^{N_0} \int_{-\infty}^{\infty} \tilde{p}(\omega,k_2,m)\mathrm{e}^{-\mathrm{i}(k_1x_1+k_2x_2)}\mathrm{d}\,k_2, \tag{5.34}$$

where

$$\tilde{p}(\omega,k_2,m) = \frac{1}{2\pi}\int_{-\infty}^{\infty} \hat{p}(\omega,m)K_m(\gamma_c\sqrt{x_2^2+H^2})\mathrm{e}^{\mathrm{i}k_2x_2}$$
$$\left(\sum_{k=0}^{[\frac{|m|}{2}]} C_{|m|}^{2k}(-1)^k \frac{H^{|m|-2k}x_2^{2k}}{\sqrt{x_2^2+H^2}^{|m|}} + \mathrm{i}\,\mathrm{sgn}(m)\sum_{k=0}^{[\frac{|m|-1}{2}]} C_{|m|}^{2k+1}(-1)^k \frac{H^{|m|-2k-1}x_2^{2k+1}}{\sqrt{x_2^2+H^2}^{|m|}}\right)\mathrm{d}\,x_2. \tag{5.35}$$

Note that the real part of equation 5.33 is an even function of x_2 while the imaginary part is an odd one. Making use of this property and properties of Fourier Transformation one can find that the $\hat{p}(\omega,k_2,m)$ can be evaluated analytically (Gradshteyn and Ryzhik, 2007):

$$\tilde{p}(\omega,k_2,m) = \frac{1}{\sqrt{2\pi}}\hat{p}(\omega,m)$$
$$\left\{\sum_{k=0}^{[\frac{|m|}{2}]} C_{|m|}^{2k}H^{-2k+\frac{1}{2}}\gamma_c^{-|m|}\frac{d^{2k}}{dk_2^{2k}}\left[(\gamma_c^2+k_2^2)^{\frac{1}{2}|m|-\frac{1}{4}}K_{|m|-\frac{1}{2}}\left(H\sqrt{\gamma_c^2+k_2^2}\right)\right] - \mathrm{sgn}(m)\right.$$
$$\left.\sum_{k=0}^{[\frac{|m|-1}{2}]} C_{|m|}^{2k+1}H^{-2k+\frac{1}{2}}\gamma_c^{-|m|}\frac{d^{2k}}{dk_2^{2k}}\left[k_2(\gamma_c^2+k_2^2)^{\frac{1}{2}|m|-\frac{3}{4}}K_{|m|-\frac{3}{2}}\left(H\sqrt{\gamma_c^2+k_2^2}\right)\right]\right\}. \tag{5.36}$$

For an incident pressure given by $\tilde{p}(\omega, k_2, m)\mathrm{e}^{-\mathrm{i}(k_1 x_1 + k_2 x_2)}$, the scattered pressure on the lower surface of the flat plate can be found using Schwarzschild technique as (Amiet, 1976a; Lyu et al., 2016)

$$p_s = \tilde{p}(\omega, k_2, m)\mathrm{e}^{-\mathrm{i}(k_1 x_1 + k_2 x_2)}\left((1+\mathrm{i})E_0(-\mu x_1) - 1\right), \tag{5.37}$$

where

$$\mu = k_1 + \sqrt{k_0^2 - k_2^2\beta^2}/\beta^2 + k_0 M_a/\beta^2, E_0(x) = \int_0^x \frac{\mathrm{e}^{-\mathrm{i}t}}{\sqrt{2\pi t}}\mathrm{d}\,t. \tag{5.38}$$

When the observer is located at $\boldsymbol{x}$, routine application of the theory of Kirchhoff and Curle yields the far-field sound pressure (Amiet, 1975; Lyu et al., 2015, 2016)

$$\begin{aligned} p_f(\omega, \boldsymbol{x}) = (1+\mathrm{i})\frac{\omega x_3}{\pi c_0 S_0^2}\mathrm{e}^{\mathrm{i}k_0(M_a x_1 - S_0)/\beta^2} \\ \sum_{m=-N_0}^{N_0}\int_{-\infty}^{\infty}\frac{\sin\left[(k_2 - k_0\frac{x_2}{S_0})d/2\right]}{k_2 - k_0\frac{x_2}{S_0}}\frac{1}{\mu_A}\Gamma(c, \mu, \mu_A)\tilde{p}(\omega, k_2, m)\mathrm{d}\,k_2 \end{aligned} \tag{5.39}$$

where c and d are the chord and span of the finite plate respectively. Note when calculating equation 5.37 we assumed that the flat-plate is semi-infinite. But when applying the theory of Kirchhoff and Curle to obtain equation 5.39 we used a finite plate of chord c and span d. The same approach was used by Amiet (1976b) and was found to be a good approximation provided the frequency is not too low (Roger and Moreau, 2005). The properly bounded function Γ in equation 5.39 is defined as

$$\Gamma(x, \mu, \mu_A) = \mathrm{e}^{\mathrm{i}\mu_A x}E_0(\mu x) - \sqrt{\frac{\mu}{\mu - \mu_A}}E_0\left[(\mu - \mu_A)x\right] + \frac{1}{1+\mathrm{i}}(1 - \mathrm{e}^{\mathrm{i}\mu_A x}), \tag{5.40}$$

and

$$\begin{aligned} S_0 &= \sqrt{x_1^2 + \beta^2(x_2^2 + x_3^2)}, \\ \mu_A &= k_1 + \frac{k_0}{\beta^2}(M_a - \frac{x_1}{S_0}). \end{aligned} \tag{5.41}$$

We note that normally aircraft wings have a large span-to-chord ratio, and d can be quite large compared to the sound wavelength at the frequency of peak noise enhancement in the low frequency regime, therefore we use

$$\lim_{d\to\infty}\frac{\sin\left[(k_2 - k_0\frac{x_2}{S_0})d/2\right]}{\pi(k_2 - k_0\frac{x_2}{S_0})} = \delta(k_2 - k_0\frac{x_2}{S_0}) \tag{5.42}$$

to simplify equation 5.39 to

$$p_f(\omega, \boldsymbol{x}) = (1+\mathrm{i})\frac{\omega x_3}{c_0 S_0^2}\sum_{m=-N_0}^{N_0}\frac{1}{\mu_A}\Gamma(c, \mu|_{k_2 = k_0\frac{x_2}{S_0}}, \mu_A)\tilde{p}(\omega, k_0\frac{x_2}{S_0}, m). \tag{5.43}$$

Using equation 5.43, one can obtain the far-field sound power density spectrum from the equation $\Phi_N(\omega,\boldsymbol{x}) = \lim_{T\to\infty}(\pi/T)\overline{p_f(\omega,x), p_f^*(\omega,x)}$, i.e.:

$$\Phi_N(\omega,\boldsymbol{x}) = 2\left[\frac{\omega x_3}{c_0 S_0^2}\right]^2 \sum_{m=-N_0}^{N_0}\sum_{m'=-N_0}^{N_0} \left.\frac{\Gamma(c,\mu|_{k_2=k_0\frac{x_2}{S_0}},\mu_A)}{\mu_A}\right|_m \left.\frac{\Gamma^*(c,\mu|_{k_2=k_0\frac{x_2}{S_0}},\mu_A)}{\mu_A^*}\right|_{m'} \lim_{T\to\infty}\frac{\pi}{T}\overline{\tilde{p}(\omega,k_0\frac{x_2}{S_0},m)\tilde{p}^*(\omega,k_0\frac{x_2}{S_0},m')} \tag{5.44}$$

It should be noted that equation 5.44 is due to the contribution of the scattered pressure only. In order to take the incident wave contribution into consideration, the term 1 in the last bracket on the right hand side of equation 5.40 defining the function $\Gamma(x,\mu,\mu_A)$ should be omitted (Amiet, 1978).

Substituting equation 5.36 into the above equation, one finds the statistical term in equation 5.44 can be evaluated to be

$$\lim_{T\to\infty}\frac{\pi}{T}\overline{\tilde{p}(\omega,k_0\frac{x_2}{S_0},m)\tilde{p}^*(\omega,k_0\frac{x_2}{S_0},m')} = \frac{1}{2\pi}\Pi(\omega,m)\delta_{mm'}$$
$$\times\left\{\sum_{k=0}^{[\frac{|m|}{2}]} C_{|m|}^{2k} H^{-2k+\frac{1}{2}}\gamma_c^{-|m|}\frac{d^{2k}}{dk_2^{2k}}\left[(\gamma_c^2+k_2^2)^{\frac{1}{2}|m|-\frac{1}{4}}K_{|m|-\frac{1}{2}}\left(H\sqrt{\gamma_c^2+k_2^2}\right)\right] - \mathrm{sgn}(m)\times\right.$$
$$\left.\sum_{k=0}^{[\frac{|m|-1}{2}]} C_{|m|}^{2k+1} H^{-2k+\frac{1}{2}}\gamma_c^{-|m|}\frac{d^{2k}}{dk_2^{2k}}\left[k_2(\gamma_c^2+k_2^2)^{\frac{1}{2}|m|-\frac{3}{4}}K_{|m|-\frac{3}{2}}\left(H\sqrt{\gamma_c^2+k_2^2}\right)\right]\right\}^2_{k_2=\frac{k_0x_2}{S0}}.$$

where $\Pi(\omega,m)$ denotes the power spectrum of mth-order near-field evanescent waves. The spectrum could be obtained from simple models, experiments or LES simulations. Substituting the above equation into equation 5.44 yields

$$\Phi_N(\omega,\boldsymbol{x}) = \frac{1}{\pi}\left[\frac{\omega x_3}{c_0 S_0^2}\right]^2 \sum_{m=-N_0}^{N_0}\left|\frac{\Gamma(c,\mu|_{k_2=k_0\frac{x_2}{S_0}},\mu_A)}{\mu_A}\right|^2 \Pi(\omega,m)$$
$$\times\left\{\sum_{k=0}^{[\frac{|m|}{2}]} C_{|m|}^{2k} H^{-2k+\frac{1}{2}}\gamma_c^{-|m|}\frac{d^{2k}}{dk_2^{2k}}\left[(\gamma_c^2+k_2^2)^{\frac{1}{2}|m|-\frac{1}{4}}K_{|m|-\frac{1}{2}}\left(H\sqrt{\gamma_c^2+k_2^2}\right)\right] - \mathrm{sgn}(m)\sum_{k=0}^{[\frac{|m|-1}{2}]}\right.$$
$$\left. C_{|m|}^{2k+1} H^{-2k+\frac{1}{2}}\gamma_c^{-|m|}\frac{d^{2k}}{dk_2^{2k}}\left[k_2(\gamma_c^2+k_2^2)^{\frac{1}{2}|m|-\frac{3}{4}}K_{|m|-\frac{3}{2}}\left(H\sqrt{\gamma_c^2+k_2^2}\right)\right]\right\}^2_{k_2=\frac{k_0x_2}{S0}}. \tag{5.45}$$

Equation 5.45 is the generic form of near-field scattering model. However, further simplifications can be made in practical cases. First if we assume that the fluctuation is symmetric with

respect to m, i.e. $\Pi(\omega, m) = \Pi(\omega, -m)$, equation 5.45 can be further simplified to

$$\Phi_N(\omega, \boldsymbol{x}) = \frac{1}{\pi}\left[\frac{\omega x_3}{c_0 S_0^2}\right]^2 \sum_{m=0}^{N_0} \left|\frac{\Gamma(c, \mu|_{k_2=k\frac{x_2}{S_0}}, \mu_A)}{\mu_A}\right|^2 \Pi_s(\omega, m)$$
$$\times \left\{ \left(\sum_{k=0}^{[\frac{|m|}{2}]} C_{|m|}^{2k} H^{-2k+\frac{1}{2}} \gamma_c^{-|m|} \frac{d^{2k}}{dk_2^{2k}} \left[(\gamma_c^2 + k_2^2)^{\frac{1}{2}|m|-\frac{1}{4}} K_{|m|-\frac{1}{2}} \left(H\sqrt{\gamma_c^2 + k_2^2} \right) \right] \right)^2 + \left(\sum_{k=0}^{[\frac{|m|-1}{2}]} \right. \right.$$
$$\left. \left. C_{|m|}^{2k+1} H^{-2k+\frac{1}{2}} \gamma_c^{-|m|} \frac{d^{2k}}{dk_2^{2k}} \left[k_2 (\gamma_c^2 + k_2^2)^{\frac{1}{2}|m|-\frac{3}{4}} K_{|m|-\frac{3}{2}} \left(H\sqrt{\gamma_c^2 + k_2^2} \right) \right] \right)^2 \right\}_{k_2=\frac{k_0 x_2}{S0}} . \quad (5.46)$$

where $\Pi_s(\omega, m)$ is mth single-sided modal power spectral density, i.e. $\Pi_s(\omega, m) = \Pi(\omega, m) + \Pi(\omega, -m)$ for $m \neq 0$. If we assume that only the 0 and $1(-1)$ modes are significant, we can show that the far-field sound spectral density in the mid-span plane ($x_2 = 0$) is

$$\Phi_N(\omega, \boldsymbol{x}) \approx \left[\frac{\omega x_3}{c_0 S_0^2}\right]^2 \left\{ \left|\frac{\Gamma(c, \mu, \mu_A)}{\mu_A}\right|^2 \Pi_s(\omega, 0) \frac{\mathrm{e}^{-2H\gamma_c}}{2\gamma_c^2} \right\}_{k_2=0, m=0}$$
$$+ \left\{ \left|\frac{\Gamma(c, \mu, \mu_A)}{\mu_A}\right|^2 \Pi_s(\omega, 1) \frac{\mathrm{e}^{-2H\gamma_c}}{2\gamma_c^2} \right\}_{k_2=0, m=1} . \quad (5.47)$$

Let $\Pi_0(\omega, 0)$ and $\Pi_0(\omega, 1)$ denote the 0th and 1st single-sided modal power spectral densities measured at the location of $\sigma = \sigma_0$, then it follows that $\Pi_s(\omega, 0) K_0^2(\gamma_c \sigma_0) = \Pi_0(\omega, 0)$ and $\Pi_s(\omega, 1) K_1^2(\gamma_c \sigma_0) = \Pi_0(\omega, 1)$. Note in equation 5.47, μ, μ_A and γ_c depend on the mode number m as the convection velocity (hence k_1) can vary with m. However, in Section 5.1.2 we show that the convection velocity for mode 0 and $(\pm)1$ do not differ significantly from each other, therefore equation 5.47 can be further simplified by assuming an averaged convection velocity profile $\overline{U}_c(\omega)$ over the two modes, such that

$$\Phi_N(\omega, \boldsymbol{x}) \approx \left[\frac{\omega x_3}{c_0 S_0^2}\right]^2 \left\{ \left|\frac{\Gamma(c, \mu, \mu_A)}{\mu_A}\right|^2 \frac{\mathrm{e}^{-2H\gamma_c}}{2\gamma_c^2} \left(\frac{\Pi_0(\omega, 0)}{K_0^2(\gamma_c \sigma_0)} + \frac{\Pi_0(\omega, 1)}{K_1^2(\gamma_c \sigma_0)} \right) \right\}_{k_2=0, U_c=\overline{U}_c(\omega)} .$$

When in the frequency of interests where $K_0(\gamma_c \sigma_0)$ and $K_1(\gamma_c \sigma_0)$ do not differ from each other significantly (such as the case to be presented in the Section 5.2), the above equation can be estimated by

$$\Phi_N(\omega, \boldsymbol{x}) \approx \left[\frac{\omega x_3}{c_0 S_0^2}\right]^2 \left\{ \left|\frac{\Gamma(c, \mu, \mu_A)}{\mu_A}\right|^2 \frac{\mathrm{e}^{-2H\gamma_c}}{2\gamma_c^2} \frac{\Pi_0(\omega)}{K_0^2(\gamma_c \sigma_0)} \right\}_{k_2=0, U_c=\overline{U}_c(\omega)} , \quad (5.48)$$

where $\Pi_0(\omega)$ is the single-sided spectrum of the incident near-field evanescent waves at $\sigma = \sigma_0$, which can be easily measured using one microphone in an isolated-jet experiment. To ensure acoustic fluctuations to be negligible, one can choose σ_0 to be small such that the microphone is sufficiently close to the jet. Since this spectrum varies with axial position, it makes more sense to put the microphone at the position where the trailing edge of the flat plate would be if a flat plate were to be present, i.e. the place where the incident wave is to be scattered.

We have now obtained the far-field sound due to the quadrupole sources, i.e. $\Phi_Q(\boldsymbol{x}, \omega)$ as shown in equation 5.13, and the sound due to the interaction between the near-field evanescent wave and the trailing edge of the flat plate, i.e. $\Phi_N(\boldsymbol{x}, \omega)$ as shown from equation 5.45 to equation 5.48, the total sound power spectra is therefore

$$\Phi(\boldsymbol{x}, \omega) = \Phi_Q(\boldsymbol{x}, \omega) + \Phi_N(\boldsymbol{x}, \omega). \tag{5.49}$$

It is useful to review the inputs of this model. First, $\Phi_Q(\boldsymbol{x}, \omega)$ is the sound predicted using Lighthill's acoustic analogy. The Green's function is obtained analytically and therefore the input of this part is the time-averaged flow statistics obtained from RANS. Secondly, the near-field scattering part, e.g. $\Phi_N(\boldsymbol{x}, \omega)$ shown in equation 5.48, requires the one-point spectrum and the local convection velocity (varying with frequency as well) of the near-field pressure fluctuation of an isolated jet at the location where the trailing edge of the flat plate would be. It is worth mentioning that though we perform an LES study in this thesis, it is mostly for validation purposes, and the hybrid model does not directly require the input of the LES (at least for the cases the where convection velocity curve still applies or is known from experiments or models of instability waves).

Note that though the new model requires the near-field pressure spectrum as an input, which is why we call it semi-empirical at this stage, this requirement could be removed if the strength of the evanescent instability waves were predicted by modelling the growth and decay of the jet instability waves, as is common in instability theory. However, to apply that to a particular experiment requires data on the perturbations at the nozzle exit. In general, the inlet boundary conditions depend on both the environment and the turbulence statistics of the flow at the inlet, therefore they are difficult to be predicted in theories and even replicated in experiments. Consequently, having a complete input-free model is rather impractical and a semi-empirical approach seems to be more feasible. For example, the information on inlet boundary condtions was not available in the experiment of Head and Fisher (1976), but the near-field pressure of the isolated jet was and we have used that as an input. The semi-analytical model developed in the chapter is also very useful in both understanding the underlying physics and developing ideas to control it. For example the near-field scattering model proposed in this

chapter is nothing more than a transfer function, which maps the input (near-field pressure) spectrum to the output (far-field sound) spectrum. The fact it works well (as shown in the next section) confirms the scattering mechanism of the installed jet noise, and therefore provides evidence of this new sound source as opposed to isolated jets. By studying this transfer function, we can also understand the transfer efficiency, i.e. at which frequency the scattering is most efficient. The identification of the sound source and the understanding of the scattering mechanism is essential for noise reduction methods.

It should also be noted that while the ambient flow is taken into consideration and the effect of source motion is accounted for by the model of the fourth-order space-time correlation function, the model for installed jet noise developed in this section does not account for the mean jet flow refraction effects. Though this means that the model cannot correctly predict the far-field sound at high frequencies, it should suffice for the sound at 90° to the jet and for low frequencies. In the next section, we will use the model developed in this section to predict the installed jet noise spectrum and the results will be compared against experimental measurements.

5.2 Results

In 1976, in order to study the acoustic characteristics of low frequency enhancement of the installed jet noise and to identify the corresponding noise sources, Head and Fisher (1976) presented a series of experimental results of the low frequency augmentation of the jet noise with the close presence of a solid shield (flat plate), as shown in figure 5.9. There was no ambient flow so $M_a = 0$. The experiment was carried out with a cold, subsonic, round jet ($D = 1$ inch) at $M_0 = 0.5$ and the separation distance between the plate and the jet centreline $H = 3D$ and the distance between the trailing edge of the flat plate and the jet nozzle $L = 6D$. The far-field spectra for both isolated and installed jet noise were measured and the microphone was located in the plane that is perpendicular to the rigid shield but at 90°, 45° and 30° to the jet centreline respectively, on both the shielded and reflected sides, as shown in figure 5.9. Since the rigid shield used in the experiment was placed sufficiently away from the jet, it can be expected to have little effect on the jet flow. Thus, in this section we use the two-part model, together with the inputs from axisymmetric jet flow field obtained in the preceding section, to calculate both the isolated and installed jet noise spectra. In the Lighthill acoustic analogy part, $\Phi_Q(\boldsymbol{x}, \omega)$, the turbulent statistics is obtained from the RANS calculation. In the near-field scattering part, we use the approximated equation 5.48 to calculate $\Phi_N(\boldsymbol{x}, \omega)$, and the spectrum of the near-field evanescent waves at the trailing-edge position was experimentally measured.

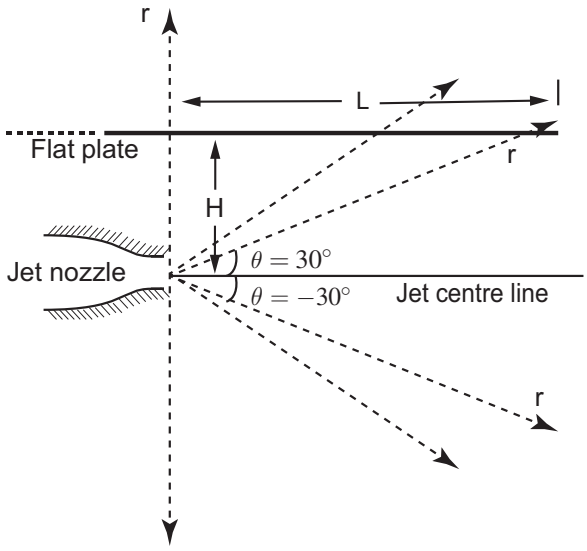

Figure 5.9: The schematic of the experiment of Head and Fisher (1976). The separation distance between the flat plate and the jet centreline $H = 3D$, the distance between the trailing edge of the flat plate and the jet nozzle $L = 6D$.

But the local convection velocity at this point makes use of the averaged frequency-dependent velocity obtained from the aforementioned LES study. The results based on the new model are then compared with the experimental results.

Before we proceed to show the comparison, however, it is useful to assess the refraction effects of the jet mean flow ($M_0 = 0.5$) on isolated jet noise. We can do this by making use of the CONJURE program developed in Chapter 4, where the convection effects are included. More specifically, we compare the predictions of the isolated spectra based on CONJURE and the model in this Chapter (equation 5.13 with a free-space Green's function). Results are shown in figures 5.10, 5.11 and 5.12, where the observer is at 90°, 45° and 30° to the jet axis, respectively.

From figure 5.10, we can see clearly that the refraction effects are negligible at 90°, and using Lighthill's acoustic analogy does not introduce noticeable changes to the predicted noise spectrum. This is also consistent to our earlier expectation. Figure 5.11, on the other hand, starts to show the differences caused by the convection effects. At low frequencies, noise is under-predicted by around 1 dB while at high frequencies it is over-predicted by around 2.5 dB. As expected, the difference is more pronounced at high frequencies. However, both of them are not significant at such an angle of 45°. The convection effects are most notable when an observer is at 30° to the jet axis, as shown in figure 5.12. At low frequencies, using Lighthill's acoustic analogy causes an under-prediction of around $3 \sim 4$ decibels and a signif-

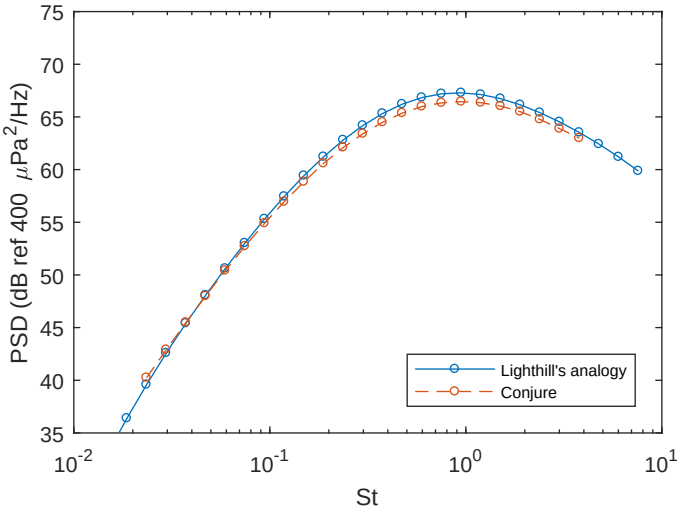

Figure 5.10: The comparison of isolated jet noise spectra in 1/3 octaves at 90° with and without convection effects.

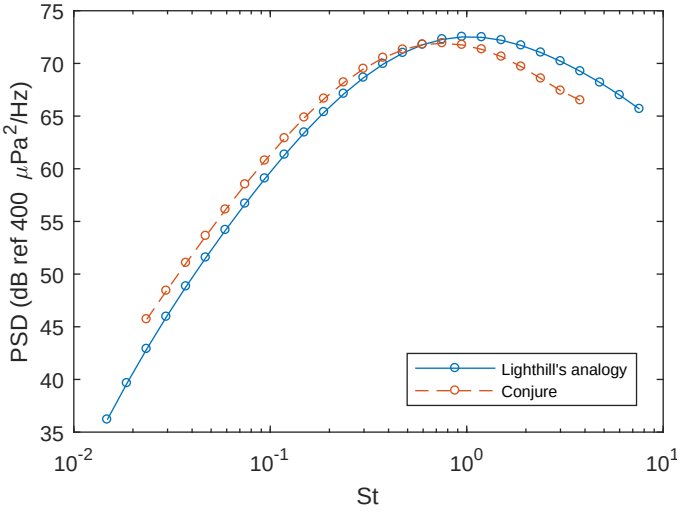

Figure 5.11: The comparison of isolated jet noise spectra in 1/3 octaves at 45° with and without convection effects.

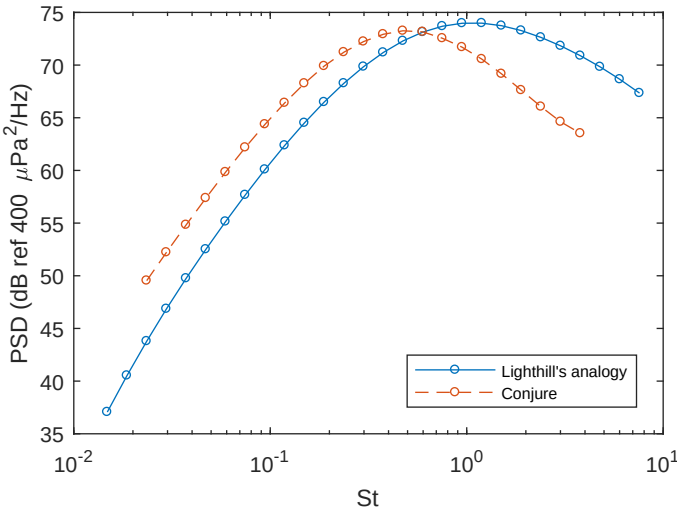

Figure 5.12: The comparison of isolated jet noise spectra in 1/3 octaves at 30° with and without convection effects.

icant over-prediction at high frequencies. In summary, the convection effects are negligible at high observer angles, especially at 90°, and they are only significant at around 30°. The convection effects are also more pronounced at high frequencies. Therefore, in the following comparisons between the experimentally measured and predicted isolated and installed noise spectra, we would expect a similar trend.

5.2.1 Installed jet noise with only the acoustic scattering of Lighthill's quadrupole sources

To demonstrate the existence of the additional near-field scattering mechanism for installed jet noise, the prediction of the far-field sound power spectrum with only the contribution of Lighthill's quadrupole sources, i.e. $\Phi_Q(\boldsymbol{x}, \omega)$, is presented first. The predictions are compared with the experimental results.

Figure 5.13(a) shows the sound power spectra at 90° to the jet on the shielded side. The isolated sound spectra are also presented. As can be seen, the predicted spectrum for an isolated jet has excellent agreement with experimental results. This shows that the RANS calculation and the fourth-order correlation model indeed work well. However, the predicted spectrum for an installed jet does not agree well with the experimental result. In particular, the predicted spectrum fails to capture the low frequency amplification. The reason is because we have not yet incorporated the near-field scattering mechanism, which will be shown to account for such a noise intensification. The discrepancy at high frequencies, however, is in fact expected, since

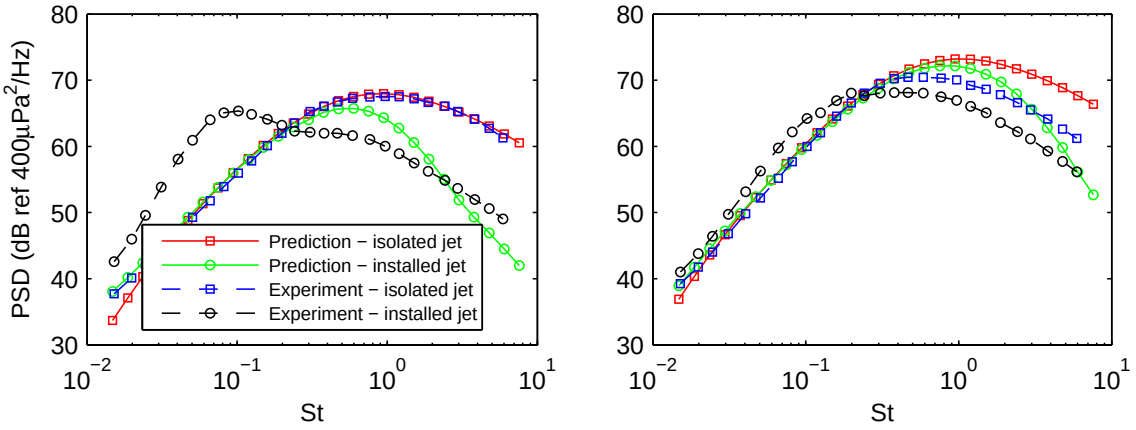

(a) 90° to the jet, shielded side

(b) 45° to the jet, shielded side

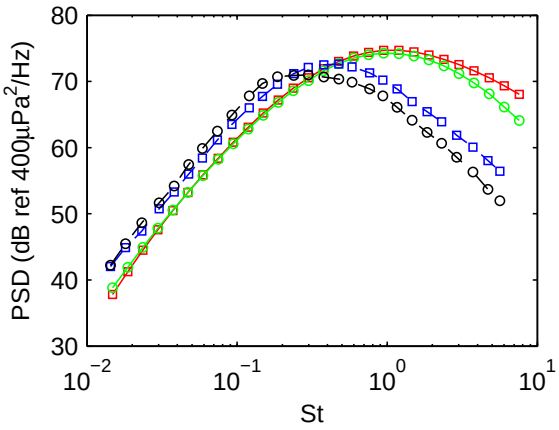

(c) 30° to the jet, shielded side

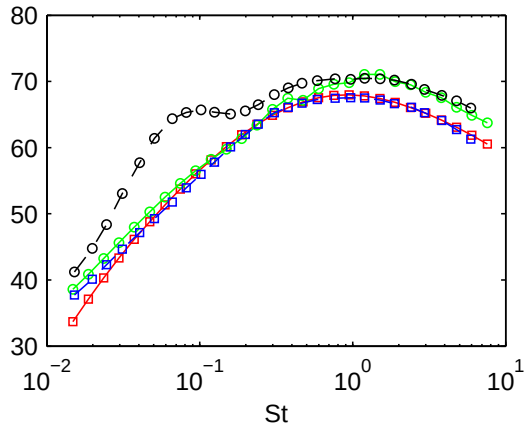

(d) 90° to the jet, reflected side

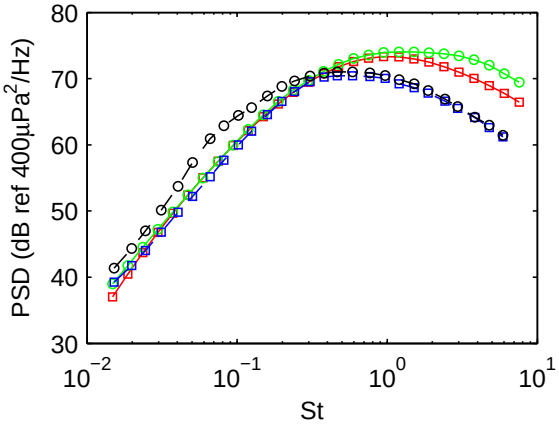

(e) 45° to the jet, reflected side

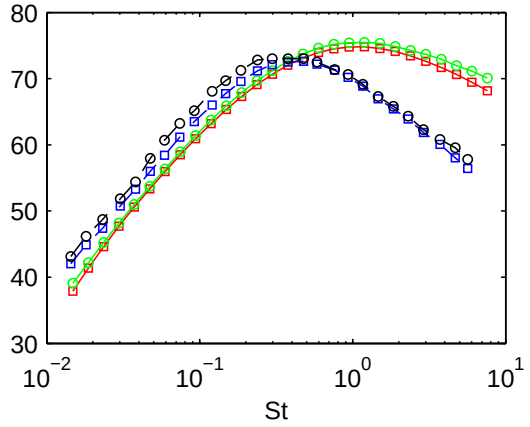

(f) 30° to the jet, reflected side

Figure 5.13: Comparison between experimental measurements and predictions for the far-field PSDs in 1/3 octaves for the installed jet with only the contribution of Lighthill's quadrupoles.

the jet refraction effect must be accounted for in order to correctly predict the shielding effect of the flat plate.

The noise spectra at 45° and 30° to the jet are shown in figures 5.13(b) and 5.13(c), respectively. The predicted spectra for isolated jet noise continues to agree well with experiment at low frequencies at 45°, while, as expected, a slight under-prediction starts to appear at 30°. More stark discrepancies start to appear at high frequencies, because the jet mean-flow refraction effect cannot be ignored at these angles. For the installed jet noise, the low frequency enhancement at low frequencies at 45° still fails to be captured and the agreement at high frequencies is also affected by the refraction effect of the jet mean flow. But the prediction does indeed give some of the correct qualitative behaviour.

Figure 5.13(d) shows the noise power spectra predicted at 90° on the reflected side. For installed jet noise spectra, despite the low frequency discrepancies, the agreement at high frequencies is in fact very good. This indicates that the high frequency reflection effect can be correctly captured at 90° to the jet. Figures 5.13(e) and 5.13(f) present the noise spectra at 45° and 30° respectively. For installed jet noise, despite the large discrepancies caused by the jet refraction effect, it is found that the qualitative behaviour of the noise increase due to the flat plate observed at high frequencies is correctly predicted. This suggests that if the refraction effect were to be included, the model would be able to give much better agreement with the experiment at high frequencies. It is worth noting that, at all the different observer angles, the low frequency amplification cannot be captured, and this suggests that the near-field scattering mechanism is responsible for the low frequency noise alteration.

5.2.2 Installed noise with two source mechanisms

From figures 5.13(a) to 5.13(f), it has been found that the noise spectrum predicted by incorporating only the contribution of the scattering of the Lighthill's quadrupole sources cannot correctly model installed jet noise. In this part of this section, the contribution of the near-field scattering, i.e. $\Phi_N(\boldsymbol{x}, \omega)$ described in Section 5.1.2, is added. As mentioned above, the convection velocity of the near-field evanescent wave obtained by examining the radial decay rate using the LES data is used. We use the averaged convection velocity profile $\overline{U}_c(\omega)$ obtained by averaging over modes 0 and $(\pm)1$. By combining the frequency-dependent convection velocity $\overline{U}_c(\omega)$ and the experimentally measured near-field spectrum, the predicted far-field sound spectra at different angles are compared with experiments.

The sound spectra for both isolated and installed jets on the shielded side are shown in figures 5.14(a) to 5.14(c). As the spectra for isolated jet is identical to those shown in figure 5.13,

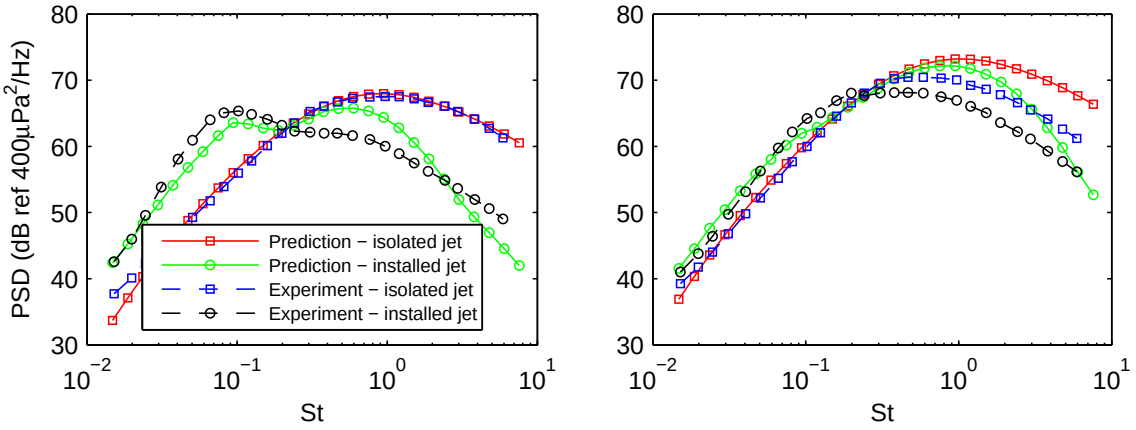

(a) 90° to the jet, shielded side

(b) 45° to the jet, shielded side

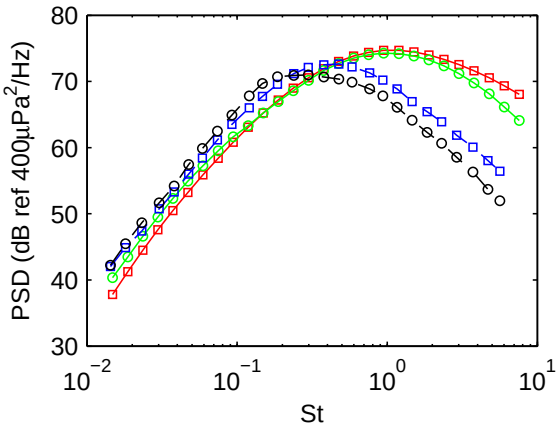

(c) 30° to the jet, shielded side

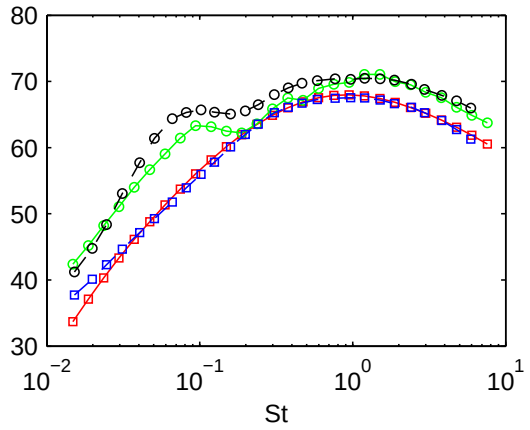

(d) 90° to the jet, reflected side

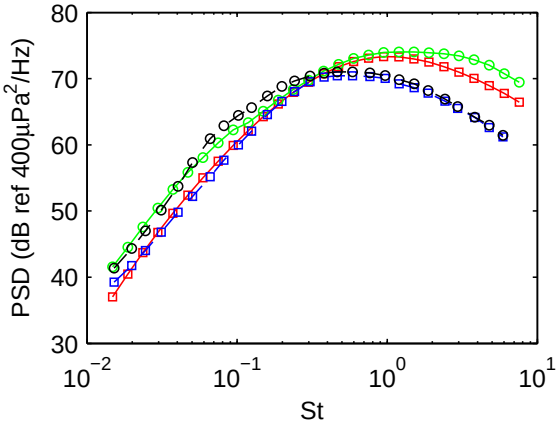

(e) 45° to the jet, reflected side

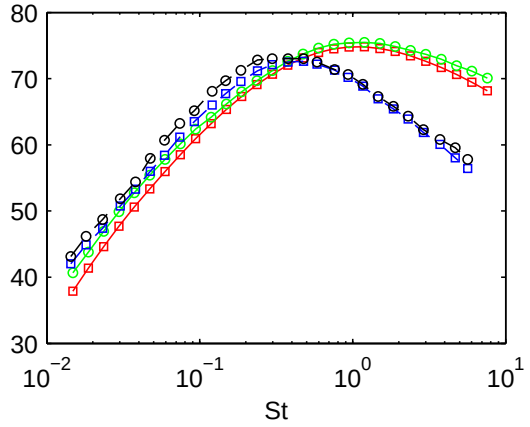

(f) 30° to the jet, reflected side

Figure 5.14: Comparison between experimental measurements and predictions for the far-field PSDs in 1/3 octaves for the installed jet with two source mechanisms.

we will only focus on the installed spectra hereafter. The predicted noise spectra at 90° to the jet on the shielded side is presented in figure 5.14(a). It can be seen that very good agreement at low frequencies was achieved between the predicted and experimental results. A few reasons can be guessed to account for the slight under-prediction near the peak frequencies. First it can be due to the slight error of estimated convection velocity since the scattering is highly sensitive to this quantity. An experimental error is also possible: since the near-field pressure decays exponentially in the radial direction, a small misalignment of 2 mm for example, can cause a PSD change of up to 2 dB. Given the solid shield used in the experiment can easily have a thickness of 2 mm, the error could have been easily introduced. The sound spectra predicted at 45° to the jet are shown in figure 5.14(b). Comparing with figure 5.13(b), where not all the low frequency enhancement is captured, figure 5.14(b) does indeed better agree with the experimental results at low frequencies. Similarly, the sound spectra at 30° is shown in figure 5.14(c), and the agreement with experimental results is good. As mentioned in the preceding subsection, the high frequency sound is not predicted quantitatively due to the mean flow refraction effect, but the qualitative behaviours are successfully captured.

Figures 5.14(d) to 5.14(f) show the comparisons on the reflected side. As can be seen from figure 5.14(d), the agreement is similar to that at 90° on the shielded side. The low frequencies enhancement is dominated by the near-field scattering while the high frequency amplification is due to the pure reflection effect which is correctly captured using Lighthill's quadrupole sources. The agreement at 45° and 30° to the jet is very similar to that on the shielded side. In particular, at 45° the model prediction agrees better with experimental results. The high frequency deviation, as already mentioned for the isolated jet, is caused by the refraction effect of the jet mean flow.

Even though overall good agreement between the model predictions and the experiment results at different observer angles is achieved at low frequencies, it should be noted that the high frequency sound at low observer angles cannot be predicted correctly due to the jet refraction effect. A more accurate model aiming to include this effect is desired, and will form part of our future work.

5.3 Summary

This chapter develops a low-order model to predict installed jet noise. The model starts with the development of a half-plane scattering Green's function. The Green's function is then used to solve the Lighthill's acoustic analogy equation together with a model for the Lighthill's quadrupole sources and the mean flow data obtained by performing RANS calculations. The

additional sound source due to near-field evanescent wave scattering is accounted for by developing a trailing-edge scattering model using Amiet's approach. Therefore, the resulting far-field sound consists of the sum of contributions from two source mechanisms: Lighthill's quadrupole sources and the near-field evanescent wave scattering. Finally, the proposed model is validated against experimental measurements.

It is found that when a solid shield (either a wing or a flat plate) is sufficiently far away from the jet, e.g. when the perpendicular distance between the shield and jet axis H is greater than $2D$, the noise at low frequencies ($St < 0.2$) due to Lighthill's quadrupole sources is hardly affected by the presence of the solid shield. For high frequencies, however, the far-field sound due to quadrupole sources is either efficiently shielded at 90° to the jet on the shielded side or enhanced by around 3 dB at 90° to the jet on the reflected side. The sound from the quadrupole sources is also significantly refracted by the jet mean flow for the $M_0 = 0.5$ jet considered. Thus, at low observer angles where the refraction effect is significant, only qualitatively agreement is achieved.

It is shown that the significant low frequency noise enhancement observed in installed jet experiments is due to the interaction between the near-field evanescent wave and the trailing edge of the solid shield near the jet. The evanescent wave is believed to originate from the Kelvin-Helmholtz instability mechanism. Using the averaged $\overline{U}_c(\omega)$ obtained from LES and the measured near-field evanescent pressure spectrum at the position where the trailing edge of the flat plate would be, the near-field scattering model can successfully predict the noise spectra at various observer angles. The sound due to near-field scattering is however only significant at low frequencies and negligible at high frequencies.

As already mentioned, one limitation of the two-part model developed in this chapter is that it does not account for the jet refraction effect which is significant at low observer angels to the jet for high frequency sound and non-negligible jet Mach numbers. Thus, even though the qualitative behaviour of the far-field sound at high frequencies due to the presence of the flat shield is successfully predicted, quantitative agreement is not achieved except for the spectrum at 90° to the jet on the reflected side. Another limitation is that the solid shield is assumed to be semi-infinite in the proposed model, and thus the effect of its side edges is ignored.

Chapter 6

Experimental Investigation

In this chapter, we carry out an experimental investigation of installed jet noise. One of the two aims of this experimental study is to advance our understanding on the characteristics of installed jet noise and the near-field pressure fluctuations (due to jet instability waves), which would aid in developing noise controlling strategies. The other is to further validate the hybrid prediction model developed in Chapter 5 using the comprehensive experimentally-obtained database. In particular, we have shown that the hybrid model requires the power spectral densities of the near-field pressure fluctuations as an input. In this experiment, we can, therefore, provide such information tailored specifically for this model. In what follows, we first describe the experimental setup, then present the experimental results, before which a comparison with the data from other experiments in the literature is provided. The next section shows the comparison of the experimental results with model predictions, and a short summary of the findings is presented subsequently.

6.1 Experimental setup

The schematic illustration of the experiment is shown in figure 6.1. The experimental rig is placed inside the anechoic chamber at the Engineering Department of the University of Cambridge, as shown in figures 6.2(a) and 6.2(b). The chamber has a lowest operation frequency of around 200 Hz. As shown in figure 6.1, 7 GRAS 46BE microphones are placed at $50D$ to the centre of the jet nozzle, at angles in the range of 30° and 120° to the jet centreline. These microphones have a flat frequency response curve up to 80 kHz. The electrical signals from these 7 microphones are conditioned, amplified, and then digitalized at a sampling frequency of 120 kHz simultaneously using the VIPER data acquisition system from the IMC Ltd. The

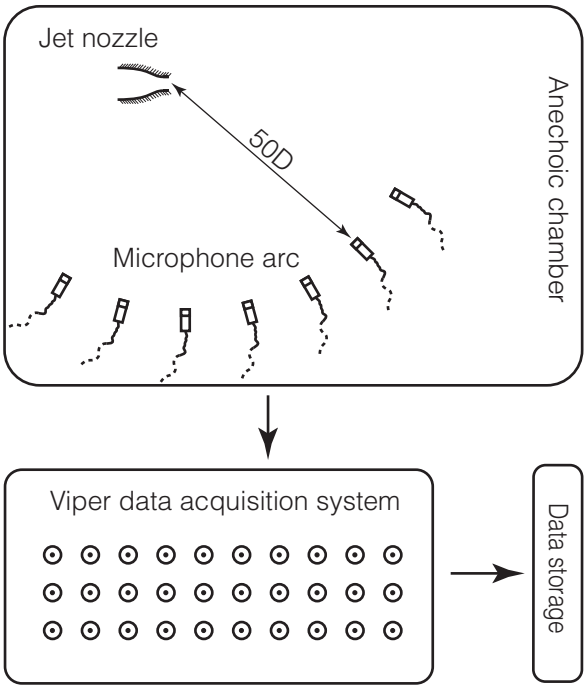

Figure 6.1: Schematic illustration of the experimental setup.

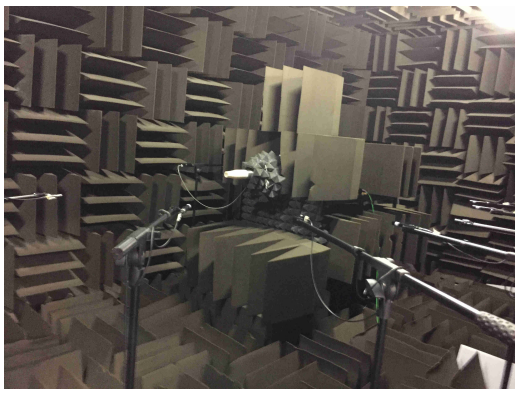

(a) The isolated jet noise experiment setup: microphones are located at 50D to the jet nozzle centre, with observer angle ranging from 30° to 120° to the jet centreline.

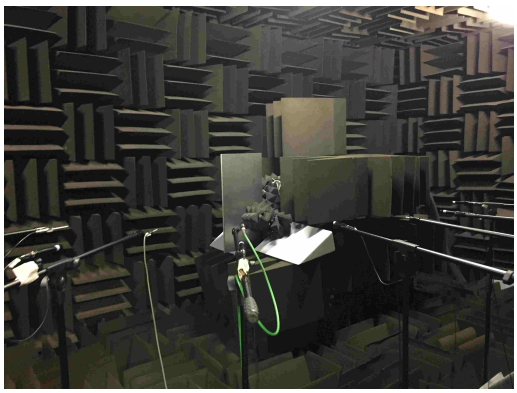

(b) The installed jet noise experiment setup: microphones are located at 50D to the jet nozzle centre on the shielded side, with observer angle ranging from 30° to 120° to the jet. centreline.

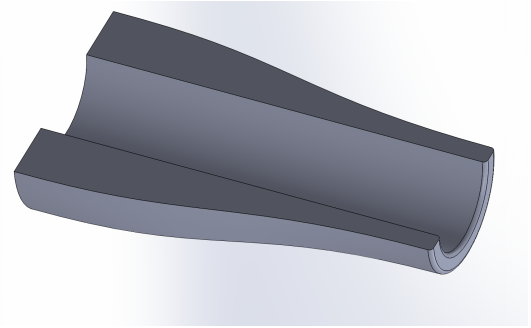

Figure 6.3: The reference round nozzle used in the experiment with a diameter of one inch.

jet Mach number is defined by $M_0 = U_j/c_0$, where U_j is the average jet exit velocity calculated from mass flow rate using an orifice plate device, and c_0, as defined in earlier chapters, is the ambient speed of sound. To facilitate fast and flexible manufacturing, the round nozzle is 3D printed with a resolution of 0.1 mm. It is because of this that the nozzle lip, as can be seen from figure 6.3, has an uncharacteristically large wall thickness. The round nozzle used in this experiment has a diameter of one inch. Data for isolated jet noise is recorded first as reference.

To study the installation effects, a flat plate of $12D \times 24D$ is subsequently placed nearby the jet, as shown in figure 6.2(b). The trailing edge of the plate is at L downstream the jet nozzle, and the separation distance between the jet and the plate is H, as defined in Chapter 2. To obtain a comprehensive database on jet installation effects, both H and L will be varied systematically. The test matrix is shown in table 6.1. As already mentioned, these tests are designed not only to study the effects of varying H and L on installed jet noise, but also to provide a further validation of the developed model in Chapter 5 for a comprehensive array of plate positions.

Test No./Configuration	Nozzle	Mach number	H	L
1	Round	0.5	$3D$	$6D$
2	Round	0.5	$2D$	$6D$
3	Round	0.5	$1.5D$	$6D$
4	Round	0.5	$2D$	$4D$
5	Round	0.5	$1.5D$	$4D$
6	Round	0.5	$1.25D$	$4D$

Table 6.1: Test parameters for studying the effects of varying H and L using a one-inch round nozzle.

Test No./Configuration	Nozzle	Mach number	H	L
7	Round	0.7	$3D$	$6D$
8	Round	0.7	$2D$	$6D$
9	Round	0.7	$1.5D$	$6D$
10	Round	0.7	$2D$	$4D$
11	Round	0.7	$1.5D$	$4D$
12	Round	0.7	$1.25D$	$4D$

Table 6.2: Test parameters for studying the effects of varying Mach numbers on jet installation effects using a one-inch round nozzle.

To study the effects of Mach numbers on installed jet noise, the jet is subsequently operated at a higher Mach number at $M_0 = 0.7$. Similar to the tests at Mach number 0.5, the plate positions are varied systematically. The complete test matrix is shown in table 6.2. One can see that the only difference from that shown table 6.1 is the Mach number. This is designed such that the Mach number effects can be studied at each of the many plate positions.

6.2 Comparison to other experimental data

Before discussing experimental results, it is worth comparing the current experimental data with others' published in the open literature to make sure the experimental rig is set up properly. It is sufficient to only compare the reference isolated jet noise spectra. We choose to compare with the data obtained by Tanna (Tanna, 1977) for a cold $M_0 = 0.5$ jet. The nozzle used in Tanna's experiment had a diameter of 2 inches, therefore implying a Reynolds number twice as large as that in this experiment. However, since both Reynolds number are in the order of $10^5 \sim 10^6$, one can expect the difference of jet noise spectra caused by different Reynolds numbers between the two experiments to be insignificant. Comparison of the noise spectra at 90° and 30° to the jet axis are shown in figures 6.4(a) and 6.4(b), respectively. As can be seen, the far-field sound spectra at 90° agree with each other well in their spectral shapes and absolute magnitudes. There is, however, a small deviation at high frequencies. This might be due to the different nozzle shapes and inlet flow conditions. The comparison for the spectra at 30° to the jet axis shows a slightly better agreement, in particular at high frequencies. Considering the many inevitable differences between the two experiments, such an agreement is good enough to show that the experiment is set up properly and the measurement is reliable.

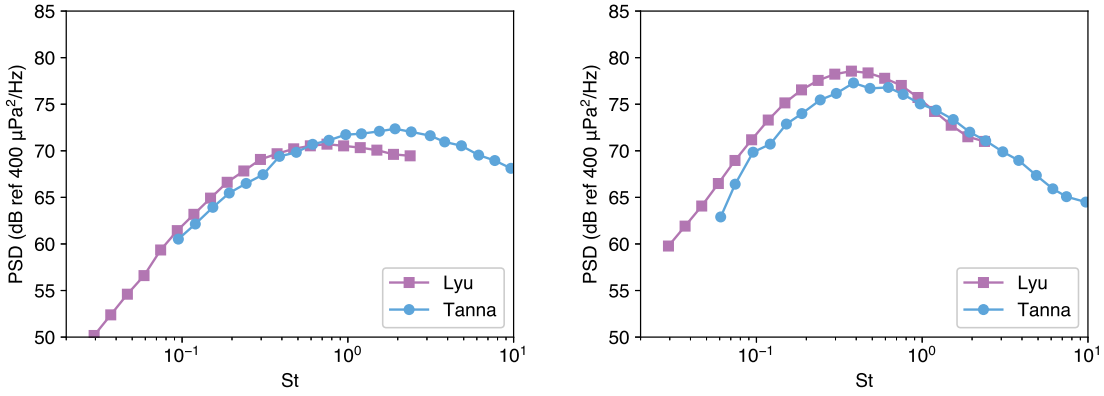

(a) $\theta = 90°$ (b) $\theta = 30°$

Figure 6.4: Comparison of isolated jet noise spectra in $1/3$ octaves with Tanna's. The microphones are placed at $50D$ from the centre of nozzle exit.

6.3 Jet noise spectra

In this section, we present the jet noise spectra at different observer angles when the flat plate is placed at different locations. To facilitate a direct comparison, both isolated and installed jet noise spectra for various plate positions (table 6.1) are shown in the same figures.

6.3.1 Mach number 0.5 jet

We present the results for $M_0 = 0.5$ first. Far-field noise spectra on the shielded and reflected sides are shown in figures 6.5 and 6.6, respectively. Figure 6.5(a-c) shows the far-field noise power spectra on the shielded side when the plate's edge is at $6D$ downstream the jet nozzle but at different radial positions. Both isolated and installed jet noise spectra are shown. In figure 6.5(a), one can clearly see that the plate enhances the lower-frequency jet noise by up to 10 dB. This noise enhancement is most pronounced at an angle close to 90° to the jet centre line. The noise enhancement at 30°, however, is virtually negligible. This is consistent with the earlier findings (Head and Fisher, 1976; Wang, 1980; Mead and Strange, 1998; Bondarenko et al., 2012; Brown, 2013; Amiet, 1976b; Roger and Moreau, 2005) reviewed in Chapter 2 and our edge-scattering mechanism proposed in Chapter 5 (at low frequencies, the scattered sound has a dipolar, rather than a cardioid directivity pattern). In the intermediate- and high-frequency range, jet noise is effectively shielded by the flat plate at angles close to 90° to the jet axis, while these shielding effects diminish at lower observer angles. Figure 6.5(b) shows the spectra when the plate is at a closer distance to the jet at $H = 2D$. It can be seen that the noise

enhancement at low frequencies is now more pronounced, increasing to more than 15 dB. Also, it can be observed that the noise increase also occurs in the intermediate frequency range at high observer angles. An observable noise increase occurs at 30° to the jet axis as well. In the high-frequency regime, one can see that the plate still serves as an effective noise shield at high observer angles, but little has changed for the shielding effects compared to figure 6.5(a). Moving the plate closer to $H = 1.5D$, as shown in figure 6.5(c), results in an even stronger noise enhancement. The peak noise increase is now up to 20 dB at 90°. At such a close distance to the plate, jet noise at 90° is larger than that at 30°. The frequency range of noise increase becomes even wider, leading to louder noise in the intermediate range. In figure 6.5(a-c), it is shown that enhanced noise spectra at low frequencies exhibit a clear oscillation pattern. This oscillation is more marked when the plate is closer to the jet.

The measured noise spectra when the plate is at $L = 4D$ are shown in figure 6.5(d-f). The observer is still on the shielded side of the plate. Figure 6.5(d) presents the results when $H = 2D$. At such a distance, the noise amplification is around 8 dB with an observable increase up to 2 kHz. Noise increase is, as expected, occurring only at high observer angles. At high frequencies, the noise is reduced by around 3 dB by the shielding effects. Moving the plate closer to the jet clearly causes a stronger noise increase, as shown in figure 6.5(e), where $H = 1.5D$. At such a distance, the maximum noise amplification observed is around 12 dB at 90° to the jet centre line. However, there is little noise increase at 30°. When the plate is placed at $H = 1.25D$, the tendency of stronger noise enhancement at a closer distance between the plate and the jet continues. A noise increase up to 16 dB is observed. The affected frequency range continues to be wider. The shielding effects remain roughly the same.

The effects of varying H on the installed spectra on the shielded side are clearly demonstrated by comparing figures 6.5(a) to 6.5(c), and figures 6.5(d) to 6.5(f). The effects of varying L at fixed H can be revealed by comparing figures 6.5(b) and 6.5(d), and figures 6.5(c) and 6.5(e). When the plate is placed at $H = 2D$, the noise amplification at $L = 6D$ is clearly much more pronounced than that at $L = 4D$, with the former one being up to 15 dB and the latter one being up to 8 dB. The affected frequency range remains roughly the same. However, it can be seen that the shielding effects are much more effective when the plate is located further downstream. Another difference is the observable noise enhancement at $L = 6D$ but negligible noise increase at $L = 4D$ at 30° to the jet centre line. When the plate is placed at $H = 1.5D$, the same tendency remains, while both configurations result in louder noise because of a closer distance to the jet.

Experimental results measured on the other side of the plate, i.e. the reflected side, are

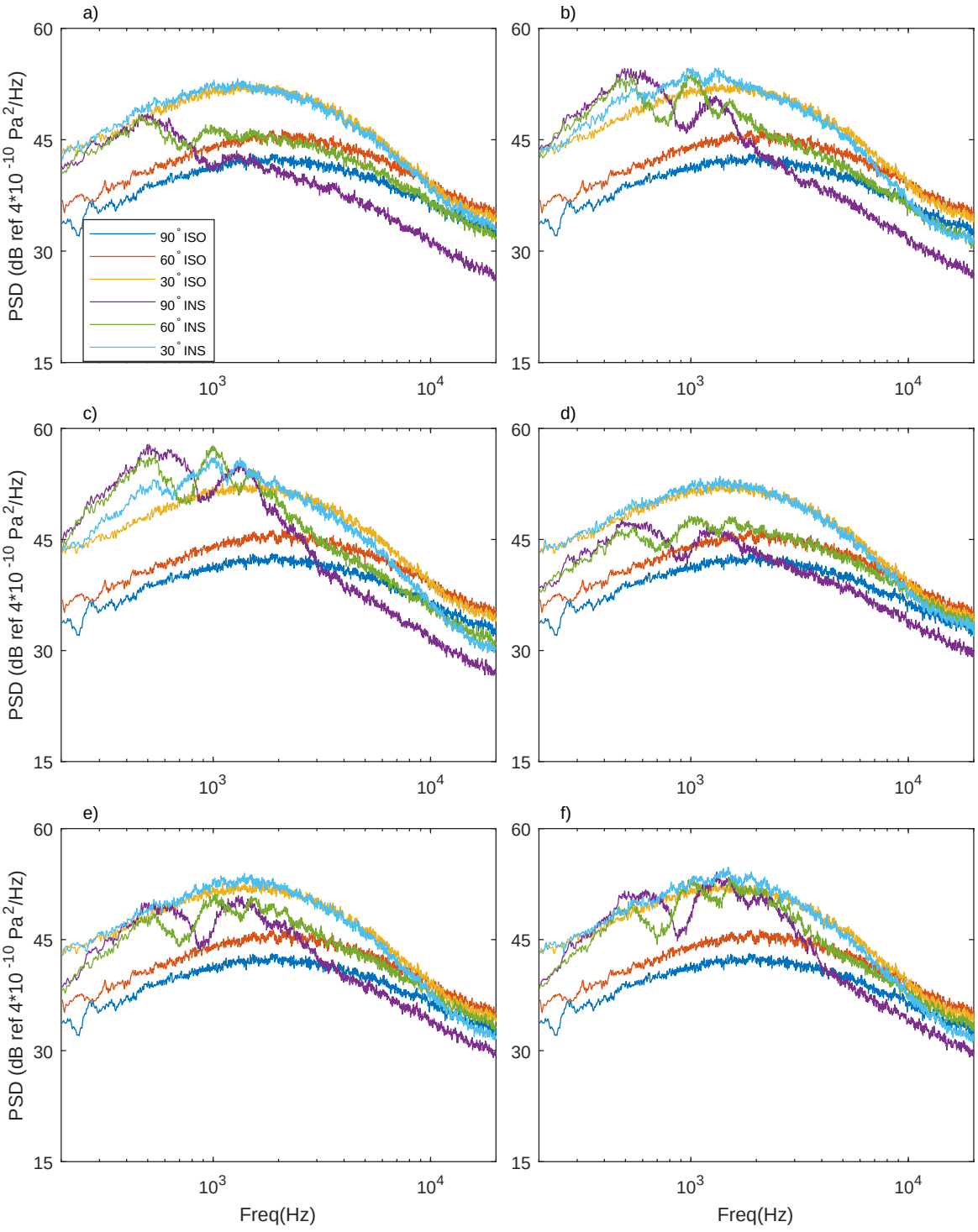

Figure 6.5: Isolated and installed noise spectra of a Mach number 0.5 jet on the shielded side for various plate positions: (a) $L = 6D,\ H = 3D$; (b) $L = 6D,\ H = 2D$; (c) $L = 6D,\ H = 1.5D$; (d) $L = 4D,\ H = 2D$; (e) $L = 4D,\ H = 1.5D$; (e) $L = 4D,\ H = 1.25D$.

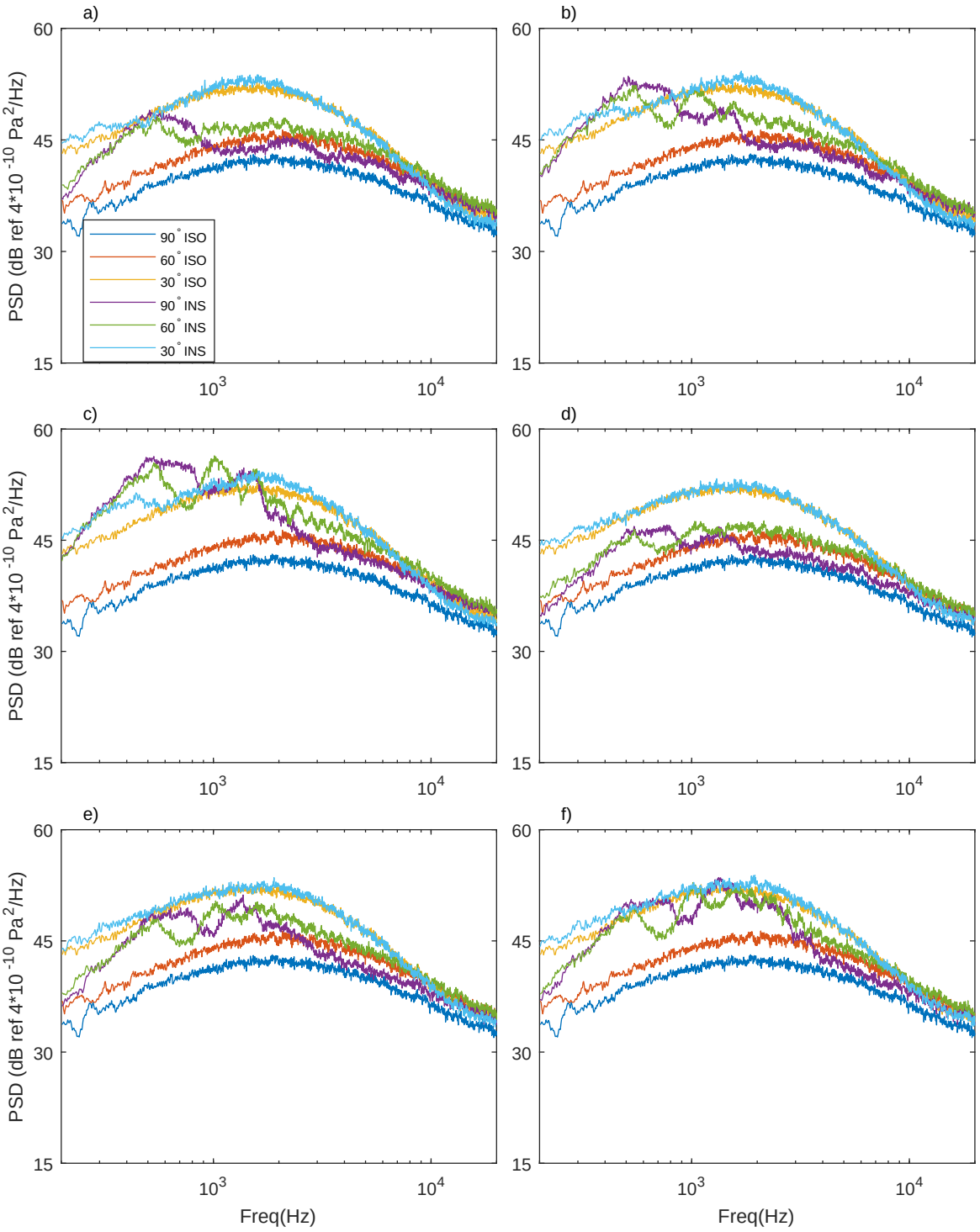

Figure 6.6: Isolated and installed noise spectra of a Mach number 0.5 jet on the reflected side for various plate positions: (a) $L = 6D,\ H = 3D$; (b) $L = 6D,\ H = 2D$; (c) $L = 6D,\ H = 1.5D$; (d) $L = 4D,\ H = 2D$; (e) $L = 4D,\ H = 1.5D$; (e) $L = 4D,\ H = 1.25D$.

presented in figure 6.6. Figure 6.6(a-f) shows the noise spectra when the plate is at the same positions as those shown in figure 6.5(a-f). At low frequencies, a significant noise increase is observed, resembling the behaviour on the shielded side, see figures 6.6(a) to 6.6(f). Moreover, comparing figures 6.6(a) to 6.6(c) (and figures 6.6(d) to 6.6(f)) reveals the same behaviour of louder noise for smaller H, when L is fixed. The enhanced sound spectra appear to be nearly identical to those shown in figure 6.6. However, a careful examination shows they do not. The most important difference occurs around the lowest frequencies. For example, comparing figures 6.5(a) and 6.6(a) indicates that the noise increase is somewhat less pronounced at 90° and 60°. On first thought, this would invalidate the proposed near-field scattering mechanism, which entails a perfectly symmetric noise radiation across the plate. However, a revisiting to

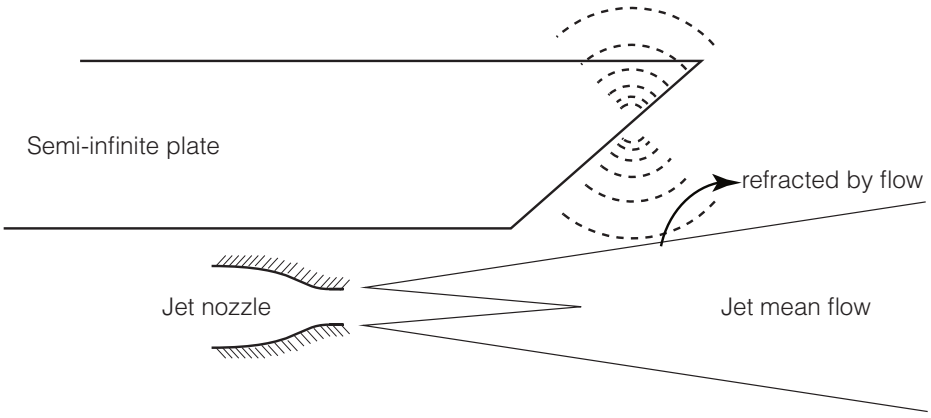

Figure 6.7: The schematic diagram illustrating the refraction effects of the jet mean flow on the reflected side of the flat plate.

the realistic problem suggests the cause to be the refraction effects of the jet mean flow on the reflected side. To show this more clearly, a schematic diagram is presented in figure 6.7. As can be seen, the scattered sound originates near the edge and propagates both above and below the edge. However, the sound has to pass through the jet plume in order to reach an observer placed in the far-field on the reflected side. This is different on the other side, where no jet plume is present. Therefore, the discrepancies between the observed spectra on both sides are due to the jet refraction effects. Decreasing the value of L, as can be seen by comparing figures 6.6(b) and 6.6(d) (or figures 6.6(c) and 6.6(e)), causes the noise increase to be less significant.

However, the installation effects in the high-frequency regime are considerably different from those on the shielded side. As suggested by its name, noise increase is observed for spectra on the reflected side due to sound reflection at high frequencies by the plate. Figure 6.6(a) shows that the high-frequency noise increase is most pronounced at 90°, and less so at small

observer angles (small θ). Comparing figures 6.6(a) to 6.6(c) (and figures 6.6(d) to 6.6(e)), one can see that changing H while L is fixed does not significantly change this reflection-caused noise increase at all observer angles, in contrast to the low-frequency noise enhancement. On the other hand, shortening L causes high-frequency reflection to be less notable. For example, one can find, by comparing figures 6.6(b) and 6.6(d), that noise increase at high frequencies is up to 3 dB when $L = 6D$ while only a half of it is achieved when $L = 4D$ (at 90°).

In summary, installed jets exhibit a significant noise increase at low frequencies compared to isolated jets. The noise spectra have slightly non-symmetric dipolar directivity patterns due to the asymmetry caused by jet refraction. At high frequencies, jet noise is noticeably suppressed due to the plate shielding effects on the shielded side and slightly (e.g. around $2 - 3$ dB) enhanced on the reflected side. Decreasing H while L is fixed results in a stronger noise increase at low frequencies. At high frequencies, on the other hand, it causes little change to both the shielding and reflecting effects. Decreasing L while H is kept constant results in less significant noise increase at low frequencies. In addition, at high frequencies, both the shielding and reflecting effects become noticeably less effective.

6.3.2 Mach number 0.7 jet

Experimentally measured installed jet noise spectra for $M_0 = 0.7$ are presented in figures 6.8 and 6.9. Since jet noise power scales as the eighth power of jet Mach number (Lighthill, 1952), one can see that considerably larger noise spectra are observed compared to those shown in figure 6.5 and 6.6. Nevertheless, figure 6.8 is qualitatively similar to figure 6.9 in nearly all aspects. For example, significant noise increase for installed jets occurs only at low frequencies, placing the plate closer to the jet (decreasing the value of H while L is fixed) results in a stronger noise increase at low frequencies, decreasing L while H is kept constant results in less significant noise increase at low frequencies, etc. A more detailed discussion on these characteristics is summarised at the end of the preceding section.

However, it is interesting to note the differences of noise spectra between $M_0 = 0.5$ and $M_0 = 0.7$ jets. One of the most striking differences is that the low-frequency noise enhancement is less significant for the $M_0 = 0.7$ jets when the plate is placed at the same positions. For instance, the maximum noise increase shown in figure 6.5(c) is around 20 dB while in figure 6.8(c) around 15 dB. The same conclusions can be reached by comparing other pairs of spectra. This is believed to be due to the dependence of the installed jet noise on jet Mach numbers. We have mentioned in Chapter 2 that the intensity of installed jet noise scales as the sixth power of the jet Mach number, while the isolated jet noise power scales as the eighth.

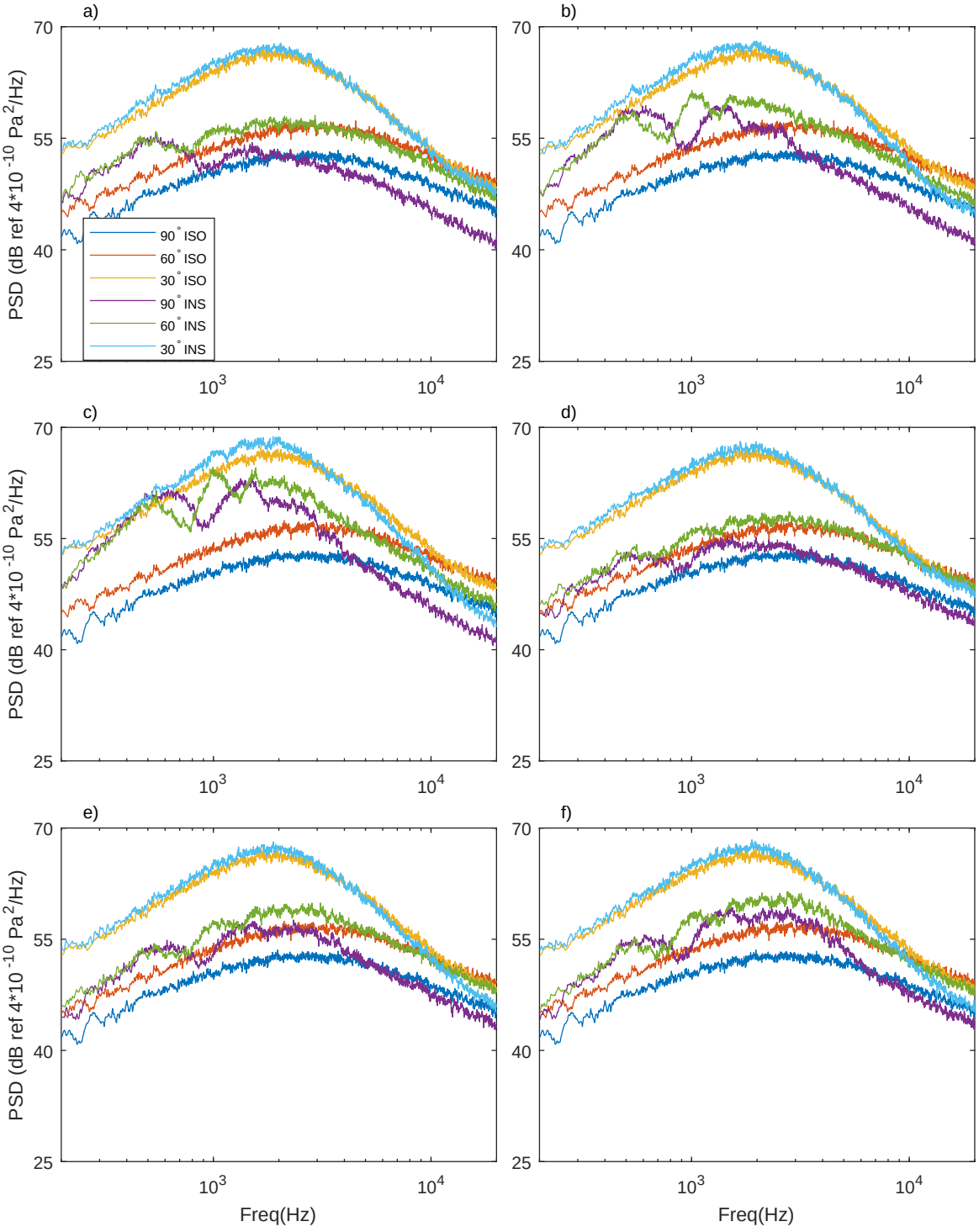

Figure 6.8: Isolated and installed noise spectra of a Mach number 0.7 jet on the shielded side for various plate positions: (a) $L = 6D,\ H = 3D$; (b) $L = 6D,\ H = 2D$; (c) $L = 6D,\ H = 1.5D$; (d) $L = 4D,\ H = 2D$; (e) $L = 4D,\ H = 1.5D$; (e) $L = 4D,\ H = 1.25D$.

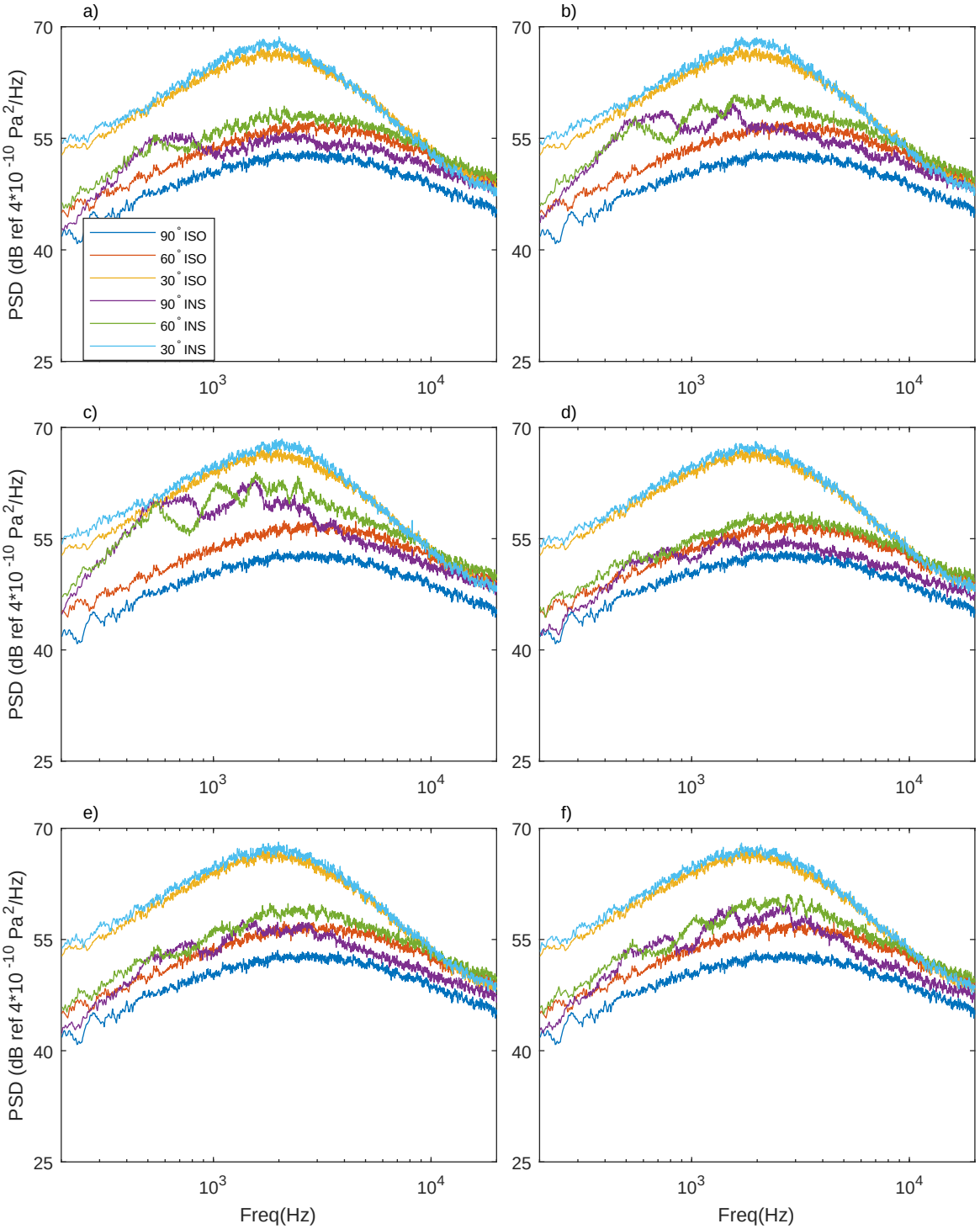

Figure 6.9: Isolated and installed noise spectra of a Mach number 0.7 jet on the reflected side for various plate positions: (a) $L = 6D,\ H = 3D$; (b) $L = 6D,\ H = 2D$; (c) $L = 6D,\ H = 1.5D$; (d) $L = 4D,\ H = 2D$; (e) $L = 4D,\ H = 1.5D$; (e) $L = 4D,\ H = 1.25D$.

Therefore, when the Mach number increases, isolated jet noise power increases more quickly, hence narrowing the relative difference between the installed and isolated noise spectra. This trend is more evident by contrasting figures 6.5(f) and 6.8(f).

6.4 Comparison with prediction model

Since we have obtained a comprehensive set of experimental data on installed jet noise for different plate positions, we can compare them to the predictions of the hybrid model developed in Chapter 5. In particular, the innovative instability-wave-scattering model can be properly validated. To do so, the PSD of the near-field pressure fluctuations must be measured and used as an input to the model.

6.4.1 The near-field pressure

Figure 6.10(a) shows the power spectral densities of the near-field pressure at $z = 6D$ but at various radial positions. It should be noted that these spectra are obtained using one micro-

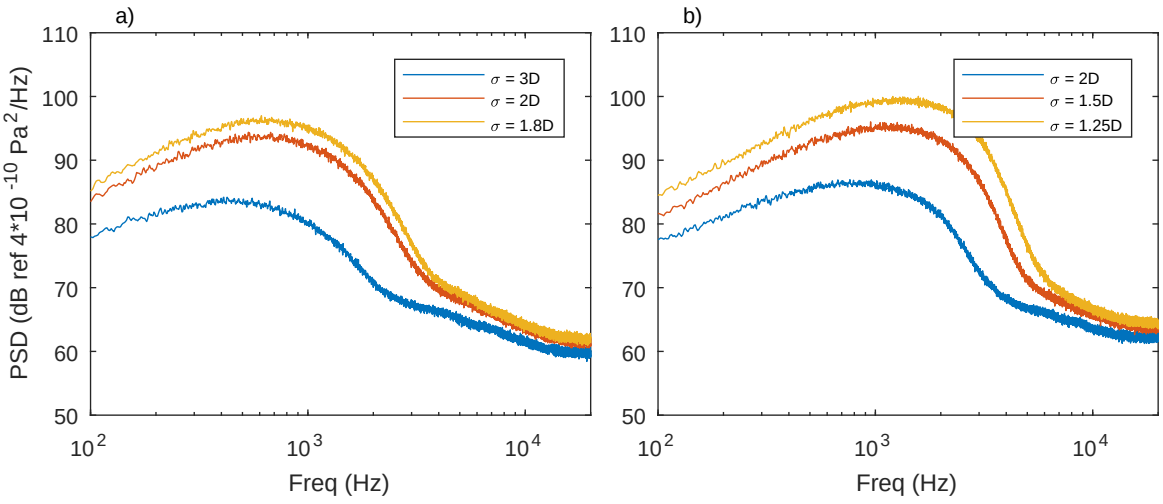

Figure 6.10: The power spectral densities of the near-field pressure at various radial positions but at two fixed streamwise locations: a) $z = 6D$; b) $z = 4D$.

phone placed at a specific azimuthal angle (not using a microphone arc). Therefore, they are different from the modal pressure spectra shown in Chapter 5. However, as noted in Chapter 5, when the frequencies of interest are low, the sound due to near-field scattering can be calculated by using the PSD of the near-field pressure at a specific point (see equation 5.48). From figure 6.10(a), it can be seen that the near-field pressure fluctuation decays quickly as the radial

coordinate σ increases in the low and intermediate frequency regime. For example, a decrease of up to 15 dB is observed from $\sigma = 2D$ to $3D$. However, in the high-frequency regime, little change occurs. This is because acoustic perturbation dominates the near-field pressure fluctuation at high frequencies, as demonstrated by figure 5.8 in Chapter 5. Also it can be observed that the spectral decay (due to moving the microphone away from the jet) gradually increases as the frequency increases, compatible with the behaviour of the Modified Bessel functions of the second kind (see equation 5.16 for example).

Figure 6.10(b) shows the spectra at $z = 4D$. Comparing with figure 6.10(a), two distinctions can be readily observed. Firstly, the spectra at $z = 4D$ but at the same radial position have smaller amplitudes, especially at low frequencies. This is consistent with the convecting growing behaviour of jet instability waves (Crow and Champagne, 1971; Michalke, 1971). It is also consistent with the observation that the installed jet noise is louder when the plate is placed further downstream (but at the same radial positions, see the discussion on this in Section 6.3). Secondly, spectra at $z = 4D$ have higher peak frequencies. This is known due to the earlier saturation of instability waves at high frequencies (Crow and Champagne, 1971; Michalke, 1984).

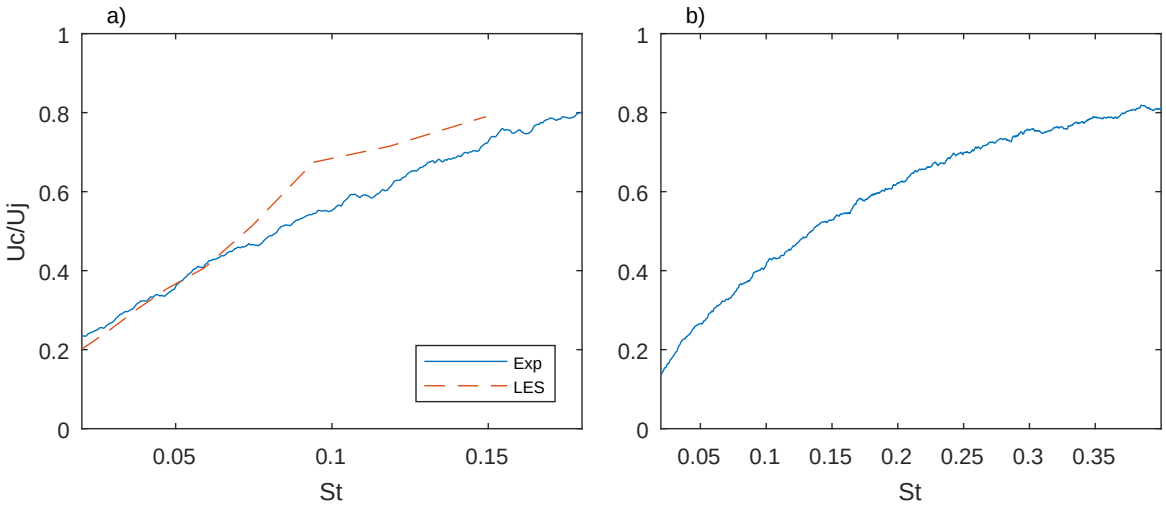

Figure 6.11: The convection velocities obtained from examining the radial decay rates of the near-field pressure PSDs at two different streamwise locations: a) $z = 6D$; b) $z = 4D$.

The hybrid model developed in Chapter 5 requires the spectral strengths and the frequency-dependent convection velocity of the near-field instability waves as inputs. In Chapter 5, this is calculated from analysing an LES database. A similar analysis can be performed with the experimental data if we measure the near-field pressure using a microphone arc, such as the one used by Tinney and Jordan (2008). But for simplicity, instead of using the modal spectra,

we use the overall spectra measured at one point. As discussed in Chapter 5, this is permissible, since the decay rates of the zero- and first- order instability waves do not differ from each other significantly, in particular at low frequencies. The convection velocity can also be estimated by making use of this fact, i.e. we assume the point spectra decay at the same rate of the zeroth-order instability waves. The convection velocities obtained by examining the decay rates of the spectra shown in figure 6.10 are plotted in figure 6.11. Only low-frequency results are shown because of the dominance of acoustic fluctuations at high frequencies. The result for $z = 6D$ is shown and compared with that obtained from LES in figure 6.11(a). Very good agreement is achieved. This not only shows that the convection velocity is indeed frequency-dependent, but also provides another piece of evidence for having an accurate LES database. Figure 6.11(b) presents the convection velocity for the instability waves at around $z = 4D$. Though the two curves in figures 6.11(a) and 6.11(b) look qualitatively similar to each other, they are not strictly identical. This is expected, since the mean flows at different streamwise directions are different, so are the characteristics of jet instability waves.

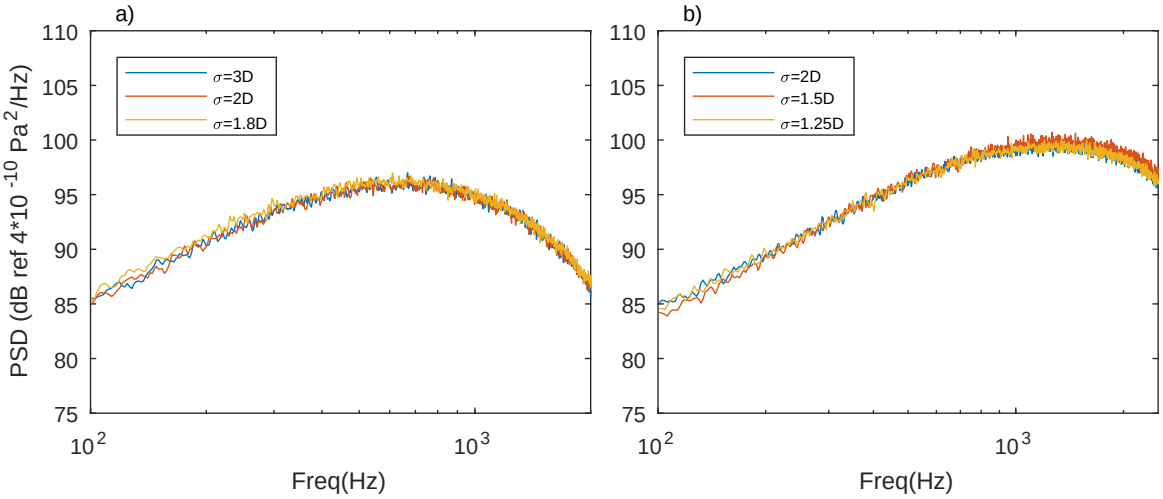

Figure 6.12: The collapsed power spectral densities of the near-field pressure using obtained convection velocities at various streamwise locations: a) $z = 6D$; b) $z = 4D$.

Using the convection velocities obtained in figure 6.11, the PSDs at various radial locations (but the same streamwise location) can be successfully collapsed, as can be seen from figure 6.12. Note that the shown frequency range is from 100 Hz to 2500 Hz, corresponding to the frequency range shown in figure 6.11. Excellent agreement is achieved for spectra at both $z = 6D$ and $z = 4D$, though there is slight disagreement only at around the highest frequency for the spectra $z = 4D$. This is somewhat expected since we assume different modal instability waves to decay at the same rate (at the rate determined by the zeroth-order Modified

Bessel function of the second kind, see equation 5.16 for example). But high-order instability waves are more likely to exist at upstream locations (Tinney et al., 2008a).

6.4.2 Validate against the hybrid prediction model

Equipped with the flow data from similar RANS simulations to that described in Chapter 4, the frequency-dependent convection velocity and the near-field pressure PSDs from experiment, the hybrid model can be evaluated readily. The predictions are compared with experimentally measured PSDs at various observer angles and for various plate positions. In the rest of this section, comparisons are shown for six observer angles for each plate position, i.e. 90°, 60° and 30° to the jet axis on both the shielded and reflected sides of the flat plate.

For plate position at $L = 6D$

Figure 6.13 shows the comparison of the isolated and installed jet noise spectra when the plate's trailing edge is at $L = 6D$ and $H = 3D$. We must emphasise that the isolated jet noise spectra are predicted using the Lighthill's acoustic analogy with a free-field Green's function (see Chapter 5), rather than the generalised acoustic analogy (hence CONJURE) developed in Chapter 4. We do so in order to be consistent with the hybrid model for installed jet noise prediction and also to quantify the discrepancies caused by the jet refraction effects. We discuss the results on the shielded side first (figure 6.13(a-c)). The agreement between the isolated spectra at $\theta = 90°$ (figure 6.13(a)) is very good, apart from a slight over-prediction at high frequencies. The installed spectra are much more interesting. At such a distance to the jet, the maximum noise enhancement at low frequencies caused by the scattering of instability waves is around 10 dB. This is well captured by the model. At high frequencies, noise is effectively shielded by the plate. This is qualitatively captured by the prediction model (though the predicted amplitude is quite close to experimental results). This is because, as we mentioned a few times in Chapter 5, jet refraction effects are not included. Figure 6.13(b) shows the comparison for $\theta = 60°$. The prediction for the isolated spectrum starts to deviate from the experimental result at high frequencies due to the lack of account for refraction effects, though at low frequencies the agreement is still acceptable. For the installed noise spectra, as discussed in the preceding section, weaker noise enhancement and shielding effects are observed experimentally. The model can successfully capture this and agrees with the experimental results at low frequencies. The trend of weaker shielding effects is also exhibited by the model. The spectra comparison at $\theta = 30°$ is more interesting. One can see that at such a low observer angle, jet refraction is significant, even for low frequencies. Therefore, the deviation between the experiment the and

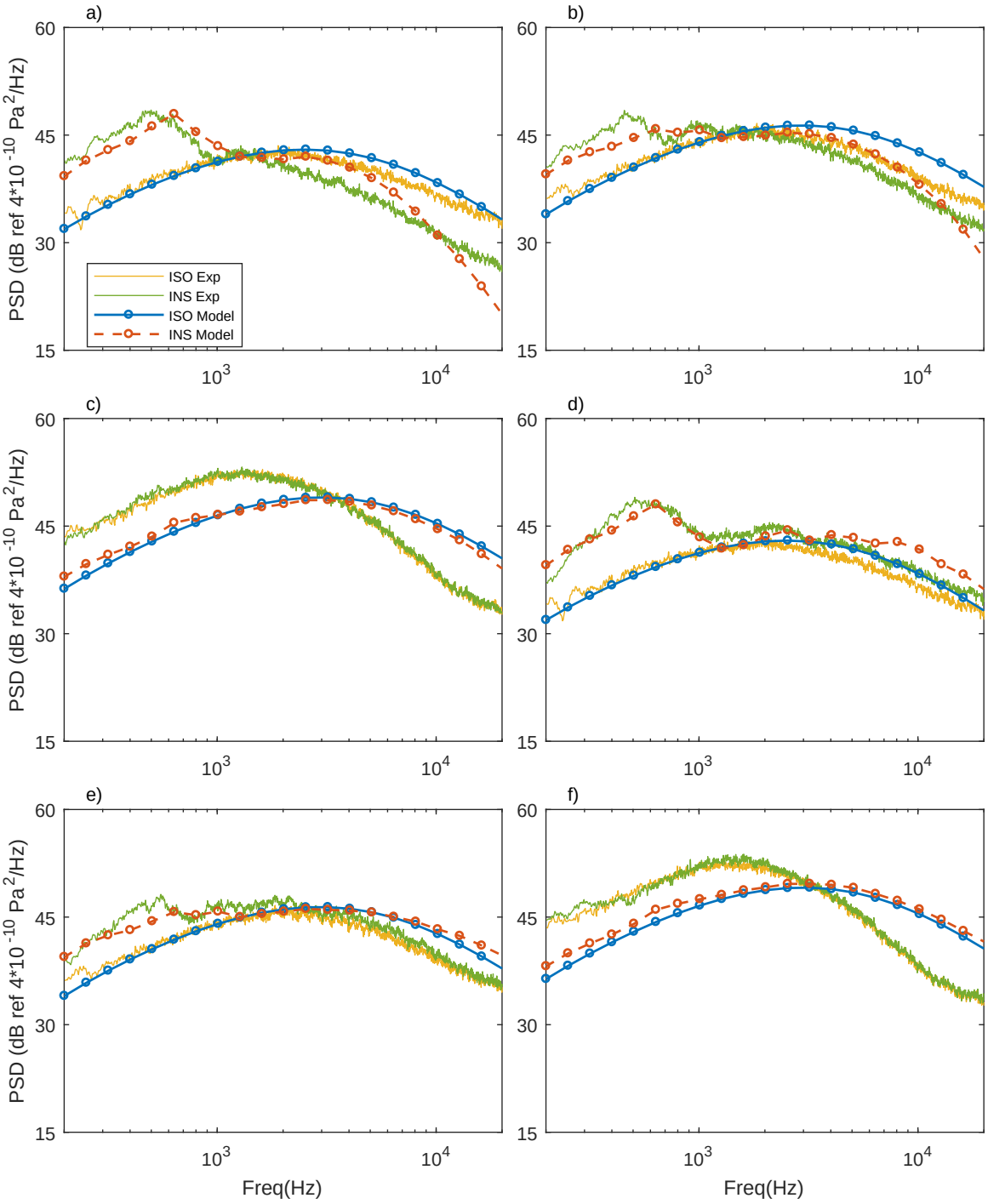

Figure 6.13: Comparison of the predicted isolated and installed noise spectra with experimental results: a) $\theta = 90°$, shielded side; b) $\theta = 60°$, shielded side; c) $\theta = 30°$, shielded side; d) $\theta = 90°$, reflected side; e) $\theta = 60°$, reflected side; f) $\theta = 30°$, reflected side; the flat plate's trailing edge is at $L = 6D$ and $H = 3D$.

prediction for isolated noise spectra can be as large as 5 dB. However, the fact that there is little noise enhancement at low frequencies and little noise suppression at high frequencies is captured remarkably well. In other words, the model successfully captures the physics of jet installation, although the absolute values of the predicted spectra are affected by the refraction effects. This indicates that if the refraction effects had been properly accounted for, the agreement for installed jet noise spectra would have been excellent.

Noise comparison on the reflected side is shown in figure 6.13(d-f). Since the isolated jet noise spectra are identical to those on the other side of the plate, we only need to focus on the installed spectra. Figure 6.13(d) shows the results at 90° to the jet axis. Excellent agreement at this observer angle is achieved since there are no (little) refraction effects. At low frequencies, the prediction is identical (symmetry) to that on the other side of the plate and the agreement continues to be good. At high frequencies, the noise increase of around 3 dB is successfully predicted by the model. The slight over-prediction for the high-frequency installed spectrum is apparently caused by the slight over-prediction of the isolated spectrum. Comparison of noise spectra at 60° to jet axis is shown in figure 6.13(e). As discussed above, the same level of agreement as on the other side of plate is achieved at low frequencies. However, we see that the predicted spectrum gradually deviates from the experimental spectrum at high frequencies due to the refraction effects. The tendency of weaker noise increase due to reflection at lower observer angles is captured. Figure 6.13(f) shows the comparison at 30° to the jet axis. This is very similar to the results on the other side of the plate, for the same reasons.

Comparison of the spectra when the plate's trailing edge is at $L = 6D$ and $H = 2D$ is shown in figure 6.14. Again, identical isolated jet noise spectra suggest that we only need to discuss installed spectra. Figure 6.14(a) shows excellent agreement between the experimental and predicted spectra at $\theta = 90°$. The low-frequency noise intensification is much more pronounced at such a plate position and is predicted remarkably well. Even the high-frequency shielding effects are predicted reasonably well. Note that there are small oscillations in the experimental spectrum, which are not captured very well by the model. One can show that this oscillation is due to the finite chord length of the flat plate. The model makes use many approximations in order to reach a simplified formula, which might be the reason for not capturing these low-frequency oscillations. However, the predicted spectrum does follow the mean experimental counterpart very closely. Figure 6.14(b) shows the results for an observer at $\theta = 60°$. Excellent agreement continues to be achieved at low frequencies, and the high-frequency prediction sees discrepancies due to refraction effects. Figure 6.14(c) deserves a detailed explanation. At first glance it appears that the prediction yields a much higher noise

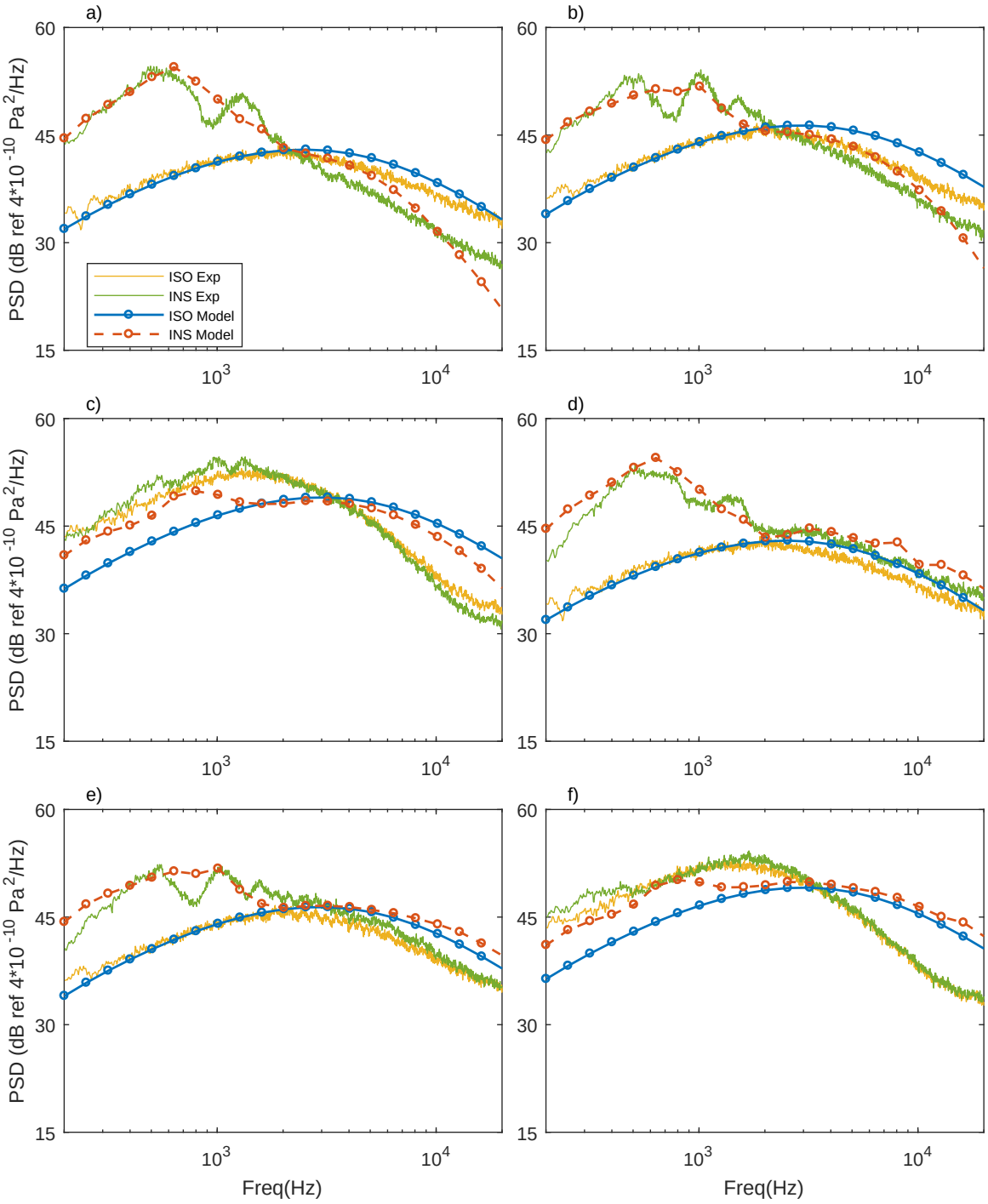

Figure 6.14: Comparison of the predicted isolated and installed noise spectra with experimental results: a) $\theta = 90°$, shielded side; b) $\theta = 60°$, shielded side; c) $\theta = 30°$, shielded side; d) $\theta = 90°$, reflected side; e) $\theta = 60°$, reflected side; f) $\theta = 30°$, reflected side; the flat plate's trailing edge is at $L = 6D$ and $H = 2D$.

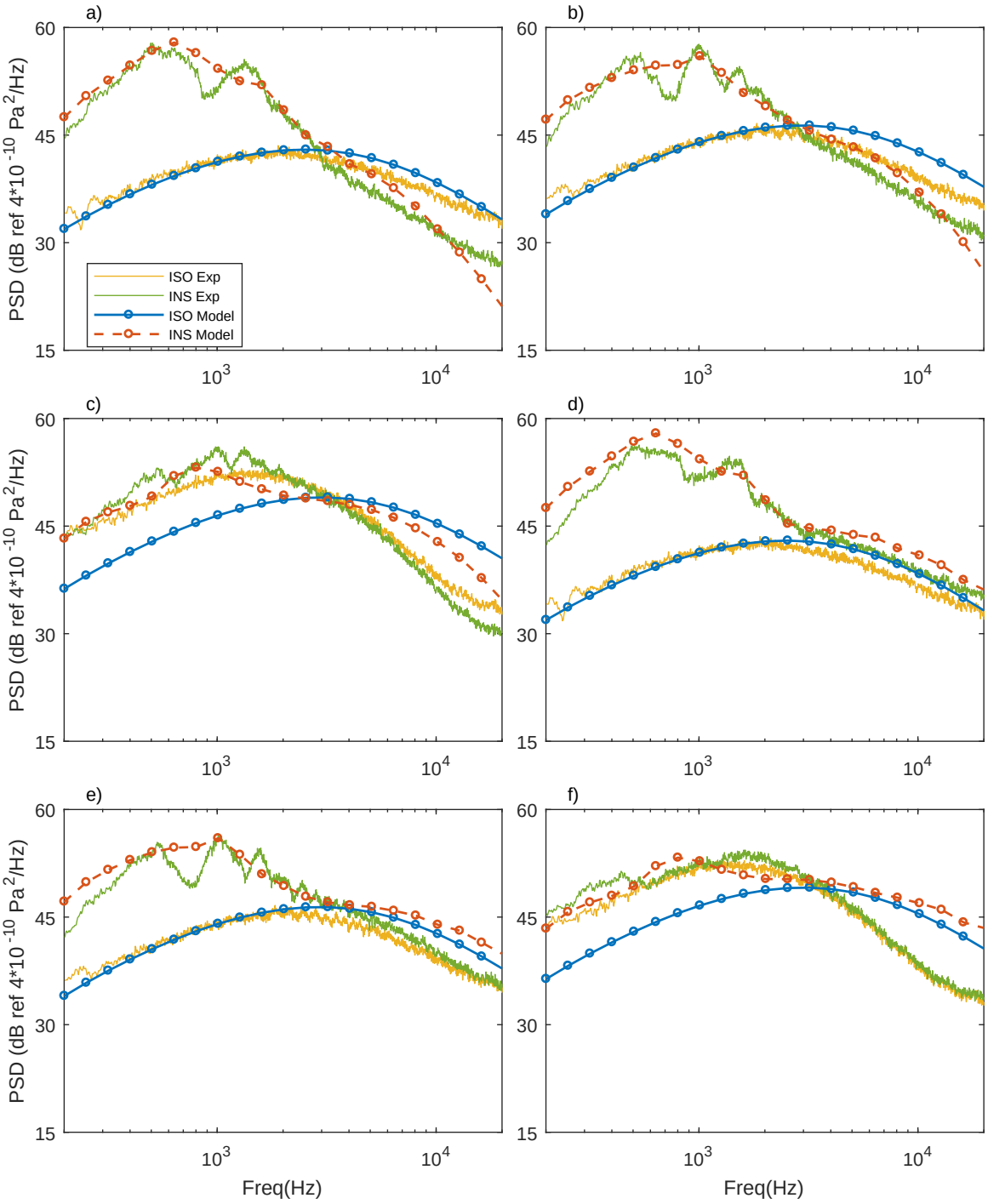

Figure 6.15: Comparison of the predicted isolated and installed noise spectra with experimental results: a) $\theta = 90°$, shielded side; b) $\theta = 60°$, shielded side; c) $\theta = 30°$, shielded side; d) $\theta = 90°$, reflected side; e) $\theta = 60°$, reflected side; f) $\theta = 30°$, reflected side; the flat plate's trailing edge is at $L = 6D$ and $H = 1.5D$.

enhancement at low frequencies, which does not agree with experimental observations. However, one should bear in mind that the total power spectral density Φ is the sum of Φ_Q and Φ_N. Therefore, a lower value of Φ_Q (which is exhibited by the much lower value of the isolated spectrum which is nearly identical to Φ_Q at low frequencies, see Chapter 5) would contribute little to Φ and the total spectrum Φ is nearly solely determined by the large value of Φ_N. Hence Φ would be much larger than Φ_Q (hence the isolated spectrum, which explains the significant noise augmentation predicted in figure 6.14(c)). However, if Φ_Q had been correctly predicted to be of large values, the contribution from Φ_N would have been much less pronounced, and one would have expected only a slight noise increase. Therefore, the seemingly discrepancy at low frequencies is due to the inaccurate prediction of the isolated jet noise spectrum and the near-field scattering model works remarkably well (we can see evidence of this if we add the Φ_N to the isolated spectra measured in the experiment).

The comparison on the reflected side is shown in figure 6.14(d-f). Excellent agreement is observed at 90° to the jet axis (see figure 6.14(d)). The less good agreement at the lowest frequencies is caused, as mentioned in the preceding section, by the refraction of the reflected sound by the jet, which is not accounted for in this model. High-frequency agreement is nearly identical to that shown in figure 6.13(d). 6.13(e) shows the results when the observer is at 60° to the jet axis. Apart from the larger noise intensification, which is correctly captured by the model, it is again similar to the comparison shown in figure 6.13(e). So are the results shown in figure 6.14(f).

When the plate is moved closer to the jet at $H = 1.5D$, a significant noise increase of up to 20 dB is achieved. The comparison of the model prediction with experimental results at such a close distance is shown in figure 6.15. The hybrid model, especially the instability-wave-scattering model predicts the noise enhancements at all angles remarkably well. Note again that the seemingly over-prediction of the low-frequency enhancement in figures 6.15(c) and 6.15(f) is caused by the inaccurate prediction of the isolated spectra.

For plate position at $L = 4D$

Comparison of the isolated and installed jet noise spectra when $L = 4D$ and $H = 2D$ is shown in figure 6.16. As already noted in the section discussing the experimental results, moving the plate towards jet nozzle causes the noise increase at low frequencies to be less significant. Results are again shown for both the shielded (figure 6.16(a-c)) and reflected sides (figure 6.16(d-f)). At $\theta = 90°$ on the shielded side, a noise increase of up to 8 dB is found. The prediction yields a noise increase of around 5 dB, slightly below the experimental results. It is suggested

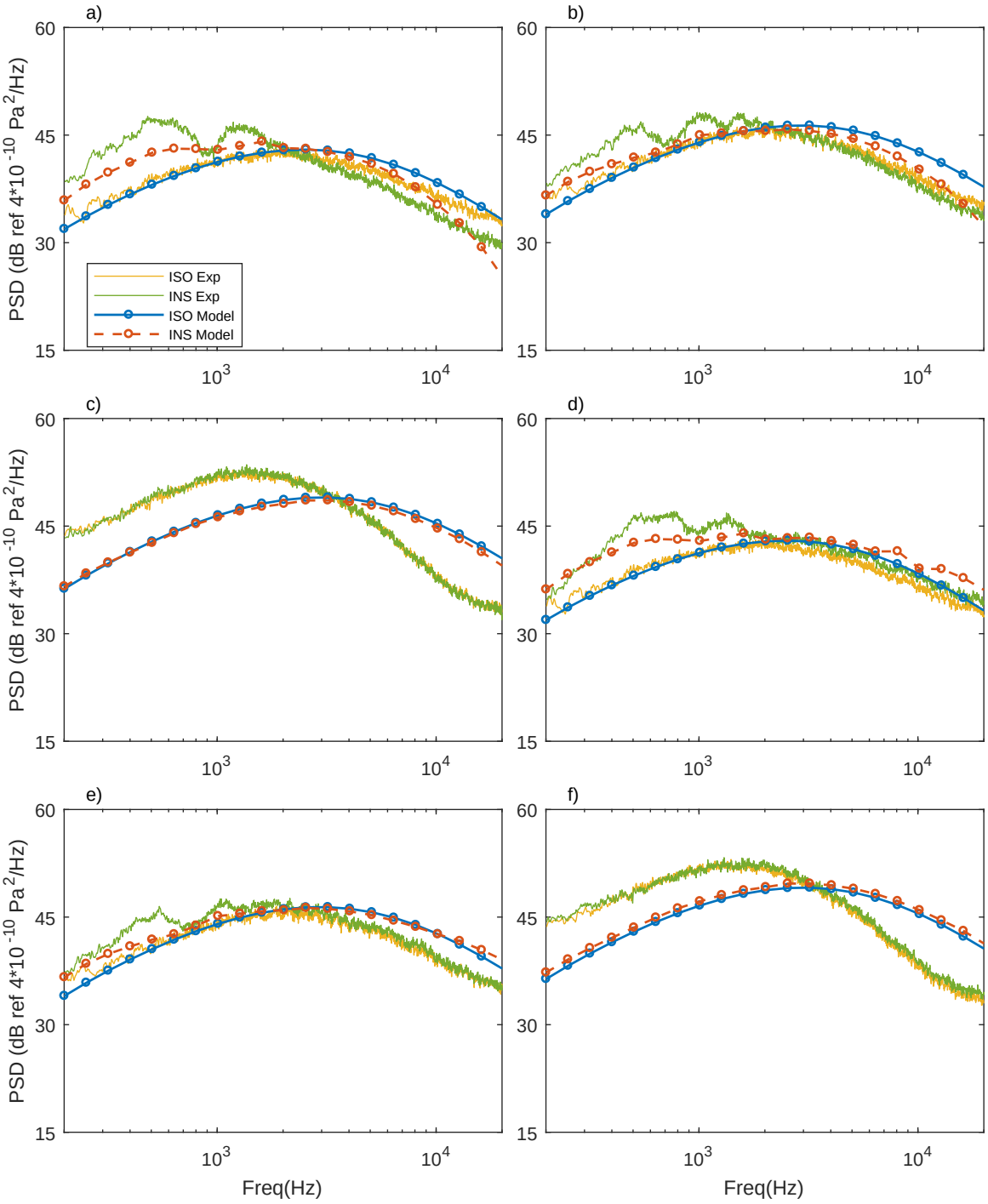

Figure 6.16: Comparison of the predicted isolated and installed noise spectra with experimental results: a) $\theta = 90°$, shielded side; b) $\theta = 60°$, shielded side; c) $\theta = 30°$, shielded side; d) $\theta = 90°$, reflected side; e) $\theta = 60°$, reflected side; f) $\theta = 30°$, reflected side; the flat plate's trailing edge is at $L = 4D$ and $H = 2D$.

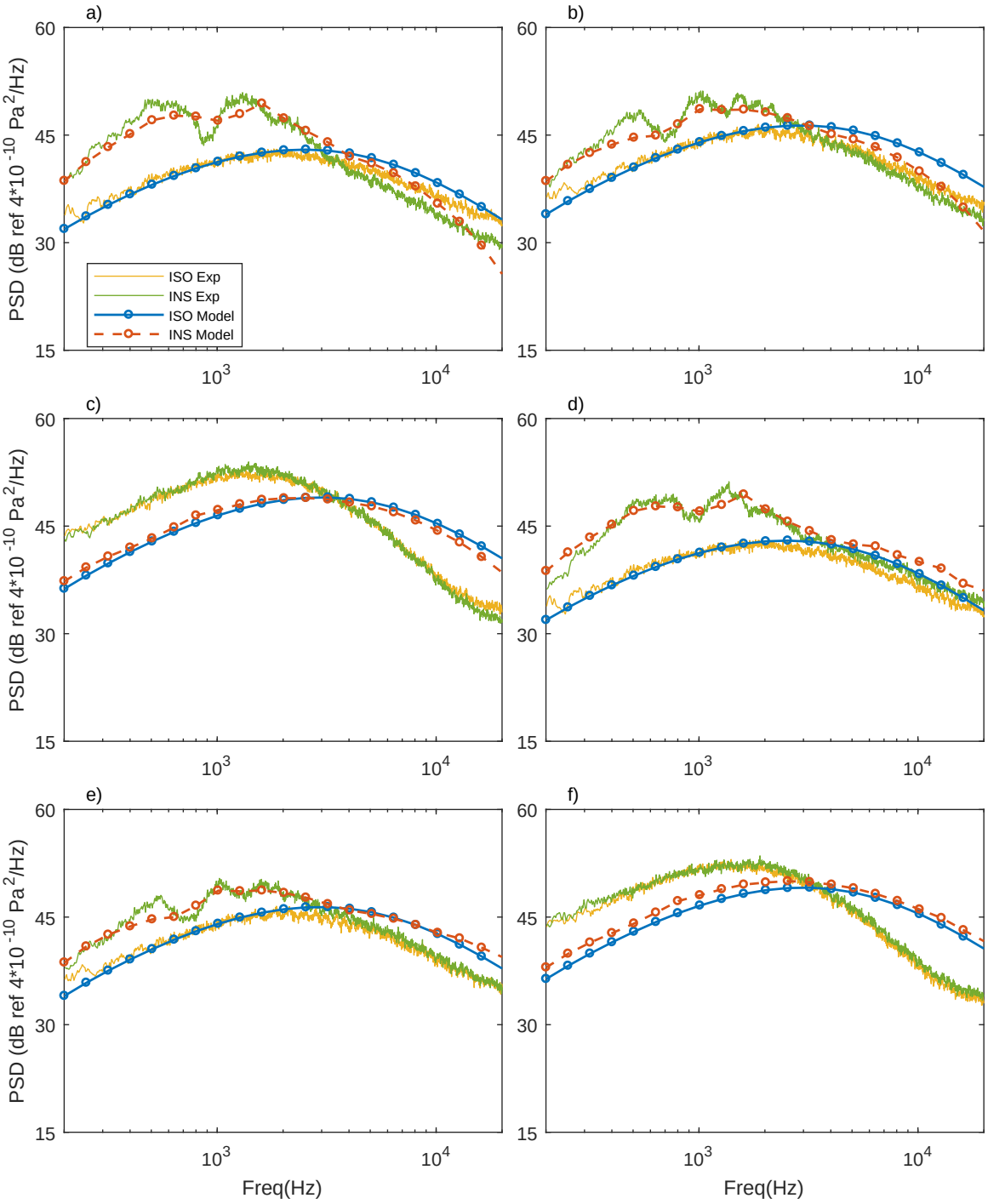

Figure 6.17: Comparison of the predicted isolated and installed noise spectra with experimental results: a) $\theta = 90°$, shielded side; b) $\theta = 60°$, shielded side; c) $\theta = 30°$, shielded side; d) $\theta = 90°$, reflected side; e) $\theta = 60°$, reflected side; f) $\theta = 30°$, reflected side; the flat plate's trailing edge is at $L = 4D$ and $H = 1.5D$.

that this could be either due to the spectral oscillations or because the approximation that the instability waves of different azimuthal modes decay at roughly the same rate is less good at $z = 4D$ (because the instability waves of higher azimuthal modes do not vanish as quickly as those at $z = 6D$, see Tinney et al. (2008a) and Tinney and Jordan (2008) for instance). Comparison at $\theta = 60°$ shows similar level of agreement as that at $\theta = 90°$, and the spectra plotted in figure 6.16(c) resemble those shown in figure 6.13(c). Results on the other side of the plate are shown in figure 6.16(d-f). Due to the similarity to those discussed above, a detailed discussion seems superfluous.

It is, however, worth noting that the agreement between the model predictions and experimental observations is much better when the plate is moved slightly closer to $H = 1.5D$, as shown in figure 6.17. The maximum noise enhancement observed at 90° on the shielded side in the experiment matches closely to the model's prediction. Even the spectral oscillations appear to be partially predicted. Noise shielding effects for this configuration are also predicted reasonably well. The agreement at both 60° and 30° to the jet axis is similar to that described above. And it is worth mentioning again the excellent noise prediction at 90° on the reflected side.

One can further compare the results when the plate's trailing-edge is placed at $L = 4D$ and $H = 1.25D$. The fact that the spectral oscillations are partially captured is more marked. The general trend, however, largely resembles that shown in figure 6.17. We therefore omit a repetitive description of them.

6.5 Summary

A series of experimental tests are carried out in this chapter to investigate jet installation effects, together with the effects of varying H, L and the jet Mach number on installed jet noise. It is found that the plate causes jet noise to be enhanced significantly at low frequencies, and jet noise is either suppressed or increased by around 3 dB at high frequencies on the shielded and reflected sides, respectively. It is demonstrated that increasing H (while L is fixed) causes the low-frequency hump to decrease exponentially but results in little change for both the shielding and reflection effects at high frequencies. Increasing L (while H is fixed), on the other hand, produces stronger noise intensification at low frequencies and slightly more effective shielding or reflection effects at high frequencies. The installation effects are found to be less pronounced as the Mach numbers increase.

The results are then compared with the predictions using the hybrid model developed in Chapter 5. Excellent agreement is achieved for the low-frequency noise enhancement caused

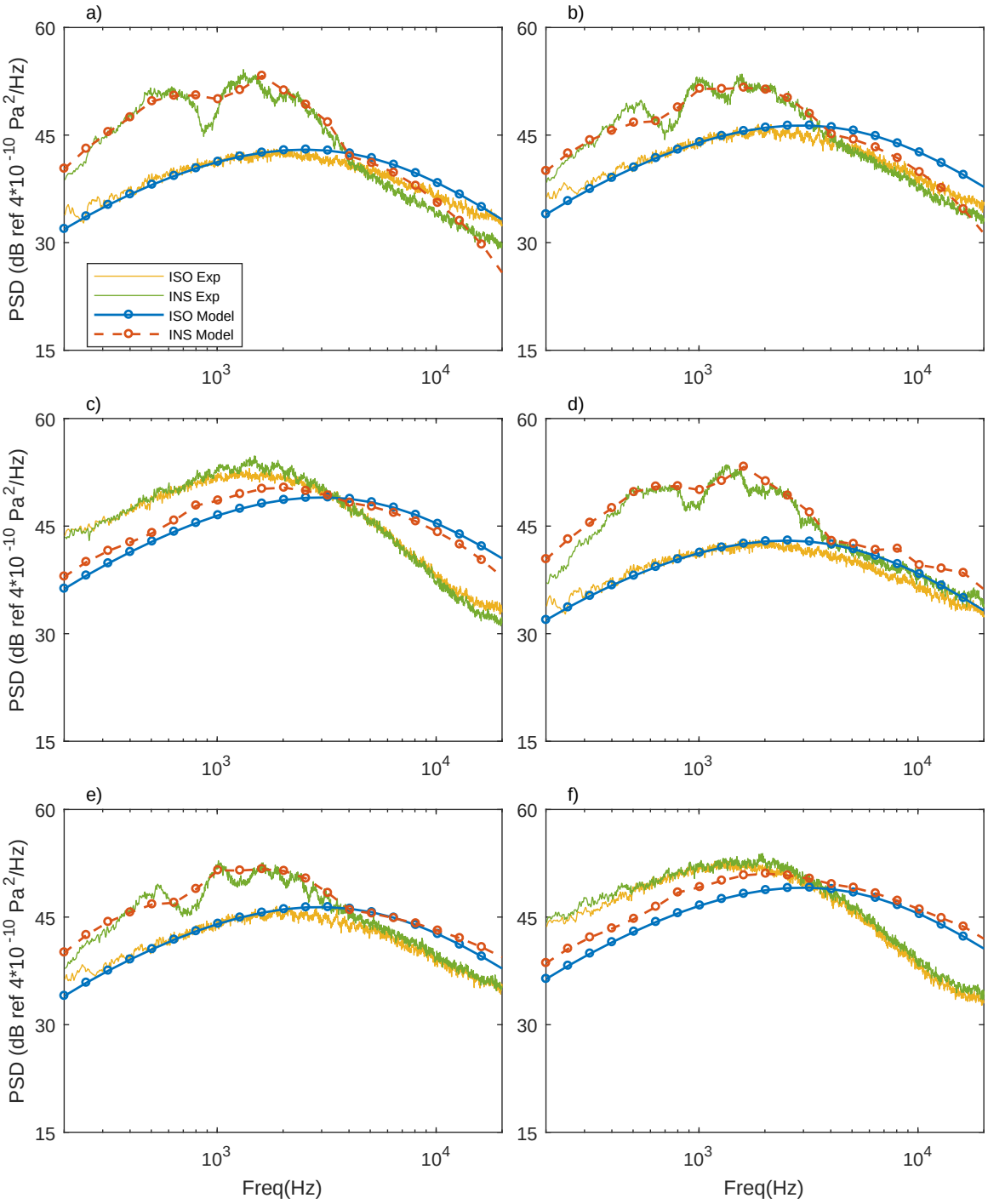

Figure 6.18: Comparison of the predicted isolated and installed noise spectra with experimental results: a) $\theta = 90°$, shielded side; b) $\theta = 60°$, shielded side; c) $\theta = 30°$, shielded side; d) $\theta = 90°$, reflected side; e) $\theta = 60°$, reflected side; f) $\theta = 30°$, reflected side; the flat plate's trailing edge is at $L = 4D$ and $H = 1.25D$.

by instability wave scattering when the plate is placed at different positions. This remarkable agreement shows that that near-field scattering model captures the correct noise mechanism for the low-frequency noise enhancement and provides a robust and accurate prediction tool. In addition, the quadrupole-scattering model can also correctly predict the noise spectra for an observer angle of 90° on the reflected side of the flat plate. At lower observer angles, deviations occur due to the jet refraction effects. However, it can qualitatively predict both the shielding and reflection effects at high frequencies. An improved model incorporating these refraction effects will be studied in our future work.

Part III

REDUCTION

Chapter 7

Noise of Lobed Jets

Jet noise reduction is extremely challenging. One of the reasons is that turbulence is poorly described and understood, but turbulence remains an extremely important jet noise source. Since the power of jet noise scales as the eighth power of the jet Mach number, the primary and perhaps the most effective noise reduction method is to reduce the jet exit velocity. This has been the main strategy for the past 6 decades and has led to a reduction of aircraft noise by around 20 dB (Casalino et al., 2008). However, this strategy cannot be continued due to the limitation of engines sizes. In recent years, using chevron nozzles on aero-engines is proposed as a way of achieving jet noise reduction and has been now used in industry. Other approaches examined in the literature include using lobed and tab nozzles (see Tam and Zaman (2000) and Zaman et al. (2003) for example). But the literature on this is sparse and the effect of nozzle geometry on isolated jet noise is not very well understood, let alone how it affects installed jet noise. In this chapter, we wish to advance our understanding on this, by studying the effects of lobed nozzles on both isolated and installed jet noise.

7.1 Experimental study

The experimental setup for round jet noise is described in Chapter 6. Using the same rig, we examine, in this section, how lobed nozzles change jet aeroacoustics. The profile of the lobed nozzle exit is given by

$$\sigma = a_\epsilon \left(1 + \epsilon \cos N\phi\right), \tag{7.1}$$

where ϕ is the azimuthal angle, N is the number of lobes, ϵ is the lobe penetration ratio and σ is the radius of the nozzle at azimuthal angle ϕ. The constant a_ϵ is chosen for specific ϵ and N (in fact it is independent of N when $N \neq 0$) such that the lobed nozzle has the same exit area

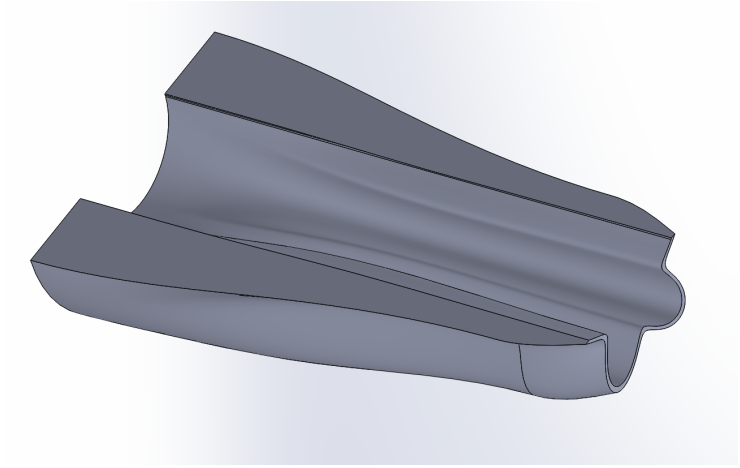

Figure 7.1: The lobed nozzle LN53 used in the experiment: it has 5 lobes with a penetration ratio $\epsilon = 0.3$.

Test No./Configuration	Nozzle	Mach number	H	L
1	Lobed	0.5	$3D$	$6D$
2	Lobed	0.5	$2D$	$6D$
3	Lobed	0.5	$1.5D$	$6D$
4	Lobed	0.5	$2D$	$4D$
5	Lobed	0.5	$1.5D$	$4D$
6	Lobed	0.5	$1.25D$	$4D$

Table 7.1: Test parameters for studying the effects of lobed nozzles on installed jet noise at Mach number 0.5 with various values of H and L.

as the reference round nozzle (the round nozzle, as mentioned in Chapter 6, has a diameter of 1 inch). The lobed nozzle used in this experiment has five lobes and a penetration ratio of 0.3, as shown in figure 7.1. From the section view of the nozzle shown in figure 7.1, one can see that the lobed structure is not formed abruptly at the nozzle exit, but rather through a continuously smooth morphing. The morphing length is around 4 jet diameters (the mean diameter) long. To have a more realistic wall thickness, the lobed nozzle exit is tapered to have a thickness of 2 mm, as can be seen from figure 7.1.

A similar set of tests to those for the round nozzle is performed for the lobed nozzle. The test matrices are shown in tables 7.1 and 7.2. The average Mach number (calculated from mass flow rates) is kept to be the same as that for the round nozzle. The results are compared and contrasted to those obtained for the round nozzle.

Test No./Configuration	Nozzle	Mach number	H	L
7	Lobed	0.7	$3D$	$6D$
8	Lobed	0.7	$2D$	$6D$
9	Lobed	0.7	$1.5D$	$6D$
10	Lobed	0.7	$2D$	$4D$
11	Lobed	0.7	$1.5D$	$4D$
12	Lobed	0.7	$1.25D$	$4D$

Table 7.2: Test parameters for studying the effects of lobed nozzles on installed jet noise at Mach number 0.7 with various values of H and L.

7.1.1 Effects of lobes on isolated jet noise

The effects of lobed nozzles on isolated jet noise spectra can be seen from figure 7.2. Figure 7.2(a) shows the noise spectra of both the round and lobed nozzles at Mach number 0.5. Before discussing these results, it is worth emphasizing again that the flow rates are kept the same for both the round and lobed nozzles. Compared with the isolated spectra of the round nozzle, a noise reduction of around $1.5 \sim 2$ dB is achieved for lobed jets except for an observer at 30° to the jet axis. The noise reduction is most evident in the intermediate frequency regime and less so at both low and high frequencies.

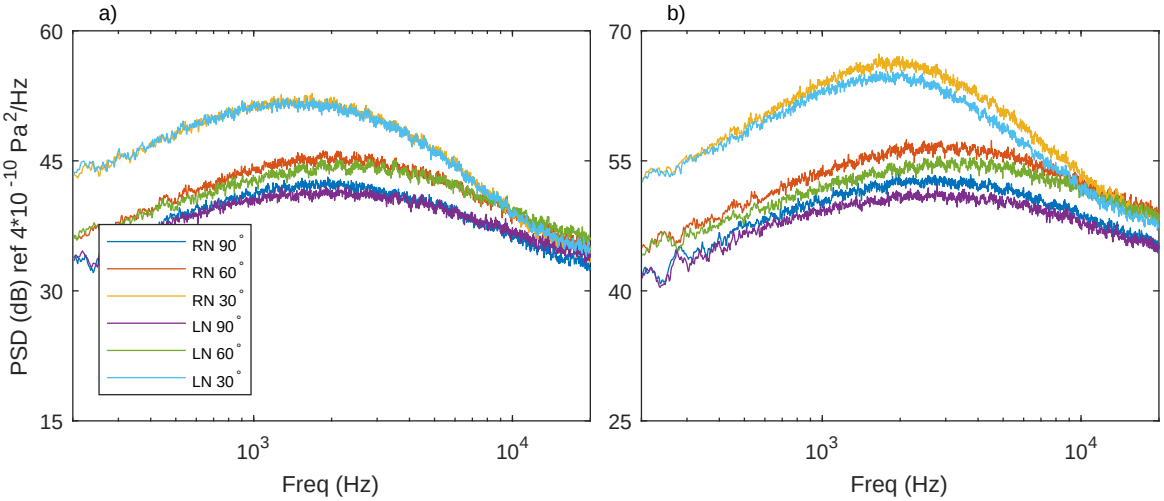

Figure 7.2: Comparison of the isolated jet noise between round and lobed nozzles: a) $M_0 = 0.5$; b) $M_0 = 0.7$.

The noise reduction is more evident for higher-speed jets. This can be seen from figure 7.2(b), where the jet Mach number is 0.7. An average noise reduction of 3 dB is observed

at all observer angles, including 30°. The noise reduction again only occurs in the intermediate frequency regime. These results show that the lobed nozzle has similar effects as chevron nozzles, both of which result in a noticeable isolated jet noise reduction.

7.1.2 Effects of lobes on installed jet noise at $M_0 = 0.5$

To show the effects of nozzle lobes on installed jet noise, we compare the installed jet noise spectra for both the round and lobed nozzles. The spectra at $M_0 = 0.5$ are presented first in figures 7.3 (on the shielded side) and 7.4 (on the reflected side). Figure 7.3(a) shows the comparison when the plate's trailing edge is at $L = 6D$ and $H = 3D$. One can see that an average 1.5 dB noise reduction is achieved for all observer angles at high frequencies. This is likely to be due to the noise reduction effects of lobes on isolated jet noise (see figure 7.2(a)). However, little sound reduction is observed at low frequencies, especially around the low-frequency hump. This suggests that lobed nozzles can result in an insignificant noise reduction for isolated jet noise, but cause little change to the low-frequency installed jet noise. Since the low-frequency noise enhancement results from the scattering of jet instability waves, this suggests that the lobed nozzle has little effect on the scattering process. Moving the plate closer to the jet axis to $H = 2D$, while L is kept at $6D$, results in, as expected, stronger noise enhancement at low frequencies, as shown in figure 7.3(b). The trend that a slight noise reduction is observed only at high frequencies remains. The same observations can be made for all other plate positions, see figure 7.3(c-f).

The comparison of noise spectra on the other side of the plate is shown in figure 7.4. The effects of lobed nozzles are slightly different from those on the other side of the plate. In particular, there is an average noise reduction of $2 \sim 3$ dB in the intermediate frequency regime, as can be clearly seen from figure 7.4(a), where the plate is placed at $L = 6D$ and $H = 3D$. This noise reduction, however, gradually diminishes at the observer angles decreases. This is not obvious on the other side of the plate, and this difference might arise from the different jet refraction profile from that of a round jet. At low frequencies, on the other hand, there is little noise reduction. A slight noise increase is even observed near the highest frequencies. Changing the plate positions does not change these tendencies, as can be seen from figure 7.4(b-f).

7.1.3 Effects of lobes on installed jet noise at $M_0 = 0.7$

Figures 7.3 and 7.4 show that the use of lobed nozzles does not change the installed jet noise spectra at low frequencies. However, it does results in a slight noise reduction at high frequencies on the shielded side. On the other side of the plate, however, the noise reduction is more

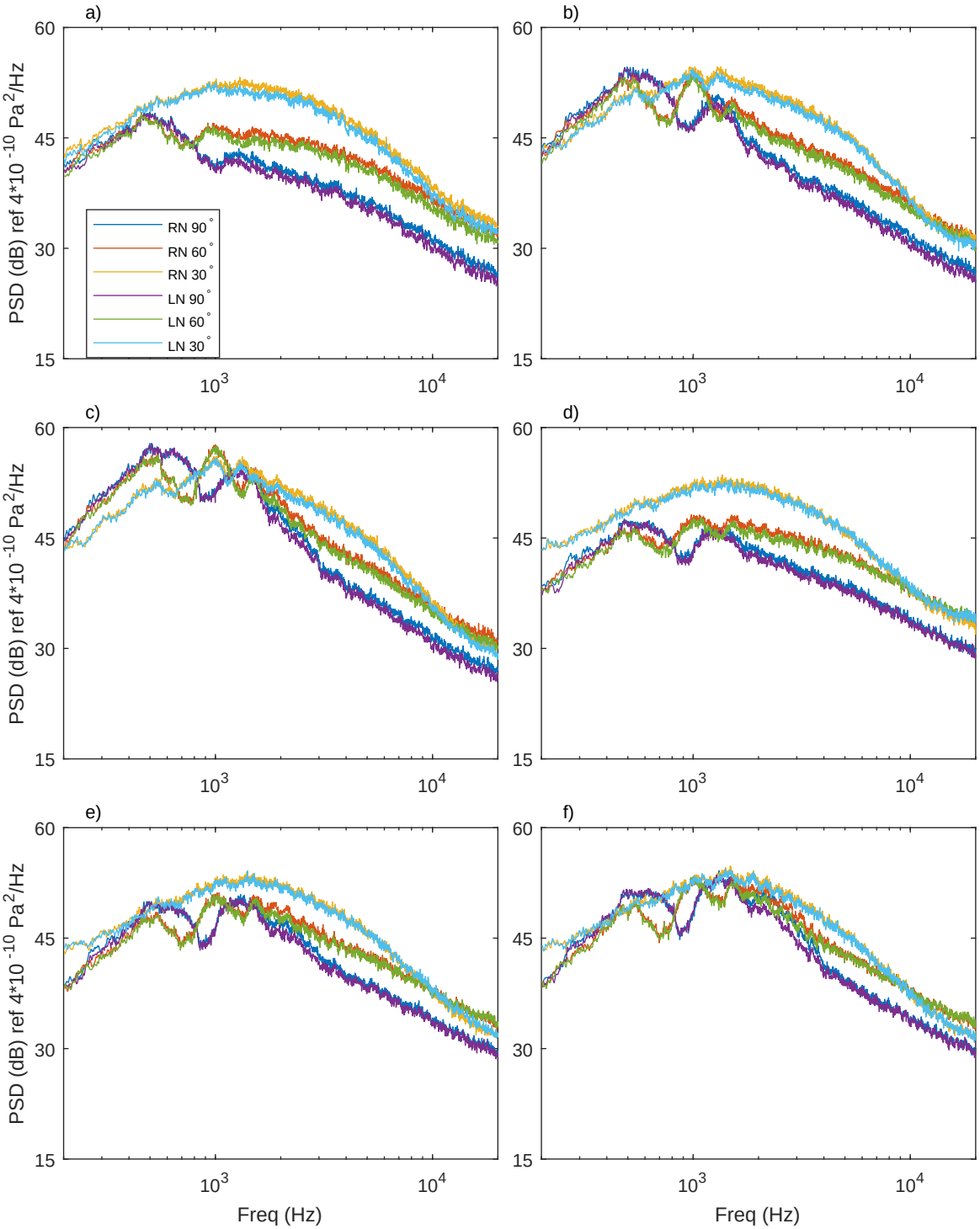

Figure 7.3: Installed noise spectra of the round and lobed jets on the shielded side for various plate positions at the Mach number of 0.5: (a) $L = 6D,\ H = 3D$; (b) $L = 6D,\ H = 2D$; (c) $L = 6D,\ H = 1.5D$; (d) $L = 4D,\ H = 2D$; (e) $L = 4D,\ H = 1.5D$; (e) $L = 4D,\ H = 1.25D$.

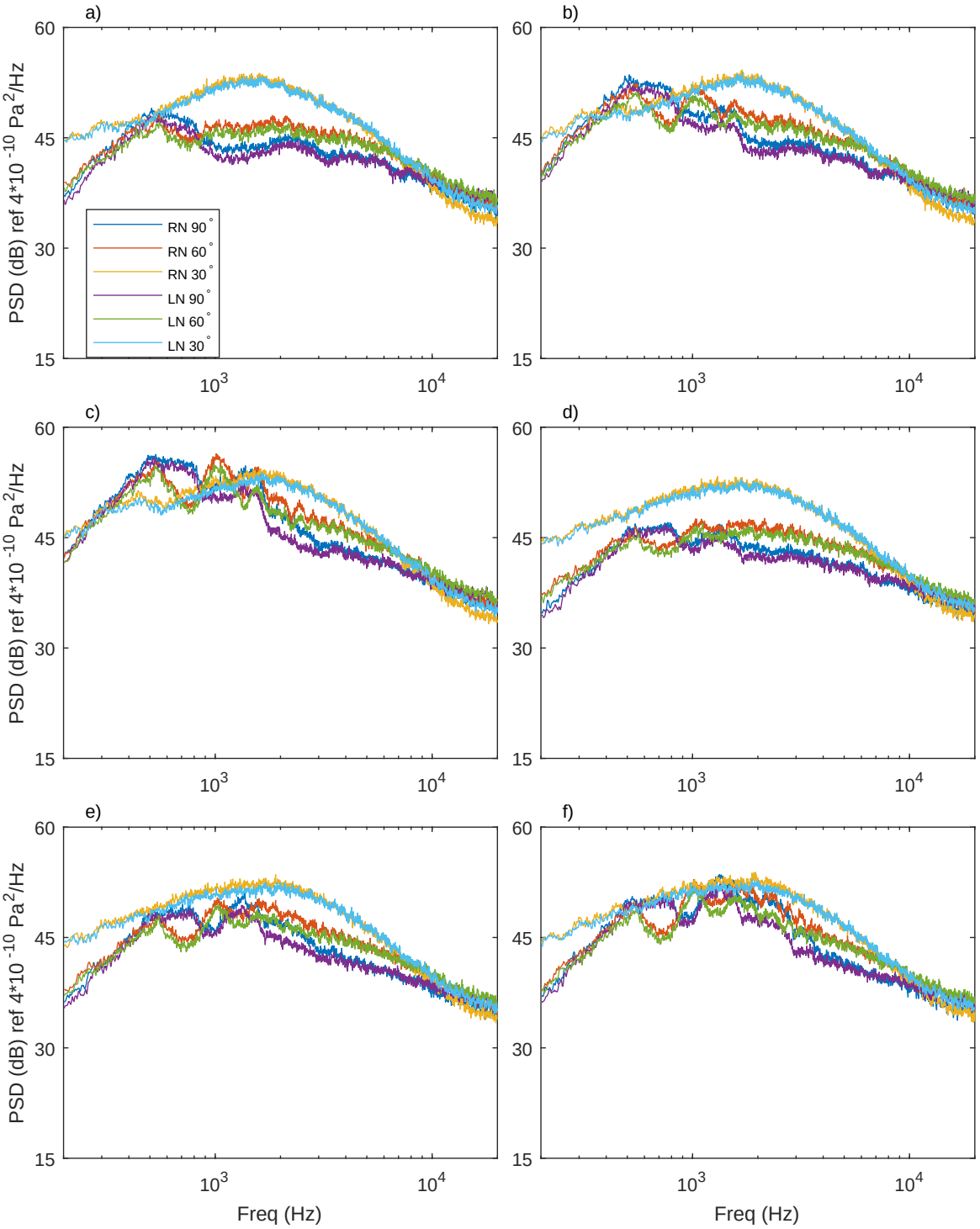

Figure 7.4: Installed noise spectra of the round and lobed jets on the reflected side for various plate positions at the Mach number of 0.5: (a) $L = 6D,\ H = 3D$; (b) $L = 6D,\ H = 2D$; (c) $L = 6D,\ H = 1.5D$; (d) $L = 4D,\ H = 2D$; (e) $L = 4D,\ H = 1.5D$; (e) $L = 4D,\ H = 1.25D$.

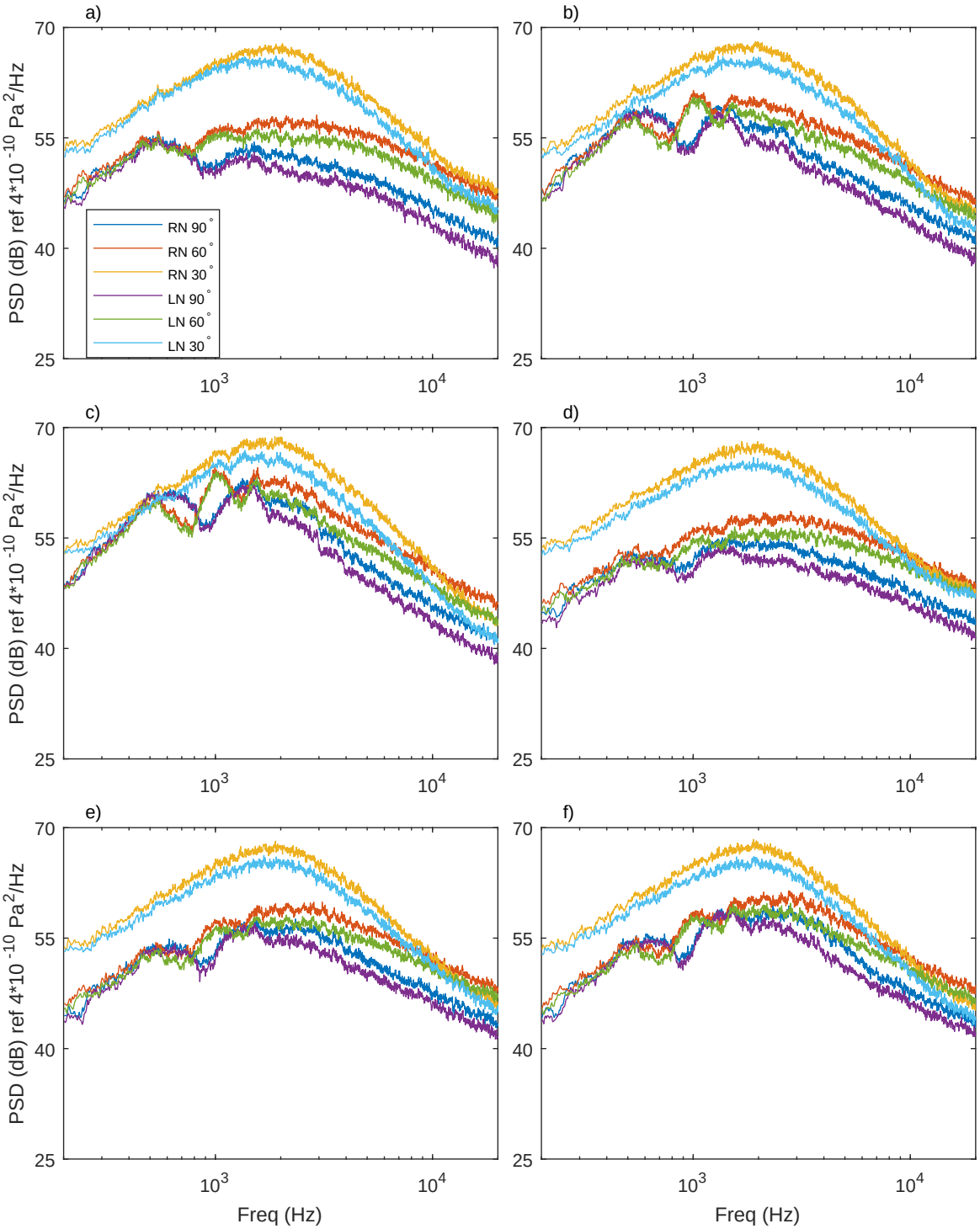

Figure 7.5: Installed noise spectra of the round and lobed jets on the shielded side for various plate positions at the Mach number of 0.7: (a) $L = 6D,\ H = 3D$; (b) $L = 6D,\ H = 2D$; (c) $L = 6D,\ H = 1.5D$; (d) $L = 4D,\ H = 2D$; (e) $L = 4D,\ H = 1.5D$; (e) $L = 4D,\ H = 1.25D$.

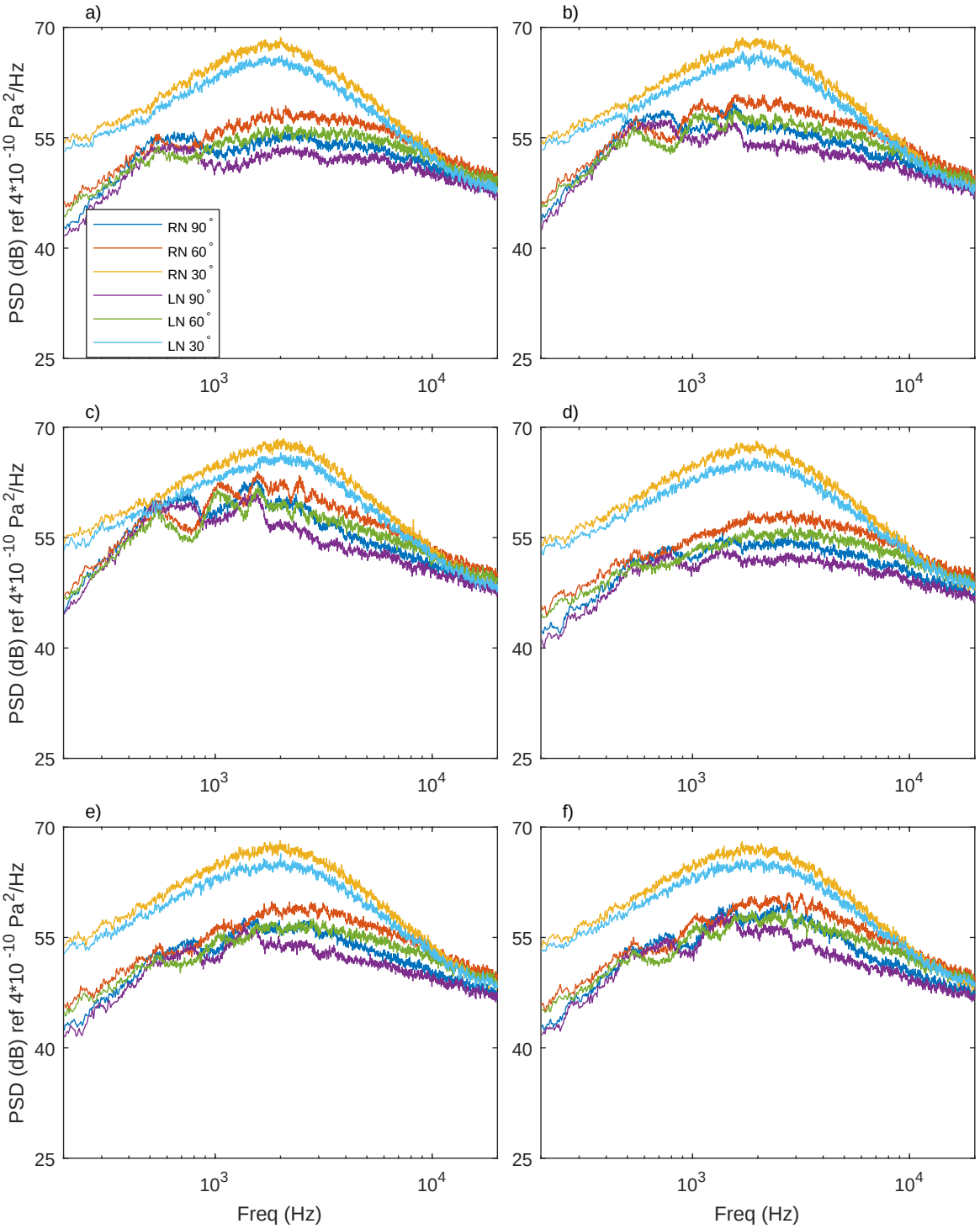

Figure 7.6: Installed noise spectra of the round and lobed jets on the reflected side for various plate positions at the Mach number of 0.7: (a) $L = 6D,\ H = 3D$; (b) $L = 6D,\ H = 2D$; (c) $L = 6D,\ H = 1.5D$; (d) $L = 4D,\ H = 2D$; (e) $L = 4D,\ H = 1.5D$; (e) $L = 4D,\ H = 1.25D$.

effective in the intermediate frequency regime, while a slight noise increase is observed at very high frequencies. Does this trend still hold for higher Mach numbers? The answer can be found in figures 7.5 and 7.6, where the comparisons of the installed noise spectra for both the round and lobed nozzles at a Mach number of 0.7 are shown.

Figure 7.5 shows the comparison of the noise spectra on the shielded side. One can clearly see that a noise reduction of up to 4 dB is achieved at high frequencies, while little noise reduction occurs at low frequencies. This tendency remains to be true for all different plate positions (see figure 7.5(a-f)). In the preceding section, we have speculated that the noise reduction observed at high frequencies is merely caused by the reduction of the isolated jet spectra. This presumption is now further validated by the higher noise reduction observed for the $M_0 = 0.7$ jets (3 dB for $M_0 = 0.7$ compared to 1.5 dB for $M_0 = 0.5$). This is because the noise reduction of the isolated spectra is around 3 dB at the Mach number of 0.7 and 1.5 dB at the Mach number of 0.5 (see figure 7.2(a-b)).

The comparison of installed jet noise spectra for $M_0 = 0.7$ on the reflected side of the plate is shown in figure 7.6. A maximum of 4 dB noise reduction is observed in the intermediate frequency regime, and this noise reduction diminishes at high frequencies. At low frequencies, the low-frequency humps do not change significantly, although compared to those at $M_0 = 0.5$, there is a marginal noise reduction of around 1 dB. Again, it is possible that this is caused by the different jet refraction profiles between the round and lobes jets.

In summary, the effects of the lobed nozzle on installed jet noise are nearly identical for all plate positions and Mach numbers: on the shielded side of the flat plate, lobed nozzles do not noticeably change the installed jet noise spectra at low frequencies. However, it does result in a slight noise reduction at high frequencies. This is thought to be caused by the reduction of isolated jet noise. On the reflected side of the flat plate, the noise has to pass through the jet plume in order to reach the observer. The jet plumes of the round and lobed nozzles are different, and this causes an insignificant change to the effects of lobed nozzles compared to those on the shielded side. For example, the noise reduction is more effective in the intermediate frequency regime, while a negligible or even slight noise increase is observed at high frequencies. Different jet plumes might also cause the low-frequency hump to be marginally less strong on the reflected side at a Mach number of 0.7.

7.2 Stability analysis for lobed jets

It can be expected that the instability waves associated with a lobed jet are different from those of a round jet since the jet mean flows are different. However, the little change of the installed

noise of a lobed jet at low frequencies suggests that the jet instability waves might not differ from those of a round jet significantly. To understand why this happens, one needs to examine the stability characteristics of lobed jets.

The open literature on the stability of lobed jets is very sparse (Morris, 2010). One of these studies was carried out by Kopiev et al. (2004) in the context of supersonic jet noise. A spatial stability analysis was undertaken to examine the effects of weak corrugation on the instability characteristics of a parallel vortex sheet with supersonic flow speed. A leading-order asymptotic correction to the complex wavenumber α for the round jet when $\epsilon \to 0$ was obtained. The results showed that at low St a small ϵ may lead to a $O(\epsilon)$ change to the spatial growth rate if the azimuthal mode number n is less than the number of lobes N. More interestingly, it was shown that if the sum of the two positive mode numbers is equal to N, the changes to the values of their α have opposite tendencies. The final asymptotic solution shown in this study, however, relies on numerically solving transcendental equations and is therefore non-trivial to compute. Also, because the correction is restricted to $O(\epsilon)$ or $O(\epsilon^2)$ only when $\epsilon \to 0$, it remains to be seen to what extent the corrugation can change the stability characteristics at a finite or larger ϵ.

Most of other relevant studies are about the stability characteristics of jets of other non-circular geometries, for example, elliptic, rectangular and chevron-like. The typical approach of tackling such a problem is numerically based (Morris, 1988; Tam and Thies, 1993; Baty and Morris, 1995; Lajús Jr. et al., 2015; Sinha et al., 2016). Of particular interest, the two recent works of Lajús Jr. et al. (2015) and Sinha et al. (2016) studied the stability characteristics of jets issued from chevron nozzles (and micro-jets (Lajús Jr. et al., 2015)), which were more geometrically similar to the lobed jets considered here. The work of Lajús Jr. et al. (2015) was based on numerically solving the compressible Rayleigh equation for an azimuthally periodic base flow. The paper explored the effects of azimuthal variations of the shear layer thickness and flow radius of the mean flow on the stability characteristics. The base flow was fitted based on a Mach 0.9 chevron jet and Mach 0.4 micro-jet. For the chevron case, the results showed that the variation of shear-layer thickness has opposite effect to that of the radius. The combination of the two, however, results in larger reduction of the spatial growth rates. It was concluded that chevron is more effective in controlling jet noise. The finally bit of this paper showed the effects of the number of lobes. The preliminary results showed that the number of lobes is not very important to the 0th instability waves, which will be seen to be consistent with the results obtained in this chapter.

In the study of Sinha et al. (2016), a viscous spatial linear stability analysis was performed

numerically using the PSE approach. The solutions to the parallel-flow stability equations were obtained first to initiate the PSE. The LST results showed that the serrations reduce the spatial growth rate of the most unstable eigenmodes of the jet, but their phase speeds are similar. The effects of serrations on spatial growth rate and convection velocities of the instability waves were found to be in accord with the finding to be shown in the rest of this chapter. The PSE results were compared with the POD modes of the near-field pressure obtained experimentally. Favourable agreement was achieved. So was the results from a further investigation using an LES database. It was concluded that the coherent hydrodynamic pressure fluctuations of jets from both round and serrated nozzles agree reasonably to the instability modes of turbulent flows.

Given the sparse analytical work on the stability of lobed jets and that the majority of studies on other non-circular jets are numerically based, it is desirable to perform some analytical studies, hoping to unveil more of the physics of lobed jets' instability waves. This section performs such an analysis within the temporal stability analysis framework, proposing an innovative analytical method of studying how a general non-axisymmetric jet mean flow changes the behaviour of instability waves. More importantly, the method does not involve solving transcendental equations and would work for finite or even large values of ϵ.

7.2.1 The governing equation for non-axisymmetric vortex-sheet flows

As a routine procedure of stability analysis, we decompose the flow into base and fluctuation parts. We start with the incompressible Navier-Stokes equations since installed jet noise is relevant primarily at low Mach numbers. At this stage, we write equations in a vector form to avoid the introduction of coordinate systems. The momentum equation can be written as

$$\frac{\mathrm{D}\boldsymbol{v}}{\mathrm{D}t} = -\frac{1}{\rho}\nabla p + \nu\nabla^2\boldsymbol{v}, \tag{7.2}$$

where, $\boldsymbol{v}$ is the fluid velocity, and ν the dynamic viscosity. We assume that base flow is steady and incompressible, with flow density, velocity, and pressure to be ρ, $\boldsymbol{U}$ and $\bar{p}$ respectively, and that that base flow satisfies

$$\frac{\mathrm{D}\boldsymbol{U}}{\mathrm{D}t} = -\frac{1}{\rho}\nabla \bar{p} + \nu\nabla^2\boldsymbol{U}. \tag{7.3}$$

The total flow field is given by the sum of the base flow and the small perturbation. After substituting the total flow into equation 7.2 and ignoring second-order quantities, we have the

following linearized equation:

$$\frac{\partial \boldsymbol{v}'}{\partial t} + \boldsymbol{U} \cdot \nabla \boldsymbol{v}' + \boldsymbol{v}' \cdot \nabla \boldsymbol{U} = -\frac{1}{\rho}\nabla p' + \nu \nabla^2 \boldsymbol{v}'. \tag{7.4}$$

When the Reynolds number is high, we expect that the viscous term plays a negligible role. Hence the term $\nu\nabla^2\boldsymbol{v}'$ can be dropped, i.e.

$$\frac{\partial \boldsymbol{v}'}{\partial t} + \boldsymbol{U} \cdot \nabla \boldsymbol{v}' + \boldsymbol{v}' \cdot \nabla \boldsymbol{U} = -\frac{1}{\rho}\nabla p'. \tag{7.5}$$

Equation 7.5, together with the incompressible continuity equation

$$\nabla \cdot \boldsymbol{v}' = 0, \tag{7.6}$$

governs the small-amplitude inviscid perturbations over a steady base flow.

The perturbation field is generally rotational for general shear base flows. Therefore, it cannot be described using a potential function. However, for parallel flows of a vortex-sheet type, the base flows inside and outside the vortex sheet are both irrotational. Hence the perturbation should also be irrotational. This suggests the existence of a potential function ψ for the velocity perturbations, i.e.

$$\boldsymbol{v}' = \nabla \psi, \tag{7.7}$$

on either side of the vortex sheet. The function ψ will be discontinuous across the shear layer. From the equation 7.6, one can see that the velocity potential satisfies the Laplace equation, i.e.

$$\nabla^2 \psi = 0. \tag{7.8}$$

The pressure perturbation is effectively decoupled from the velocity potential and can be easily obtained from equation 7.5.

The vortex-sheet simplification was used extensively in stability analysis, due in large to the fact that an analytical dispersion relationship can be generally found (Batchelor and Gill, 1962; Crighton, 1973; Kawahara et al., 2003). From these dispersion relationships, one can gain more insight than that numerical simulations can offer. Besides, the vortex-sheet simplification is often permissible, particularly for analysing low-frequency instability waves. Though the realistic jet mean flow spreads slowly and has an increasingly thick mixing layer towards downstream, the vortex-sheet simplification should serve as a good approximation to the realistic flow close to the jet nozzle. Therefore, as a starting point, in this section we assume the base flow to be parallel and is of a vortex-sheet type.

Since the velocity potentials exist for the vortex-sheet problem, we let ψ^+ and ψ^- denote the potentials outside and inside of the vortex sheet, respectively, i.e.

$$\boldsymbol{v}'^{\pm} = \nabla\psi^{\pm}, \tag{7.9}$$

where $\boldsymbol{v}'^{+}$ and $\boldsymbol{v}'^{-}$ denote the velocity perturbations outside and inside the vortex sheet, respectively. Under the same cylindrical coordinate system ($\{\sigma, \phi, z\}$) introduced in earlier chapters, the velocity potentials $\psi^{\pm}(\sigma, \phi, z, t)$ satisfy the following Laplace equation:

$$\nabla^2\psi^{\pm}(\sigma, \phi, z, t) = 0. \tag{7.10}$$

Note that we have not yet restricted the profiles of the vortex sheet. It therefore can be of arbitrary geometry, such as rectangular, elliptic or lobed. One can therefore let a general function $\mathcal{R}(\phi)$ denote the radius of the vortex sheet at polar angle ϕ. Consequently, the profile of the vortex sheet can be specified as

$$\mathcal{F}(\sigma, \phi) = \sigma - \mathcal{R}(\phi) = 0. \tag{7.11}$$

7.2.2 The eigenvalue problem

Without losing generality, one may assume

$$\psi^{\pm} = \sum_{m=-\infty}^{\infty} A_m E_m^{\pm}(\sigma, \phi)\mathrm{e}^{\mathrm{i}\alpha z}e^{-\mathrm{i}\omega t}, \tag{7.12}$$

where A_m are complex constants, α and ω are the streamwise wavenumber and frequency, respectively. The functions $E_m^{\pm}(\sigma, \phi)$ are linearly independent of each other and each pair of them at a given m satisfies both the governing equations and appropriate boundary conditions. The functions $E_m^{+}(\sigma, \phi)$ and $E_m^{-}(\sigma, \phi)$ are therefore defined in the two-dimensional regions outside ($\sigma > \mathcal{R}(\phi)$) and inside ($\sigma \leq \mathcal{R}(\phi)$) the vortex-sheet profile, respectively, as shown in figure 7.7. We choose to normalize the functions $E_m^{-}(\sigma, \phi)$ such that for any integer m

$$\frac{1}{2\pi}\int_0^{2\pi} E_m^{-}(a, \phi)E_m^{-*}(a, \phi)\mathrm{d}\,\phi = 1, \tag{7.13}$$

where a is the mean radius of the vortex sheet, which is defined by

$$a = \frac{1}{2\pi}\int_0^{2\pi} \mathcal{R}(\phi)\mathrm{d}\,\phi. \tag{7.14}$$

We cannot normalize $E_m^+(\sigma,\phi)$ according to equation 7.13, because $E_m^-(\sigma,\phi)$ and $E_m^-(\sigma,\phi)$ are not independent. In fact, either the dynamic or the kinematic boundary condition is sufficient to determine $E_m^+(\sigma,\phi)$ from a given $E_m^-(\sigma,\phi)$. Therefore, $E_m^+(\sigma,\phi)$ has to be normalized such that for the same mode number m, the functions $E_m^+(\sigma,\phi)$ and $E_m^-(\sigma,\phi)$ satisfy the boundary conditions. One should note that $E_m^-(a,\phi)$ are not properly defined within some ranges of ϕ (because $E_m^-(\sigma,\phi)$ is defined for $\sigma \leq \mathcal{R}(\phi)$ and $a > \mathcal{R}(\phi)$ in some ranges of ϕ, see figure 7.7 for example). However, they can be naturally defined using analytical continuation, which will become clear at a later stage. Hence, the normalization defined by equation 7.13 is valid.

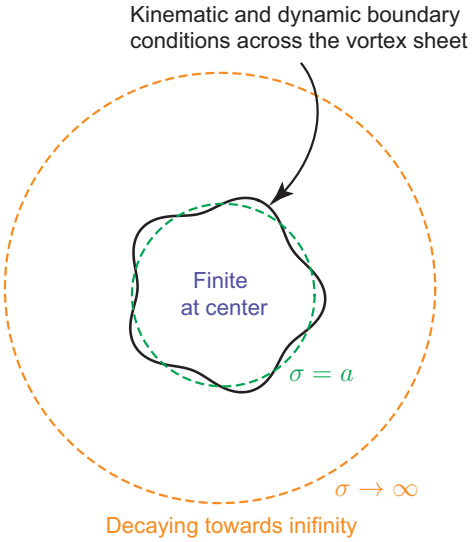

Figure 7.7: The schematic illustration of the boundary conditions of the stability problem of a parallel lobed vortex sheet.

Substituting $E_m^{\pm}(\sigma,\phi)$ into equation 7.10 yields the governing equation

$$\left[\frac{\partial^2}{\partial\phi^2} + \sigma\frac{\partial}{\partial\sigma}\left(\sigma\frac{\partial}{\partial\sigma}\right) - \alpha^2\sigma^2\right] E_m^{\pm}(\sigma,\phi) = 0. \tag{7.15}$$

Equation 7.15, however, does not describe a fully-defined mathematical problem. Boundary conditions are needed. The appropriate boundary conditions, as shown from figure 7.7, include a finite value of $E_m^-(0,\phi)$, a decay behaviour for $E_m^+(\sigma,\phi)$ as $\sigma \to \infty$, and the kinematic and dynamic boundary conditions on the vortex sheet (Batchelor and Gill, 1962; Crighton, 1973). Because all the function pairs $E_m^{\pm}(\sigma,\phi)$ satisfy both equation 7.15 and their relevant boundary conditions, they are referred to as the eigenfunctions of this system. The functions $\{E_m^{\pm}(\sigma,\phi)\}$ should form a complete set of basis for the Hilbert space determined by the equation 7.15 and appropriate boundary conditions. The aim of this section is to calculate these eigenfunctions analytically (without discretizing equation 7.15 and then solving it numerically).

7.2.3 The calculation of eigenfunctions

Due to the coupling of σ and ϕ of the boundary conditions, $E_m^{\pm}(\sigma,\phi)$ are not generally expected to be of a separable form. However, in the case of a cylindrical vortex sheet (round jet), the eigenfunctions $E_m^{\pm}(\sigma,\phi)$ are known to be separable. Before proceeding to the case of lobed vortex sheets, it is instructive to examine the characteristics of $E_m^{\pm}(\sigma,\phi)$ for a cylindrical vortex sheet.

The solution for a cylindrical vortex sheet

For the cylindrical vortex-sheet flow, the potentials $\psi^{\pm}$ are known to be able to be expanded as

$$\psi^{\pm} = \sum_{n=-\infty}^{\infty} \Psi_n^{\pm}(\sigma)\mathrm{e}^{in\phi}\mathrm{e}^{\mathrm{i}\alpha z}\mathrm{e}^{-\mathrm{i}\omega t}, \tag{7.16}$$

where the functions $\Psi_n^{\pm}(\sigma)$ satisfy the Modified Bessel Equation

$$\sigma^2\frac{\mathrm{d}^2\Psi_n^{\pm}}{\mathrm{d}\sigma} + \sigma\frac{\mathrm{d}\Psi_n^{\pm}}{\mathrm{d}\sigma} - \left(\alpha^2\sigma^2 + n^2\right)\Psi_n^{\pm} = 0. \tag{7.17}$$

Considering the boundary condition at the centre of the mean flow and at infinity, one can show that

$$\begin{aligned}\Psi_n^{-}(\sigma) &= C_n^{-}\frac{1}{I_n(\alpha a)}I_n(\alpha\sigma),\\ \Psi_n^{+}(\sigma) &= C_n^{+}\frac{1}{K_n(\alpha a)}K_n(\alpha\sigma).\end{aligned} \tag{7.18}$$

where C_n^{-} and C_n^{+} are arbitrary complex constants.

Applying the kinematic and dynamic boundary condition on the vortex sheet (see the derivations in Chapter 3), one obtains

$$\begin{cases}(\omega-\alpha U)\dfrac{\partial\Psi_n^{+}}{\partial\sigma} = \omega\dfrac{\partial\Psi_n^{-}}{\partial\sigma}, & \text{(7.19a)}\\ \omega\Psi_n^{+} = (\omega-\alpha U)\Psi_n^{-}, & \text{(7.19b)}\end{cases}$$

where use is made of the fact that the function set $\{\mathrm{e}^{in\phi}\}$ is orthogonal. For a non-trivial pair of solutions to exist ($C_n^{-}C_n^{+} \neq 0$), equations 7.19a and 7.19b can be rearranged to yield the dispersion relationship

$$\left(\frac{\alpha U}{\omega}-1\right)^2 = \frac{I_n'(\alpha a)K_n(\alpha a)}{I_n(\alpha a)K_n'(\alpha a)}. \tag{7.20}$$

In this special case, one can verify that the eigenfunctions, $E_n^+(\sigma,\phi)$ and $E_n^-(\sigma,\phi)$, take the separable form of

$$\begin{aligned} E_n^-(\sigma,\phi) &= \frac{1}{I_n(\alpha a)} I_n(\alpha\sigma)\mathrm{e}^{in\phi}, \\ E_n^+(\sigma,\phi) &= \Big(1-\frac{\alpha U}{\omega}\Big)\frac{1}{K_n(\alpha a)} K_n(\alpha\sigma)\mathrm{e}^{in\phi}, \end{aligned} \tag{7.21}$$

where $(1-\alpha U/\omega)$ is obtained from equation 7.20. Here, $E_n^{\pm}(\sigma,\phi)$ take these simple forms because the boundary condition involves no coupling between σ and ϕ (separable), and therefore these separable solutions are just the eigenfunction of the mathematical problem.

The solution for a vortex sheet of arbitrary geometry

For the case of a lobed vortex sheet, the perturbations outside and inside the vortex sheet still remain determined by the Laplace equation. However, the boundary condition is now more complicated. If we were to find an orthogonal coordinate system in which the lobed profile can be represented by one of the constant coordinate axes, we may be able to find a separable solution. For elliptic profiles, such a coordinate system exists and eigenfunctions of separable form can be obtained (Crighton, 1973). However, it seems rather unlikely to find such a coordinate system for a general lobe profile.

However, in light of the completeness of the orthogonal function set $\{e^{in\phi}\}$, we are still able to write the solutions inside and outside the vortex sheet as

$$\begin{aligned} \psi^- &= \sum_{-\infty}^{\infty} C_n^- \frac{1}{I_n(\alpha a)} I_n(\alpha\sigma)\mathrm{e}^{in\phi}\mathrm{e}^{\mathrm{i}\alpha z}\mathrm{e}^{-\mathrm{i}\omega t}, \\ \psi^+ &= \sum_{-\infty}^{\infty} C_n^+ \frac{1}{K_n(\alpha a)} K_n(\alpha\sigma)\mathrm{e}^{in\phi}\mathrm{e}^{\mathrm{i}\alpha z}\mathrm{e}^{-\mathrm{i}\omega t}, \end{aligned} \tag{7.22}$$

respectively. We must emphasize here that neither the solution $I_n(\alpha\sigma)\mathrm{e}^{in\phi}/I_n(\alpha a)$ nor that $K_n(\alpha\sigma)\mathrm{e}^{in\phi}/K_n(\alpha a)$ is the eigenfunction for this problem, since they do not satisfy the boundary conditions on the vortex sheet (although they satisfy equation 7.15). However, since they form a complete set, a suitable combination of these separable solutions which satisfies the boundary conditions will be the eigenfunction that we aim to obtain in this section. There may be multiple such combinations, which are corresponding to eigenfunctions of different orders. For a more compact presentation of the rest of the derivation, let

$$\bar{C}_n^- = C_n^- \frac{1}{I_n(\alpha a)}, \tag{7.23}$$

$$\bar{C}_n^+ = C_n^+ \frac{1}{K_n(\alpha a)}. \tag{7.24}$$

Hence, equation 7.22 becomes

$$\begin{aligned}\psi^- &= \sum_{-\infty}^{\infty} \bar{C}_n^- I_n(\alpha\sigma)\mathrm{e}^{\mathrm{i}n\phi}\mathrm{e}^{\mathrm{i}\alpha z}\mathrm{e}^{-\mathrm{i}\omega t},\\ \psi^+ &= \sum_{-\infty}^{\infty} \bar{C}_n^+ K_n(\alpha\sigma)\mathrm{e}^{\mathrm{i}n\phi}\mathrm{e}^{\mathrm{i}\alpha z}\mathrm{e}^{-\mathrm{i}\omega t}.\end{aligned} \tag{7.25}$$

The two equations shown in equation 7.25, together with the kinematic and dynamic boundary conditions on the vortex sheet, need to be combined to obtain the dispersion relationship. The kinematic and dynamic boundary conditions can be obtained as follows. As defined above, the vortex sheet profile is given by $\mathcal{F}(\sigma,\phi) = \sigma - \mathcal{R}(\phi) = 0$. One can assume that the perturbed profile can be described by the function

$$\mathcal{F}_p(\sigma,\phi,z,t) = \mathcal{F}(\sigma,\phi) - \eta'(\phi,z,t) = 0, \tag{7.26}$$

where $\eta'(\phi,z,t)$ denotes a small-amplitude perturbation of the radius of the vortex-sheet profile. The kinematic boundary condition states that, on the perturbed vortex sheet,

$$\frac{\mathrm{D}\mathcal{F}_p(\sigma,\phi,z,t)}{\mathrm{D}t} = 0. \tag{7.27}$$

Substituting the velocity on both sides of the vortex sheet to equation 7.27 and linearising around the unperturbed vortex sheet yields

$$\begin{cases}\dfrac{\partial\eta'}{\partial t} + U\dfrac{\partial\eta'}{\partial z} - \nabla\psi^-\cdot\nabla\mathcal{F} = 0,\\ \dfrac{\partial\eta'}{\partial t} - \nabla\psi^+\cdot\nabla\mathcal{F} = 0.\end{cases} \tag{7.28}$$

After invoking the harmonic time and z dependence ($\mathrm{e}^{\mathrm{i}\alpha z}\mathrm{e}^{-\mathrm{i}\omega t}$) and eliminating η', one can show that equation 7.28 reduces to

$$(\omega - \alpha U)\nabla\psi^+\cdot\boldsymbol{n} = \omega\nabla\psi^-\cdot\boldsymbol{n}, \tag{7.29}$$

where $\boldsymbol{n}$ denotes the unit vector perpendicular to the lobed profile, which can be readily shown to be $\nabla\mathcal{F}/|\nabla\mathcal{F}|$. The dynamic boundary condition requires pressure continuity across the vortex sheet. From the linearized momentum equation, i.e. equation 7.5, one can readily show that

$$p' = -\rho\left(\frac{\partial}{\partial t} + U_z\frac{\partial}{\partial z}\right)\psi, \tag{7.30}$$

where U_z can be either U and 0 depending on which side of the vortex sheet is considered. Hence substituting the velocity potentials on both sides of the vortex sheet yields that on the unperturbed vortex sheet (after linearising around the unperturbed vortex sheet)

$$\omega\psi^+ = (\omega - \alpha U)\psi^-, \tag{7.31}$$

Substituting equation 7.22 into the two boundary conditions, i.e. when $\sigma = \mathcal{R}(\phi)$

$$\begin{cases} (\omega - \alpha U)\nabla\psi^+ \cdot \boldsymbol{n} = \omega\nabla\psi^- \cdot \boldsymbol{n}, & \text{(7.32a)} \\ \omega\psi^+ = (\omega - \alpha U)\psi^-, & \text{(7.32b)} \end{cases}$$

we obtain

$$\begin{cases} (\omega - \alpha U)\left(\displaystyle\sum_{n=-\infty}^{\infty} \alpha\bar{C}_n^+ K_n'(\alpha\mathcal{R})\mathrm{e}^{\mathrm{i}n\phi} - \frac{\mathcal{R}'}{\mathcal{R}^2}\sum_{n=-\infty}^{\infty} \bar{C}_n^+(\mathrm{i}n)K_n(\alpha\mathcal{R})\mathrm{e}^{\mathrm{i}n\phi}\right) = \\ \qquad\qquad \omega\left(\displaystyle\sum_{n=-\infty}^{\infty} \alpha\bar{C}_n^- I_n'(\alpha\mathcal{R})\mathrm{e}^{\mathrm{i}n\phi} - \frac{\mathcal{R}'}{\mathcal{R}^2}\sum_{n=-\infty}^{\infty} \bar{C}_n^-(\mathrm{i}n)I_n(\alpha\mathcal{R})\mathrm{e}^{\mathrm{i}n\phi}\right) \\ \omega\displaystyle\sum_{n=-\infty}^{\infty} \bar{C}_n^+ K_n(\alpha\mathcal{R})\mathrm{e}^{\mathrm{i}n\phi} = (\omega - \alpha U)\sum_{n=-\infty}^{\infty} \bar{C}_n^- I_n(\alpha\mathcal{R})\mathrm{e}^{\mathrm{i}n\phi}, \end{cases} \tag{7.33}$$

where the prime symbol on a function denotes the first derivative of the function with respect to its argument.

7.2.4 Analysis for lobed vortex sheets

Generally, $\mathcal{R}$ can be an arbitrary function of ϕ. Since we are concerning with the stability of lobed jets, which have a number of identical lobes, it follows that the function $\mathcal{R}$ is a periodic function of ϕ. This suggests that $\mathcal{R}$ can be readily expanded using Fourier series. As a starting point, we restrict our attention to the case used in the experiment, in which case $\mathcal{R}$ is given by

$$\mathcal{R}(\phi) = a\left(1 + \epsilon\cos N\phi\right), \tag{7.34}$$

where, as defined in the preceding section, a is the mean nozzle radius. For weakly lobed nozzles, $\epsilon \ll 1$, while $\epsilon \sim 0.2$ represents a strongly lobed profile. Figure 7.8(a) shows some weakly lobed profiles when $\epsilon = 0.1$, while figure 7.8(b) shows some strongly lobed profiles when $\epsilon = 0.2$. In either case, we see that ϵ is a small quantity, and this suggests that the Taylor expansion of a well-behaved function around $\epsilon = 0$ should converge sufficiently quickly. For more general lobed profiles, function $\cos N\phi$ can be replaced by a sum of $\cos mN\phi$ and $\sin mN\phi$. When $\mathcal{R}$ is given by equation 7.34, we see that

$$\boldsymbol{n} = \frac{\nabla\mathcal{F}}{|\nabla\mathcal{F}|}, \tag{7.35}$$

and

$$\nabla \mathcal{F} = \boldsymbol{e}_\sigma + \boldsymbol{e}_\phi \frac{a}{\sigma} \epsilon N \sin N\phi, \tag{7.36}$$

where $\boldsymbol{e}_\sigma$ and $\boldsymbol{e}_\phi$ denote the unit vectors in the radial and azimuthal directions, respectively. Substituting equations 7.34 and 7.35 into equation 7.33 yields

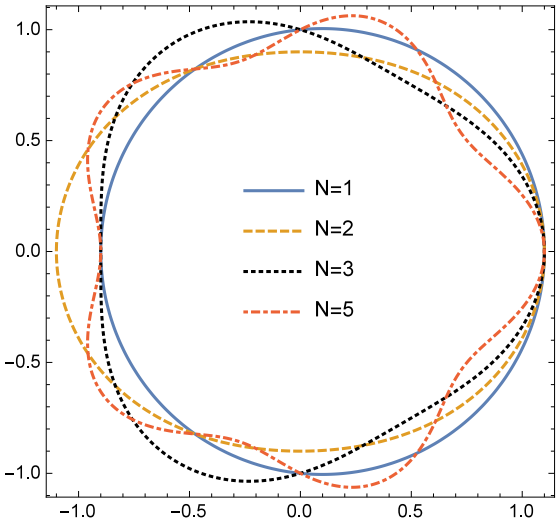

(a) The weakly lobed profiles when $\epsilon = 0.1$.

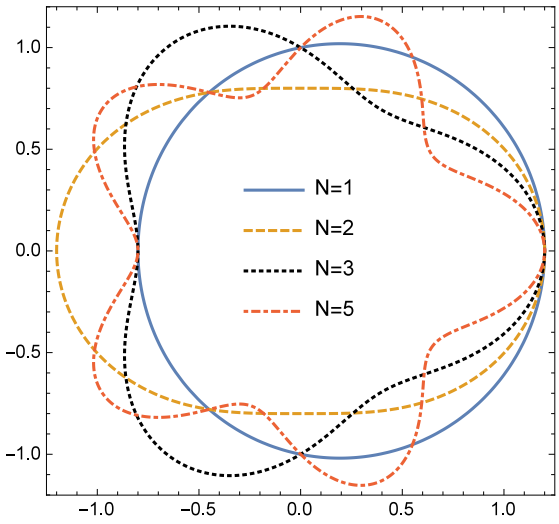

(b) Strongly lobed profiles when $\epsilon = 0.2$.

$$\begin{cases} \left(1 - \dfrac{\alpha U}{\omega}\right) \left(\displaystyle\sum_{n=-\infty}^{\infty} \bar{C}_n^+ K_n'(\alpha a(1+\epsilon\cos N\phi)) \mathrm{e}^{in\phi} \right. \\ \qquad \left. + \dfrac{\epsilon N \sin N\phi}{\alpha a(1+\epsilon\cos N\phi)^2} \displaystyle\sum_{n=-\infty}^{\infty} \bar{C}_n^+ (in) K_n(\alpha a(1+\epsilon\cos N\phi)) \mathrm{e}^{in\phi} \right) = \\ \qquad \left(\displaystyle\sum_{n=-\infty}^{\infty} \bar{C}_n^- I_n'(\alpha a(1+\epsilon\cos N\phi)) \mathrm{e}^{in\phi} \right. \\ \qquad \left. + \dfrac{\epsilon N \sin N\phi}{\alpha a(1+\epsilon\cos N\phi)^2} \displaystyle\sum_{n=-\infty}^{\infty} \bar{C}_n^- (in) I_n(\alpha a(1+\epsilon\cos N\phi)) \mathrm{e}^{in\phi} \right), \\ \displaystyle\sum_{n=-\infty}^{\infty} \bar{C}_n^+ K_n(\alpha a(1+\epsilon\cos N\phi)) \mathrm{e}^{in\phi} = \left(1 - \dfrac{\alpha U}{\omega}\right) \displaystyle\sum_{n=-\infty}^{\infty} \bar{C}_n^- I_n(\alpha a(1+\epsilon\cos N\phi)) \mathrm{e}^{in\phi}. \end{cases} \tag{7.37}$$

Weakly lobed profile

For weakly lobed profile, $\epsilon \ll 1$, therefore we may expand both left and right hand sides of equation 7.33 around $\epsilon = 0$ and keep only the first order without causing too much error. In

doing so, the following first-order equations can be obtained.

$$\begin{cases} \left(1-\dfrac{\alpha U}{\omega}\right)\left(\displaystyle\sum_{n=-\infty}^{\infty}\bar{C}_n^+\left(K_n'(\alpha a)+K_n''(\alpha a)\alpha a\epsilon\cos N\phi\right)\mathrm{e}^{in\phi}\right. \\ \qquad\left.+\dfrac{\epsilon N\sin N\phi}{\alpha a}\displaystyle\sum_{n=-\infty}^{\infty}\bar{C}_n^+(in)K_n(\alpha a)\mathrm{e}^{in\phi}\right)= \\ \qquad\left(\displaystyle\sum_{n=-\infty}^{\infty}\bar{C}_n^-\left(I_n'(\alpha a)+I_n''(\alpha a)\alpha a\epsilon\cos N\phi\right)\mathrm{e}^{in\phi}\right. \\ \qquad\left.+\dfrac{\epsilon N\sin N\phi}{\alpha a}\displaystyle\sum_{n=-\infty}^{\infty}\bar{C}_n^-(in)I_n(\alpha a)\mathrm{e}^{in\phi}\right), \\ \displaystyle\sum_{n=-\infty}^{\infty}\bar{C}_n^+\left(K_n(\alpha a)+K_n'(\alpha a)\alpha a\epsilon\cos N\phi\right)\mathrm{e}^{in\phi}= \\ \qquad\left(1-\dfrac{\alpha U}{\omega}\right)\displaystyle\sum_{n=-\infty}^{\infty}\bar{C}_n^-\left(I_n(\alpha a)+I_n'(\alpha a)\alpha a\epsilon\cos N\phi\right)\mathrm{e}^{in\phi}. \end{cases} \tag{7.38}$$

Equations 7.38 can be further reduced to

$$\begin{cases} \displaystyle\sum_{n=-\infty}^{\infty}\left[\bar{C}_n^+K_n'(\alpha a)+\bar{C}_{n-N}^+\left(K_{n-N}''(\alpha a)\frac{\alpha a}{2}+K_{n-N}(\alpha a)\frac{(n-N)N}{2\alpha a}\right)\epsilon\right. \\ \qquad\left.+C_{n+N}^+\left(K_{n+N}''(\alpha a)\frac{\alpha a}{2}-K_{n+N}(\alpha a)\frac{(n+N)N}{2\alpha a}\right)\epsilon\right]\mathrm{e}^{in\phi}= \\ \left(\dfrac{1}{1-\frac{\alpha U}{\omega}}\right)\displaystyle\sum_{n=-\infty}^{\infty}\left[\bar{C}_n^-I_n'(\alpha a)+\bar{C}_{n-N}^-\left(I_{n-N}''(\alpha a)\frac{\alpha a}{2}+I_{n-N}(\alpha a)\frac{(n-N)N}{2\alpha a}\right)\epsilon\right. \\ \qquad\left.+\bar{C}_{n+N}^-\left(I_{n+N}''(\alpha a)\frac{\alpha a}{2}-I_{n+N}(\alpha a)\frac{(n+N)N}{2\alpha a}\right)\epsilon\right]\mathrm{e}^{in\phi}, \\ \displaystyle\sum_{n=-\infty}^{\infty}\left(\bar{C}_n^+K_n(\alpha a)+\bar{C}_{n-N}^+K_{n-N}'(\alpha a)\frac{\alpha a}{2}\epsilon+\bar{C}_{n+N}^+K_{n+N}'(\alpha a)\frac{\alpha a}{2}\epsilon\right)\mathrm{e}^{in\phi}= \\ \left(1-\dfrac{\alpha U}{\omega}\right)\displaystyle\sum_{n=-\infty}^{\infty}\left(\bar{C}_n^-I_n(\alpha a)+\bar{C}_{n-N}^-I_{n-N}'(\alpha a)\frac{\alpha a}{2}\epsilon+\bar{C}_{n+N}^-I_{n+N}'(\alpha a)\frac{\alpha a}{2}\epsilon\right)\mathrm{e}^{in\phi}. \end{cases} \tag{7.39}$$

The above equations can be written in a more compact matrix form, from which the effects of lobed jets can be seen more clearly. Let $\boldsymbol{K}(\alpha a)$ denote the diagonal matrix

$$\boldsymbol{K}(\alpha a) = \begin{bmatrix} \ddots & & & & \\ \dots & K_{-1}(\alpha a) & \dots & \dots & \dots \\ \dots & \dots & K_0(\alpha a) & \dots & \dots \\ \dots & \dots & \dots & K_1(\alpha a) & \dots \\ & & & & \ddots \end{bmatrix}, \tag{7.40}$$

and let $\boldsymbol{K}_c(\alpha a)$ and $\boldsymbol{K}_s(\alpha a)$ to be

$$\boldsymbol{K}_c(\alpha a) = \begin{bmatrix} \dots & \dots \\ \dots K_{-N-1}(\alpha a) & \dots K_{N-1}(\alpha a) \dots\dots\dots \\ \dots\dots K_{-N}(\alpha a) & \dots\dots K_N(\alpha a) \dots\dots \\ \dots\dots\dots K_{-N+1}(\alpha a) & \dots\dots\dots K_{N+1}(\alpha a) \dots \\ \dots\dots\dots\dots & \dots\dots\dots\dots \end{bmatrix}, \tag{7.41}$$

and

$$\boldsymbol{K}_s(\alpha a) = \begin{bmatrix} \dots & \dots \\ \dots K_{-N-1}(\alpha a)(-N-1) & \dots - K_{N-1}(\alpha a)(N-1) \dots\dots\dots \\ \dots\dots K_{-N}(\alpha a)(-N) & \dots\dots - K_N(\alpha a)N \dots\dots \\ \dots\dots\dots K_{-N+1}(\alpha a)(-N+1) & \dots\dots\dots - K_{N+1}(\alpha a)(N+1) \dots \\ \dots\dots\dots\dots & \dots\dots\dots\dots \end{bmatrix}. \tag{7.42}$$

Clearly, each element of the matrices $\boldsymbol{K}(\alpha a)$, $\boldsymbol{K}_c(\alpha a)$ and $\boldsymbol{K}_s(\alpha a)$ is a function of αa, and consequently, these matrices are essentially function matrices with an argument αa. We can therefore define the nth derivative of a matrix to be the matrix formed by the nth derivative of each element function. For example, the first directive of $\boldsymbol{K}_c(\alpha a)$ is

$$\boldsymbol{K}'_c(\alpha a) = \begin{bmatrix} \dots & \dots \\ \dots K'_{-N-1}(\alpha a) & \dots K'_{N-1}(\alpha a) \dots\dots\dots \\ \dots\dots K'_{-N}(\alpha a) & \dots\dots K'_N(\alpha a) \dots\dots \\ \dots\dots\dots K'_{-N+1}(\alpha a) & \dots\dots\dots K'_{N+1}(\alpha a) \dots \\ \dots\dots\dots\dots & \dots\dots\dots\dots \end{bmatrix}. \tag{7.43}$$

If one replaces the Modified Bessel function of the second kind $K_n(\alpha a)$, in matrices $\boldsymbol{K}(\alpha a)$, $\boldsymbol{K}_c(\alpha a)$ and $\boldsymbol{K}_s(\alpha a)$, with function $I_n(\alpha a)$, the matrices $\boldsymbol{I}(\alpha a)$, $\boldsymbol{I}_c(\alpha a)$ and $\boldsymbol{I}_s(\alpha a)$

can be defined. Hence they are

$$\boldsymbol{I}(\alpha a)=\begin{bmatrix} \ddots & & & & \\ \dots & I_{-1}(\alpha a) & \dots & \dots & \dots \\ \dots & \dots & I_0(\alpha a) & \dots & \dots \\ \dots & \dots & \dots & I_1(\alpha a) & \dots \\ & & & & \ddots \end{bmatrix}, \tag{7.44}$$

$$\boldsymbol{I}_c(\alpha a)=\begin{bmatrix} \dots & \dots \\ \dots I_{-N-1}(\alpha a) & \dots I_{N-1}(\alpha a)\dots\dots\dots \\ \dots\dots I_{-N}(\alpha a) & \dots\dots I_N(\alpha a)\dots\dots \\ \dots\dots\dots I_{-N+1}(\alpha a) & \dots\dots\dots I_{N+1}(\alpha a)\dots \\ \dots\dots\dots\dots & \dots\dots\dots\dots \end{bmatrix}, \tag{7.45}$$

and

$$\boldsymbol{I}_s(\alpha a)=\begin{bmatrix} \dots & \dots \\ \dots I_{-N-1}(\alpha a)(-N-1) & \dots - I_{N-1}(\alpha a)(N-1)\dots\dots\dots \\ \dots\dots I_{-N}(\alpha a)(-N) & \dots\dots - I_N(\alpha a)N\dots\dots \\ \dots\dots\dots I_{-N+1}(\alpha a)(-N+1) & \dots\dots\dots - I_{N+1}(\alpha a)(N+1)\dots \\ \dots\dots\dots\dots & \dots\dots\dots\dots \end{bmatrix}, \tag{7.46}$$

respectively. The derivative of these matrices are defined in a similar manner as the matrix $\boldsymbol{K}_c'(\alpha a)$.

Upon defining the vector

$$\bar{\boldsymbol{C}}^{\pm}=\left[\dots,\bar{C}_{-n}^{\pm},\dots,\bar{C}_0^{\pm},\dots,\bar{C}_n^{\pm},\dots\right]^T, \tag{7.47}$$

where $[\ ]^T$ denotes the transpose of matrix $[\ ]$, equation 7.39 can be readily written as

$$\begin{cases} \left(1-\dfrac{\alpha U}{\omega}\right)\left[\boldsymbol{K}'(\alpha a)+\epsilon\left(\boldsymbol{K}_c''(\alpha a)\dfrac{\alpha a}{2}+\boldsymbol{K}_s(\alpha a)\dfrac{N}{2\alpha a}\right)\right]\bar{\boldsymbol{C}}^{+}= \\ \qquad\qquad\left[\boldsymbol{I}'(\alpha a)+\epsilon\left(\boldsymbol{I}_c''(\alpha a)\dfrac{\alpha a}{2}+\boldsymbol{I}_s(\alpha a)\dfrac{N}{2\alpha a}\right)\right]\bar{\boldsymbol{C}}^{-}, \\ \left[\boldsymbol{K}(\alpha a)+\epsilon\boldsymbol{K}_c'(\alpha a)\dfrac{\alpha a}{2}\right]\bar{\boldsymbol{C}}^{+}=\left(1-\dfrac{\alpha U}{\omega}\right)\left[\boldsymbol{I}(\alpha a)+\epsilon\boldsymbol{I}_c'(\alpha a)\dfrac{\alpha a}{2}\right]\bar{\boldsymbol{C}}^{-}. \end{cases} \tag{7.48}$$

Equation 7.48 represents the dispersion relationships for the considered lobed jet to the first-order accuracy. It is worth noting that both $\boldsymbol{K}(\alpha a)$ and $\boldsymbol{I}(\alpha a)$ are diagonal matrices. Therefore, in the case of $\epsilon=0$, i.e. the axisymmetric vortex sheet, equation 7.48 represents a set

of decoupled dispersion relation equations. Consequently, stability analysis can be performed for each mode individually and the results are identical to those obtained by Batchelor and Gill (1962), as shown above. When $\epsilon \neq 0$, the equations governing the dispersion relations for different order n are coupled together, hence the equations must be solved together.

Before proceeding to solve these equations, it is informative to examine how lobed vortex-sheet profiles affect the characteristic matrices. Firstly, one can see that the coupling only occurs between modes n, $n-N$ and $n+N$. Had we included higher order terms ($\epsilon^2, \epsilon^3 \ldots$), the coupling would involve modes $n \pm kN$ ($k = 0, \pm 1, \pm 2 \ldots$). This shows that the lobed profile affects the instability waves by modulating them with its own periodicity. Secondly, the modulating effects occur in two ways: modifying the radial length scales and changing the normal directions of vortex sheet. The effects of modifying the radial length scales are represented by the $\boldsymbol{K}_c^{(i)}(\alpha a)$ and $\boldsymbol{I}_c^{(i)}(\alpha a)$ matrices (i here denotes the ith derivative). Take the strongly-lobed profile of $N = 2$, as shown in figure 7.8(b), as an example. At such a large value of ϵ, the lobe profile resembles that of an elliptic vortex sheet. Hence, the radial length scales of the major and the minor axes are different. It is known that this causes different behaviour for instability waves orientated with different axes (Crighton, 1973). In the dynamic boundary conditions shown in equation 7.48, the $\boldsymbol{K}_c'(\alpha a)$ and $\boldsymbol{I}_c'(\alpha a)$ terms account for the different length scales (to the first order accuracy) and ensure pressure is continuous across the vortex sheet. The $\boldsymbol{K}_s(\alpha a)$ and $\boldsymbol{I}_s(\alpha a)$ matrices, on the other hand, account for changing of the restrictions on the normal perturbation velocities across the vortex sheet. Equation 7.32a shows that it is the normal (to the vortex sheet) perturbation velocities that have to satisfy the jumped condition. From equation 7.36 it is evident that the use of lobed nozzles can significantly change the local normal directions of the vortex sheet and hence the instability characteristics. Also, it is clear from equation 7.36 that the normal direction changes more pronouncedly as N increases.

To solve equation 7.48, we write the two matrix equations in a more compact form as

$$\begin{cases} \left(1 - \dfrac{\alpha U}{\omega}\right) \boldsymbol{K}_k \bar{\boldsymbol{C}}^+ = \boldsymbol{I}_k \bar{\boldsymbol{C}}^-, & \text{(7.49a)} \\ \boldsymbol{K}_d \bar{\boldsymbol{C}}^+ = \left(1 - \dfrac{\alpha U}{\omega}\right) \boldsymbol{I}_d \bar{\boldsymbol{C}}^-. & \text{(7.49b)} \end{cases}$$

The definitions of $\boldsymbol{K}_k$, $\boldsymbol{I}_k$, $\boldsymbol{K}_d$ and $\boldsymbol{I}_k$ should be obvious when compared with equation 7.48, and from now on we omit the argument αa of relevant matrices for brevity. Equations 7.49a and 7.49b are in terms of $\bar{\boldsymbol{C}}^{\pm}$, it is necessary to obtain an equation in terms of $\boldsymbol{C}^{\pm}$ ($\boldsymbol{C}^{\pm}$ is the column vector with elements $C_n^{\pm}$ rather than $\bar{C}_n^{\pm}$). This is because $C_n^{\pm}$ are the coefficients in front of normalized functions, and hence represent the proper amplitudes of their correspond-

ing eigenfunctions. On the other hand, $\bar{C}_n^{\pm}$ denote the non-normalized coefficients, hence their values would depend on the amplitudes of their eigenfunctions. For example, because the value of $I_n(\alpha a)$ at a fixed αa decreases exponentially as n increases, $\bar{C}_n^-$ would have to increase exponentially in order to ensure a physically meaningful result is obtained. This is apparently not suitable for any numerical evaluations at a later stage. Therefore, it is essential to rewrite the above two equations in terms of $\bar{C}^{\pm}$. It is straightforward to show $\boldsymbol{C}^+ = \boldsymbol{K}\bar{\boldsymbol{C}}^+$ and $\boldsymbol{C}^- = \boldsymbol{I}\bar{\boldsymbol{C}}^-$. Since both $\boldsymbol{I}$ and $\boldsymbol{K}$ are diagonal matrices, it is trivial to calculate their inverse matrices $\boldsymbol{I}^{-1}$ and $\boldsymbol{K}^{-1}$. Equations 7.49a and 7.49b can be easily changed to

$$\begin{cases} \left(1 - \dfrac{\alpha U}{\omega}\right)\widetilde{\boldsymbol{K}}_k\boldsymbol{C}^+ = \widetilde{\boldsymbol{I}}_k\boldsymbol{C}^-, & \text{(7.50a)} \\ \widetilde{\boldsymbol{K}}_d\boldsymbol{C}^+ = \left(1 - \dfrac{\alpha U}{\omega}\right)\widetilde{\boldsymbol{I}}_d\boldsymbol{C}^-, & \text{(7.50b)} \end{cases}$$

where $\widetilde{\boldsymbol{K}}_k = \boldsymbol{K}_k\boldsymbol{K}^{-1}$, $\widetilde{\boldsymbol{K}}_d = \boldsymbol{K}_d\boldsymbol{K}^{-1}$, $\widetilde{\boldsymbol{I}}_k = \boldsymbol{I}_k\boldsymbol{I}^{-1}$, $\widetilde{\boldsymbol{I}}_d = \boldsymbol{I}_d\boldsymbol{I}^{-1}$. These tilde matrices can be calculated quickly since both $\boldsymbol{I}^{-1}$ and $\boldsymbol{K}^{-1}$ are diagonal.

From equation 7.50b, we see that

$$\boldsymbol{C}^+ = \left(1 - \frac{\alpha U}{\omega}\right)\widetilde{\boldsymbol{K}}_d^{-1}\widetilde{\boldsymbol{I}}_d\boldsymbol{C}^-. \tag{7.51}$$

Substituting equation 7.51 into equation 7.50a, we have

$$\left(1 - \frac{\alpha U}{\omega}\right)^2\widetilde{\boldsymbol{K}}_k\widetilde{\boldsymbol{K}}_d^{-1}\widetilde{\boldsymbol{I}}_d\boldsymbol{C}^- = \widetilde{\boldsymbol{I}}_k\boldsymbol{C}^-. \tag{7.52}$$

Upon multiplying $\widetilde{\boldsymbol{I}}_k^{-1}$ on both sides of equation 7.52 and defining $\boldsymbol{A} = \widetilde{\boldsymbol{I}}_k^{-1}\widetilde{\boldsymbol{K}}_k\widetilde{\boldsymbol{K}}_d^{-1}\widetilde{\boldsymbol{I}}_d$, we obtain the following eigenvalue problem

$$\boldsymbol{A}\boldsymbol{C}^- = \lambda\boldsymbol{C}^-, \tag{7.53}$$

where

$$\lambda = \left(1 - \frac{\alpha U}{\omega}\right)^{-2}. \tag{7.54}$$

The matrix $\boldsymbol{A}$ is of an infinite dimension. In order to calculate its eigenvalues in practical cases, we may drop all the modes higher than order M (and less than $-M$). Though we expect results to become inaccurate for large modes close to M, it may yield satisfactory results for relatively low-order modes when M is taken to be adequately large. These low-order modes are of our primary interest in this study, since high-order modes vanish sufficiently quickly according to experimental results (Tinney and Jordan, 2008). Besides, the vortex-sheet assumption would fail for high-order modes anyway. By truncating high-order terms, we obtain a matrix of $(2M+$

$1)\times(2M+1)$, and there are $2M+1$ eigenvalues (degenerate eigenvalues are counted more than once) and their corresponding eigenvectors. For each obtained eigenvector $\boldsymbol{C}^-$, we can obtain the corresponding $\boldsymbol{C}^+$ easily from equation 7.51. The fact that the non-zero eigenvector $\boldsymbol{C}^-$ satisfies equation 7.53 entails that the non-trivial velocity potential ψ^-, determined by $\boldsymbol{C}^-$, and the corresponding ψ^+, determined by $\boldsymbol{C}^+$, satisfy both the kinematic and dynamic boundary conditions on the vortex sheet. Therefore, each eigenvector represents an eigenfunction of the lobed problem, i.e.

$$\begin{aligned} E_n^-(\sigma,\phi) &= \sum_{n=-\infty}^{\infty} C_n^- \frac{1}{I_n(\alpha a)} I_n(\alpha\sigma)\mathrm{e}^{in\phi}, \\ E_n^+(\sigma,\phi) &= \sum_{n=-\infty}^{\infty} C_n^+ \frac{1}{K_n(\alpha a)} K_n(\alpha\sigma)\mathrm{e}^{in\phi}. \end{aligned} \tag{7.55}$$

One can readily verify that, when $\boldsymbol{C}^-$ is normalized such that $(\boldsymbol{C}^-)^{*T}\boldsymbol{C}^- = 1$ and $\boldsymbol{C}^+$ is obtained from the dynamic boundary conditions shown in equation 7.51, both $E_n^-(\sigma,\phi)$ and $E_n^+(\sigma,\phi)$ are normalized as described in Section 7.2.2.

Since the eigenvector $\boldsymbol{C}^-$ of the matrix $\boldsymbol{A}$ fully determines the eigenfunction $E_n^-(\sigma,\phi)$, it is important to examine the properties of $\boldsymbol{A}$ and its eigenvectors. In order to do this, we need to define the rotation of any vector $\boldsymbol{C}$ as $\boldsymbol{C}^\dagger$, such that

$$(\boldsymbol{C}^\dagger)_n = C_{-n}, \tag{7.56}$$

where $(\boldsymbol{C}^\dagger)_n$ denotes the nth the element of the rotation vector $\boldsymbol{C}^\dagger$ and C_n is the nth element of $\boldsymbol{C}$. Note here the index of the vector $\boldsymbol{C}$ ranges from $-M$ to M. Similarly, we can define the rotation of any matrix $\boldsymbol{B}$ as

$$(\boldsymbol{B}^\dagger)_{ij} = B_{(-i)(-j)}, \tag{7.57}$$

where $(\boldsymbol{B}^\dagger)_{ij}$ denotes the element of $\boldsymbol{B}^\dagger$ at the ith row and the jth column, and B_{ij} are the indexed elements of matrix $\boldsymbol{B}$. If a vector $\boldsymbol{C}$ is equal to its rotation, we define it as symmetric. If, on the other hand, $\boldsymbol{C} = -\boldsymbol{C}^\dagger$, we define it as antisymmetric. Similarly, if a matrix $\boldsymbol{B}$ is equal to its rotation, we define it as rotationally symmetric. Anti-rotational symmetry follows a self-explanatory definition. One can now show that $(\boldsymbol{BC})^\dagger = \boldsymbol{B}^\dagger\boldsymbol{C}^\dagger$, because

$$\left((\boldsymbol{BC})^\dagger\right)_i = \sum_{j=-M}^{M} B_{(-i)j}C_j = \sum_{j=-M}^{M} B_{(-i)(-j)}C_{-j} = \left(\boldsymbol{B}^\dagger\boldsymbol{C}^\dagger\right)_i, \tag{7.58}$$

where i can be any number between $-M$ to M. Replacing the vector $\boldsymbol{C}$ in the above equations with a matrix $\boldsymbol{B}_2$ does not invalidate the formula, i.e. $(\boldsymbol{BB}_2)^\dagger = \boldsymbol{B}^\dagger\boldsymbol{B}_2^\dagger$ also holds. Therefore,

if both $\boldsymbol{B}$ and $\boldsymbol{B}_2$ are rationally symmetric matrices, then the product of them is also rotationally symmetric. This is because

$$(\boldsymbol{B}\boldsymbol{B}_2)^\dagger = \boldsymbol{B}^\dagger \boldsymbol{B}_2^\dagger = \boldsymbol{B}\boldsymbol{B}_2. \tag{7.59}$$

We now prove that the inverse of a rotationally symmetric matrix, if exists, is also rotationally symmetric. First, because it is assumed that the inverse of the rotationally symmetric $\boldsymbol{B}$ exists, we denote its column vectors by $\boldsymbol{D}_i$ ($i = -M \ldots M$), i.e.

$$\boldsymbol{B}^{-1} = [\boldsymbol{D}_{-M} \ldots \boldsymbol{D}_0 \ldots \boldsymbol{D}_M]. \tag{7.60}$$

Then according to the definition of the inverse matrix, one has

$$[\boldsymbol{B}\boldsymbol{D}_{-M} \ldots \boldsymbol{B}\boldsymbol{D}_0 \ldots \boldsymbol{B}\boldsymbol{D}_M] = [\boldsymbol{I}_{-M} \ldots \boldsymbol{I}_0 \ldots \boldsymbol{I}_M], \tag{7.61}$$

where $\boldsymbol{I}_i$ is the ith column of the identity matrix. Now for any positive number i, one has

$$\boldsymbol{B}\boldsymbol{D}_i = \boldsymbol{I}_i. \tag{7.62}$$

If taking the rotation of both sides of equation 7.62, one obtains

$$\boldsymbol{B}\boldsymbol{D}_i^\dagger = \boldsymbol{I}_{-i}, \tag{7.63}$$

where use is made of the fact that $\boldsymbol{I}_i^\dagger = \boldsymbol{I}_{-i}$ and $\boldsymbol{B}$ is equal to its own rotation. Comparing equation 7.63 with the $-i$ column of equation 7.61, we have $\boldsymbol{D}_i^\dagger = \boldsymbol{D}_{-i}$. This is because $\boldsymbol{B}$ is invertible, its has a full rank and the solution of equation 7.63 is unique. We have now proved that $\boldsymbol{B}^-$ is indeed a rationally symmetric matrix.

Examining the definitions of all the relevant $\boldsymbol{I}$ and $\boldsymbol{K}$ matrices, it is trivial to show that they are all rotationally symmetric. Based on the two conclusions discussed above, because the matrix $\boldsymbol{A}$ can be written as

$$\boldsymbol{A} = \widetilde{\boldsymbol{I}}_k^{-1} \widetilde{\boldsymbol{K}}_k \widetilde{\boldsymbol{K}}_d^{-1} \widetilde{\boldsymbol{I}}_d,$$

it can be easily shown that $\boldsymbol{A}$ is rotationally symmetric. One important property that follows is that if a vector $\boldsymbol{C}^-$ is one of the eigenvectors of $\boldsymbol{A}$, so is $\boldsymbol{C}^{-\dagger}$. This follows naturally after taking the rotation of both sides of the eigenvalue equation $\boldsymbol{A}\boldsymbol{C}^- = \lambda \boldsymbol{C}^-$. One consequence of this property is that if an eigenvalue λ_n of matrix $\boldsymbol{A}$ has no multiplicity, its eigenvector $\boldsymbol{C}^-$ must be either symmetric or antisymmetric. The second important property is that, for each multiple-folded eigenvalue λ_n, we can always construct both a symmetric (e.g. $\boldsymbol{C}^- + \boldsymbol{C}^{-\dagger}$) and an antisymmetric (e.g. $\boldsymbol{C}^- - \boldsymbol{C}^{-\dagger}$) eigenvector. These properties are essential when we try to assign an order to each obtained eigenvector as follows.

It is not difficult to show that, when $\epsilon = 0$, $\boldsymbol{A}$ is diagonal and its eigenvalues (diagonal elements) are

$$\lambda_n = \frac{K_n'(\alpha a) I_n(\alpha a)}{K_n(\alpha a) I_n'(\alpha a)} \tag{7.64}$$

and their corresponding normalized eigenvectors are

$$\boldsymbol{C}^- = [\ldots, 0, \ldots, 0, \ldots, 1, \ldots]^T, \tag{7.65}$$

where 1 appears at the position of C_n^-. The well-known results for the cylindrical vortex-sheet flow are recovered. When ϵ increases gradually, we expect that the eigenvector gradually changes to

$$\boldsymbol{C}^- = [\ldots, a_{-n}, \ldots, a_0, \ldots, 1 - a_n, \ldots]^T, \tag{7.66}$$

where a_n are complex numbers and $|a_n| \ll 1$. We may use this dominant-component property of $\boldsymbol{C}^-$ to label the order of the eigenfunctions. That is, the eigenfunction determined by the eigenvector

$$\boldsymbol{C}^- = \left[\ldots, C_{-n}^-, \ldots, C_0^-, \ldots, C_n^-, \ldots\right]^T \tag{7.67}$$

has an order n, if

$$||\boldsymbol{C}^- - \boldsymbol{G}|| = \sqrt{\sum_{j=-M}^{M} (|C_j^-| - G_j)^2} \tag{7.68}$$

yields a minimum value when

$$\boldsymbol{G} = [\ldots, 0, \ldots, 0, \ldots, g_n = 1, \ldots]^T, \tag{7.69}$$

where g_n is the element of the vector $\boldsymbol{G}$.

However, this is not always possible for the following reasons. From equation 7.64, where $\epsilon = 0$, it is clear that $\lambda_n = \lambda_{-n}$ ($n > 0$). Therefore, the eigenvectors corresponding to λ_n and λ_{-n} form a linear vector subspace. Any linear combination of these two vectors is also an eigenvector of matrix $\boldsymbol{A}$. For example,

$$\boldsymbol{C}^- = \left[\ldots, C_{-n}^- = \sqrt{2}/2, \ldots, 0, \ldots, C_n^- = \sqrt{2}/2, \ldots\right]^T \tag{7.70}$$

is also an eigenvector for matrix $\boldsymbol{A}$ when $\epsilon = 0$. When $\epsilon \neq 0$, one may similarly obtain some eigenvectors that have two dominant components. But if $\lambda_n = \lambda_{-n}$, we can always re-define them by linear combinations so that each eigenvector would have only one dominant component. Therefore, the above-mentioned labelling strategy would result in no ambiguity. However, when $\epsilon \neq 0$, λ_n and λ_{-n} do not necessarily have to be same any more. As we

discussed above, the eigenvector must be either symmetric or antisymmetric. Since both symmetric and antisymmetric eigenvectors have two dominant components at n and $-n$ respectively ($\lambda_n \neq \lambda_{-n}$, therefore one cannot perform a linear combination of the two corresponding eigenvectors), it is hard to determine whether this mode should be called mode n or $-n$.

To overcome this problem, if $\lambda_n = \lambda_{-n}(n > 0)$, we make use the second property of the eigenvectors and redefine one of the two corresponding eigenvectors to be symmetric and the other antisymmetric. In doing so, no matter whether λ_n and λ_{-n} are equal or not, each eigenvector would have two dominant components. Now if $||\boldsymbol{C}^- - \boldsymbol{G}||$ obtains its minimum when

$$\boldsymbol{G} = \Big[\ldots, g_{-n} = \sqrt{2}/2, \ldots, 0, \ldots, g_n = \sqrt{2}/2, \ldots\Big]^T, \tag{7.71}$$

we label the eigenvector as mode n if it is symmetric, and $-n$ if antisymmetric. For $n = 0$, it is trivial to label its order, and because we require $C_0^- \neq 0$, it can be shown that the eigenvector is also symmetric. By labelling the eigenvectors in this way, from equation 7.55, this means that all nonnegative eigenfunctions are even functions of ϕ and negative ones odd.

In the following analysis, the mode number for the obtained eigenfunction is designated according to the above conventions. Then for each mode n, we can calculate its corresponding eigenvalue λ_n at a given value of αa. The complex frequency ω can be directly obtained from λ_n according to equation 7.54. This complex number determines both the growth rate and the convection velocity of its corresponding instability wave. Therefore, by varying the values of ϵ and N, one can easily examine how different lobe geometry changes both the growth rate and convection velocity of instability waves of different orders.

Strongly lobed nozzle

For strongly lobed nozzles, e.g. $\epsilon \sim 0.2$, it is necessary to include high-order terms ϵ^n. Luckily this is not a difficult extension, and all the aforementioned procedures used to solve the eigenvalue problem remain the same. It suffices to find the high-order coefficient matrices and add them into equation 7.48, i.e.

$$\begin{aligned}
\boldsymbol{K}_k &= \boldsymbol{K}'(\alpha a) + \epsilon\Big(\boldsymbol{K}''_c(\alpha a)\frac{\alpha a}{2} + \boldsymbol{K}_s(\alpha a)\frac{N}{2\alpha a}\Big) + \epsilon^2\Big(\ldots\Big) + \cdots, \\
\boldsymbol{I}_k &= \boldsymbol{I}'(\alpha a) + \epsilon\Big(\boldsymbol{I}''_c(\alpha a)\frac{\alpha a}{2} + \boldsymbol{I}_s(\alpha a)\frac{N}{2\alpha a}\Big) + \epsilon^2\Big(\ldots\Big) + \cdots, \\
\boldsymbol{K}_d &= \boldsymbol{K}(\alpha a) + \epsilon\boldsymbol{K}'_c(\alpha a)\frac{\alpha a}{2} + \epsilon^2(\ldots) + \cdots, \\
\boldsymbol{I}_d &= \boldsymbol{I}(\alpha a) + \epsilon\boldsymbol{I}'_c(\alpha a)\frac{\alpha a}{2} + \epsilon^2(\ldots) + \cdots.
\end{aligned} \tag{7.72}$$

It is worth noting that incorporating higher-order terms does not invalidate the matrix $\boldsymbol{A}$ being rotationally symmetric, hence all the previous conclusions about its eigenvectors still remain valid. Due to the nature of higher-order Modified Bessel functions, expanding them around αa results in a slow convergence when ϵ is large. Therefore, the number of high-order terms needed increases quickly as ϵ increases. It also increases when we increase the value of M. However, this problem can be readily overcome by expanding properly scaled Modified Bessel functions. Since in this study we only need a relatively small M, and the extension of incorporating more higher-order terms can be promptly automated using computer programming, it is not strictly necessary to expand the scaled Modified Bessel functions instead. For example, a MATLAB code has been developed that can automatically incorporate as many orders of terms as needed. Due to its analytical nature, the computation is very fast. For example, a comprehensive eigenvalue analysis of order 10 with $M = 20$ takes less than 50 milliseconds. All the results shown in the following sections are obtained by incorporating higher-order terms to the order of 10 (ϵ^{10}) and with $M = 20$. We have carried out an analysis with higher number of modes ($M = 50$) with higher orders of accuracy and little change to the results occurs.

Validation

Before presenting any results, it is necessary to validate this new analysis framework. Luckily, it is very straightforward to do so. Since the entire analysis is devoted to calculating the eigenfunctions that satisfy both the kinematic and dynamic boundary conditions on the vortex sheet, we can examine the obtained eigenfunctions to ensure that they indeed satisfy the two boundary conditions. More precisely, we can show that for each pair of eigenfunctions obtained above, we have, on the vortex sheet,

$$\begin{cases} (1 - \alpha U/\omega)\nabla E_m^+(\sigma, \phi) \cdot \boldsymbol{n} = \nabla E_m^-(\sigma, \phi) \cdot \boldsymbol{n}, & \text{(7.73a)} \\ 1/(1 - \alpha U/\omega) E_m^+(\sigma, \phi) = E_m^-(\sigma, \phi). & \text{(7.73b)} \end{cases}$$

In the rest of this chapter, we refer to both sides of equation 7.73a and 7.73b as the normalized normal perturbation velocity and pressure, respectively. One can first evaluate both sides of the above two equations on the vortex sheet (similar to equation 7.37) and plot them together, and if the results are accurate, the normalized normal perturbation velocity and pressure would collapse. Since the eigenvector of mode n ($n \geq 0$) is symmetric, if it is also real, then it is effortless to show that the imaginary parts of $E_n^-(\sigma, \phi)$ are strictly zero. Similarly, the real parts of $E_{-n}^-(\sigma, \phi)$ also vanish when the eigenvector of mode $-n$ is real. For the results shown in this chapter, all the eigenvectors are real. Therefore, for mode n ($n \geq 0$), it suffices to plot only the real parts of equations 7.73a and 7.73b. Likewise, for mode $-n$ ($n > 0$), one only

needs to plot the imaginary parts. The results are shown in figures 7.9 to 7.11. These results are obtained with $M = 20$ and the involved matrices are approximated to ϵ^{10}.

Figure 7.9 shows how the boundary conditions are satisfied by the 0th-order eigenfunctions. These results are obtained with $\alpha a = 1$ and $\epsilon = 0.1$. Figures 7.9(a) and 7.9(b) show the matches of the left and right sides of equations 7.73b and 7.73a, respectively, when the number of lobes is $N = 1$. From figure 7.8(a), one can see that when $N = 1$, the lobed profile is not very significantly different from the axisymmetric one. The single lobe merely causes a displacement of the profile centre of the circular vortex sheet. Therefore, one expects that the dynamics of instability waves shall remain largely unchanged. Figure 7.9(a,b) indeed confirms this. Like that of an axisymmetric vortex-sheet flow, the amplitudes of the 0th pressure and normal velocity remain nearly constant. When N increases to 2, the lobed profile stops resembling a circle, and the effects of lobes are more pronounced, as shown in figure 7.9(c,d). The number of amplitude peaks for the normalized pressure is identical to N. This is expected, because, as we discussed above, the 0th mode is modulated by the periodicity of the lobed profile. When one uses a lobed profile of $N = 3$, the modulation effects are more marked. All these figures show an excellent match of the normalized pressure and normal velocity across the vortex sheet. This shows that $E_0^-(\sigma, \phi)$ and $E_0^+(\sigma, \phi)$ are indeed the eigenfunctions of the lobe problem, and the 0th-order results obtained are accurate.

Figure 7.10(a, f), on the other hand, shows the matches of the normalized pressure and normal velocity across the vortex sheet for modes ± 1. In the case of one single lobe, mode 1 and -1 resemble those of an axisymmetric vortex sheet in every aspect, as shown in figure 7.10(a, b). When two lobes are used, the antisymmetric (with respect to $\phi = 0$) eigenfunction starts to deviate from the normal $\sin\phi$ function, with its peak and valley somewhat flattened. The mode 1, on the other hand, remains largely similar to $\cos\phi$. When N increases to 3, both mode 1 and -1 respond to the change of vortex-sheet geometry and change their shapes accordingly. The important observation, however, is the continuously excellent match of the pressure and normal velocity across the vortex sheet. This shows that the analytical method also works well for modes ± 1. It is worth noting that, for $N = 1$ and $N = 2$, the eigenvalues $\lambda_1 \neq \lambda_{-1}$. Therefore, both $E_1^-(\sigma, \phi)$ and $E_{-1}^-(\sigma, \phi)$ have a standing wave pattern with respect to ϕ and they cannot be combined to produce a travelling wave. However, for $N = 3$ we find that $\lambda_1 = \lambda_{-1}$. Therefore, a travelling-wave pattern can be obtained.

Figure 7.11(a, f) shows the results for mode ± 2. From figure 7.11(a-d), one can see that a single lobe and two lobes do not significantly change the shapes of the eigenfunctions $E_2^-(\sigma, \phi)$ and $E_{-2}^-(\sigma, \phi)$. However, a significant change of shapes occurs for $N = 3$. Similar to the

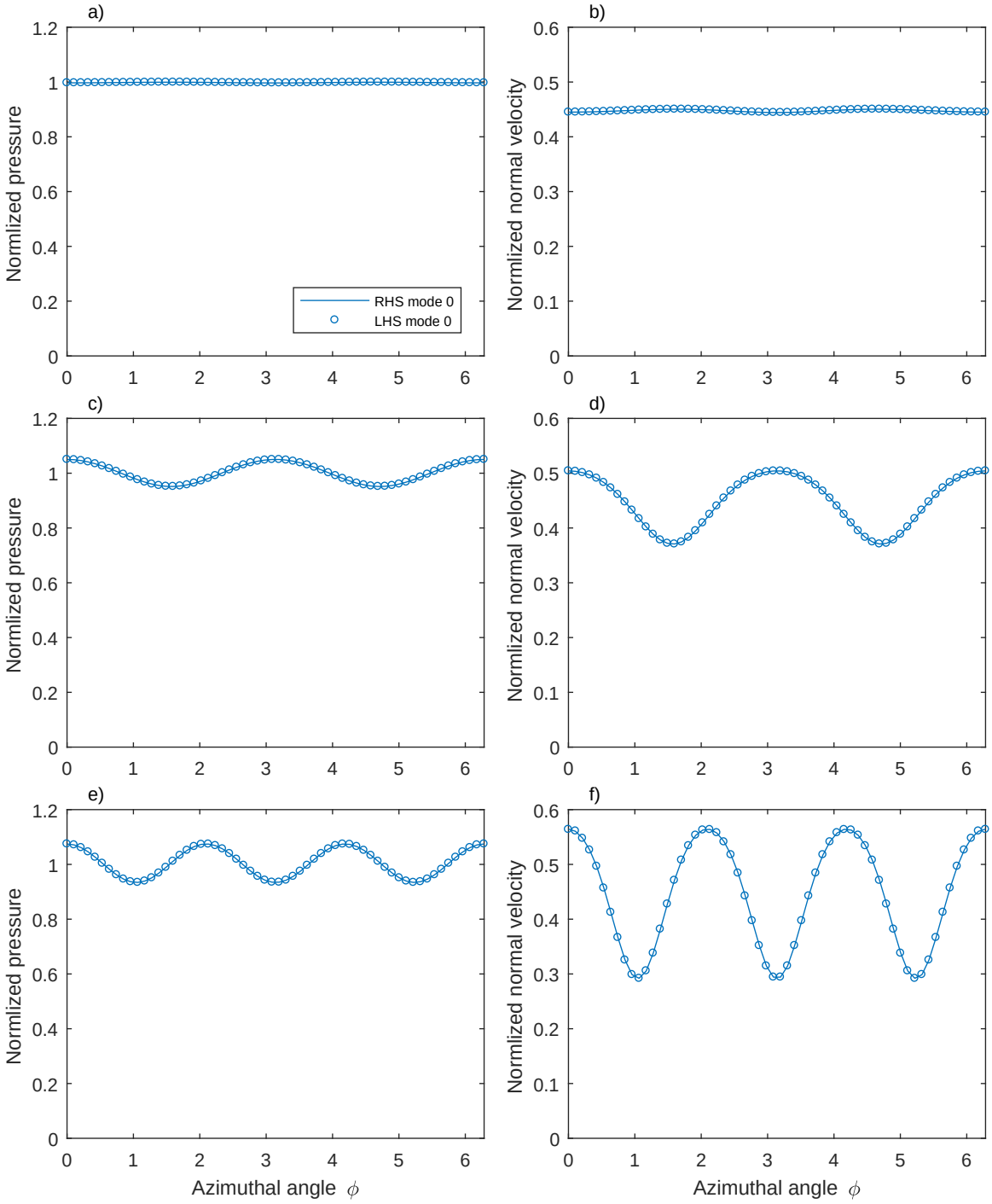

Figure 7.9: The match validation of the dynamic (left) and kinematic (right) boundary conditions for the eigenfunctions of mode 0 when the number of lobes N are different: a, b) $N = 1$; c, d) $N = 2$; e, f) $N = 3$. The normalized wavenumber is $\alpha a = 1$ and the lobed profile has a penetration ratio $\epsilon = 0.1$.

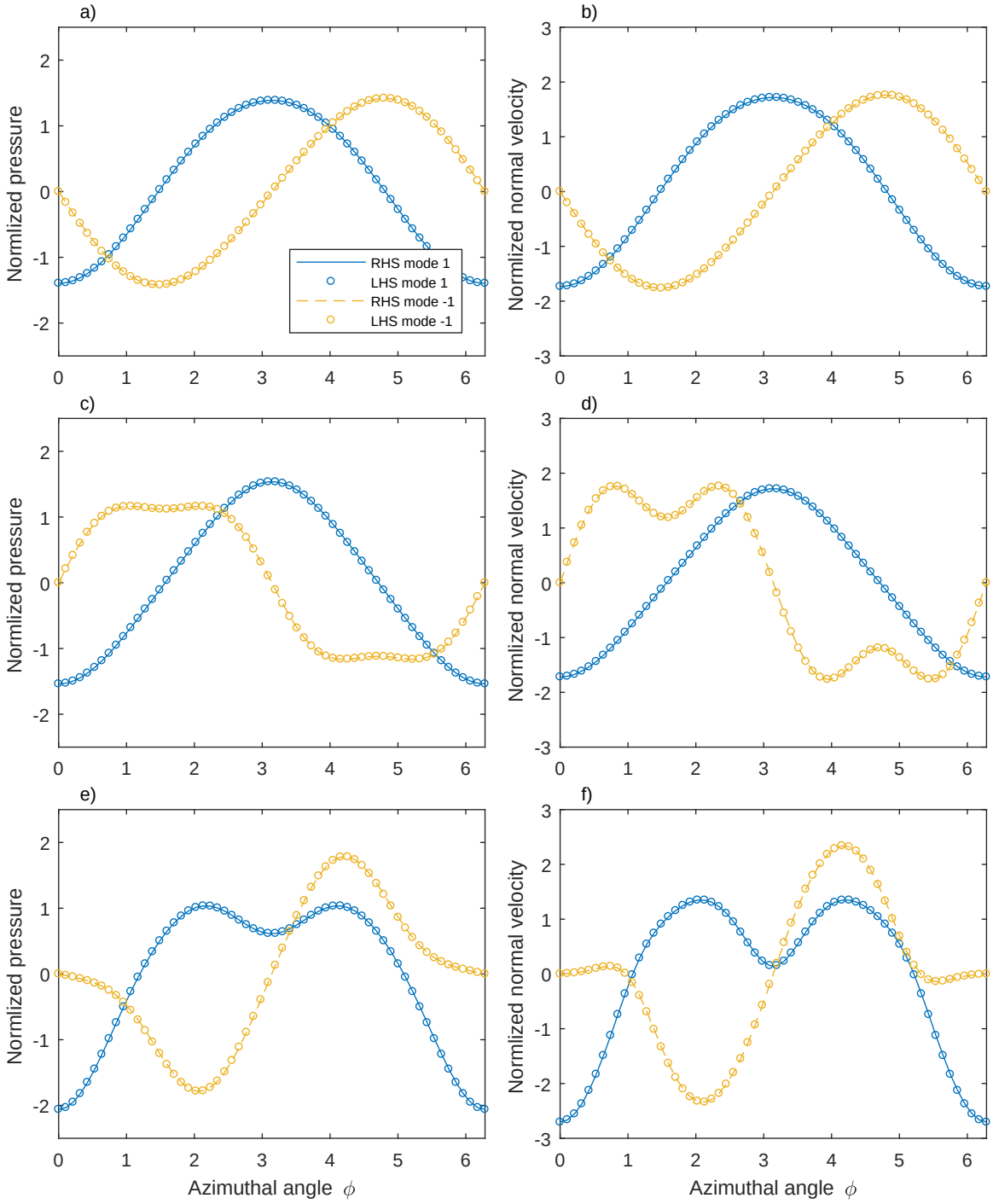

Figure 7.10: The match validation of the dynamic (left) and kinematic (right) boundary conditions for the eigenfunctions of modes ± 1 when the number of lobes N are different: a, b) $N = 1$; c, d) $N = 2$; e, f) $N = 3$. The normalized wavenumber is $\alpha a = 1$ and the lobed profile has a penetration ratio $\epsilon = 0.1$.

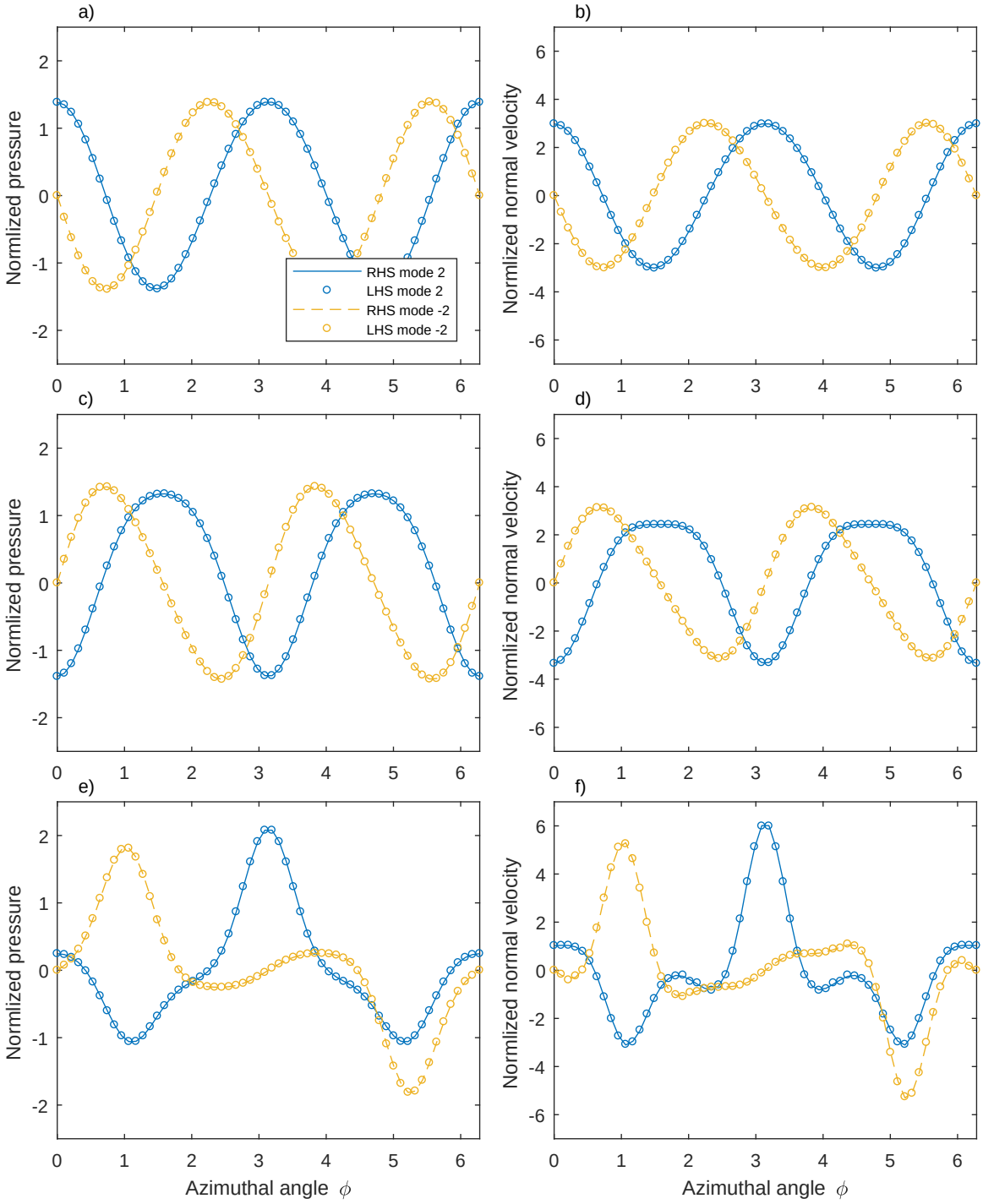

Figure 7.11: The match validation of the dynamic (left) and kinematic (right) boundary conditions for the eigenfunctions of modes ± 2 when the number of lobes N are different: a, b) $N = 1$; c, d) $N = 2$; e, f) $N = 3$. The normalized wavenumber is $\alpha a = 1$ and the lobed profile has a penetration ratio $\epsilon = 0.1$.

behaviour of the instability waves of modes ± 1, only a standing-wave pattern is allowed for $N = 1$ and $N = 2$, whereas two travelling-wave patterns can occur for $N = 3$. Again, for all the six figures, one can see the exceptionally good matches of the pressure and normal velocity across the layer of vortex sheet. The excellent agreement seen from figures 7.9 to 7.11 shows that the analytical framework developed in this section works exceptionally well, at least for the low-order modes like those we have just shown.

The effects of lobed profiles on the convection velocity and growth rate of instability waves

Having validated the analytical framework, we are now in a position to examine the effects of lobed profiles on the convection velocity and growth rate of instability waves. It is known that both quantities are frequency-dependent. Therefore, in the rest of this section, we plot both quantities versus the normalized frequency αa, for lobed profiles of different geometry.

We start from showing results for the 0th-order instability waves. These are shown in figure 7.12. Figure 7.12(a) shows the convection velocity and growth rate for a single-lobe profile. To facilitate a direct comparison to the results of a cylindrical vortex sheet, both quantities are plotted when $\epsilon = 0$ first. As can be seen, when the frequency αa increases, the normalized convection velocity ($\Re U_c/U$) decreases from unity to around 0.5, whereas the normalized growth rate ($\Im U_c/U$) increases from 0 to the same limit value. However, it shows that a single lobe does not cause any observable changes to the characteristics of 0th-order instability waves at all frequencies, no matter what value of ϵ is used. The same conclusion can be reached for $N = 2$, which is shown in figure 7.12(b). Keeping increasing the number of lobes to 3, however, starts to cause a slightly larger convection velocity and a marginally lower growth rate. These results are shown in figure 7.12(c), from which we see that the changes are only observable at high frequencies. However, they become more pronounced when the penetration ratio ϵ increases. The increase of the convection velocity and the reduction of the temporal growth rate, caused by lobed vortex-sheet profiles, are more evident when the number of lobes is increased to 5. As shown in figure 7.12(d), at high frequencies ($\alpha a > 1.5$), a large penetration ratio results in an effective rise of the convection velocity and a less effective drop of the growth rate. These results are in accord with the findings of Lajús Jr. et al. (2015) and Sinha et al. (2016). However, one should note that although these changes are observable, they are not in any way significant.

Figure 7.12 shows that 0th-order instability waves are not very sensitive to both the number of lobes and the penetration ratio. Figure 7.13, however, shows a different story for mode 1. The eigenfunctions corresponding to mode 1 are even functions of ϕ. Figure 7.13(a) still

indicates that a single lobe does not noticeably change the characteristics of the 1st-order instability waves. This is somewhat expected. Because, as we observed before, one single lobe merely causes a displacement of the profile's geometrical centre. Therefore, the physics should more or less stay the same as that of an axisymmetric vortex-sheet. This is consistent with the results shown in figure 7.13(a). However, figure 7.13(b) shows that the use of 2 lobes leads to

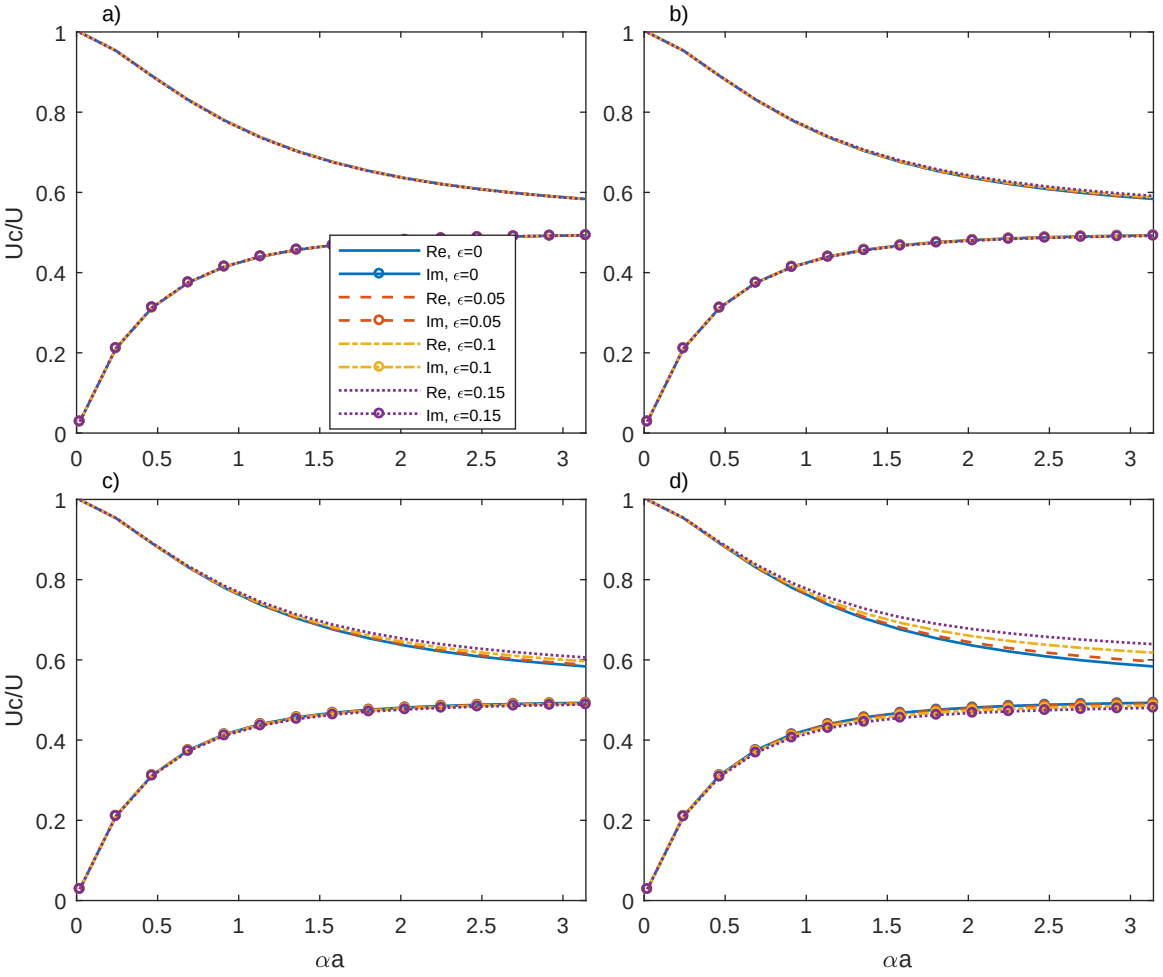

Figure 7.12: The convection velocity and growth rate of the 0th-order jet instability waves for vortex sheets of different lobed geometry: a) $N = 1$; b) $N = 2$; c) $N = 3$; d) $N = 5$.

a pronounced increase of the convection velocity, and a slight decrease of the temporal growth rate. In contrast to those shown in figure 7.12, the increase of the convection velocity is more marked at low frequencies. Similarly, increasing ϵ results in a stronger rise of the convection velocity. It is very increasing to note that the rise of the convection velocity is nearly linear with respect to ϵ. The decrease of the temporal growth rate, however, is most notable in the intermediate frequency range, and the maximum decrease is very small. Figure 7.13(c) shows

the results for $N = 3$. Compared to figure 7.13(b), the effects of lobes on both the convection velocity and the growth rate appear to be more effective. The most pronounced change, however, occurs when N increases to 5, as shown in figure 7.13(d). Again, these results are consistent with the findings of Sinha et al. (2016). The dependence of both the convection velocity and the temporal growth rate on ϵ appears to linear. But the relative change of the former is significantly larger than that of the latter.

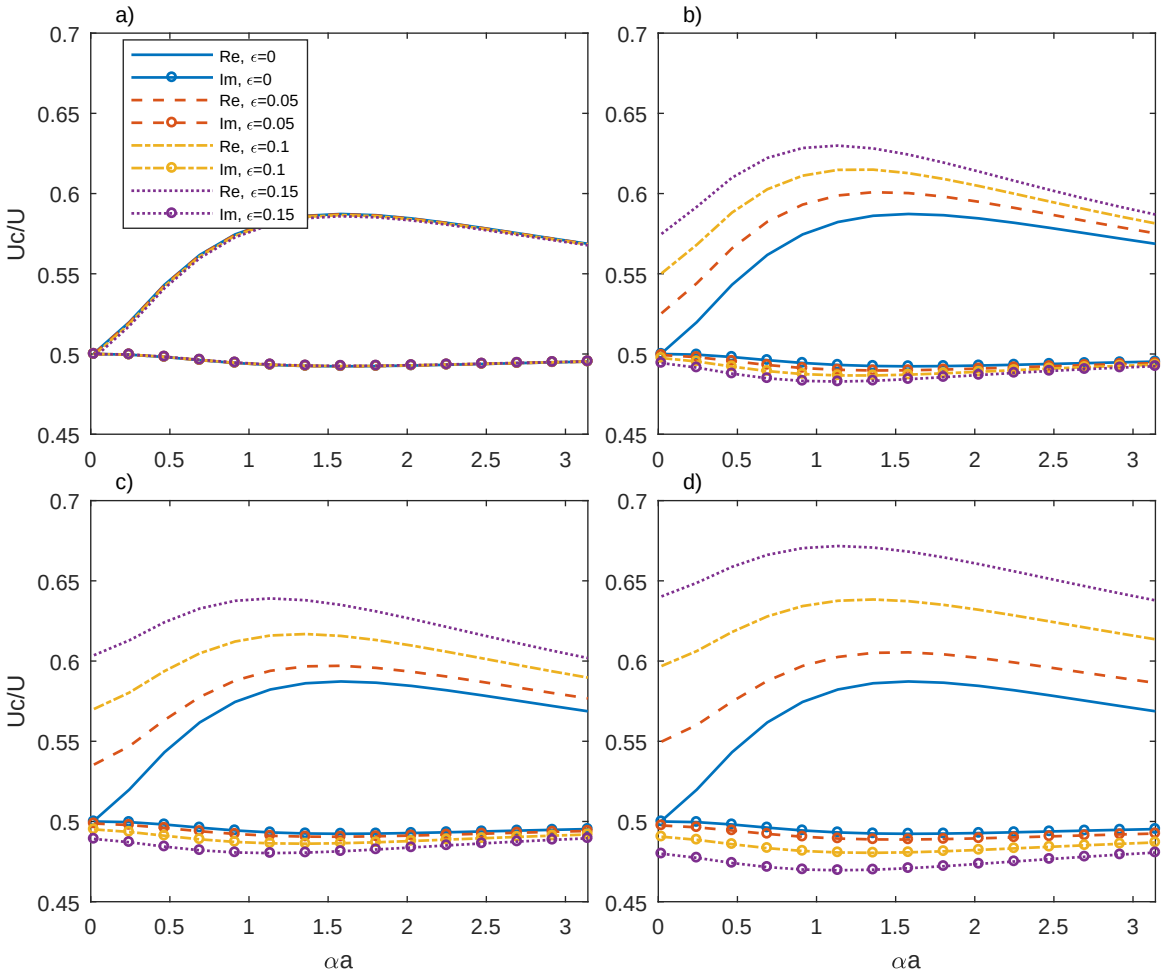

Figure 7.13: The convection velocity and growth rate of the 1th-order jet instability waves for vortex sheets of different lobed geometry: a) $N = 1$; b) $N = 2$; c) $N = 3$ d) $N = 5$.

Figure 7.14 presents the results for the mode -1. The eigenfunctions are odd functions of ϕ. Still, figure 7.14(a) does not show observable changes when ϵ increases. However, zooming in this figure, one can see that the convection velocity is weakly increasing as ϵ increases, and this is opposite to that observed in figure 7.13(a)! This different behaviour is because λ_1 is not identical to λ_{-1} any more. Therefore, the odd and even eigenfunctions are now independent

to each other and they change towards opposite directions as ϵ increases. If figures 7.14(a) and 7.13(a) are too similar to each other to make this trend clear, figure 7.14(b) makes it much more evident. The number of lobes is now 2, and the lobed profile is approximately elliptic. In-

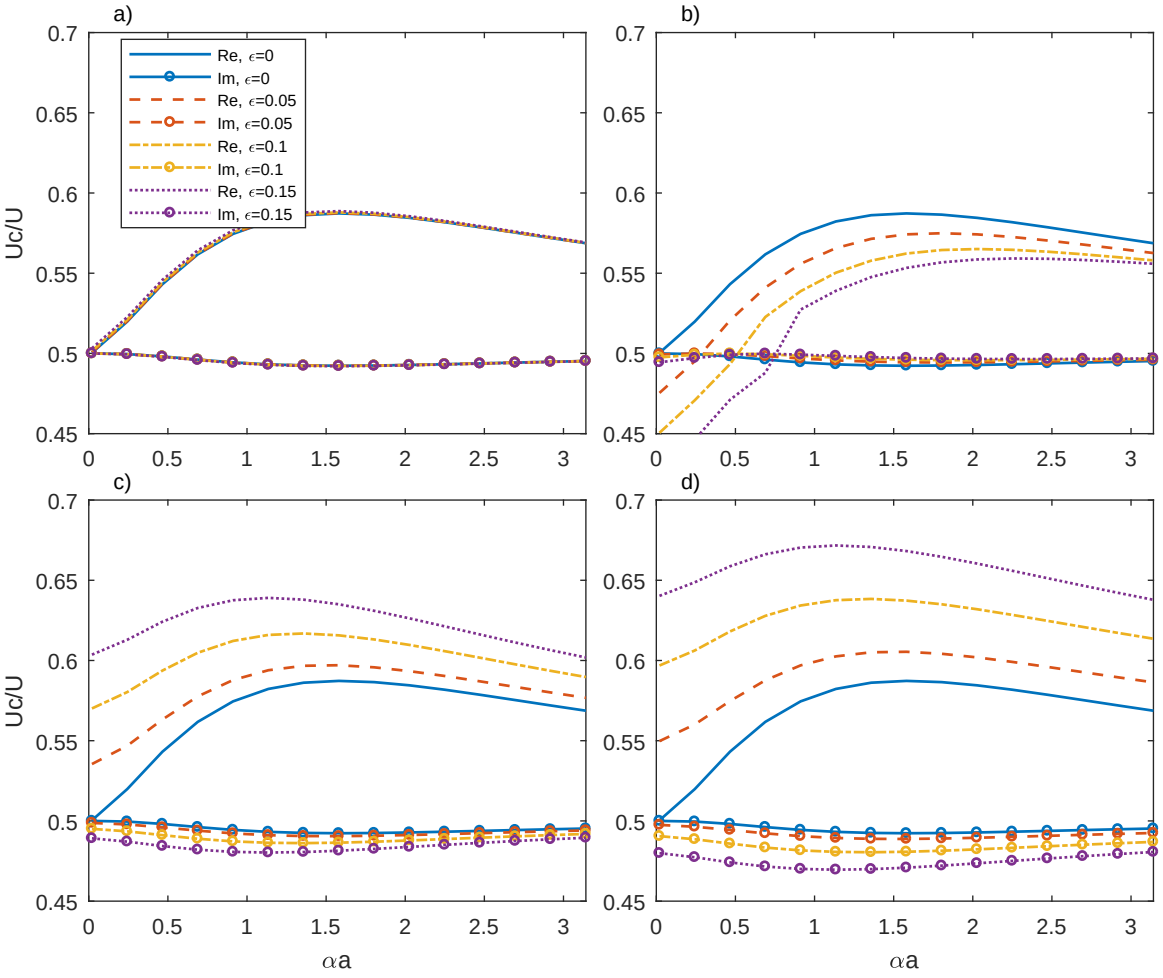

Figure 7.14: The convection velocity and growth rate of the -1th-order jet instability waves for vortex sheets of different lobed geometry: a) $N = 1$; b) $N = 2$; c) $N = 3$; d) $N = 5$.

stead of obtaining higher convection velocities, increasing ϵ from 0 now results in increasingly smaller convection velocities. The temporal growth rate, on the other hand, starts to drop at low frequencies ($\alpha a < 0.5$), but gradually changes to increase at high frequencies, although both of which are on a small scale. The different eigenvalues of modes ± 1, hence distinctive characteristics of instability waves of modes ± 1, are consistent with the analytical results obtained by Crighton (1973) for elliptic vortex sheets and also agree with the findings in the spatial stability analysis carried out by Kopiev et al. (2004) (because the mode number 1 is a half of the number of lobes $N = 2$). Figure 7.14(c,d) shows the results for $N = 3$ and $N = 5$, respec-

tively. One can easily verify that they are identical to those shown in figure 7.13(c, d). This is because, for both $N = 3$ and $N = 5$, the eigenvalues λ_n remain identical to λ_{-n}. As discussed in Section 7.2.4, this also implies that azimuthally travelling waves can exist, in contrast to the case of $\lambda_n \neq \lambda_{-n}$, where only azimuthally standing waves are allowed.

Figure 7.15 shows results for the 2nd-order instability waves. Figure 7.15(a) is for $N = 1$. We expect little change caused by one single lobe, and this is demonstrated clearly by the figure. The results for $N = 2$ are shown in figure 7.15(b). The 2nd-order instability waves have

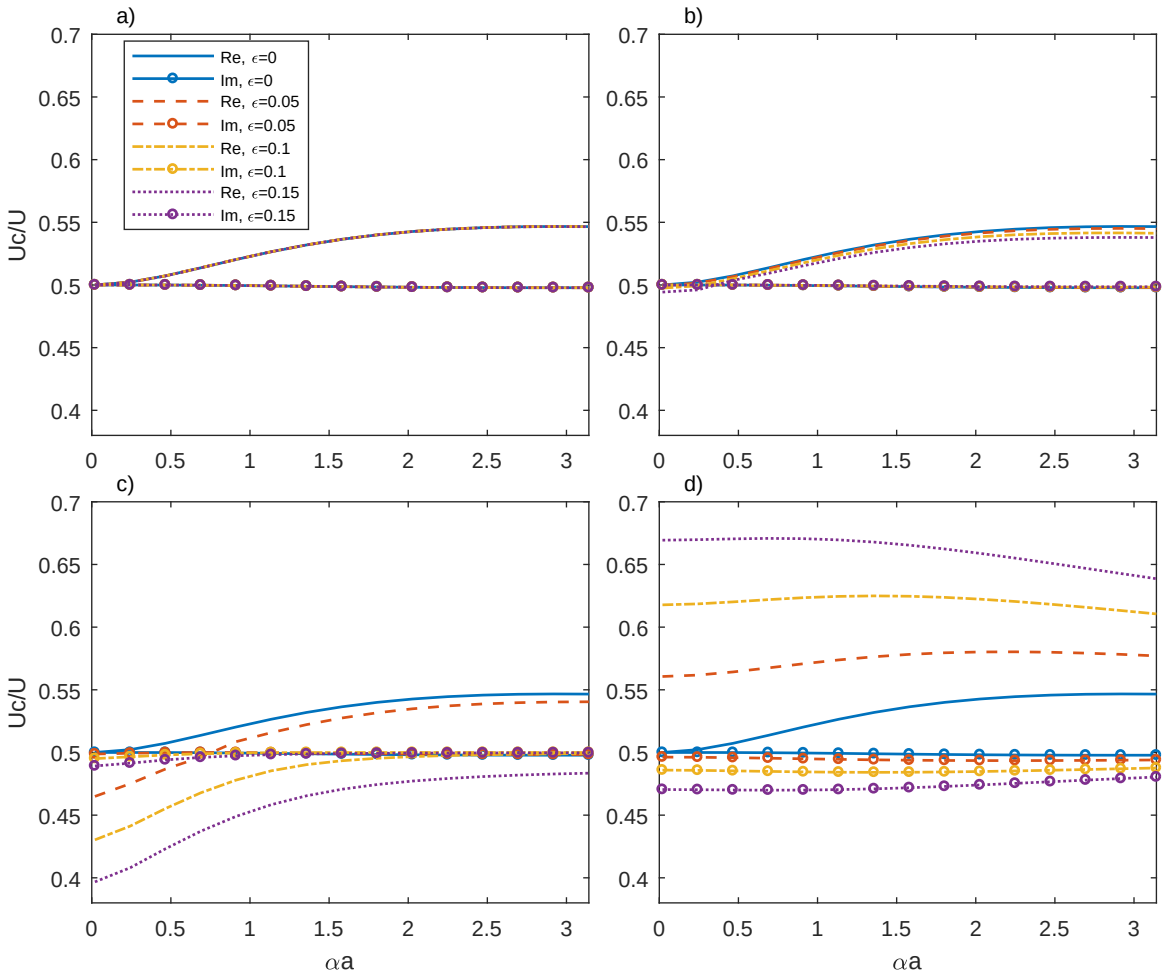

Figure 7.15: The convection velocity and growth rate of the 2th-order jet instability waves for vortex sheets of different lobed geometry: a) $N = 1$; b) $N = 2$; c) $N = 3$; d) $N = 5$.

increasingly lower convection velocities when ϵ increases. But the changes are very small. The changes of the temporal growth rate are nearly unobservable. However, using 3 lobes can still effectively reduce the convection velocity while marginally altering the temporal growth rate of the 2nd-order instability waves. Like all the results we have reported, the use of 5 lobes is the

most effective way of increasing the convection velocity and decreasing the temporal growth rate. Figure 7.16 shows the results for the -2nd-order instability waves. Figure 7.16(a) exhibits expected behaviour for a lobed profile of $N = 1$. Figure 7.16(b) shows a very slight increase of the convection velocity and no change to the temporal growth rate. We emphasize again that this is due to $\lambda_n \neq \lambda_{-n}$. Figures 7.16(c) and 7.16(d) are identical to figures 7.15(c) and 7.15(d) respectively because of identical eigenvalues.

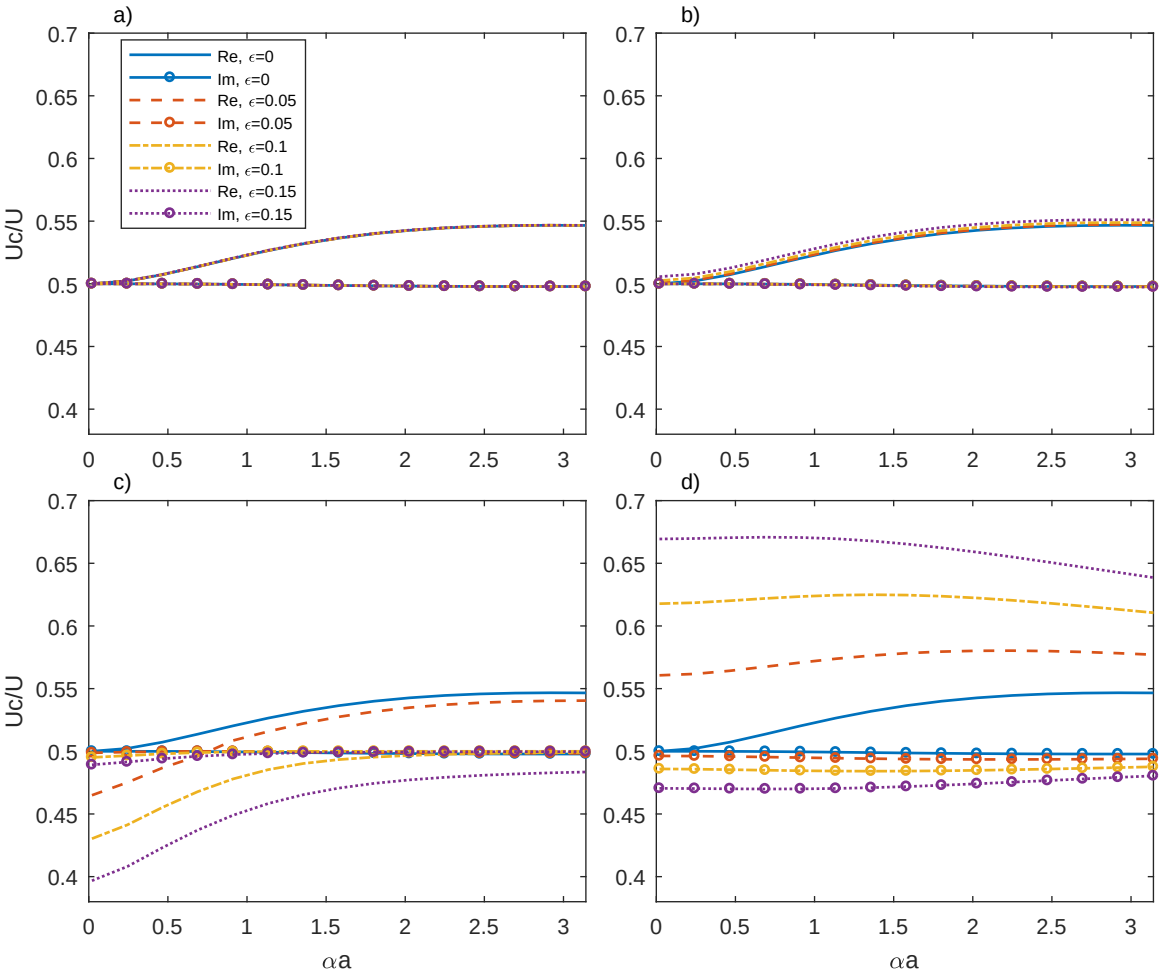

Figure 7.16: The convection velocity and growth rate of the -2th-order jet instability waves for vortex sheets of different lobed geometry: a) $N = 1$; b) $N = 2$; c) $N = 3$; d) $N = 5$.

In summary, the stability characteristics of base flows of a lobed vortex-sheet type are different from those of axisymmetric ones. The differences consist of changes to both the convection velocity and the temporal growth rate of instability waves. The changes become more pronounced as the number of lobes N and the penetration ratio ϵ increase. However, instability waves of different orders are affected differently by the lobe geometry. In particular,

little change occurs for mode 0, no matter how large both N and ϵ are. On the other hand, an evident alteration of the characteristics of high-order jet instability waves occurs when $N > 1$. For $N = 3$ and $N = 5$, azimuthally even and odd instability waves evince the same characteristics. However, for $N = 2$ and $N = 1$, even and odd instability waves of lobed jets exhibit two different types of behaviour, with one having favourable effects on installed jet noise reduction and the other having adverse. Therefore, for the sake of suppressing instability waves, or achieving installed jet noise reduction, it is desired to use a lobed profile of large N with a large penetration ratio, such as $N = 5$.

Discussion on the experimental results

In Section 7.1, we see that the use of lobed nozzles does not notably change installed jet noise. Combined with the analytical results obtained in this section, we may guess the possible causes.

The analytical framework developed in this section shows that a lobed vortex sheet with $N = 5$ should cause an observable increase of the convection velocity for instability waves of modes ± 1 and ± 2. It should also cause a slight reduction of the temporal growth rate. Both changes are favourable to installed jet noise reduction, since the first of which results in a less efficient scattering of instability waves into sound, and the second of which results in less strong instability waves. However, one should note that the above conclusion is based on a vortex-sheet-type jet mean flow. The realistic jet mean flow is different and the slight advantage obtained with the use of lobed profiles might be smeared out by the realistic jet mean flow profiles. Therefore, the first reason that one can guess is that the realistic jet mean flow might become axisymmetric too quickly to affect the jet instability waves due to strong jet mixing. In particular, the number of lobes used in the experiment is 5, and a large number of lobes are likely to cause a quicker mixing. The second reason, however, can be guessed from the fact that the 0th-order jet instability waves of a lobed jet of a vortex-sheet type are not sensitive to the lobed geometry. This is especially true for low frequencies, where installed jet noise is relevant (see figure 7.12(d) for example). Therefore, although higher-order instability waves are somewhat suppressed, the mode 0 still remains roughly the same. And if mode 0 is the dominant instability mode, little change of the installed jet noise can be expected.

7.3 Summary

This chapter explores the potential of lobed nozzles on reducing installed jet noise. It starts with an experimental study of the isolated and installed jet noise using lobed nozzles. It is shown

that the lobed nozzle has nearly identical effects on installed jet noise for all plate positions and Mach numbers: on the shielded side of the flat plate, lobed nozzles do not noticeably change the installed jet noise spectra at low frequencies. However, it does result in a slight noise reduction at high frequencies. This is thought to be caused by the reduction of isolated jet noise. On the reflected side of the flat plate, the noise reduction is more effective in the intermediate frequency regime, while a negligible or even slight noise increase is observed at high frequencies. This different behaviour between the shielded and reflected sides is thought to be due to the refraction effects caused by jet plumes.

To understand why lobed nozzles have little effect on reducing the low-frequency noise hump due to the scattering of instability waves, an analytical study of the stability characteristics of a parallel jet mean flow of vortex sheet type is performed. It is shown that the lobed geometry changes both the convection velocity and the temporal growth rate of the instability waves. The effects are more pronounced as the number of lobes N and the penetration ratio ϵ increase. However, instability waves of different orders are affected differently by the lobes. For instance, the mode 0 is particularly insensitive to the geometry changes. Higher modes are more likely to be changed significantly when both N and ϵ are sufficiently large. An intersting finding is that when $N = 1$ and $N = 2$ different behaviour occurs between the even and odd instability waves of certain orders. It is concluded that in order to suppressing instability waves for the sake of reducing installed jet noise, a large N, such as $N = 5$, and a large ϵ are desirable. Based on these analytical findings, it is postulated that the little change to the installed jet noise observed experimentally at low-frequencies is either due to the dominance of the 0th instabilty wave, or the fact that the jet mean flow downstream becomes axisymmetric too quickly to affect the jet instability waves.

Chapter 8

Noise for Round Nozzles with Modified Pylons

In Chapter 7, we carried out an experimental study on the aeroacoustics of installed lobed jets and found that the noise is slightly reduced at high frequencies but remains largely unchanged at low frequencies. We postulated that this could be due to two different reasons, the details of which are discussed at the end of Chapter 7. This leads us to consider a different approach to control instability waves, and hence installed jet noise at low frequencies. Considering realistic aircraft configurations, we can achieve the same goal of changing instability waves, in addition to nozzle treatments, by modifying the pylons.

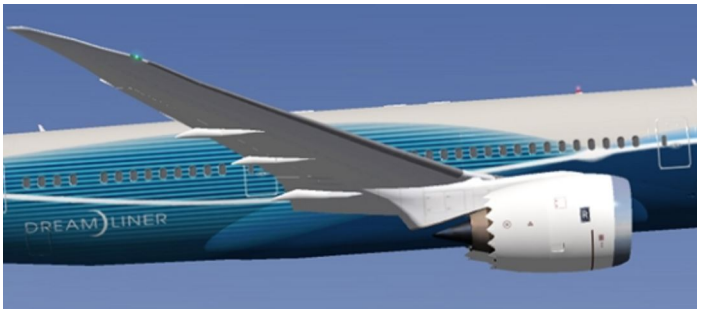

Figure 8.1: The wing, engine and pylon used in a Boeing 787 Dreamliner, courtesy of the Boeing Company.

Figure 8.1 shows the pylon used in a modern Boeing 787 Dreamliner. We can see that the pylon is rather long and sits directly inside the jet flow. Therefore, it has the potential of affecting instability waves. A crucial consequence of using such a pylon is that it changes the boundary conditions that the instability waves must satisfy, i.e. vanishing normal velocities on

both sides of the pylon. However, using a single pylon does not impose a severe restriction on the instability waves of different orders. In particular, each mode can still exist as long as it is symmetric with respect to the pylon (because of the zero normal velocities). A stringent restriction would occur if we have two pylons at different azimuthal angles, on both of which normal velocities have to vanish. This thus inspires us to examine the effects of using two pylons on installed jet noise, in particular, to investigate the low-frequency peak caused by the scattering of instability waves.

8.1 Experimental setup

The experimental rig remains largely unchanged compared to that described in Chapter 6, except the addition of two pylons, which is shown in figure 8.2. The pylons are around 4 jet diam-

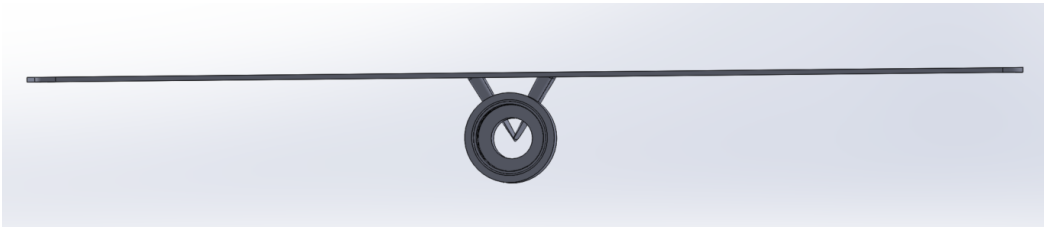

(a) Front view.

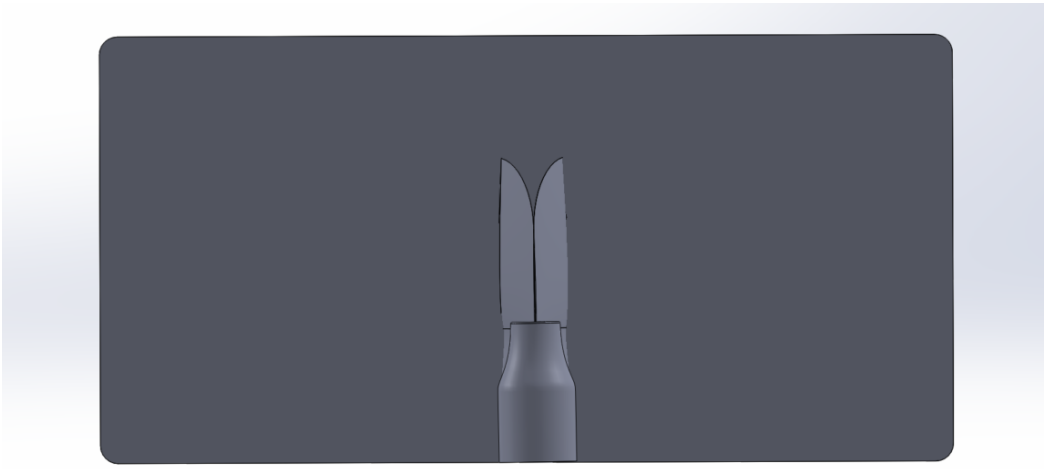

(b) Bottom view.

Figure 8.2: The flat plate, round nozzle and two pylons used in the experiments.

eters long. The angle between the two pylons is 60°. One can easily verify that this excludes the instability waves of order 1 and 2, but allows the existence of mode 0 and 3. However, as shown

in Chapter 5, modes higher than 2 contain a small amount of energy while mode 1 contains the same order of magnitude of energy as mode 0 at downstream locations such as $z = 6D$. Therefore, by eliminating modes 1 and 2, we expect the installed jet noise to be reduced by an observable amount. To ensure the most stringent restriction on instability waves, the pylons are extended to the centre of the nozzle, as can be seen from figure 8.2(a). However, this also results in blockage of the jet flow and effectively reduces the area of the nozzle exit. Because we keep the mass flow rate to be the same in this experiment as that described in Chapter 6, the jet exit velocity is higher, hence produces louder isolated jet noise. But if installed noise reduction is still achieved, an even more effective noise abatement can be naturally expected when the thrust is kept the same in practical cases.

8.2 Experimental results

The experimentally measured noise spectra at different observer angles are compared with those for the round nozzle shown in Chapter 6. We emphasize again that this is the most conservative comparison. Firstly, the effective area of the nozzle exit is smaller, therefore a higher average jet velocity, hence louder noise, is expected. Secondly, the addition of pylons would inevitably cause the formation of boundary layers on the surface of pylons, and even a small region of flow separation, which in turn cause a noise increase. If this most conservative comparison yields a reduction of the low-frequency bump, a larger noise reduction can be achieved in realistic cases, where the thrust is kept the same and a single pylon is used in the datum case.

To assess the blockage and boundary-layer effects of the pylons, we first remove the flat plate and measure the isolated noise spectra (but with two pylons) at different angles. We then compare the results with the isolated noise spectra for a round nozzle obtained in Chapter 6. The results are shown in figure 8.3. As can be seen, an average noise increase of 4 dB is observed at all different angles when two pylons are placed near a round nozzle. This is consistent with the fact that the jet exit velocity is higher due to the blockage effects of the pylons. However, we can also see that, at 90° and 60° to the jet axis, a significant noise increase is observed in the intermediate frequency regime. This is thought to be due to increased turbulence due to boundary layers and possibly flow separations. It should be noted that these effects would also occur in realistic aircraft configurations, where a single pylon is used. Therefore, if we were to compare the results with those for a round nozzle but with a single pylon with the same blockage effects, the noise increase would probably be significantly reduced or even negligible.

With the knowledge of the pylons' effects, we now place the flat plate at $L = 6$ and $H =$

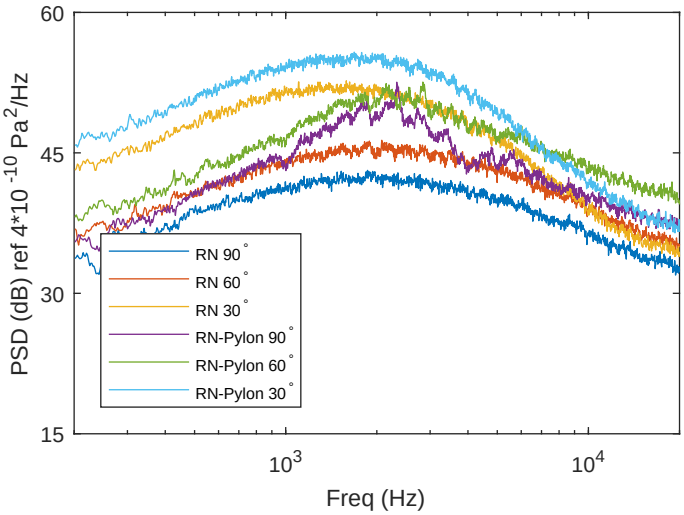

Figure 8.3: Comparison of the isolated noise spectra for a round nozzle with two pylons and those for an individual round nozzle at the same flow rate.

1.5, and evaluate how the two pylons affect the instability waves, and hence the installed jet noise. The results are shown in figure 8.4. When the observer is at 90° to the jet axis, we can

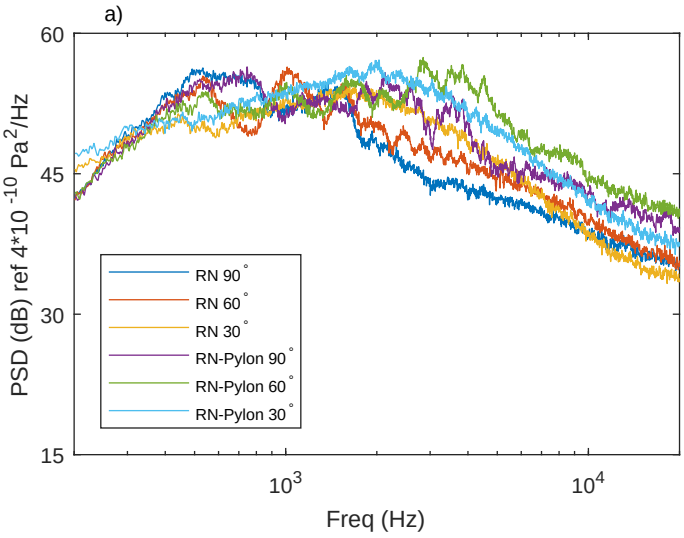

Figure 8.4: Comparison of the installed noise spectra for a round nozzle with two pylons and those for an individual round nozzle at the same flow rate.

see that using two pylons results in a noise reduction of around $2 \sim 3$ dB around the low-frequency bump caused by the scattering of instability waves. This is a very encouraging result considering that the jet exit velocity is higher for the nozzle-and-pylon case. The noise reduction is most pronounced at the installation peak. As the frequency increases further, this advantage

is gradually overtaken by the adverse influence of the higher jet velocity. When the observer is at 60° to the jet axis, we see a similar trend, whereas only noise increase is observed at 30°. This is expected, because we have shown that, at 30° to the jet axis, the installation effects are virtually negligible. Hence the noise increase is purely due to the higher jet exit velocity. From this figure, we see that although at a higher jet exit velocity, a non-negligible noise reduction is observed at low frequencies. Hence, the reduction of installed jet noise would be more effective when the thrust is kept the same instead. Moreover, if we were to compare these results with a realistic configuration, where a single pylon with the same blockage effects is used, the noise increase observed in high frequencies may become negligible. Hence the proposition of using two pylons instead of one to control instability waves, and hence to reduce installed jet noise, is shown to be feasible.

8.3 Summary

This chapter explores experimentally the possibility of controlling jet instability waves, and hence reducing installed jet noise, using two pylons installed at different azimuthal angles experimentally. The results show that installed jet noise is reduced by around $2 \sim 3$ dB at low frequencies. At high frequencies, a noise increase is observed. However, this is because the comparison is made with an ideal case where no pylon is present and the mass flow rate is kept the same. The noise increase at high frequencies would be much less significant, or even negligible, and the noise reduction at low frequencies more effective, when comparison is made with a more realistic case with a single pylon. Therefore, using two pylons to reduce installed jet noise has significant practical potential.

Chapter 9

Conclusion and Future Work

In the first part of this chapter, a conclusion for this thesis is presented. The conclusion lists the main research work carried out during the course of this project. It then summarises the main findings and lists relevant limitations of each part of this study. The next part sets out a brief plan for future work.

9.1 Conclusion

This thesis is concerned with installed jet noise, including understanding the noise generation mechanism, developing a prediction model and exploring innovative approaches for noise reduction. It starts with formulating a highly-efficient prediction model for isolated jet noise, based on Goldstein's general acoustic analogy. Firstly, this model demonstrates that acoustic analogy theories, together with a space-time correlation model for the fluctuation Reynolds stresses, can be combined with RANS simulations to predict isolated jet noise accurately. The same approach is therefore extended to predict installed jet noise at a later stage. Secondly, the model provides a way to assess the convection effects of the jet mean flow on noise propagation, which will be made use of in the prediction model of installed jet noise. Last but not least, an exceptionally fast computer code has been developed implementing this isolated jet noise model, proving to be very useful in many practical areas.

The second part of this thesis focuses on developing a prediction model for installed jet noise. The model consists of two parts, the first of which is based on the Lighthill's acoustic analogy theory. It starts with the development of a half-plane scattering Green's function. The Green's function is then used to solve the Lighthill's acoustic analogy equation together with the space-time correlation model for fluctuation Reynolds stresses and flow data obtained by

performing RANS calculations. The second part embraces Amiet's approach to model the sound due to the scattering of jet instability waves. This scattering model takes the PSD of near field pressure fluctuations and a frequency-dependent convection velocity as its inputs. The two quantities can be obtained from either experiments or unsteady CFD calculations. Therefore, the resulting far-field sound consists of contributions from two different source mechanisms: the scattering of Lighthill's quadrupole sources and jet instability waves by the nearby semi-infinite flat plate.

It is shown that the significant low-frequency noise enhancement observed in installed jet experiments is due to the scattering of near-field instability waves. The trailing edge scattering model can successfully predict noise spectra at all distinct angles. It is also demonstrated that the sound due to instability wave scattering is only significant at low frequencies and it is negligible at high frequencies. The high-frequency sound alteration, however, is due to the scattering of Lighthill's quadruple sources. It is found, from both the prediction model and experiments, that the far-field sound due to quadrupole sources is either efficiently shielded at 90° to the jet axis on the shielded side or enhanced by around 3 dB at 90° on the reflected side. But these effects gradually diminish as the observer angle decreases. In Chapter 4, it is demonstrated that, at lower observer angles, the sound from quadrupole sources is significantly refracted by the jet mean flow for an $M_0 = 0.5$ jet. The prediction model for installed jet noise does not account for these refraction effects. Consequently, at these angles, only qualitative agreement is achieved. The quadruple sources, however, hardly contribute to low-frequency sound alteration. This is particularly the case when the flat plate is placed sufficiently far away from the jet (e.g. $H > 2D$).

As mentioned above, one limitation of the hybrid model developed in this thesis is that it does not account for the refraction effects of the jet mean flow on high-frequency sound. These effects are non-negligible at lower observer angles and relatively large jet Mach numbers. Thus, quantitative agreement at high frequencies is only achieved at 90° to the jet on the reflected side. Another limitation is that the installed jet noise is particularly relevant to modern commercial aircraft, but the finite aircraft wing is assumed to be semi-infinite in the proposed model, thus the effects of its side edges are ignored. However, these effects have been shown to be insignificant.

The next part of the thesis presents an experimental study on installed jet noise. Cold and single-stream air jets of Mach number 0.5 and 0.7 are examined acoustically. The isolated jet noise spectra are measured first for reference. Then a sufficiently large rectangular flat plate is placed at different positions nearby the jet to investigate installed jet noise and its depen-

dence on the plate positions. This experimental study serves two purposes. First, it provides a comprehensive experimental database on installed jet noise and near-jet pressure fluctuations. The database is of significant importance in understanding both near-jet instability waves and installed jet noise. Second, it is used to validate the hybrid prediction model developed in Chapter 5, for an extensive array of plate positions.

Being consistent with previous experimental results in the literature, the study finds that installed jets exhibit significant noise alteration compared to isolated jets. It is found that the plate causes jet noise to be enhanced significantly at low frequencies, and jet noise is either suppressed or increased by around 3 dB at high frequencies on the shielded and reflected sides, respectively. It is demonstrated that increasing H (while L is fixed) causes the low-frequency hump to decrease exponentially but results in little change for both the shielding and reflection effects at high frequencies. Increasing L (while H is fixed), on the other hand, produces stronger noise intensification at low frequencies and slightly more effective shielding or reflection effects at high frequencies. The installation effects are found to be less pronounced as the Mach number increases.

When comparing the experimentally obtained data with the predictions using the hybrid model developed in Chapter 5, we find excellent agreement at low frequencies. This is so at all tested Mach numbers and when the plate is placed at different positions. This remarkable agreement shows that the near-field scattering model captures the correct mechanism for low-frequency noise enhancement, and therefore, can be used as a robust and accurate prediction tool. At high frequencies, the noise spectra at 90° on the reflected side on can also be correctly predicted. At lower observer angles, deviations occur due to jet refraction effects. However, it can qualitatively predict both the shielding and reflection effects.

The fourth part of this thesis studies the effects of lobed nozzles on installed jet noise. A lobed nozzle is used in experiments to study its effects on installed jet noise. The lobed nozzle is designed to have the same exit area as the round nozzle used in Chapter 6. The same Mach numbers based on flow rates are used. It is found that the effects of the lobed nozzle on installed jet noise are nearly identical for all plate positions and Mach numbers: on the shielded side of the flat plate, lobed nozzles do not noticeably change the installed jet noise spectra at low frequencies. However, they do result in a slight noise reduction at high frequencies. This is thought to be caused by the reduction of isolated jet noise. On the reflected side of the flat plate, the noise has to pass through the jet plume in order to reach the observer. The plumes of the round and lobed jets are different, hence their effects on sound propagation. This thus results in a slight difference for the effects of the lobed nozzle compared to the other side of the

plate. For example, the noise reduction is more effective in the intermediate frequency regime, while a negligible or even slight noise increase is observed at high frequencies. The difference of the jet plume might also cause the low-frequency hump to be marginally less strong on the reflected side at a Mach number of 0.7.

To understand why lobed nozzles hardly change low-frequency installed jet noise, an analytical stability analysis is performed. The base flow is assumed to be of a lobed vortex-sheet type. Inviscid and incompressible stability analysis is carried out using an innovative analytical framework. It is found that the stability characteristics of base flows of a lobed vortex-sheet type are different from those of axisymmetric ones. The differences consist of changes to both the convection velocity and the temporal growth rate of instability waves. The changes become more pronounced as the number of lobes N and the penetration ratio ϵ increase. However, instability waves of different orders are affected differently by the lobe geometry. In particular, little change occurs for mode 0, no matter how large both N and ϵ are. On the other hand, an evident alteration of the characteristics of high-order jet instability waves occurs when $N > 1$. For $N = 3$ and $N = 5$, azimuthally even and odd instability waves evince the same characteristics. However, for $N = 1$ and $N = 2$, even and odd instability waves exhibit two different types of behaviour, with one having favourable effects on installed jet noise reduction and the other having adverse. Therefore, for the sake of suppressing instability waves, or achieving installed jet noise reduction, it is desired to use a lobed profile of large N with a large penetration ratio, such as $N = 5$ in the experiment.

Based on the analytical results, it is postulated that the little change of low-frequency installed jet noise observed in the experiment could be due to two reasons. First, the realistic jet mean flow might become axisymmetric too quickly downstream the jet nozzle due to strong jet mixing. Hence, it is possible that jet instability waves are not significantly affected by the short extent of the strongly lobed mean flow. The second reason, however, is guessed to be due to the fact that the 0th-order jet instability waves are not sensitive to the lobed geometry. This is especially true for low frequencies, where installed jet noise is relevant (see figure 7.12(d) for example). This is because installed jet noise at low frequencies consists of scattering contributions from instability waves of all orders. Therefore, if mode 0 is the dominant instability mode, little change of the installed jet noise can be expected.

The last part of this thesis explores the possibility of reducing installed jet noise by using two pylons. It is proposed that the two pylons may be able to suppress jet instability waves, and hence to reduce installed jet noise, by imposing two normal-velocity-vanishing boundary conditions at different azimuthal angles. An installed experiment using a round nozzle with

two pylons is carried out. The flat plate is placed at $L = 6D$ and $H = 1.5D$. The results show that installed jet noise is reduced by around $2 \sim 3$ dB at low frequencies. At high frequencies, a noise increase is observed. However, this is because the comparison is made with an ideal case where no pylon is present and the mass flow rate is kept the same. The noise increase at high frequencies would be much less significant, or even negligible, and the noise reduction at low frequencies more effective, when comparison is made with a more realistic case of a single pylon with the same blockage. Therefore, using two pylons to reduce installed jet noise has significant practical potential.

9.2 Future work

The first part of future work addresses some of the limitations of the hybrid prediction model for installed jet noise. As clearly demonstrated in Chapter 6, the predicted noise spectra agree with experimental results very well at low frequencies. However, the agreement deteriorates at high frequencies, because the jet mean-flow refraction effects are not negligible for high-speed jets, especially at high frequencies and low observer angles. To better predict the behaviour of high-frequency installed jet noise, an improved model incorporating these refraction effects will be studied.

In Chapters 5 and 6, both LES and experimental data show a frequency-dependent convection velocity for the near-field pressure fluctuations. Although this has been reported by a few authors before, it is not in any way conclusive. In particular, it is not yet known whether it is due to jet instability waves. It is intended that a detailed stability analysis will be performed at relevant frequencies, such that the observed frequency dependence can be further confirmed and better understood.

The third piece of future study is concerned with numerical validation of the stability analysis performed for lobed jets in Chapter 7. Numerical stability analysis for non-axisymmetric jets, such as those of elliptic profiles, has been studied in a number of previous works. Hence, standard numerical methods and codes in this area exist and can be readily modified to perform a similar analysis for lobed jets. The analytical framework developed in Chapter 7 reveals some very interesting stability characteristics of lobed jets, which have not been reported before. It would be interesting to compare the results from a numerical stability analysis with those obtained from the analytical framework. This is therefore intended to be part of future work.

Chapter 8 shows that a $2 \sim 3$ dB noise reduction is achieved for installed jet noise at low frequencies by using two pylons. At high frequencies, a noise increase is observed. As noted,

the comparison is between the two-pylon noise spectra and those for a round nozzle without pylons at constant flow rates. However, the addition of pylons causes a higher jet velocity and the formation of boundary layers on pylon surfaces, both of which lead to louder jet noise. This are likely to be the causes of the high-frequency noise increase. Since in a practical case, a single pylon is used, the effects of two pylons can be accessed more appropriately by comparing the two-pylon results with those for a single pylon with the same blockage. Moreover, the results shown in Chapter 8 demonstrate that using modified pylons to suppress jet instability waves is feasible. This opens the possibility of controlling instability waves by modifying the geometry of near-jet boundaries. Therefore, more extensive pylon (or flap) geometries can be tested experimentally to study their effects on instability waves and/or installed jet noise. These form the last part of our future work.

Appendix A

Derivatives of Green's function

The following differentiations are crucial in calculating the derivatives of the Green's function. The first group is that of the first derivatives of $u_{\bar{R}}$ and $u_{\bar{R}'}$, which can be found as follows,

$$\begin{aligned}
\frac{\partial u_{\bar{R}}}{\partial y_1} &= -\frac{1}{\beta}\sqrt{\frac{k_0 \sin\bar{\theta}}{2\bar{\sigma}_0}}\cos\left(\frac{\bar{\varphi}+\bar{\varphi}_0}{2}\right), \quad \frac{\partial u_{\bar{R}'}}{\partial y_1} = -\frac{1}{\beta}\sqrt{\frac{k_0 \sin\bar{\theta}}{2\bar{\sigma}_0}}\cos\left(\frac{\bar{\varphi}-\bar{\varphi}_0}{2}\right), \\
\frac{\partial u_{\bar{R}}}{\partial y_3} &= \sqrt{\frac{k_0 \sin\bar{\theta}}{2\bar{\sigma}_0}}\sin\left(\frac{\bar{\varphi}+\bar{\varphi}_0}{2}\right), \qquad \frac{\partial u_{\bar{R}'}}{\partial y_3} = -\sqrt{\frac{k_0 \sin\bar{\theta}}{2\bar{\sigma}_0}}\sin\left(\frac{\bar{\varphi}-\bar{\varphi}_0}{2}\right).
\end{aligned} \tag{A.1}$$

Similarly, the second derivatives of $u_{\bar{R}}$ and $u_{\bar{R}'}$ can also be found as

$$\begin{aligned}
\frac{\partial^2 u_{\bar{R}}}{\partial y_1^2} &= \frac{-1}{2\beta\bar{\sigma}_0}\sqrt{\frac{k_0 \sin\bar{\theta}}{2\bar{\sigma}_0}}\cos\left(\bar{\varphi}_0+\frac{\bar{\varphi}+\bar{\varphi}_0}{2}\right), \\
\frac{\partial^2 u_{\bar{R}'}}{\partial y_1^2} &= \frac{-1}{2\beta\bar{\sigma}_0}\sqrt{\frac{k_0 \sin\bar{\theta}}{2\bar{\sigma}_0}}\cos\left(\bar{\varphi}_0-\frac{\bar{\varphi}-\bar{\varphi}_0}{2}\right), \\
\frac{\partial^2 u_{\bar{R}}}{\partial y_3^2} &= \frac{\beta}{2\bar{\sigma}_0}\sqrt{\frac{k_0 \sin\bar{\theta}}{2\bar{\sigma}_0}}\cos\left(\bar{\varphi}_0+\frac{\bar{\varphi}+\bar{\varphi}_0}{2}\right), \\
\frac{\partial^2 u_{\bar{R}'}}{\partial y_3^2} &= \frac{\beta}{2\bar{\sigma}_0}\sqrt{\frac{k_0 \sin\bar{\theta}}{2\bar{\sigma}_0}}\cos\left(\bar{\varphi}_0-\frac{\bar{\varphi}-\bar{\varphi}_0}{2}\right), \\
\frac{\partial^2 u_{\bar{R}}}{\partial y_3 \partial y_1} &= \frac{1}{2\bar{\sigma}_0}\sqrt{\frac{k_0 \sin\bar{\theta}}{2\bar{\sigma}_0}}\sin\left(\bar{\varphi}_0+\frac{\bar{\varphi}+\bar{\varphi}_0}{2}\right), \\
\frac{\partial^2 u_{\bar{R}'}}{\partial y_3 \partial y_1} &= \frac{1}{2\bar{\sigma}_0}\sqrt{\frac{k_0 \sin\bar{\theta}}{2\bar{\sigma}_0}}\sin\left(\bar{\varphi}_0-\frac{\bar{\varphi}-\bar{\varphi}_0}{2}\right).
\end{aligned} \tag{A.2}$$

Detailed expression for the directivity terms D_{ij}^{k} are shown as follows,

$$D_{12}^{0}(y_1,y_3)=-\frac{\cos\bar{\theta}(-M_a+\cos\bar{\alpha})}{\beta^3}\left(E(u_{\bar{R}})\mathrm{e}^{\mathrm{i}\frac{k_0}{\beta}\cos\bar{\gamma}y_3}+E(u_{\bar{R}'})\mathrm{e}^{-\mathrm{i}\frac{k_0}{\beta}\cos\bar{\gamma}y_3}\right), \tag{A.2a}$$

$$D_{12}^{1}(y_1,y_3)=-\frac{\mathrm{i}\cos\bar{\theta}\mathrm{e}^{\mathrm{i}\frac{\pi}{4}}\sqrt{\sin\bar{\theta}}}{\beta^2\sqrt{2\pi}} \left(\mathrm{e}^{-\mathrm{i}u_{\bar{R}}^2}\cos\frac{\bar{\varphi}+\bar{\varphi}_0}{2}\mathrm{e}^{\mathrm{i}\frac{k_0\cos\bar{\gamma}}{\beta}y_3}+\mathrm{e}^{-\mathrm{i}u_{\bar{R}'}^2}\cos\frac{\bar{\varphi}-\bar{\varphi}_0}{2}\mathrm{e}^{-\mathrm{i}\frac{k_0\cos\bar{\gamma}}{\beta}y_3}\right), \tag{A.2b}$$

$$D_{23}^{0}(y_1,y_3)=\frac{-\cos\bar{\theta}\cos\bar{\gamma}}{\beta^2}\left(E(u_{\bar{R}})\mathrm{e}^{\mathrm{i}\frac{k_0}{\beta}\cos\bar{\gamma}y_3}-E(u_{\bar{R}'})\mathrm{e}^{-\mathrm{i}\frac{k_0}{\beta}\cos\bar{\gamma}y_3}\right), \tag{A.2c}$$

$$D_{23}^{1}(y_1,y_3)=\frac{\mathrm{i}\cos\bar{\theta}\mathrm{e}^{\mathrm{i}\frac{\pi}{4}}\sqrt{\sin\bar{\theta}}}{\beta\sqrt{2\pi}} \left(\mathrm{e}^{-\mathrm{i}u_{\bar{R}}^2}\sin\frac{\bar{\varphi}+\bar{\varphi}_0}{2}\mathrm{e}^{\mathrm{i}\frac{k_0\cos\bar{\gamma}}{\beta}y_3}-\mathrm{e}^{-\mathrm{i}u_{\bar{R}'}^2}\sin\frac{\bar{\varphi}-\bar{\varphi}_0}{2}\mathrm{e}^{-\mathrm{i}\frac{k_0\cos\bar{\gamma}}{\beta}y_3}\right), \tag{A.2d}$$

$$D_{11}^{0}(y_1,y_3)=-\left(\frac{-M_a+\cos\bar{\alpha}}{\beta^2}\right)^2\left(E(u_{\bar{R}})\mathrm{e}^{\mathrm{i}\frac{k_0}{\beta}\cos\bar{\gamma}y_3}+E(u_{\bar{R}'})\mathrm{e}^{-\mathrm{i}\frac{k_0}{\beta}\cos\bar{\gamma}y_3}\right), \tag{A.2e}$$

$$\begin{aligned}D_{11}^{1}(y_1,y_3)=&-\frac{2\mathrm{i}(-M_a+\cos\alpha)\mathrm{e}^{\mathrm{i}\frac{\pi}{4}}\sqrt{\sin\bar{\theta}}}{\beta^3\sqrt{2\pi}}\left(\mathrm{e}^{-\mathrm{i}u_{\bar{R}}^2}\cos\frac{\bar{\varphi}+\bar{\varphi}_0}{2}\mathrm{e}^{\mathrm{i}\frac{k_0\cos\bar{\gamma}}{\beta}y_3}\right.\\ &\left(1+\frac{\sin\bar{\theta}}{(-M_a+\cos\bar{\alpha})}\cos\left(\frac{\bar{\varphi}+\bar{\varphi}_0}{2}\right)\cos\left(\frac{\bar{\varphi}-\bar{\varphi}_0}{2}\right)\right)\\ &+\mathrm{e}^{-\mathrm{i}u_{\bar{R}'}^2}\cos\frac{\bar{\varphi}-\bar{\varphi}_0}{2}\mathrm{e}^{-\mathrm{i}\frac{k_0\cos\bar{\gamma}}{\beta}y_3}\\ &\left.\left(1+\frac{\sin\bar{\theta}}{(-M_a+\cos\bar{\alpha})}\cos\left(\frac{\bar{\varphi}+\bar{\varphi}_0}{2}\right)\cos\left(\frac{\bar{\varphi}-\bar{\varphi}_0}{2}\right)\right)\right),\end{aligned} \tag{A.2f}$$

$$\begin{aligned}D_{11}^{2}(y_1,y_3)=&-\frac{\mathrm{e}^{\mathrm{i}\frac{\pi}{4}}\sqrt{\sin\bar{\theta}}}{2\beta\sqrt{2\pi}}\left(\mathrm{e}^{-\mathrm{i}u_{\bar{R}}^2}\cos\left(\bar{\varphi}_0+\frac{\bar{\varphi}+\bar{\varphi}_0}{2}\right)\mathrm{e}^{\mathrm{i}\frac{k_0\cos\bar{\gamma}}{\beta}y_3}\right.\\ &\left.+\mathrm{e}^{-\mathrm{i}u_{\bar{R}'}^2}\cos\left(\bar{\varphi}_0-\frac{\bar{\varphi}-\bar{\varphi}_0}{2}\right)\mathrm{e}^{-\mathrm{i}\frac{k_0\cos\bar{\gamma}}{\beta}y_3}\right),\end{aligned} \tag{A.2g}$$

$$D_{33}^{0}(y_1,y_3) = -\left(\frac{\cos\bar{\gamma}}{\beta}\right)^2\left(E(u_{\bar{R}})\mathrm{e}^{\mathrm{i}\frac{k_0}{\beta}\cos\bar{\gamma}y_3} + E(u_{\bar{R}'})\mathrm{e}^{-\mathrm{i}\frac{k_0}{\beta}\cos\bar{\gamma}y_3}\right), \tag{A.2h}$$

$$\begin{aligned} D_{33}^{1}(y_1,y_3) = {} & \frac{2\mathrm{i}\cos\bar{\gamma}\mathrm{e}^{\mathrm{i}\frac{\pi}{4}}\sqrt{\sin\bar{\theta}}}{\beta\sqrt{2\pi}}\left(\mathrm{e}^{-\mathrm{i}u_{\bar{R}}^2}\sin\frac{\bar{\varphi}+\bar{\varphi}_0}{2}\mathrm{e}^{\mathrm{i}\frac{k_0\cos\bar{\gamma}}{\beta}y_3}\right. \\ & \left(1-\frac{\sin\bar{\theta}}{\cos\bar{\gamma}}\cos\left(\frac{\bar{\varphi}-\bar{\varphi}_0}{2}\right)\sin\left(\frac{\bar{\varphi}+\bar{\varphi}_0}{2}\right)\right) \\ & +\mathrm{e}^{-\mathrm{i}u_{\bar{R}'}^2}\sin\frac{\bar{\varphi}-\bar{\varphi}_0}{2}\mathrm{e}^{-\mathrm{i}\frac{k_0\cos\bar{\gamma}}{\beta}y_3} \\ & \left.\left(1-\frac{\sin\bar{\theta}}{\cos\bar{\gamma}}\cos\left(\frac{\bar{\varphi}+\bar{\varphi}_0}{2}\right)\sin\left(\frac{\bar{\varphi}-\bar{\varphi}_0}{2}\right)\right)\right), \end{aligned} \tag{A.2i}$$

$$\begin{aligned} D_{33}^{2}(y_1,y_3) = {} & \frac{\beta\mathrm{e}^{\mathrm{i}\frac{\pi}{4}}\sqrt{\sin\bar{\theta}}}{2\sqrt{2\pi}}\left(\mathrm{e}^{-\mathrm{i}u_{\bar{R}}^2}\cos\left(\bar{\varphi}_0+\frac{\bar{\varphi}+\bar{\varphi}_0}{2}\right)\mathrm{e}^{\mathrm{i}\frac{k_0\cos\bar{\gamma}}{\beta}y_3}\right. \\ & \left.+\mathrm{e}^{-\mathrm{i}u_{\bar{R}'}^2}\cos\left(\bar{\varphi}_0-\frac{\bar{\varphi}-\bar{\varphi}_0}{2}\right)\mathrm{e}^{-\mathrm{i}\frac{k_0\cos\bar{\gamma}}{\beta}y_3}\right), \end{aligned} \tag{A.2j}$$

$$D_{13}^{0}(y_1,y_3) = -\left(\frac{(-M_a+\cos\bar{\alpha})\cos\bar{\gamma}}{\beta^3}\right)\left(E(u_{\bar{R}})\mathrm{e}^{\mathrm{i}\frac{k_0}{\beta}\cos\bar{\gamma}y_3} - E(u_{\bar{R}'})\mathrm{e}^{-\mathrm{i}\frac{k_0}{\beta}\cos\bar{\gamma}y_3}\right), \tag{A.2k}$$

$$\begin{aligned} D_{13}^{1}(y_1,y_3) = {} & \frac{2\mathrm{i}(-M_a+\cos\bar{\alpha})\mathrm{e}^{\mathrm{i}\frac{\pi}{4}}\sqrt{\sin\bar{\theta}}}{\beta^2\sqrt{2\pi}} \\ & \left(\mathrm{e}^{-\mathrm{i}u_{\bar{R}}^2}\mathrm{e}^{\mathrm{i}\frac{k_0\cos\bar{\gamma}}{\beta}y_3}\left(\frac{1}{2}\sin\frac{\bar{\varphi}+\bar{\varphi}_0}{2}-\frac{\cos\bar{\gamma}}{2(-M_a+\cos\bar{\alpha})}\cos\frac{\bar{\varphi}+\bar{\varphi}_0}{2}\right.\right. \\ & \left.+\frac{\sin\bar{\theta}}{-M_a+\cos\bar{\alpha}}\cos\left(\frac{\bar{\varphi}-\bar{\varphi}_0}{2}\right)\sin\left(\frac{\bar{\varphi}+\bar{\varphi}_0}{2}\right)\cos\left(\frac{\bar{\varphi}+\bar{\varphi}_0}{2}\right)\right) \\ & +\mathrm{e}^{-\mathrm{i}u_{\bar{R}'}^2}\mathrm{e}^{-\mathrm{i}\frac{k_0\cos\bar{\gamma}}{\beta}y_3}\left(-\frac{1}{2}\sin\frac{\bar{\varphi}-\bar{\varphi}_0}{2}+\frac{\cos\bar{\gamma}}{2(-M_a+\cos\bar{\alpha})}\cos\frac{\bar{\varphi}-\bar{\varphi}_0}{2}\right. \\ & \left.\left.\left.-\frac{\sin\bar{\theta}}{-M_a+\cos\bar{\alpha}}\cos\left(\frac{\bar{\varphi}+\bar{\varphi}_0}{2}\right)\sin\left(\frac{\bar{\varphi}-\bar{\varphi}_0}{2}\right)\cos\left(\frac{\bar{\varphi}-\bar{\varphi}_0}{2}\right)\right)\right), \end{aligned} \tag{A.2l}$$

$$\begin{aligned} D_{13}^{2}(y_1,y_3) = {} & \frac{\mathrm{e}^{\mathrm{i}\frac{\pi}{4}}\sqrt{\sin\bar{\theta}}}{2\sqrt{2\pi}}\left(\mathrm{e}^{-\mathrm{i}u_{\bar{R}}^2}\sin\left(\bar{\varphi}_0+\frac{\bar{\varphi}+\bar{\varphi}_0}{2}\right)\mathrm{e}^{\mathrm{i}\frac{k_0\cos\bar{\gamma}}{\beta}y_3}+\right. \\ & \left.\mathrm{e}^{-\mathrm{i}u_{\bar{R}'}^2}\sin\left(\bar{\varphi}_0-\frac{\bar{\varphi}-\bar{\varphi}_0}{2}\right)\mathrm{e}^{-\mathrm{i}\frac{k_0\cos\bar{\gamma}}{\beta}y_3}\right). \end{aligned} \tag{A.2m}$$

Appendix B

The full Goldstein acoustic analogy theory

Equations 4.6, 4.14 and 4.17 are in terms of the new variables ρ', p' and m_i'. They are not the final equations obtained in the Goldstein acoustic analogy theory. For the sake of completeness and a better understanding of the theory, this section starts from these equations and continues to reproduce the final equations. To start, the independent variables are now changed to p_e' and u_i', which are defined as

$$p_e' \equiv p' + \frac{\gamma - 1}{2}\rho v''^2 + (\gamma - 1)\tilde{H}_0, \tag{B.1}$$

$$u_i' \equiv \frac{m_i}{\bar{\rho}}. \tag{B.2}$$

By noting that

$$\bar{\rho}\frac{\overline{\mathrm{D}}}{\overline{\mathrm{D}}t}\frac{\rho'}{\bar{\rho}} = \frac{\overline{\mathrm{D}}}{\overline{\mathrm{D}}t}\rho' - \frac{\rho'}{\bar{\rho}}\frac{\overline{\mathrm{D}}}{\overline{\mathrm{D}}t}\bar{\rho} = \mathrm{D}_0\rho', \tag{B.3}$$

where $\overline{\mathrm{D}}/\overline{\mathrm{D}}t$ is defined in Chapter 3, it is obvious that the continuity equation becomes

$$\bar{\rho}\frac{\overline{\mathrm{D}}}{\overline{\mathrm{D}}t}\frac{\rho'}{\bar{\rho}} + \frac{\partial}{\partial x_j}\bar{\rho}u_j' = 0. \tag{B.4}$$

The momentum equation can also be written in terms of the new independent variables, i.e.

$$\begin{aligned}&\bar{\rho}\frac{\overline{\mathrm{D}}}{\overline{\mathrm{D}}t}u_i' + \bar{\rho}u_j'\frac{\partial\tilde{v}_i}{\partial x_j} + \frac{\partial(p' + \frac{\gamma-1}{2}\rho v''^2 + (\gamma-1)\tilde{H}_0)}{\partial x_i} - \frac{\rho'}{\bar{\rho}}\frac{\partial\tilde{\tau}_{ij}}{\partial x_j}\\ &= \frac{\partial}{\partial x_j}(-\rho v_i'' v_j'' - \tilde{T}_{ij} + \sigma_{ij}' + \delta_{ij}\frac{\gamma-1}{2}\rho v''^2 + \delta_{ij}(\gamma-1)\tilde{H}_0).\end{aligned} \tag{B.5}$$

Equation B.5 simplifies to

$$\bar{\rho}\frac{\overline{\mathrm{D}}}{\overline{\mathrm{D}}t}u_i' + \bar{\rho}u_j'\frac{\partial\tilde{v}_i}{\partial x_j} + \frac{\partial p_e'}{\partial x_i} - \frac{\rho'}{\bar{\rho}}\frac{\partial\tilde{\tau}_{ij}}{\partial x_j} = \frac{\partial}{\partial x_j}(e_{ij}' - \tilde{e}_{ij}), \tag{B.6}$$

if one defines

$$\begin{aligned} e_{ij}' &= (-\rho v_i'' v_j'' + \sigma_{ij}' + \delta_{ij}\frac{\gamma-1}{2}\rho v''^2), \\ \tilde{e}_{ij} &= (\tilde{T}_{ij} - \delta_{ij}(\gamma-1)\tilde{H}_0). \end{aligned}$$

The energy equation can be rewritten in the same way. We first collect every term under the operator D_0, then expand D_0 to obtain

$$\begin{aligned} &\frac{1}{\gamma-1}\left(\frac{\overline{\mathrm{D}}}{\overline{\mathrm{D}}t}p_e' + p_e'\frac{\partial\tilde{v}_j}{\partial x_j} + (\gamma-1)p'\frac{\partial\tilde{v}_j}{\partial x_j}\right) + \frac{\partial m_j\tilde{h}}{\partial x_j} - \frac{m_i}{\bar{\rho}}\frac{\partial\tilde{\tau}_{ij}}{\partial x_j} \\ &= \frac{1}{\gamma-1}\left(\frac{\overline{\mathrm{D}}}{\overline{\mathrm{D}}t}p_e' + \gamma p_e'\frac{\partial\tilde{v}_j}{\partial x_j} - (\gamma-1)(\frac{\gamma-1}{2}\rho v''^2 + (\gamma-1)\tilde{H}_0)\frac{\partial\tilde{v}_j}{\partial x_j}\right) \\ &\quad + \frac{\partial m_j c_p(\bar{p}/R\bar{\rho})}{\partial x_j} - u_i'\frac{\partial\tilde{\tau}_{ij}}{\partial x_j}. \end{aligned} \tag{B.7}$$

With the definition of

$$\eta_i' \equiv -\rho v_i'' h_0'' - q_i' + \sigma_{ij}v_j'', \tag{B.8}$$

$$\tilde{\eta}_i \equiv \tilde{H}_i - \tilde{T}_{ij}\tilde{v}_j, \tag{B.9}$$

the energy equation becomes

$$\frac{1}{\gamma-1}\left(\frac{\overline{\mathrm{D}}}{\overline{\mathrm{D}}t}p_e' + \gamma p_e'\frac{\partial\tilde{v}_j}{\partial x_j} + \gamma\frac{\partial\bar{p}u_j'}{\partial x_j}\right) - u_i'\frac{\partial\tilde{\tau}_{ij}}{\partial x_j} = \frac{\partial}{\partial x_j}(\eta_j' - \tilde{\eta}_j) + \left(e_{ij}' - \tilde{e}_{ij}\right)\frac{\partial\tilde{v}_i}{\partial x_j}. \tag{B.10}$$

Equations B.4, B.6 and B.10 are collected together as

$$\bar{\rho}\frac{\overline{\mathrm{D}}}{\overline{\mathrm{D}}t}\frac{\rho'}{\bar{\rho}} + \frac{\partial}{\partial x_j}\bar{\rho}u_j' = 0, \tag{B.11a}$$

$$\bar{\rho}\frac{\overline{\mathrm{D}}}{\overline{\mathrm{D}}t}u_i' + \bar{\rho}u_j\frac{\partial\tilde{v}_i}{\partial x_j} + \frac{\partial p_e'}{\partial x_i} - \frac{\rho'}{\bar{\rho}}\frac{\partial\tilde{\tau}_{ij}}{\partial x_j} = \frac{\partial}{\partial x_j}(e_{ij}' - \tilde{e}_{ij}), \tag{B.11b}$$

$$\frac{1}{\gamma-1}\left(\frac{\overline{\mathrm{D}}}{\overline{\mathrm{D}}t}p_e' + \gamma p_e'\frac{\partial\tilde{v}_j}{\partial x_j} + \gamma\frac{\partial\bar{p}u_j'}{\partial x_j}\right) - u_i'\frac{\partial\tilde{\tau}_{ij}}{\partial x_j} = \frac{\partial}{\partial x_j}(\eta_j' - \tilde{\eta}_j) + \left(e_{ij}' - \tilde{e}_{ij}\right)\frac{\partial\tilde{v}_i}{\partial x_j}. \tag{B.11c}$$

These are the final equations obtained by Goldstein (2003) in terms of the new variables ρ', u_i' and p_e'. This is a particularly convenient form from which one can calculate the far-field sound via the acoustic analogy approach for the following reasons.

Firstly, one can see that the left hand sides of these equations involve only linear terms, and the right hand sides are fluctuation sources. The linear operators on the left hand side properly account for the effects of sound propagation in shear flows. The generation and propagation effects of sound have therefore been separated; consequently, this formulation tends to be more robust than the traditional Lighthill's acoustic analogy theory. Secondly, when time and Favre averages are chosen for the bar and tilde quantities, respectively, the source terms on the right hand side of these equations can be shown to be of zero time mean. In other words, they are proper fluctuation quantities. Lastly, the redefined independent variables u_i and p_e are also of zero mean and they represent pure fluctuations quantities. In particular, p_e reduces to the sound pressure in the far field, because sound is defined as the linear motion of fluid, therefore ignoring all the second-order quantities in the definition of p_e.

Appendix C

Acoustic analogies

Green's function for isolated jet

The free-space Green's function corresponding to the wave equation $(\mathrm{i}\omega)^2 G - c_0^2 \nabla G = \delta(\boldsymbol{x} - \boldsymbol{y})$ is

$$G(\boldsymbol{x}, \boldsymbol{y}, \omega) = \frac{e^{-\mathrm{i}k_0|\boldsymbol{x}-\boldsymbol{y}|}}{4\pi c_0^2 |\boldsymbol{x} - \boldsymbol{y}|}. \tag{C.1}$$

Thus, under the far-field approximation, the second derivatives of the Green's function can be shown as

$$\frac{\partial^2 G(\boldsymbol{x}, \boldsymbol{y}, \omega)}{\partial y_i y_j} = -\frac{A(\boldsymbol{x})}{c_0^2} k_i k_j e^{\mathrm{i}(k_1 y_1 + k_2 y_2 + k_3 y_3)}, \tag{C.2}$$

where, $k_i = k_0 x_i / |\boldsymbol{x}|$ and $A(\boldsymbol{x}) = e^{-\mathrm{i}k_0|\boldsymbol{x}|}/4\pi|\boldsymbol{x}|$.

Detailed integral in numerical codes

The detailed integral used in the numerical code for the installed jet are as follows,

$$\begin{aligned}\Phi(\boldsymbol{x}, \omega) = c_0^4 \frac{\sqrt{\pi}}{2(\ln 2)^{3/2}} \int_{V_y} \frac{l_1(\boldsymbol{y}) l_2(\boldsymbol{y}) l_3(\boldsymbol{y})}{\bar{v}_1(\boldsymbol{y})} A_{ijkl}(\boldsymbol{y}) \exp\left[-\frac{l_1(\boldsymbol{y})^2 \omega^2}{4\bar{v}_1^2 \ln 2}\right] \frac{\partial^2 G(\boldsymbol{x};\, \boldsymbol{y}\,, \omega)}{\partial y_i \partial y_j} \\ \int_{-3\bar{v}_1(\boldsymbol{y})\tau_s(\boldsymbol{y})}^{3\bar{v}_1(\boldsymbol{y})\tau_s(\boldsymbol{y})} \frac{\partial^2 G(\boldsymbol{x};\, y_1 + \Delta y_1,\, y_2,\, y_3,\, \omega)}{\partial y_k \partial y_l} \times \\ \exp\left[-\left(\frac{\pm 1}{\bar{v}_1(\boldsymbol{y})\tau_s(\boldsymbol{y})} + \mathrm{i}\frac{\omega}{\bar{v}_1(\boldsymbol{y})}\right) \Delta y_1\right] \mathrm{d}\,\Delta y_1 \mathrm{d}^{\,3} y,\end{aligned} \tag{C.3}$$

and for the small region where the source location is sufficiently close to the edge,

$$\begin{aligned}\Phi(\boldsymbol{x},\omega) = c_0^4 \frac{1}{2(\ln 2)} \int_{V_y} \frac{l_1(\boldsymbol{y}) l_2(\boldsymbol{y})}{\bar{v}_1(\boldsymbol{y})} A_{ijkl}(\boldsymbol{y}) \exp\left[-\frac{l_1(\boldsymbol{y})^2 \omega^2}{4\bar{v}_1^2 \ln 2}\right] \frac{\partial^2 G(\boldsymbol{x};\, \boldsymbol{y}\,, \omega)}{\partial y_i \partial y_j} \\ \int_{-3\bar{v}_1(\boldsymbol{y})\tau_s(\boldsymbol{y})}^{3\bar{v}_1(\boldsymbol{y})\tau_s(\boldsymbol{y})} \exp\left[-\left(\frac{\pm 1}{\bar{v}_1(\boldsymbol{y})\tau_s(\boldsymbol{y})} + \mathrm{i}\frac{\omega}{\bar{v}_1(\boldsymbol{y})}\right)\Delta y_1\right] \\ \int_{-2.5 l_3(\boldsymbol{y})}^{2.5 l_3(\boldsymbol{y})} \frac{\partial^2 G(\boldsymbol{x};\, y_1 + \Delta y_1,\, y_2,\, y_3 + \Delta y_3,\, \omega)}{\partial y_k \partial y_l} \times \\ \exp\left[-\ln 2 \left(\frac{\Delta y_3}{l_3(\boldsymbol{y})}\right)^2\right] \mathrm{d}\,\Delta y_1 \mathrm{d}\,\Delta y_3 \mathrm{d}^{\,3} y.\end{aligned} \tag{C.4}$$

Bibliography

Afsar, M. Z. (2009). *Theory and modelling of jet noise*. PhD thesis, University of Cambridge.

Agarwal, A., Morris, P. J., and Mani, R. (2004). Calculation of sound propagation in nonuniform flows: suppression of instability waves. *AIAA Journal*, 42(1):80–88.

Amiet, R. K. (1975). Acoustic radiation from an airfoil in a turbulent stream. *Journal of Sound and Vibration*, 41(4):407–420.

Amiet, R. K. (1976a). High frequency thin-airfoil theory for subsonic flow. *AIAA Journal*, 14(8):1076–1082.

Amiet, R. K. (1976b). Noise due to turbulent flow past a trailing edge. *Journal of Sound and Vibration*, 47(3):387–393.

Amiet, R. K. (1978). Effect of the incident surface pressure field on noise due to turbulent flow past a trailing edge. *Journal of Sound and Vibration*, 57:305–306.

ANSYS (2015). *Fluent theory guide release 16.0*. ANSYS, Inc., Southpointe, 2600 ANSYS Drive, Canonsburg, PA 15317.

Arndt, R., Long, D. F., and Glauser, M. N. (1997). The proper orthogonal decomposition of pressure fluctuations surrounding a turbulent jet. *Journal of Fluid Mechanics*, 340:1–33.

Bailly, C., Candel, S., and Lafon, P. (1996). Prediction of supersonic jet noise from a statistical acoustic model and a compressible turbulence closure. *Journal of Sound and Vibration*, 194:219–242.

Bailly, C., Lafon, P., and Candel, S. (1994). Computation of subsonic and supersonic jet mixing noise using a modified $k - \epsilon$ model for compressible free shear flows. *Acta Acustica*, 2:101–112.

Bastos, L., Deschamps, C., and da Silva, A. (2017). Experimental investigation of the far-field noise due to jet-surface interaction combined with a chevron nozzle. *Applied Acoustics*, 127:240–249. cited By 0.

Batchelor, G. K. and Gill, A. E. (1962). Analysis of the stability of axisymmetric jets. *Journal of Fluid Mechanics*, 14:529–551.

Baty, R. S. and Morris, P. J. (1995). The instability of jets of arbitrary exit geometry. *International Journal for Numerical Methods in Fluids*, 21(9):763–780.

Bechara, W., Lafon, P., Bailly, C., and Candel, S. M. (1995). Application of a $k - \epsilon$ turbulence model to the prediction of noise for simple and coaxial jets. *Journal of Acoustical Society of America*, 97:3518–3513.

Berkooz, G., Holmes, P., and Lumley, J. L. (1993). The proper orthogonal decomposition in the analysis of turbulent flow. *Annual Review of Fluid Mechanics*, 25:539–575.

Bertolotti, F. P. and Herbert, T. (1991). Analysis of the linear stability of compressible boundary layers using the PSE. *Theoretical Computational Fluid Dynamics*, 3:117–124.

Bhat, T. R. S. and Blackner, A. M. (1998). Installed jet noise prediction model for coaxial jets. In *Proceedings of 9th AIAA/CEAS Aeroacoustics Conference*, Aeroacoustics Conferences. American Institute of Aeronautics and Astronautics. AIAA 98-79.

Bondarenko, M., Hu, Z., and Zhang, X. (2012). Large-Eddy Simulation of the interaction of a jet with a wing. In *Proceedings of 18th AIAA/CEAS Aeroacoustics Conference*, Aeroacoustics Conferences. American Institute of Aeronautics and Astronautics. AIAA 2012-2254.

Bridges, J. and Wernet, M. P. (2010). Establishing consensus turbulence statistics for hot subsonic jets. In *Proceedings of 16th AIAA/CEAS Aeroacoustic Conference*, Aeroacoustics Conferences. American Institute of Aeroacoustic and Astronautics. AIAA 2010-3751.

Brown, C. A. (2013). Jet-surface interaction test: far-field noise results. *Journal of Engineering for Gas Turbines and Power*, 135(7):71201.

Brown, G. L. and Roshko, A. (1974). On density effects and large structure in turbulent mixing layers. *Journal of Fluid Mechanics*, 64:775–816.

Bryce, W. D. (1979). Experiments concerning the anomalous behaviour of aero-engine exhaust noise in flight. In *Proceedings of 5th Aeroacoustics Conference*, Aeroacoustics Conferences. American Institute of Aeronautics and Astronautics. AIAA 79-648.

Bushell, K. (1975). Measurement and prediction of jet noise in flight. In *Proceedings of 2nd Aeroacoustics Conference*, Aeroacoustics Conferences. American Institute of Aeronautics and Astronautics. AIAA 75-461.

Bychkov, O. P. and Faranosov, G. A. (2014). On the possible mechanism of the jet noise intensification near a wing. *Acoustical Physics*, 60(6):633–646.

Casalino, D., Diozzi, F., Sannino, R., and Paonessa, A. (2008). Aircraft noise reduction technologies: a bibliographic review. *Aerospace Science and Technology*, 12:1–17.

Cavalieri, A. V. G., Jordan, P., Wolf, W., and Gervais, Y. (2014). Scattering of wavepackets by a flat plate in the vicinity of a turbulent jet. *Journal of Sound and Vibration*, 333:6516–6531.

Colonius, T., Lele, S. K., and Moin, P. (1997). Sound generation in a mixing layer. *Journal of Fluid Mechanics*, 330:375–409.

Crighton, D. G. (1973). Instability of an elliptic jet. *Journal of Fluid Mechanics*, 59(4):665–672.

Crighton, D. G. and Gaster, M. (1976). Stability of slowly diverging jet flow. *Journal of Fluid Mechanics*, 77:397–413.

Crow, S. C. and Champagne, F. H. (1971). Orderly structure in jet turbulence. *Journal of Fluid Mechanics*, 48:547–591.

Curle, N. (1955). The influence of solid boundaries upon aerodynamic sound. *Proceedings of the Royal Society A: Mathematical, Physical and Engineering Sciences*, 231:505–514.

Dimotakis, P. E. and Brown, G. L. (1976). The mixing layer at high Reynolds number: large structure dynamics and entrainment. *Journal of Fluid Mechanics*, 78:535–560.

Dowling, A. P., Williams, J. E. F., and Goldstein, M. E. (1978). Sound production in a moving stream. *Philosophical Transactions of the Royal Society of London A: Mathematical, Physical and Engineering Sciences*, 288(1353):321–349.

Federal Aviation Administration (2011). FAA Aerospace Forecast Fiscal Years 2011-2013. http://www.faa.gov/about/office_org/headquarters_offices/apl/aviation_forecasts/aerospace_forecasts/2011-2031/.

Fisher, M. J., Harper-Bourne, M., and Glegg, S. A. L. (1977). Jet engine noise source location: The polar correlation technique. *Journal of Sound and Vibration*, 51:23–54.

Fuchs, H. (1972). Space correlations of the fluctuating pressure in subsonic turbulent jets. *Journal of Sound and Vibration*, 23:77–99.

Goldstein, M. E. (1976). *Aeroacoustics*. McGraw-Hill, Inc, 1 edition.

Goldstein, M. E. (2001). An exact form of lilley's equation with a velocity quadrupole/temperature dipole source term. *Journal of Fluid Mechanics*, 443:231–236.

Goldstein, M. E. (2003). A generalized acoustic analogy. *Journal of Fluid Mechanics*, 488:315–333.

Gradshteyn, I. S. and Ryzhik, I. M. (2007). *Table of integrals, series, and products*. Elsevier Academic Press, 30 Corporate Drive, Suite 400, Burlington, MA 01803, USA, 7 edition.

Gudmundsson, K. and Colonius, T. (2011). Instability wave models for the near-field fluctuations of turbulent jets. *Journal of Fluid Mechanics*, 689:97–128.

Head, R. and Fisher, M. (1976). Jet/surface interaction noise - analysis of farfield low frequency augmentations of jet noise due to the presence of a solid shield. In *Proceedings of 3rd Aeroacoustics Conference*, Aeroacoustics Conferences. American Institute of Aeronautics and Astronautics. AIAA 76-502.

Herbert, T. (1997). Parabolized stability equations. *Annual Review of Fluid Mechanics*, 29:245–283.

Ho, C. and Huerre, P. (1984). Perturbed free shear layers. *Annual Review of Fluid Mechanics*, 16:365–424.

Howe, M. S. (1978). A review of the theory of trailing edge noise. *Journal of Sound and Vibration*, 61:437–465.

Huber, J., Jordan, P., Roger, M., Gervais, Y., Lizarazu, D., and Wlassow, F. (2017). Exploring flight effects for installed jet noise using a wavepacket sound-source model. cited By 0.

Hussain, A. K. M. F. (1986). Coherent structures and turbulence. *Journal of Fluid Mechanics*, 173:303–356.

Hussain, A. K. M. F. and Zaman, K. B. M. Q. (1981). The "preferred mode" of the axisymmetric jet. *Journal of Fluid Mechanics*, 110:39–71.

Jameson, A. (2008). Formulation of kinetic energy preserving conservative schemes for gas dynamics and direct numerical simulation of one-dimensional viscous compressible flow in a

shock tube using entropy and kinetic energy preserving schemes. *Journal of Scientific Computing*, 34(2):188–208.

Jaunet, V., Cavalieri, A. V. G., and Jordan, P. (2017). Two-point coherence of wavepackets in turbulent jets. *Physical Review Fluids*, 2(2).

Jaunet, V., Jordan, P., and Cavalieri, A. V. G. (2016). Two-point coherence of wavepackets in turbulent jets. In *Proceedings of 22nd AIAA/CEAS Aeroacoustics Conference*. AIAA 2016-3058.

Jeun, J., Nichols, J. W., and Jovanović, M. R. (2016). Input-output analysis of high-speed axisymmetric isothermal jet noise. *Physics of Fluids*, 28(4):047101.

Jones, D. S. (1972). Aerodynamic sound due to a source near a half-plane. *Journal of the Institute of Mathematical and Its Applications*, 9:114–122.

Jordan, P. and Colonius, T. (2013). Wave packets and turbulent jet noise. *Annual Review of Fluid Mechanis*, 45:173–195.

Karabasov, S. A. (2010). Understanding jet noise. *Philosophical Transactions of the Royal Society A: Mathematical, Physical and Engineering Sciences*, 368:3593–3608.

Karabasov, S. A., Afsar, M. Z., Hynes, T. P., Dowling, A. P., McMullan, W. A., Pokora, C. D., Page, G. J., and McGuirk, J. J. (2010). Jet noise: acoustic analogy informed by large eddy simulation. *AIAA Journal*, 48(7):1312–1325.

Karhuen, K. (1946). Zur spektral theories stochastischer prozesse. *Annales Academiae scientiarum Fennicae. Series A1: Mathematica, physica*, 34.

Kawahara, G., Jiménez, J., Uhlmann, M., and Pinelli, A. (2003). Linear instability of a corrugated vortex sheet - a model for streak instability. *Journal of Fluid Mechanics*, 483:315–342.

Kerhervé, F., Fitzpatick, J., and Jordan, P. (2006). The frequency dependence of jet turbulence for noise source modelling. *Journal of Sound and Vibration*, 296:209–225.

Khavaran, A., Krejsa, E. A., and Kim, C. M. (1994). Computation of supersonic jet mixing noise for an axisymmetric convergent-divergent nozzle. *Journal of Aircraft*, 31(5):603–609.

Kopiev, V. F., Ostrikov, N. N., Chernyshev, S. A., and Elliot, J. W. (2004). Aeroacoustics of supersonic jet issued from corrugated nozzle: new approach and prospects. *International Journal of Aeroacoustics*, 3(3):199–228.

Kosambi, D. D. (1943). Statistics in function space. *Journal of Indian Mathematical Society*, 7:76–88.

Lajús Jr., F. C., Cavalieri, A. V. G., and Deschamps, C. J. (2015). Spatial stability characteristics of non-circular jets. In *Proceedings of 21st AIAA/CEAS Aeroacoustics Conference*. American Institute of Aeronautics and Astronautics. 2015-2537.

Launder, B. E. and Spalding, D. B. (1974). The numerical computation of turbulent flows. *Computer Methods in Applied Mechanics and Engineering*, 3:269–289.

Lawrence, J. L. T., Azarpevand, M., and Self, R. H. (2011). Interaction between a flat plate and a circular subsonic jet. In *Proceedings of 17th AIAA/CEAS Aeroacoustic Conference*. American Institute of Aeronautics and Astronautics. AIAA 2011-2754.

Leconte, J. (1858). On the influence of musical sounds on the flame of a jet of coal-gas. *The Philosophical Magazine*, 15:235–239.

Lessen, M., Fox, J. A., and Zien, H. M. (1965). The instability of inviscid jets and wakes in compressible fluid. *Journal of Fluid Mechanics*, 21:129–143.

Lessen, M. and Singh, P. J. (1973). Analysis of the stability of axisymmetric jets. *Journal of Fluid Mechanics*, 14:529–551.

Lesshafft, L., Huerre, P., and Sagaut, P. (2010). Aerodynamic sound generation by global modes in hot jets. *Journal of Fluid Mechanics*, 647:473–489.

Lighthill, M. J. (1952). On sound generated aerodynamically. I. General theory. *Proceedings of the Royal Society A: Mathematical, Physical and Engineering Sciences*, 211(1107):564–587.

Lighthill, M. J. (1954). On sound generated aerodynamically. II. Turbulence as a source of sound. *Proceedings of the Royal Society A: Mathematical, Physical and Engineering Sciences*, 222:1–32.

Lilley, G. M. (1974). On the noise from jets. *AGARD Noise Mechanism CP-131*, 13:12.

Loeve, M. (1945). Functions aleatoire de second ordre. *Comptes Rendus Mathématique. Académie des Sciences. Paris*, 220.

Lumley, J. L. (1967). The structure of inhomogeneous turbulence. *Atmospheric Turbulence and Wave Propagation*, pages 166–178. ed. AM Yaglom, VI Tatarsky, Nauka, Moscow.

Lyu, B., Azarpeyvand, M., and Sinayoko, S. (2015). A trailing-edge noise model for serrated edges. In *Proceedings of 21th AIAA/CEAS Aeroacoustics Conference*, Aeroacoustics Conferences. American Institute of Aeronautics and Astronautics. AIAA 2015-2362.

Lyu, B., Azarpeyvand, M., and Sinayoko, S. (2016). Noise prediction for serrated trailing edges. *Journal of Fluid Mechanics*, 793:556–588.

Lyu, B. and Dowling, A. P. (2016). Noise prediction for installed jets. In *Proceedings of 22nd AIAA/CEAS Aeroacoustics Conference*, Aeroacoustics Conferences. American Institute of Aeronautics and Astronautics. AIAA 2016-2986.

Macdonald, H. M. (1915). A class of diffraction problem. *Proceedings of the London Mathematical Society*, 14:410–427.

Mani, R. (1976). The influence of jet flow on jet-noise, parts 1 and 2. *Journal of Fluid Mechanics*, 73:753–793.

Mattingly, G. E. and Chang, C. C. (1974). Unstable waves on an axisymmetric jet column. *Journal of Fluid Mechanics*, 65:541–560.

Mead, C. and Strange, P. (1998). Under-wing installation effects on jet noise at sideline. In *Proceedings of 4th AIAA/CEAS Aeroacoustics Conference*, Aeroacoustics Conferences. American Institute of Aeronautics and Astronautics. AIAA 98-2207.

Michalke, A. (1971). Instabilität eines kompressiblen runden freistrahls unter berücksichtigung des einflusses der strahlgrenzschichtdicke. *Zeitschrift für Flugwissenschaften*, 19:319–328.

Michalke, A. (1984). Survey on jet instability theory. *Progress in Aerospace Science*, 21:159–199.

Miller, W. (1983). Flight effects for jet-airframe interaction noise. In *Proceedings of 8th Aeroacoustic Conference*, Aeroacoustics Conferences. American Institute of Aeroacoustic and Astronautics. AIAA 83-784.

Mohan, N. K. D., Dowling, A. P., Karabasov, S. A., Xia, H., Graham, O., Hynes, T. P., and Tucker, P. G. (2015). Acoustic sources and far-field noise of chevron and round jets. *AIAA Journal*, 53(9):2421–2436.

Moore, A. (2004). A 3D prediction of the wing reflection of aero engine noise. In *Proceedings of 10th AIAA/CEAS Aeroacoustics Conference*, Aeroacoustics Conferences. American Institute of Aeronautics and Astronautics. AIAA 2004-2865.

Moore, A. and Mead, C. (2003). Reflection of noise from aero engines installed under an aircraft wing. In *Proceedings of 9th AIAA/CEAS Aeroacoustics Conference*, Aeroacoustics Conferences. American Institute of Aeronautics and Astronautics. AIAA 2003-3151.

Morris, P. J. (1976). The spatial viscous instability of axisymmetric jets. *Journal of Fluid Mechanics*, 77:511–529.

Morris, P. J. (1983). Viscous stability of compressible axisymmetric jets. *AIAA Journal*, 21:481–481.

Morris, P. J. (1988). Instability of elliptic jets. *AIAA Journal*, 26(2):172–178.

Morris, P. J. (2010). The instability of high speed jets. *International Journal of Aeroacoustics*, 9(1-2):1–50.

Morris, P. J. and Farassat, F. (2002). Acoustic analogy and alternative theories for jet-noise prediction. *AIAA Journal*, 40:671–680.

Naqavi, I. Z., Wang, Z., Tucker, P. G., Mahak, M., and Strange, P. (2016). Far-field noise prediction for jets using Large-eddy Simulation (LES) and Ffowcs Williams-Hawkings (FW-H) method. *Internal Journal of Aeroacoustics*, 15(8).

Nogueira, P., Cavalieri, A., and Jordan, P. (2017). A model problem for sound radiation by an installed jet. *Journal of Sound and Vibration*, 391:95–115.

Orszag, S. A. (1970). Analytical theories of turbulence. *Journal of Fluid Mechanics*, 41(2):363–386.

Papamoschou, D. (2010). Prediction of jet noise shielding. In *Proceedings of the 48th AIAA Aerospace Sciences Meeting*. American Institute of Aeronautics and Astronatics. AIAA 2010-653.

Pastouchenko, N. N. and Tam, C. K. W. (2007). Installation effects on the flow and noise of wing mounted jets. *AIAA Journal*, 45(12):2851–2860.

Pepper, C. B., Nascarella, M. A., and Kendall, R. J. (2003). A review of the effects of aircraft noise on wildlife and humans, current control mechanisms, and the need for further study. *Environmental Management*, 32:3024.

Piantanida, S., Jaunet, V., Huber, J., Wolf, W., Jordan, P., and Cavalieri, A. (2016). Scattering of turbulent-jet wavepackets by a swept trailing edge. *Journal of the Acoustical Society of America*, 140(6):4350–4359. cited By 2.

Pridmore-Brown (1958). Sound propagation in a fluid flowing through an attenuating duct. *Journal of Fluid Mechanics*, 4:393–406.

Rayleigh, L. (1879). On the instability of jets. *Proceedings of the London Mathematical Society*, 10:4–13.

Rienstra, S. W. (1981). Sound diffraction at a trailing edge. *Journal of Fluid Mechanics*, 108:443–460.

Roger, M. and Moreau, S. (2005). Back-scattering correction and further extensions of Amiet's trailing-edge noise model. part 1: theory. *Journal of Sound and Vibration*, 286(1-2):477–506.

Roger, M., Moreau, S., and Kucukcoskun, K. (2016). On sound scattering by rigid edges and wedges in a flow, with applications to high-lift device aeroacoustics. *Journal of Sound and Vibration*, 362:252–275.

Samanta, A., Freund, J. B., Wei, M., and Lele, S. K. (2006). Robustness of acoustic analogies for predicting mixing-layer noise. *AIAA Journal*, 44:2780–2786.

Saric, W. S. and Nayfeh, A. H. (1975). Nonparallel stability of boundary layer flows. *Physics of Fluids*, 18:945–950.

Schmidt, O., Towne, A., Colonius, T., Cavalieri, A. V. G., Jordan, P., and Brès, G. A. (2017). Wavepackets and trapped acoustic modes in a Mach 0.9 turbulent jet. *Journal of Fluid Mechanics*, 825:1153–1181.

Self, R. H. (2004). Jet noise prediction using Lighthill acoustic analogy. *Journal of sound and vibration*, 275(3-5):757–768.

Semeraro, O., Lesshafft, L., Jaunet, V., and Jordan, P. (2016). Modeling of coherent structures in a turbulent jet as global linear instability wavepackets: Theory and experiment. *International Journal of Heat and Fluid Flow*, 62:24–32.

Semiletov, V., Yakovlev, P., Karabasov, S., Faranosov, G., and Kopiev, V. (2016). Jet and jet–wing noise modelling based on the cabaret miles flow solver and the ffowcs williams–hawkings method. *International Journal of Aeroacoustics*, 15(6-7):631–645. cited By 1.

Sengupta, G. (1983). Analysis of jet-airframe interaction noise. In *Proceedings of 8th Aeroacoustics Conference*, Aeroacoustics Conferences. American Institute of Aeronautics and Astronautics. AIAA 83-783.

Shearin, J. G. (1983). Investigation of jet-installation noise sources under static conditions. NASA Technical Report 2181, NASA Langley Research Center, , Hampton, Virgina.

Sinha, A., Gudmundsson, K., Xia, H., and Colonius, T. (2016). Parabolized stability analysis of jets from serrated nozzles. *Journal of Fluid Mechanics*, 789:36–63.

Sirovich, L. (1987). Turbulence and the dynamics of coherent structures, parts I-III. *Quarterly of Applied Mathematics*, 45(3):561–590.

Stevens, R., Bryce, W., and Szewczyk, V. (1983). Model and full-scale studies of the exhaust noise from a bypass engine in flight. In *Proceedings of 8th Aeroacoustics Conference*, Aeroacoustics Conferences. American Institute of Aeronautics and Astronautics. AIAA 83-751.

Sukuzi, T. and Colonius, T. (2006). Instability waves in a subsonic round jet detected using a near-field phased microphone array. *Journal of Fluid Mechanics*, 565:197–226.

Szewczyk, V. (1979). Coaxial jet noise in flight. In *Proceedings of 5th Aeroacoustics Conference*, Aeroacoustics Conferences. American Institute of Aeronautics and Astronautics. AIAA 79-636.

Tam, C. K. W. (1995). Supersonic jet noise. *Annual Review of Fluid Mechanics*, 27:17–43.

Tam, C. K. W. (1998). Jet noise: since 1952. *Theoretical and Computational Fluid Dynamics*, 10:393–405.

Tam, C. K. W. and Auriault, L. (1998). Mean flow refraction effects on sound radiated from localized sources in a jet. *Journal of Fluid Mechanics*, 370:149–174.

Tam, C. K. W. and Auriault, L. (1999). Jet mixing noise from fine-scale turbulence. *AIAA Journal*, 37(2):145–153.

Tam, C. K. W., Golebiowski, M., and Seiner, J. M. (1996). On the two components of turbulent mixing noise from supersonic jets. In *Proceedings of 2nd AIAA/CEAS Aeroacoustic Conference*, Aeroacoustics Conferences. American Institute of Aeroacoustic and Astronautics. AIAA 96-1716.

Tam, C. K. W. and Morris, P. J. (1980). The radiation of sound by instability waves of a compressible plane turbulent shear layer. *Journal of Fluid Mechanics*, 98:349–381.

Tam, C. K. W. and Thies, A. T. (1993). Instability of rectangular jets. *Journal of Fluid Mechanics*, 248:425–448.

Tam, C. K. W. and Zaman, K. B. M. Q. (2000). Subsonic jet noise from nonaxisymmetric and tabbed nozzles. *AIAA Journal*, 38(4):592–599.

Tanna, H. K. (1977). An experimental study of jet noise part I: Turbulent mixing noise. *Journal of sound and Vibration*, 50:405–428.

Tinney, C. E., Glauser, M. N., and Ukeiley, L. S. (2008a). Low-dimensional characteristics of a transonic jet. part 1. proper orthogonal decomposition. *Journal of Fluid Mechanics*, 612:107–141.

Tinney, C. E. and Jordan, P. (2008). The near pressure field of co-axial subsonic jets. *Journal of Fluid Mechanics*, 611:175–204.

Tinney, C. E., Ukeiley, L. S., and Glauser, M. N. (2008b). Low-dimensional characteristics of a transonic jet. part 2. estimate and far-field prediction. *Journal of Fluid Mechanics*, 615:53–92.

Tissot, G., Zhang, M., Jr., F. L., Cavalieri, A. V. G., and Jordan, P. (2016). Sensitivity of wavepackets in jets to non-linear effects: the role of the critical layer. *Journal of Fluid Mechanics*, 811:95–137.

Towne, A., Brès, G. A., and Lele, S. K. (2017). A statistical jet-noise model based on the resolvent framework. In *Proceedings of 23rd AIAA/CEAS Aeroacoustics Conference*. American Institute of Aeronautics and Astronautics. AIAA 2017-3706.

Tyndall, J. (1867). On the action of sonorous vibrations on gaseous and liquid jets. *The Philosophical Magazine*, 33:375–391.

Vera, J., Self, R. H., and Kingan, M. J. (2015). The prediction of the radiated pressure spectrum produced by jet-wing interaction. In *Proceedings of 21st AIAA/CEAS Aeroacoustic Conference*, Aeroacoustics Conferences. American Institute of Aeroacoustic and Astronautics. AIAA 2015-2216.

Viswanathan, K. (2009). Mechanisms of jet-noise generation: classical theories and recent developements. *International Journal of Aeroacoustics*, 8:355–407.

Wang, M. (1980). Wing effect on jet noise propagation. In *Proceedings of 6th Aeroacoustics Conference*, Aeroacoustics Conferences. American Institute of Aeronautics and Astronautics. AIAA 80-1047.

Wang, M. (1981). Wing effect on jet noise propagation. *Journal of Aircraft*, 18:295–302.

Way, D. and Turner, B. (1980). Model tests demonstrating under-wing installation effects on engine exhaust noise. In *Proceedings of 6th Aeroacoustics Conference*, Aeroacoustics Conferences. American Institute of Aeronautics and Astronautics. AIAA 80-1048.

White, F. M. (2005). *Fluid Mechanics*. McGraw-Hill, 5th edition.

Williams, J. E. F. (1963). The noise from turbulence convected at high speed. *Philosophical Transactions of the Royal Society A: Mathematical, Physical and Engineering Sciences*, 255:469–503.

Williams, J. E. F. and Hall, L. H. (1970). Aerodynamic sound generation by turbulent flow in the vicinity of a scattering half plane. *Journal of Fluid Mechanics*, 40:657–670.

Winant, C. D. and Browand, F. K. (1974). Vortex pairing: the mechanism of turbulent mixing-layer growth at moderate Reynolds number. *Journal of Fluid Mechanics*, 63:237–255.

Zaman, K. B. M. Q., Wang, F. Y., and Georgiadis, N. J. (2003). Noise, turbulence and thrust of subsonic free jets from lobed nozzles. *AIAA Journal*, 41(3):389–407.